

**ESTIMATION OF PRECIPITABLE WATER OVER THE
AMAZON BASIN USING GOES IMAGERY**

by

John Andrew Callahan

A thesis submitted to the Faculty of the University of Delaware in partial fulfillment of the requirements for the degree of Master of Science in Geography

Spring 2014

© 2014 John Andrew Callahan
All Rights Reserved

UMI Number: 1562375

All rights reserved

INFORMATION TO ALL USERS

The quality of this reproduction is dependent upon the quality of the copy submitted.

In the unlikely event that the author did not send a complete manuscript and there are missing pages, these will be noted. Also, if material had to be removed, a note will indicate the deletion.



UMI 1562375

Published by ProQuest LLC (2014). Copyright in the Dissertation held by the Author.

Microform Edition © ProQuest LLC.

All rights reserved. This work is protected against unauthorized copying under Title 17, United States Code



ProQuest LLC.
789 East Eisenhower Parkway
P.O. Box 1346
Ann Arbor, MI 48106 - 1346

ESTIMATION OF PRECIPITABLE WATER OVER THE
AMAZON BASIN USING GOES IMAGERY

by

John Andrew Callahan

Approved: _____
Tracy L. DeLiberty, Ph.D.
Professor in charge of thesis on behalf of the Advisory Committee

Approved: _____
Tracy L. DeLiberty, Ph.D.
Chair of the Department of Geography

Approved: _____
Nancy M. Targett, Ph.D.
Dean of the College of Earth, Ocean, and Environment

Approved: _____
James G. Richards, Ph.D.
Vice Provost for Graduate and Professional Education

ACKNOWLEDGMENTS

As with any research project, this study is the result of a team effort. There are several people who deserve acknowledgement for their support and contributions, for without them, the last page of this thesis would be the one you are reading now. I would like to thank Mr. Anthony Guillory, Mr. Ron Suggs and Dr. Gary Jedlovec (all at the NASA Marshall Space Flight Center, Huntsville, AL) for allowing me to visit their facilities and to learn the "ins and outs" of the Physical Split Window (PSW) algorithm. I especially appreciate Anthony's enthusiasm and willingness to answer my many questions and emails. I would also like to thank Elaine Prins, Cooperative Institute for Meteorological Space Studies (CIMSS), Madison, WI, for supplying the GOES imagery McIDAS areas of South America and for sharing her knowledge about the Amazon Basin.

To my committee members, Dr. Dan Leathers, Department of Geography, University of Delaware for always making himself available to me for advice and general guidance, and never turning down a question of mine, no matter how trivial. And to Dr. Tom McKenna, Delaware Geological Survey, for the many hallway conversations and insights about both the practice and theory of remote sensing and for helping me think about water from a new perspective (it is not always "from the ground up.") I would like to thank Anita Schwartz, UD Information Technologies, for her help in working with the UD thesis templates and expert LaTeX advice, and to my current and former DGS Directors, Dr. David Wunsch and Mr. John Talley, respectively, for their encouragement and support in furthering my education.

I would like to thank my advisor Dr. Tracy DeLiberty. It was Tracy's enthusiasm and encouragement that initiated my transition from the Department of Physics to Geography early in graduate school as well as inspired and encouraged my own interests

in climatology and remote sensing. I especially want to thank Tracy for her continued support. Many years have come and gone since the beginning of this research. Life happened in between, as it always does, and Tracy welcomed me back with open arms to complete this work.

Last but not least I would like to thank my family. To my parents, it must have been hard to watch me leave home to start my own life. An appreciation and respect I didn't realize at the time, particularly to pursue a career that is continuously challenging, often under-appreciated, with little pay and even less sleep. To my children, Andrew and Emily, who many times had to "leave daddy alone" during many long hours at night and on the weekends. Mostly I'd like to thank my wife, Tina, for giving encouragement, inspiration and patience along the way. We met in graduate school, started our careers together, got married, bought a house and had two kids together, and then restarted our careers together. Thank you for the time, love, understanding, everything else I ever needed to finally bring this work to fruition.

TABLE OF CONTENTS

LIST OF TABLES	viii
LIST OF FIGURES	x
ABSTRACT	xiv
 Chapter	
1 INTRODUCTION	1
1.1 Significance of Water Vapor	1
1.1.1 Measuring Atmospheric Water Vapor	3
1.1.2 Definition of Precipitable Water	7
1.2 Significance of the Amazon Basin	8
1.2.1 Hydrology	12
1.2.2 Deforestation Effects on Climate	14
1.3 Objectives of Study	18
2 REVIEW OF AMAZON BASIN FIELD STUDIES	20
2.1 The Amazon Basin Region	20
2.2 Deforestation in the Amazon	22
2.3 Regional Field Campaigns	31
2.4 Local Hydrometeorological Studies	37
3 REVIEW OF PRECIPITABLE WATER MEASUREMENT TECHNIQUES	44
3.1 Satellite-based Remote Sensing Methods	44
3.1.1 Thermal-IR Studies	52
3.1.2 Near-IR Studies	59

3.1.3	Optical Methods	61
3.1.4	Microwave Studies.....	63
3.2	Global Positioning System (GPS) Technique	64
3.3	Surface-based and Other Methods	68
3.4	Global Water Vapor Data Inventories	72
3.4.1	Satellite-based	72
3.4.2	Radiosondes	75
3.4.3	Others	82
4	STUDY DATA	85
4.1	GOES Imagery	85
4.1.1	GOES-7 VAS and GOES-8 Imager	86
4.2	NCEP/NCAR Reanalysis Model	90
4.3	Radiosonde Observations in the Amazon	94
4.4	NVAP Data	95
5	METHODOLOGY	100
5.1	Geographic Extent of Study Area	101
5.2	Calculation of Precipitable Water from Radiosondes	103
5.3	Preparation of First Guess Estimates	105
5.4	Performing the Precipitable Water Retrievals	106
5.4.1	Regional Field Retrievals	106
5.4.2	Individual Location Retrievals	113
5.5	The Physical Split Window (PSW) Technique	114
5.5.1	Formulation of the PSW Technique	115
6	PSW TECHNIQUE PERFORMANCE	119
6.1	PSW-Derived Precipitable Water vs Radiosonde Observations	121
6.1.1	Comparison by Time of Day	124
6.1.2	Comparison by Month and Year	126
6.1.3	Comparison by Location	131

7	ANALYSIS OF PRECIPITABLE WATER FIELDS	136
7.1	Regional Precipitable Water Climatology	138
7.2	PSW-Derived Precipitable Water Monthly Fields	142
7.2.1	Spatial Distribution of PSW-Derived Precipitable Water	142
7.2.2	PSW-Derived Precipitable Water Daily Timeseries	146
7.3	Diurnal Behavior of Precipitable Water	151
7.3.1	Diurnal Variations	151
7.3.2	Diurnal Range Variations	161
8	CONCLUSION	169
8.1	Summary and Discussion	169
8.2	Further Research	176
8.3	Conclusion	178
	BIBLIOGRAPHY	179
	Appendix	
	RELEVANT ACRONYMS AND ABBREVIATIONS	203
A.1	Organizations and Programs	203
A.2	Field Experiments	204
A.3	Satellites and Sensors	205
A.4	Datasets	206
A.5	Miscellaneous	207

LIST OF TABLES

2.1	Annual deforestation rates for the Brazilian Amazon for 1977 through 2012	29
2.2	Summary of intensive field campaigns in the Amazon	36
3.1	Relevant infrared wavelength bands on common satellite sensors for monitoring atmospheric water vapor	49
3.2	Summary of global data inventories containing precipitable water. . .	84
4.1	Bandwidths and IGFOV spatial resolution for comparable channels on GOES-7 VAS-MSI mode and GOES-8 Imager.	89
4.2	Sensor characteristics of GOES-7 VAS and GOES-8 Imager.	90
4.3	Radiosonde sites in and around the Amazon Basin obtained from the NOAA CARDS network for the present study.	95
4.4	Radiosonde data report for each station for June 1988.	96
4.5	Radiosonde data report for each station for October 1988.	97
4.6	Radiosonde data report for each station for June 1995.	97
4.7	Radiosonde data report for each station for October 1995.	98
6.1	Statistics for PSW-derived vs radiosonde precipitable water including observations from all months and stations.	122
6.2	Statistics for PSW-derived vs radiosonde precipitable water observations for 12Z and 24Z, including data from all months and stations.	125

6.3	Statistics for PSW-derived vs radiosonde precipitable water observations for each month and year combination, including data from both times and all stations	128
6.4	Statistics for PSW-derived vs radiosonde precipitable water observations for each station, including data from both 0Z and 12Z launch times and all months	131
7.1	Monthly averages of PSW-derived and NVAP precipitable water in each zone for each month and year	143
7.2	Average peak time of day for precipitable water in each zone for each month and year.	151
7.3	Monthly mean diurnal range of PSW-derived precipitable water in each zone for each month and year	161
7.4	Monthly mean diurnal range of PSW-derived precipitable water in each zone for each month and year as percentage of zone mean	161

LIST OF FIGURES

1.1	Components of the hydrologic cycle.	3
1.2	Global radiosonde distribution.	5
1.3	Digital Elevation Model (DEM) map of South America	9
1.4	Political and land cover map of South America	10
1.5	Land cover map of South America legend	11
2.1	Causes of Deforestation in the Brazilian Amazon, 2000 - 2005	23
2.2	Annual deforestation rates of the Brazilian Amazon for the years 1988 through 2012	28
2.3	Large-scale Biosphere-Atmosphere (LBA) experiment sites	32
3.1	Atmospheric radiation transmittance/absorption spectrum for 0.2 μm to 70 μm	46
3.2	IGRA annual global radiosonde station density from 1940 through 2003.	79
3.3	IGRA global radiosonde network map	80
3.4	Global Climate Observing System (GCOS) Upper-Air Network (GUAN) global map as of January 2013	81
4.1	Images of the GOES-7 (left) and GOES-8 (right) satellites.	87
4.2	Atmospheric transmittance focused on the thermal infrared split window region, 10 μm to 13 μm	91

4.3	Map of the radiosonde sites, listed in table 4.3, in and around the Amazon Basin obtained from the NOAA CARDS network for the present study.	96
5.1	Outline of the Amazon River Basin and surrounding South American countries.	102
5.2	Geographic extent of the GOES satellite imagery and output (0.5° data grid for the present study.	103
5.3	The expected random noise (in mm) in the PSW-derived precipitable water (solid line) and the horizontal resolution (dashed line) versus the linear template size used for neighborhood averaging during retrievals, where 4 represents a 4x4 pixel template. (Guillory et al., 1993)	107
5.4	Example PSW retrieval field for June 6, 1988 at 21Z.....	111
6.1	PSW-derived vs radiosonde precipitable water scatter plot and linear regression line of observations from all months and stations.	123
6.2	PSW-derived vs radiosonde precipitable water histogram of residuals for all months and stations.	124
6.3	PSW-derived vs radiosonde precipitable water scatter plots and linear regression line based on time of day of radiosonde launch, 12Z (left) and 24Z (right).	126
6.4	PSW-derived vs radiosonde precipitable water box plots based on time of day of radiosonde launch, 12Z and 24Z.....	127
6.5	PSW-derived vs radiosonde precipitable water box plots of observations in October and June, 1988 and 1995.	129
6.6	PSW-derived vs radiosonde precipitable water scatter plots and linear regression line based on month of observation, June (left) and October (right), for both 1988 and 1995 data combined	129
6.7	PSW-derived vs radiosonde precipitable water scatter plots and linear regression line based on year of observation, 1988 (left) and 1995 (right), for both June and October month data combined	130

6.8	PSW-derived vs radiosonde precipitable water box plots based on radiosonde stations 1 - 3 (top) and 4 - 6 (bottom), including data from both launch times and months	133
6.9	PSW-derived vs radiosonde precipitable water scatter plots and linear regression line of all observations for stations 1 and 2.	134
6.10	PSW-derived vs radiosonde precipitable water scatter plots and linear regression line of all observations for stations 3 and 4.	134
6.11	PSW-derived vs radiosonde precipitable water scatter plots and linear regression line of all observations for stations 5 and 6.	135
6.12	Land cover map with radiosonde stations	135
7.1	Local zones used in the analysis of precipitable water fields	137
7.2	Monthly climatology of precipitable water in the Amazon from the NASA Water Vapor Project (NVAP)	140
7.3	Monthly climatology of cloud cover in the Amazon from International Satellite Cloud Climatology Program (ISCCP)	141
7.4	PSW-derived precipitable water fields for June and October, 1988 and 1995	144
7.5	Difference maps between PSW-derived and NVAP precipitable water fields for June and October, 1988 and 1995	145
7.6	Daily mean PSW-derived and NVAP precipitable water in each zone for June 1988	147
7.7	Daily mean PSW-derived and NVAP precipitable water in each zone for October 1988.	148
7.8	Daily mean PSW-derived and NVAP precipitable water in each zone for June 1988-95	149
7.9	Daily mean PSW-derived and NVAP precipitable water in each zone for October 1995.	150
7.10	Monthly 3-hourly mean PSW-derived precipitable water in each zone for June 1988	153

7.11	Monthly 3-hourly mean PSW-derived precipitable water in each zone for October 1988.....	154
7.12	Monthly 3-hourly mean PSW-derived precipitable water in each zone for June 1995	155
7.13	Monthly 3-hourly mean PSW-derived precipitable water in each zone for October 1995.....	156
7.14	Monthly 3-hourly mean number of valid retrievals in each zone for June 1988	157
7.15	Monthly 3-hourly mean number of valid retrievals in each zone for October 1988	158
7.16	Monthly 3-hourly mean number of valid retrievals in each zone for June 1995	159
7.17	Monthly 3-hourly mean number of valid retrievals in each zone for October 1995.....	160
7.18	Monthly mean fields of the diurnal range of PSW-derived precipitable water for June and October, 1988 and 1995	164
7.19	Daily mean diurnal range of PSW-derived precipitable water in each zone for June 1988	165
7.20	Daily mean diurnal range of PSW-derived precipitable water in each zone for October 1988	166
7.21	Daily mean diurnal range of PSW-derived precipitable water in each zone for June 1995	167
7.22	Daily mean diurnal range of PSW-derived precipitable water in each zone for October 1995	168

ABSTRACT

The Amazon Rainforest is the largest continuous rainforest on Earth. It holds a rich abundance of life containing approximately one-half of all existing plant and animal species and 20% of the world's fresh water. Climatologically, the Amazon Rainforest is a massive storehouse of carbon dioxide and water vapor and hosts hydrologic and energy cycles that influence regional and global patterns. However, this region has gone through vast land cover changes during the past several decades. Lack of conventional, in situ data sources prohibits detailed measurements to assess the climatological impact these changes may cause. This thesis applies a satellite-based, thermal infrared remote sensing algorithm to determine precipitable water in the Amazon Basin to test its applicability in the region and to measure the diurnal changes in water vapor.

Imagery from the GOES geostationary satellite and estimated atmospheric conditions and radiance values derived from the NCEP/NCAR Reanalysis project were used as inputs to the Physical Split Window (PSW) technique. Retrievals of precipitable water were made every 3 hours throughout each day from 12Z to 24Z for the months of June and October, 1988 and 1995. These months correspond to when the atmosphere is not dominated by clouds during the rainy (wet) season or smoke and haze during the burning (dry) season. Monthly, daily, and diurnal aggregates of precipitable water fields were analyzed spatially through seven zones located uniformly throughout the region. Monthly average precipitable water values were found to be 20 mm to 25 mm in the southeast and 45 mm to 50 mm in the northwest zones. Central and northwest zones showed little variation throughout the day with most areas peaking between 15Z and 21Z, representing early to late afternoon local time. Comparisons were made to nearby, coincident radiosonde observations with r ranging from 0.7 to 0.9 and MAE from 6 mm to 12 mm.

Chapter 1

INTRODUCTION

The Amazon River Basin is the world's largest hydrologic system (Marengo et al., 2002) with a complex mixture of precipitation, evapotranspiration, soil moisture, surface runoff, and atmospheric water vapor. Covering over 6.0 million km², the Amazon rainforests (generally also known as Amazonia or simply the Amazon Basin) constitutes over half of the world's remaining rainforests, and this region has gone through significant land cover changes since the 1970s. Changes in the local water and energy balances of the Amazon significantly affect the regional and global circulation and balances of water and energy (D'Almedia et al., 2007). Although intense scientific study in this area has taken place for several decades, observations of the components of the hydrologic cycle are spatially and temporally sparse and also unreliable when depicting long-term trends. Remote sensing techniques and modeling studies try to overcome this weakness in the observational network, but they are still being validated and results interpreted. With increasing interest and discussion over environmental concerns, such as global warming, sea-level rise, frequency and intensification of severe storms, and in particular, the deforestation of the rainforests, the amount of moisture present in our atmosphere is an extremely important factor in understanding and predicting our future climate.

1.1 Significance of Water Vapor

Water vapor is arguably one of the most important variables of the human-Earth-climate system. Atmospheric water vapor is a storage component in the hydrologic cycle and the bridge between precipitation and evapotranspiration from the Earth's surface (land and ocean.) Figure 1.1 shows the components of the hydrologic

cycle. Water vapor is intricately linked to cloud formation and the production of rain, which fills streams, rivers, reservoirs, groundwater, and other fresh-water sources, and is critical for the existence and abundance of life. Areas located in the humid tropics, such as the Amazonian Rainforest, experience significantly high atmospheric moisture and large amounts of rainfall.

Atmospheric moisture also plays a significant role in many other critical atmospheric processes, such as the greenhouse effect, global warming, atmospheric dynamics, cyclogenesis, and the global energy budget. It correlates (positively) very well with the precipitation and tropospheric temperature in the tropics and sub-tropics (Trenberth, 2011; Sun and Held, 1996), is closely related to both the health and vigor of surface vegetation (Shukla and Mintz, 1982), and the development of severe weather (Liu et al., 1995). Condensation of water vapor into precipitation provides latent heating which dominates the structure of tropospheric diabatic heating (i.e, the heating of the troposphere by any forces not associated with the vertical rising or sinking of the air) (Trenberth et al., 2007b). Water vapor is also the dominant gas contributing to the infrared radiation absorption by the atmosphere (greenhouse effect), accounting for about 60% of the natural greenhouse effect for clear skies (Kiehl and Trenberth, 1997), thereby providing additional warmth for the earth's surface.

Owing to its infrared absorption properties, water vapor also provides the largest positive feedback in model projections of temperature increases in climate change scenarios (Held and Soden, 2000). As temperature of the atmosphere increases, the saturation vapor pressure of the atmosphere also increases according to the Clausius-Clapeyron equation. Therefore, even if the relative humidity remains relatively constant (the ratio of the water vapor concentration to its maximum saturated amount) in a warming scenario, total water vapor amounts will generally increase as the temperature increases (Trenberth et al., 2007a; ESA, 2010; Randall et al., 2007). Assuming constant relative humidity, typical values are about 7% increase of total water vapor for every 1° C warming.

Despite the importance of water vapor in nearly all aspects of the Earth-climate

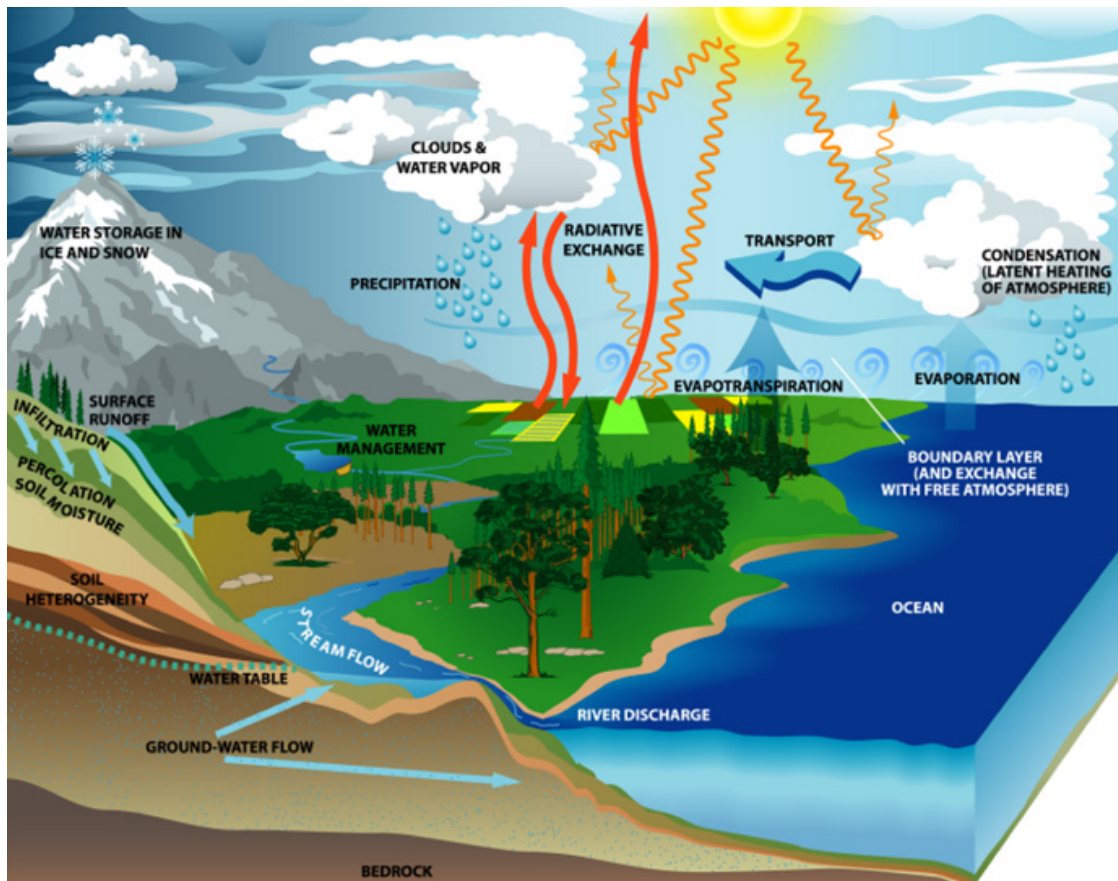


Figure 1.1: Components of the hydrologic cycle. Courtesy NASA/JPL-Caltech.

system, relatively little is known about its contributions to the global hydrological cycle (Trenberth and Guillemot, 1995). Ross and Elliott (2001) also state that the distribution and variability of water vapor in the troposphere is not completely understood, and a major reason is the difficulty in reliably and continuously monitoring its spatial and temporal distribution.

1.1.1 Measuring Atmospheric Water Vapor

The most common method for determining atmospheric water vapor is by direct in situ measurement. Surface-based hygrometers measure the humidity or dewpoint at one location in space and little information can be extracted outside of its immediate

vicinity. Although relationships can be made to estimate water vapor from these measurements, such as by statistical correlations, or by indirect measurement, such as delays in GPS signal timing or infrared absorption data, direct measurement at vertical levels throughout the atmosphere, via radiosondes, is ultimately preferred. Radiosondes are balloon-like vehicles carrying temperature, humidity, and pressure instruments vertically sounding the atmosphere, typically up to the tropopause level. (The term *sonde* is derived from the French word for *probe*.) Water vapor amounts derived from radiosondes constitute the longest running source of tropospheric moisture data (Durre et al., 2009). This data began in the 1930s in the United States, with more regular sampling frequencies beginning after WWII in the mid-1940s (Ross and Elliott, 1996; DuBois et al., 2002; Trenberth et al., 2007b) and nearly global coverage by 1958 (Trenberth et al., 2007b). They are generally considered the most accurate and reliable estimate of atmospheric meteorological parameters when compared against values derived from other measuring techniques (Trenberth et al., 2005, 2007b; Elliott et al., 2002; Seidel et al., 2011).

Unfortunately, issues exist when analyzing radiosonde data. In the United States, the National Weather Service (NWS) supports 102 radiosonde sites located in the contiguous United States and Alaska, the Pacific Islands, and the Caribbean Cooperative Hurricane Upper-air Stations. Globally, there are over 800 upper-air observation stations (NWS, 2011). Nearly all of the observations are taken at the same time each day (00Z and/or 12Z time of day), 365 days a year, although when severe weather is expected, additional soundings may be taken at a select number of stations (NWS, 2011; Elliott, 1995). This leaves a sampling bias without the ability to capture the diurnal variation, which is significant for temperature and water vapor. Additionally, most of these stations are located in terrestrial, populated locations with few being launched from ships or in remote areas, leaving large, unpopulated areas under-represented, such as much of the oceans, South America, and central Africa, as shown in Figure 1.2 (Dai et al., 2002; Trenberth et al., 2007b; McCarthy et al., 2009). The Amazon is an excellent example of both issues with being remote enough to have

few reliable radiosonde observations and having launch times of 0Z and 12Z representing 8:00 am and 8:00 pm local time (for the western half of the region), and 9:00 am and 9:00 pm (for the eastern half), respectively, that does not capture the diurnal peak water vapor values or convective activity. Additionally, the usefulness of radiosonde data for long-term studies is limited by changing technology of the instrument itself and altering data processing procedures with time (Wang et al., 2007).

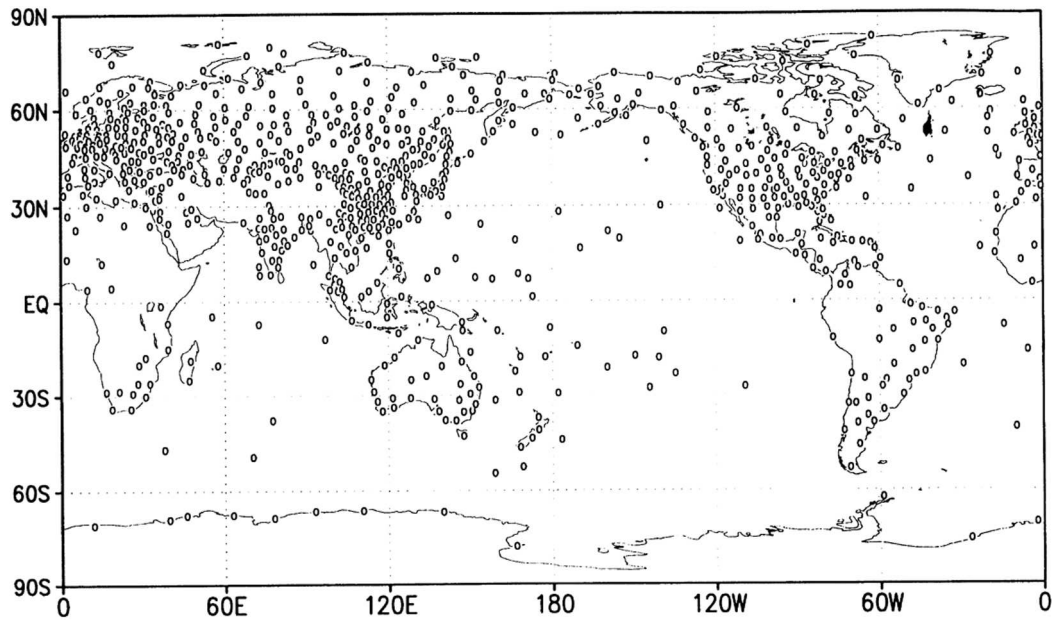


Figure 1.2: Global radiosonde distribution. Location of land-based radiosonde stations that have relatively long records during 1973-94 period. Also included are some Ocean Weather Stations, most of which are no longer active. Figure taken from Elliott, 1995.

Another common method for estimating the quantity of water vapor in the atmosphere is through the use of remote sensing. Remote sensing is a technology used to observe characteristics of an object that is not in physical contact with the measuring device (i.e., the observer does not directly interact with the object being observed.) In typical meteorological or climatological remote sensing platforms, the sensors record the amount of electromagnetic radiation emanating from, or reflected by, the Earth. Sensor devices that record the electromagnetic radiation can be installed

on ground-based towers (for local-scale observations), carried on weather balloons, mounted to the bottom of airplanes, or on satellites that orbit the Earth (for regional- and hemispheric-scale observations.) In fact, the term "remote sensing" was coined by Ms. Evelyn Pruitt in the mid-1950s, a geographer/oceanographer at the US Office of Naval Research, to take into account the new views from space obtained by the early meteorological satellites, which were obviously more "remote" from their Earth surface targets than the airplanes most often used up to that time ([Short, 2009](#)).

Satellites have the potential to provide high spatial and temporal resolution measurements of water vapor not available by the radiosonde network or through airborne or surface-based studies. Geostationary satellites orbit above a fixed position along the equator (at altitudes of approximately 36,000 km) and continuously monitor the same region on the Earth's surface. Polar-orbiting satellites orbit the Earth at altitudes typically less than 1000 km, providing a much higher spatial resolution than geostationary satellites, and cross close to the north and south poles. Orbital periods of polar orbiters are on the order of approximately 100 minutes, capable of generating global coverage maps weekly or even daily. Energy received at the satellite sensor is composed of radiation originating from both the Earth's surface as well as being absorbed and re-emitted from various levels in the atmosphere which the radiation traveled through, making satellites an ideal platform for monitoring the Earth's dynamic meteorology. Remote sensing from satellites for Earth observation has been in operation since the 1970s, with the US National Oceanic and Atmospheric Administration (NOAA) Geostationary Operational Environmental Satellite (GOES) and NASA Land Satellite (Landsat) programs.

In addition to the high spatial and temporal resolution that satellite imagery can provide, possibly the most significant advantage of remote sensing is the ability to measure large regions, such as the open oceans, deserts, and tropical rainforests, with little to no ground access for humans. Remote sensing techniques, being completely digital and automated, also offer very high statistical precision by averaging the millions of observations from individual pixels ([Wentz and Schabel, 2000](#)), and the

techniques can be modified without affecting the raw source observations. Though remote sensing data may not have a long enough time series to conduct optimal climate change analysis, they do provide a more unique, larger scale perspective than do surface observations. Elliott (1995, p. 363) emphasizing this by stating,

”From the standpoint of monitoring climate change, moisture may be better monitored above the surface rather than at the surface. Changes aloft should more readily reflect broad scale changes rather than reflect changes in local conditions.”

1.1.2 Definition of Precipitable Water

Total columnar water vapor, better known as total columnar precipitable water or simply precipitable water, is a commonly used measure of atmospheric moisture. Precipitable water is defined as the total amount of water vapor in a 1.0 m^2 (cross-section) column of atmosphere from the ground surface to the top of the atmosphere (TOA). Normally, precipitable water is given as the height, in millimeters (mm) or centimeters (cm), the water would attain if all of the water vapor in the column were condensed into liquid. This can also be thought of as a volumetric amount (m^3) of liquid water, or as a density, kg of liquid water per cubic m^3 of air. It is sometimes labeled as kg m^{-2} , which is identical to mm in a 1.0 m^2 cross-section.

Precipitable water is calculated by integrating specific humidity, kg of water vapor per kg of moist air, from the surface to the TOA. It is also common to calculate it by substituting mixing ratio, kg of water vapor per kg of dry air, for specific humidity.

Precipitable water may be computed by integrating radiosonde atmospheric data (temperature and moisture profiles) vertically throughout the atmosphere. A large percentage of radiosondes include data measured from the ground surface to at least the 100 mb level ([NOAA NESDIS, 2011](#)) (roughly 11 km in altitude near the poles to 17 km at the equator) which captures nearly all of the water vapor content in the atmospheric column. (Calculations for the present study are based on radiosonde profiles of pressure, temperature, and relative humidity, described in Section 5.2.)

1.2 Significance of the Amazon Basin

The Amazonian Rainforest, located in the northern half of South America, is the largest continuous rainforest in the world (Margulis, 2004; Correia et al., 2007). It represents about 56% of all broadleaf forests on Earth with very low land elevations for much of the central area. Andes Mountains are to the west with elevations over 5000 meters above sea level, such as near the source of the Amazon River. Figure 1.3 shows a digital elevation model (DEM) for South America. The region transitions from the tropical rainforest in the center and northwest to the cerrado (savannah) region in the south and east. The cerrado is characterized by a semi-humid tropical climate with an enormous range of plant and animal biodiversity lying within the Brazilian Highlands (higher elevation than the flood plains in the center of the basin.) Figure 1.4 shows the various types of vegetative land cover in the region with Figure 1.5 displaying the map legend. Although most of the region experiences a seasonal cycle of wet and dry periods, temperatures do not experience this variability, with daily maximum temperature staying within a few degrees of 28°C. Temperature differences between day and night are greater than they are between seasons, common to areas in the tropics.

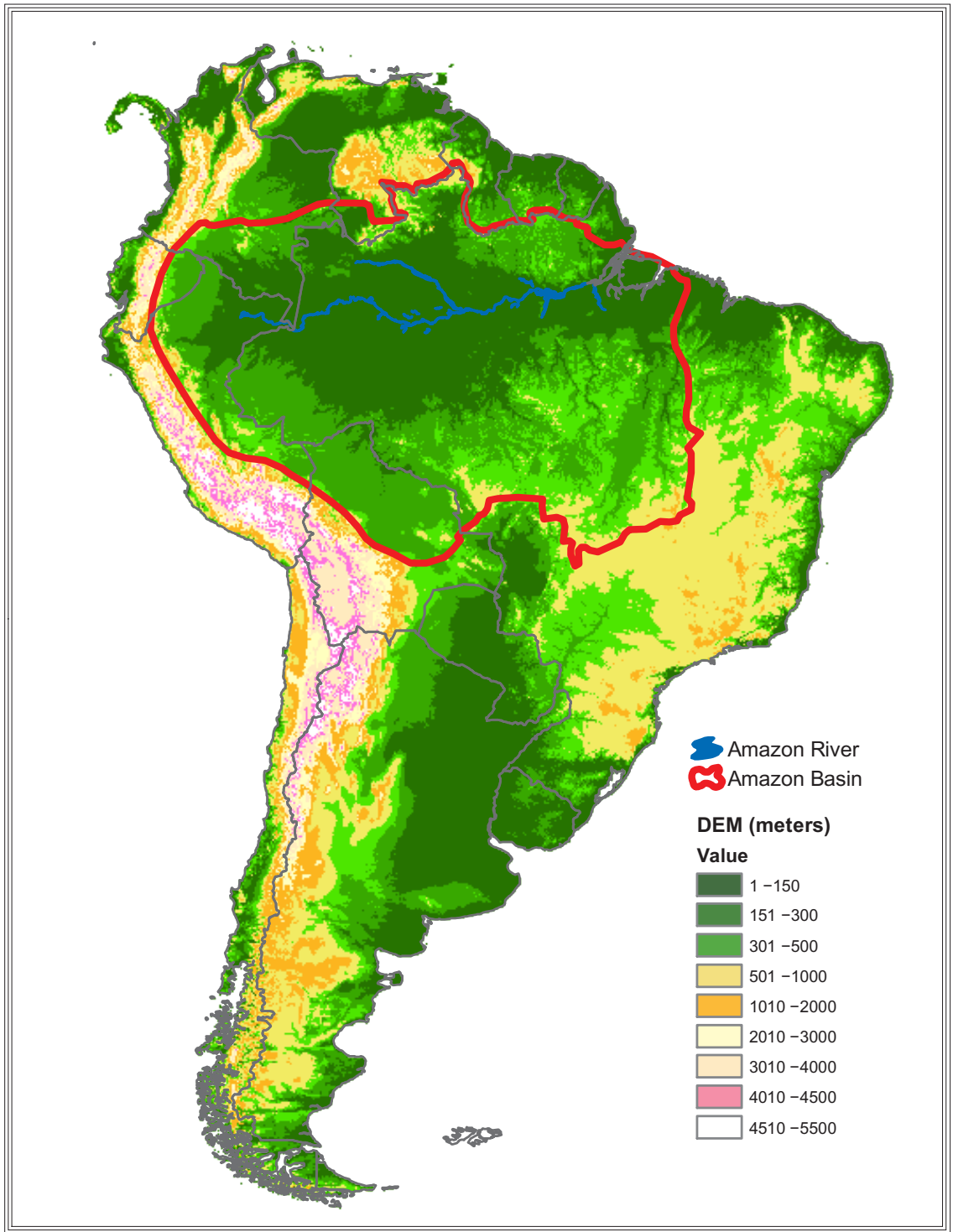


Figure 1.3: Digital Elevation Model (DEM) map of South America. The Amazon Basin is delineated in red. Source: Digital Chart of the World



Figure 1.4: Political and land cover map of South America. Source: European Commission Global Land Cover 2000 database ([European Commission, 2003](#)).

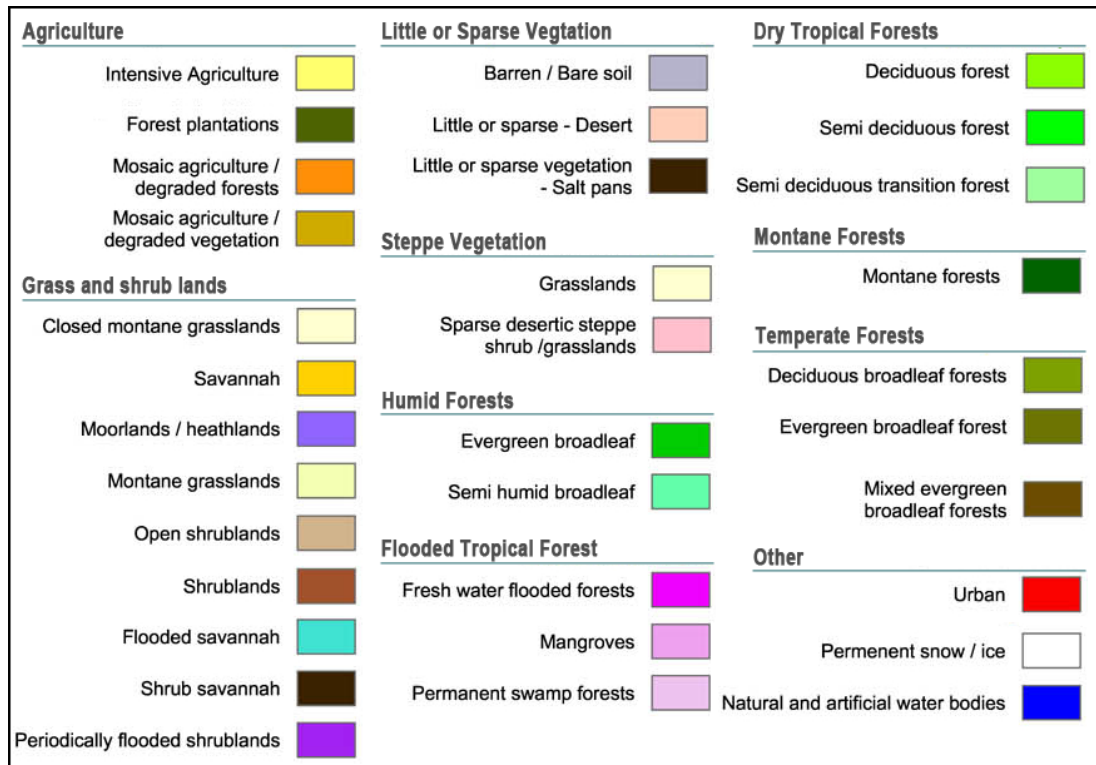


Figure 1.5: Land cover map of South America legend. Source: European Commission Global Land Cover 2000 database ([European Commission, 2003](#)).

Tropical rainforests are well-known for their enormous biodiversity. More than half of the world's estimated 10 million species of plants, animals and insects live in the tropical rainforests even though they cover only 5% of the Earth's surface. The Amazon forests hosts more than one third of all species in the world. This includes some 2,500 tree species and nearly 30,000 plant species ([The World Bank, 2011](#)). More than 2,100 species of fish have been identified in the Amazon River and its tributaries, which is greater than the number of fish species in the entire Atlantic Ocean ([Albert and Reis, 2011](#)).

The Amazon Rainforest has been described as the "Lungs of our Planet" because it provides the essential environmental service of continuously recycling carbon dioxide into oxygen. More than 20% of the world oxygen is produced in the Amazon Rainforest ([Taylor, 2004](#); [UNEP, 2008](#)). It acts as a sink of atmospheric moisture, with precipitation exceeding evapotranspiration, in most areas of the basin. The region is also considered both a source and a sink of carbon, with photosynthesis as the sink and biomass burning as the source. In fact, the Amazon is the world's largest store of aboveground carbon ([Keller et al., 2009](#)). In general, tropical forests account for approximately 40% of the terrestrial carbon stocks with about a 3:1 ratio of above ground to below ground biomass ([Phillips et al., 2007](#)).

1.2.1 Hydrology

The hydrologic cycle of the Amazon region plays a critical role in the water balance and in the functioning of the regional and global circulation and climate ([Marengo et al., 2002](#); [Marengo, 2005](#); [da Rocha et al., 2004](#)). The basin of the Amazon River is the largest in the world covering approximately 6,100,000 km² to 7,165,281 km², depending on the measurement technique. Moreover, it is the single largest source of freshwater in the world, holding up to one-fifth (20%) of all the Earth's fresh water that flows on its surface ([Ferreira, 1987](#); [Margulis, 2004](#); [UNEP, 2008](#); [Marengo, 2007](#)). By volume, the Amazon River discharges the largest volume of water of any river. Average discharge is from 200,000 m³ s⁻¹ to 220,000 m³ s⁻¹ with peak amounts during

the rainy season up to $300,000 \text{ m}^3 \text{ s}^{-1}$ (Marengo, 2007; UNEP, 2008). This amount is more than the discharge of the next 9 largest rivers by volume combined, not including Amazon tributaries (Wohl, 2008). Freshwater discharged from the Amazon is lighter than the salty water in the Atlantic Ocean and typically alters the color and salinity content of the surface ocean waters. The plume of water can extend up to 300 km to 400 km away from the mouth of the river.

The Amazon region receives a vast amount of annual rainfall, much of it coming from afternoon convective showers. Basin-averaged precipitation totals are roughly 2200 mm yr^{-1} with regions in northwest Amazonia receiving as high as 6000 mm yr^{-1} (Scott Webber, personal communication, 1998) and southeast Amazonia receiving as low as 1500 mm yr^{-1} . Marengo (2007) analyzed the spatial distribution of rainfall in the Amazon and identifies three major centers of precipitation: northwest Amazonia receiving about 3600 mm yr^{-1} , central Amazonia around 5°S receiving about 2400 mm yr^{-1} , and close to the mouth of the Amazon near the city of Belém receiving about 2800 mm yr^{-1} . Trenberth (1998) estimates that, for extratropical cyclones, on average about 70% of the precipitation comes from moisture that was already in the atmosphere at the time the storm formed, while the rest comes from surface evapotranspiration during the course of the storm. Averaging over longer periods of time, 50% of the precipitation in the region comes from local evapotranspiration with the remaining 50% coming from moisture advection off the Atlantic Ocean (Nobre et al., 1991; Marengo, 2007).

Much of the Amazon River and many of its tributaries are characterized by extensive flooding during the rainy or wet season each year. Peaks of the wet season generally occur earlier as you move from north to south through the Amazon, associated with the movement of the ITCZ. The northwest part of Amazonia receives abundant rainfall throughout the year, with the peak of the rainy season around April to June. The south and east parts of Amazonia have more pronounced wet and dry seasons, with the peak of the rainy season in southern Amazonia in December to February. Central Amazonia rainy season peaks in March to May (Marengo, 2007). These flooded areas are critical to the diversity of the vegetation, flora and fauna of the area, and hence

the local population's way of life.

In terms of hydrologic efficiency and precipitation recycling, the Amazon Rainforest is one of the most efficient on Earth and has been studied quite intensively in the past (Lettau et al., 1979). Large amounts of precipitation cycle quickly into the soil and into the water table. Bruno et al. (2006) confirmed that the zone of active water withdrawal extended to a depth of at least 10 m and found indications of a vertical upward movement of water to the top 1 meter of soil. The Bruno et al. (2006) study, as well as others (da Rocha et al., 2004; Karam and Bras, 2008), found very little difference in evapotranspiration during the dry vs wet seasons, altering the previously held ideas that the lack of rain during the dry season was the limiting factor in water balance causing decreases in evapotranspiration.

The Amazonian hydrologic cycle seems to be extremely robust and very well adapted to the intense wet seasons and prolonged dry season, likely due to its enormous size. However, it is yet to be known whether anthropogenic modifications to the land-surface (e.g., deforestation) can cause permanent changes to the local and region's hydrologic cycle.

1.2.2 Deforestation Effects on Climate

Deforestation and rapid changes in land cover have been occurring in the Amazon region since the late 1960s, at least initially driven by government practices to encourage settlement and expand the country's agricultural sector and economic activities (Skole et al., 1994; Butler, 2008; Rust, 2011). One such example is the completion of the Trans-Amazonian highway in 1972, one of Brazil's largest government projects. The natural ecosystem of the region is rainforest and many of the areas have been turned into pasture or agricultural land. When these types of land cover modifications take place, unpredictable changes may occur in atmospheric conditions, especially in water vapor concentration (Gash et al., 1996). Surface albedo, surface roughness, and root depth change, as do evapotranspiration and the amount of carbon added to the atmosphere through biomass burning, all of which affect atmospheric absorption and

other microphysical processes, ultimately manifesting as changes in the energy and hydrologic budgets (Betts et al., 2009). In Brazil, deforestation and forest fires together are responsible for 75% of their greenhouse gas emissions (Fund, 2009). Marengo (2002) states that it is reasonable to expect a significant impact on the regions’s climatology and hydrology from large-scale land cover changes.

There have been many studies on the effects of deforestation on the local and global climate. The clearing of forests will likely have a significant impact on components of the local hydrology cycle, such as evapotranspiration, precipitation and precipitable water (Sapucci et al., 2007; Marengo, 2007). There is general agreement among most General Circulation Models (GCMs), at scales of roughly 2° to 5°, predicting that Amazon deforestation leads to decreased evapotranspiration, decreased rainfall, a reduction in vertically integrated water vapor, and increased surface temperature (Werth and Avissar, 2002; Nobre et al., 2009; Avissar and Werth, 2005; Negri et al., 2004; da Silva and Avissar, 2006; Marengo et al., 2009). Essentially, these reductions are in response to decreased soil moisture in the winter/dry season and the continental convergence of moisture transport (Saad et al., 2010). Using several data sources, Chen (2001) suggests that the full effects of Amazonian deforestation have been masked by long-term climatic changes. They found an increase in moisture convergence into the Amazon region over the past few decades, which offset some of the predicted rainfall reduction.

However, mesoscale resolution models fail to find the same pattern as the GCM simulations (D’Almedia et al., 2007; Marengo, 2007). They show complex patterns of change, some areas with increasing and others with decreasing precipitation (Gullison et al., 2007). The coarse spatial resolution GCMs are dependent upon parameterizations of numerous subgrid physical processes and they fail to capture smaller scale circulations, which are critical factors in convective precipitation (da Silva and Avissar, 2006). It’s found that the shape, size, and pattern of the deforested lands influences the local and regional circulation, and therefore precipitation changes by different amounts (Nobre et al., 2009; Avissar and Werth, 2005). Unfortunately, many

of the smaller-scale models provide contrasting results when compared to each other or to coarser GCMs, and Saad (2010) makes the argument that the question of rainfall changes due to Amazonian deforestation remains open.

Nobre (2009) finds that in deforestation scenarios, the resultant ocean-atmosphere circulation changes lead to enhanced El Niño Southern Oscillation (ENSO) activity over the Pacific, which in turn further decreases the rainfall over the Amazon. Avissar (2005) demonstrates deforestation of Amazonia and Central Africa severely reduces rainfall in the lower U.S. Midwest during the spring and summer seasons and in the upper U.S. Midwest during the winter and spring, respectively.

From observational experiments, changing the land surface from forest to grassland alters the meteorological conditions locally. Numerous studies have demonstrated the local impacts of deforestation in forested regions (Shuttleworth, 1988; Shuttleworth et al., 1991; Marengo et al., 1997; Zeng et al., 1996; Zhang and Henderson-Sellers, 1996; O'Brien, 1995; Lean and Rowntree, 1993; Nobre et al., 1991; Mantovani and Setzer, 1997; Saad et al., 2010). O'Brien (1996), for example, describes and quantifies three primary effects of deforestation related to the energy balance:

- increases in the ratio of sensible heat to latent heat transfer (Bowen ratio) from the surface to lower atmosphere (0.43 to 0.81) caused by decreased evapotranspiration,
- increases in surface reflection caused by increased albedo (0.12 for forest to 0.20 for grass),
- decrease in momentum transfer due to a dramatic decrease in roughness length (2.65 m for tree tops to 0.12 m for grass).

Bonan (2008) states that in addition to an increase in surface albedo and a reduction of transpiration, a net release of CO_2 increases the heat-trapping capacity of the atmosphere that also provides a local positive feedback on temperature increase. Several studies have shown an increase in convective development and precipitation

over deforested areas (Cutrim et al., 1995; Wang et al., 2009; Negri et al., 2004). The mesoscale circulations induced by land-cover changes, caused by thermal gradients between forest and pasture sites, is termed the deforestation breeze. This lifting from the deforestation breeze causes shallow but active (precipitation generating) convection over the deforested areas, although with smaller amounts of energy compared with the deeper convection over the forested areas (Wang et al., 2009). Avissar (2002) suggested while precipitation does increase with increasing deforestation, after a certain unknown threshold, the trend would reverse and precipitation would decrease with further deforestation.

Other geophysical changes due to deforestation that have been reported by either observational or modeling studies are decrease in rooting depth, leaf area index (LAI), and vegetation fraction cover and increases in stomatal and canopy resistance (Xue et al., 1996; Sud et al., 1996; Eltahir and Bras, 1994). Bastable (1993) found an intensified diurnal signature in pasture areas for wind speed, air temperature, and specific humidity. Negri (2004) also found changes in diurnal activity with increased convection shifting toward the morning hours.

Deforestation also has an indirect affect on the climate. As one example, increases in cleared lands could lead to an increase of surface runoff from precipitation. Some studies have demonstrated increases in the volume discharge near the mouth of the Tocantins and Amazon Rivers (Marengo, 2007; Marengo et al., 2009). Increased volume of fresh water would penetrate further into the Atlantic Ocean, decreasing the salinity and altering the sea surface temperature (by decreasing its density.) Another example, deforestation causes a significant release of carbon into the atmosphere, with tropical deforestation releasing approximately 1.5 billion tonnes of carbon into the atmosphere each year (Gullison et al., 2007). Additional carbon and water vapor in the atmosphere results in a positive feedback on global warming.

It is obvious that the interplay of the local energy and water balances with the regional and global general circulation, coupled with climate change, forms an extremely complex system, one in which our current numeric models fail to represent

well. Deforestation and massive land use changes upset these balances, alter the hydrology and climatology of the area, and may have far reaching teleconnections not yet realized (Marengo, 2007). However, the extent and frequency of deforestation and land degradation activities have little to do with science and more to do with the global economy, local government behavior and individual practice. Butler (2008, p. 1) sums up the situation nicely:

”As global demand grows for agricultural commodities produced in the Amazon, the region is being increasingly affected by drought, fragmentation, and forest fires, all of which are exacerbated by climate change. The synergistic impact of these forces, coupled with the emergence of new feedstocks, the entrance of oil palm development, and continued expansion of infrastructure, loom large for the future of Amazonia.”

Carlos Nobre, scientist at the Brazilian National Institute for Space Research (INPE), presents a more positive outlook in a recent UNEP report (2008, p. 150) :

”Amazonia needs to be preserved to study it, to explore the forest without extracting from it but in a totally new way. Brazil should lead the development of the new forest economy.”

1.3 Objectives of Study

The primary objective of this study is to apply a remote sensing technique that can measure atmospheric water vapor in regions with sparse in situ observational data to the Amazon River Basin region. Secondary objectives are to capture and analyze the diurnal signal and mesoscale spatial distribution of atmospheric total columnar precipitable water in the Amazon region for the months of June and October, just before and after the dry season. These months have fewer issues with cloud contamination as compared with most other months, as haze and smoke are common due to biomass burning in the middle of the dry season, and clouds due to afternoon convection and advection from the easterly trade winds are dominant in the rainy season. Describing the behavior of precipitable water over the wide expanses of the Amazon may aid in assessing future climate change through a better understanding of the water cycle, particularly in the Amazon where standard 0Z and 12Z radiosonde launches do not

adequately capture diurnal processes. In studying the diurnal characteristics of the region, Hastenrath (1985) states, "In the Amazon, where diurnal phenomena are the dominant feature of the local and regional climate, the success of future numerical experiments or the successful monitoring of climate change will ultimately depend on the proper formulation of the diurnal cycle."

Chapter 2 continues with an overview of deforestation in Amazonia and previous field studies in the region that incorporated atmospheric hydrologic observations. Chapter 3 provides a background on several techniques for deriving precipitable water, with a heavy emphasis on remote sensing methods, and includes additional resources for obtaining global water vapor datasets. Data utilized for this study are described in Chapter 4 and the incorporated methodology, including a description of the selected remote sensing Physical Split Window (PSW) algorithm that is used in this study, is detailed in Chapter 5. Chapter 6 then compares PSW-derived precipitable water values to colocated radiosonde observations. The spatial distribution and diurnal cycle of precipitable water throughout the Amazon region are then analyzed for the selected months in Chapter 7. Chapter 8 concludes by summarizing the impetus and methodology, describes some of the study's findings and lessons learned, and provides a short discussion of related potential future research.

Chapter 2

REVIEW OF AMAZON BASIN FIELD STUDIES

This background chapter reviews the deforestation activities that have taken place in the Amazonia region, including remote sensing methods of monitoring and listing the most recent numbers of acres deforested. Previous regional (large-scale) field campaigns and localized (small-scale) in situ experiments that include relevant components of the hydrologic cycle of the area are also covered.

2.1 The Amazon Basin Region

The Amazon River is considered the longest, largest, and deepest river in the world (Facility, 2006). The width of the Amazon River varies from 1.6 km to 10 km at low stage, however, it expands during the wet season to over 40 km to 50 km in some places. It is sometimes called "The River Sea" and at no point along the main river is the Amazon crossed by bridges. The first bridge in the Amazon River system, the Manaus Iranduba Bridge crossing the Rio Negro tributary, only recently opened in October, 2011 (The Guardian, 2010). In 2007, a group of Brazilian scientists determined the source of the Amazon River to be a location in the Andes Mountains, Peru, at an altitude of 5000 m, which is further south than previously thought. It had been second to the Nile River in length; the Nile River running approximately 6695 km. Although the new length of 6800 km has been accepted by at least the Brazilian Institute of Geography and Statistics (IGBE) (and the Brazilian National Institute for Space Research (INPE) has increased this to 6992 km), it is not universally accepted and currently under debate (UNEP, 2008; Duffy, 2007; Roach, 2007). There also exist 1100 significant tributaries in the Amazon River system, where over 200 of them are

major tributaries, 17 of which are over 1600 km long and 3 of which are over 3000 km long (Sombroek, 2001; UNEP, 2008; Raintree, 2011; Marengo, 2007).

As mentioned in Section 1.2, the Amazon region is well-known for its immense size (56% of the world's broadleaf forests, 20% of the world's freshwater, and the world's largest carbon stock) and huge biodiversity. However, culturally, it is also a very diverse area, covering eight countries (Bolivia, Brazil, Colombia, Ecuador, Guyana, Suriname, Peru, and Venezuela) each with varying rules and regulations concerning their portion of the Amazon forests and waters. There are hundreds of individual tribes and cultures present there: 420 indigenous peoples, 86 languages and 650 dialects with approximately 60 populations living in isolation. About 70% of the population lives in urban areas now due to accelerated unplanned urbanization and non-sustainable agricultural practices. There is also a wide range of economic development, where the economics are closely linked to demand of the global economic market with very little profits invested back into the region.

Perhaps not surprisingly, due to the region's complexity and heterogeneity, there is no national definition of the "Amazon region"; there is no agreement among the Amazon Cooperation Treaty Organization (ACTO) member countries. GEO Amazonia (UNEP, 2008) looked at three ways to define the region through three sets of criteria: ecological/biome, hydrographic, and political/administrative. Areas that are considered part of Amazonia by at least one of the three criteria constitutes "Greater Amazonia" and covers approximately 8,187,965 km², about 6% of the world's land surface. "Lesser Amazonia" is made up of areas that match all three criteria, approximately 5,147,970 km², roughly equal to 4% of the world's land surface. "Legal Amazonia" is a commonly referred geopolitical term. It follows the boundaries of the nine states in northern Brazil that intersect the rainforest biome, encompassing 58% of Brazil's total land area, whereas the rainforest biome alone makes up 48% (Millikan, 2009).

Needless to say, Amazonia is a complex region, culturally, economically, politically, and physically, and in a state of constant flux (Margulis, 2004; Millikan, 2009).

Salati in Gash (1996, p. xv) states:

”Conservation must be combined with sustainable development. Equally, from the development point of view, it is now acknowledged that the settlement of Amazonia over the past 30 years has not been successful — people and farming methods cannot simply be transferred from relatively temperate areas to the humid tropics. The climate, rainfall distribution and intensity, and the nature and structure of soils, as well as crop pests and diseases, all combine to create a very different environment.”

2.2 Deforestation in the Amazon

Tropical deforestation is the source of nearly 20% of annual, human-induced emissions of greenhouse gases, and during years of severe drought, emissions from tropical rainforest fires can potentially double ([Woods Hole Research Center, 2007](#); [Solomon et al., 2007](#); [Gullison et al., 2007](#)). There are many drivers of deforestation in the Amazon rainforest ([Fearnside, 1989](#); [Gash et al., 1996](#); [Laurance et al., 2001](#); [Margulis, 2004](#); [Ferreira et al., 2007](#); [Lindsey, 2007](#); [Butler, 2008](#); [Keller et al., 2009](#); [UNEP, 2008](#); [Fund, 2009](#)) , with a breakdown of deforestation causes for 2000 to 2005 in the Brazilian Amazon shown in Figure 2.1. The largest driver is clearing for cattle, accounting for 65-70% of all deforestation in the Brazilian Amazon. Clearing for small-scale (subsistence) and large-scale (commercial) agriculture makes up the next 25-35%, most of it taking place in the southeastern region known as the ”arc of deforestation”, in the states of Pará, Mato Grosso, and Rondônia. This area is the most active land-use frontier in the world in terms of total forest loss and intensity of fire activity ([Morton et al., 2006](#)). The primary product is soybean, mostly through large commercial plantations used for feeding livestock and biofuel production. Other crops include bananas, palms, manioc, maize, and rice as well as plantations for pulp and paper, timber and fiber production. The remaining 5-10% make up a combination of logging, natural fires, mining, urbanization, road construction, and hydroelectric dams ([Butler, 2008](#)).

Agriculture also has an additional indirect, though active, effect on deforestation. Tropical soils are nutrient poor, and can only live through a few crop cycles before

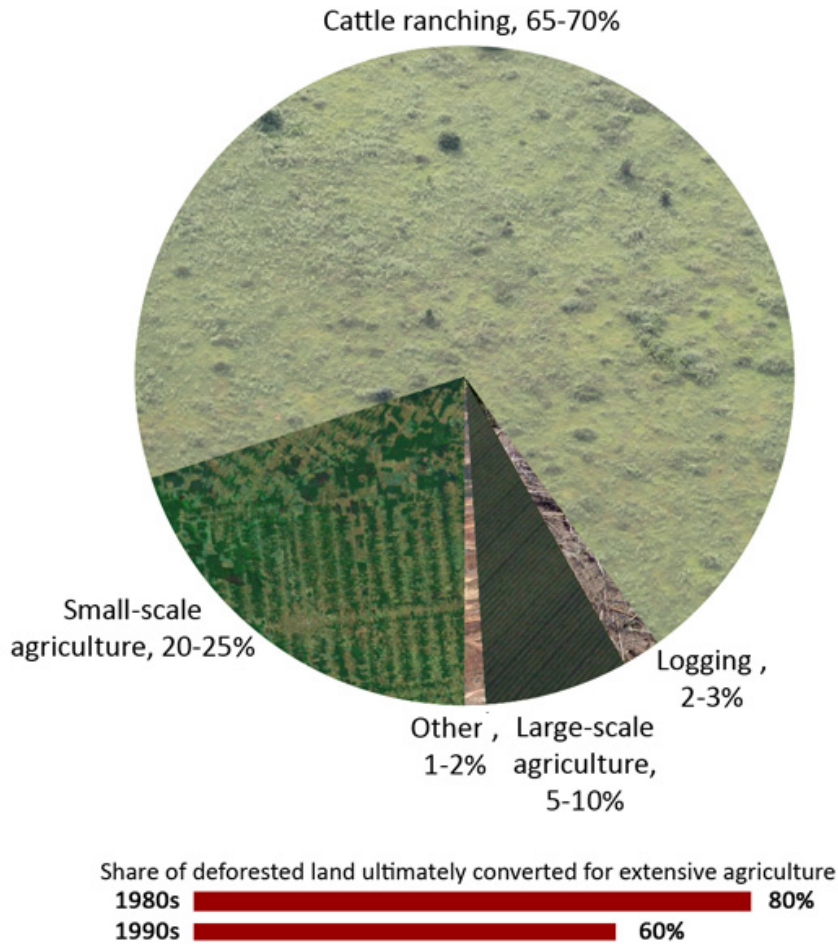


Figure 2.1: Causes of Deforestation in the Brazilian Amazon, 2000 - 2005. Other category includes fires, mining, urbanization, road construction, and dams. Source: <http://www.mongabay.com>

new land must be cleared. This is particularly true for soybean, which deplete the soil's nutrients at a much faster rate than other crops. Although many of these new fields are being constructed in the savannah and shrubland region, this takes up space where the cattle ranchers would be, pushing them and other farmers into the forest (Lindsey, 2007; Morton et al., 2006). Soybean farming also provides a key economic and political impetus for new highways and infrastructure construction further accelerating deforestation (Laurance et al., 2004). In addition, Gibbs (2010) found that across the global tropics, between 1980 and 2000, more than 55% of new agricultural land came at the

expense of intact forests, and another 28% came from disturbed forests, highlighting the potential consequences of unabated agricultural expansion for forest conservation and carbon emissions.

Internal to the region, there are many other factors that have facilitated deforestation. Non-indigenous population has increased significantly, especially along Amazonia's frontier region (Laurance et al., 2001; Margulis, 2004). Large amounts of public infrastructure has been built by the Brazilian government to facilitate transportation of people and goods in and out of the forest, such as constructing or paving large stretches of roads (e.g., the 300 km long Trans-Amazonia Highway in the 1970s, the 800 km long BR-163, Cuiabá-Santarém Highway in the 2000s) or expanding the railway system, all of which leads to direct and indirect land degradation along and near those routes (Fearnside, 1989; Laurance et al., 2001, 2004; Margulis, 2004; Millikan, 2009). Brazil also has provided financial incentives via subsidized loans for development in this region, as well as the Brazilian constitution which actually grants a person tenure of land if they occupy that area (less than 50 ha) for at least 5 years and makes beneficial use out of it, which commonly includes clear-cutting for cattle ranching or agricultural uses (Butler, 2008; Rust, 2011). One of the most significant causes of deforestation is Brazil's inability to appropriate land in a way that preserves the health of the rainforest (Margulis, 2004).

More recently, global supply and demand have played an additional increasing role in Amazonia deforestation (Butler, 2008; Margulis, 2004; UNEP, 2008; Gibbs et al., 2010). Since 2000 annual forest clearing has shown an increasingly tight correlation to commodity prices, especially with soy and beef (Butler, 2008). Brazil is the world's largest exporter of beef, with 96% of growth in the country's herd size since the end of 2003 occurring in the Amazon. Brazil has also become a agricultural superpower, becoming the world's leading exporter in cotton, coffee, orange juice, soybeans, and sugar, among other products, within one generation (Butler, 2008). Large demand is coming from a growing Asian market for many products, including timber, encouraging the development of more transportation infrastructure to transport goods more quickly

to Peruvian ports on the Pacific.

It is important to note how to define deforestation. The Brazil National Institute of Space Research (INPE), whose estimates have come to be regarded by both the central government and state governments in Brazil as the officially accepted statistics on deforestation, defines deforestation as "the conversion of areas of primary forest by human activities aiming at the development of agriculture/cattle ranching activities, as detected by orbiting satellites" (Margulis, 2004). The United Nations Framework Convention on Climate Change (UNFCCC) defines deforestation as "measurable sustained decrease in crown cover below a 10–30% threshold", which may be difficult to measure using available data (Olander et al., 2008). Degradation, defined similarly but does not go below the 10–30% threshold, is even more difficult to measure. Having a definition that can provide consistent, repeatable results is important for monitoring long-term change. It is also important to adopt a definition and methodology when performing automated analysis through remote sensing techniques, which is key for tropical nations because of the remote areas and lack of reliable field survey data.

INPE employs several remote sensing based systems for monitoring deforestation and land degradation, all of which serve complimentary roles as part of their overall Amazon forest monitoring and control plan. The primary system for measuring annual deforestation rates is the Amazon Deforestation Monitoring Program (PRODES) (Shimabukuro et al., 2006). PRODES uses moderate resolution data (20 m to 30 m) from Landsat, the Brazilian-Chinese Earth Resources Satellite (CBERS), and satellites that are part of the Disaster Monitoring Constellation (an international collection of satellites designed to provide emergency Earth imaging for disaster relief under the International Charter for Space and Major Disasters). Only areas larger than 0.0625 km² that have been totally cleared of native forest are mapped and included in the deforestation estimates (UNFCCC, 2009; Chokkalingam, 2010). Reports have been released annually for the Brazilian Amazon since 1988. PRODES has been extremely beneficial in providing consistent and systematically acquired estimates of deforestation (UNFCCC, 2009).

Although the PRODES system achieves high spatial detail in its estimates, complete coverage of the land surface takes quite a while, due to the repeat passing times of the satellites and pervasive and persistent cloudiness of the region (Hansen et al., 2008). The Real Time Deforestation Detection System (DETER) was developed in 2004 for estimating changes in forest cover and different stages of deforestation on a more frequent time scale (Anderson et al., 2005; Amaral and D’Alge, 2009). DETER uses data from the Moderate Resolution Imaging Spectroradiometer (MODIS) aboard the NASA Aqua and Terra satellites and from the CBERS WFI sensor. The higher temporal coverage of these satellites provides estimates on a weekly to biweekly basis, although with a sacrifice of spatial resolution of 0.25 km^2 (Amaral and D’Alge, 2009; Chokkalingam, 2010). The main use of DETER information has been in quickly deploying law enforcement personnel in deforestation control activities (UNFCC, 2009). To improve upon DETER, Brazil has announced a new satellite monitoring system, Imaging and Radar Deforestation Indicator (INDICAR), that can work under cloudy conditions due to its cloud-penetrating radar (Butler, 2010). INDICAR will use data from the Japan’s Aerospace Exploration Agency’s Advanced Land Observation Satellite (ALOS) to map degraded land at 0.10 km^2 .

In 2008, the Brazilian Amazon Forest Degradation Mapping (DEGRAD) system was put in place to map stages of land degradation that are in the process of deforestation, before the clear-cutting is complete (Chokkalingam, 2010; Amaral and D’Alge, 2009). DEGRAD uses the same satellites (and hence mapping resolution of 0.0625 km^2) and same reporting period as the PRODES system. Selective Forest Exploitation Detection System (DETEX) also uses the same data and reporting times as PRODES but monitors the patterns and intensity of selective logging activities (UNFCC, 2009). INPE’s Fire Monitoring System (QUEIMADAS) focuses on monitoring forest fires produced from data of 19 different satellites, including both polar orbiters and geostationary satellites (Amaral and D’Alge, 2009). Unlike the other programs, QUEIMADAS maps of fires are produced automatically by algorithms rather than technicians. All of these systems emphasize the benefit and effectiveness of remote sensing

data in monitoring rich remote areas with limited human resources. In fact, Brazil has offered to make these data and monitoring systems available to other countries to help them advance their own forest monitoring ([Chokkalingam, 2010](#)) and many of these systems have been released as free and open source software (FOSS) projects. Also released as FOSS, TerraAmazon was a software platform that integrates GIS, image processing and database management functionality and was developed for performing many of the monitoring and analytic tasks.

Other agencies are also responsible for providing deforestation estimates in the Brazilian Amazon, albeit for different reasons. The Brazil Federal Environmental Agency's (IBAMA) purpose is to carry out licensing and law enforcement operations, and the National Geography and Statistics Institute (IGBE) conducts agricultural census surveys. Imazon, a non-governmental research organization, has been monitoring deforestation and land degradation since 2007 based on MODIS imagery but using a different technique than DETER ([Amaral and D'Alge, 2009](#)). As well, the Food and Agriculture Organization (FAO) of the United Nations has been conducting global forest assessments, including deforestation figures, every five to ten years based on survey data, models and expert opinions, although the FAO data have been criticized for their lack of consistency between countries and between assessment reports ([Olander et al., 2008](#)). INPE PRODES estimates have come to be regarded both at the central government and individual state level as the officially accepted statistics on deforestation in Brazilian Amazonia ([Margulis, 2004](#)).

Skole and Tucker (1993) presented the first scientific method of estimating deforested areas through analyzing more than 200 Landsat satellite images to cover the entire legal Amazonia. Their technique not only provided a systematic way to determine the amount of deforested land but they noted that habitat fragmentation (fringe areas) has increased dramatically and severely affects the biodiversity of the area. Developing a systematic method is critical for consistency when describing events on an annual basis. [Figure 2.2](#) and [table 2.1](#) list estimates of annual deforestation rates for the Brazilian Amazon. Deforestation amounts for the period 1978 to 1988 range from

15,000 km² per year to 80,000 km² per year, averaging 21,130 km² per year, with global estimates as high as 169,000 km² during the late 1980s (Downton, 1995; Skole and Tucker, 1993; Chu et al., 1994). INPE reports current deforestation estimates based on satellite imagery taken during the dry season, usually in July, when weather effects are not dominated by the large-scale synoptic systems and cloud cover is minimal, allowing high resolution imagery to be used. These values represent removal of the forest biome only and do not investigate land use, such as loss of natural savannah or grassland within the forests or loss of biodiversity due to fragmentation. Accumulated amounts also do not take into account secondary regrowth and therefore may be underestimates of the current amount of forest cover. (INPE released in 2009 an estimate that at least 20% land deforested in the Brazilian Amazon is regrowing forest.) According to INPE, the original Amazon rainforest (pre-1970) biome in Brazil contained 4,100,000 km², while today it is down to 3,350,140 km², representing a loss of approximately 18% by 2012.

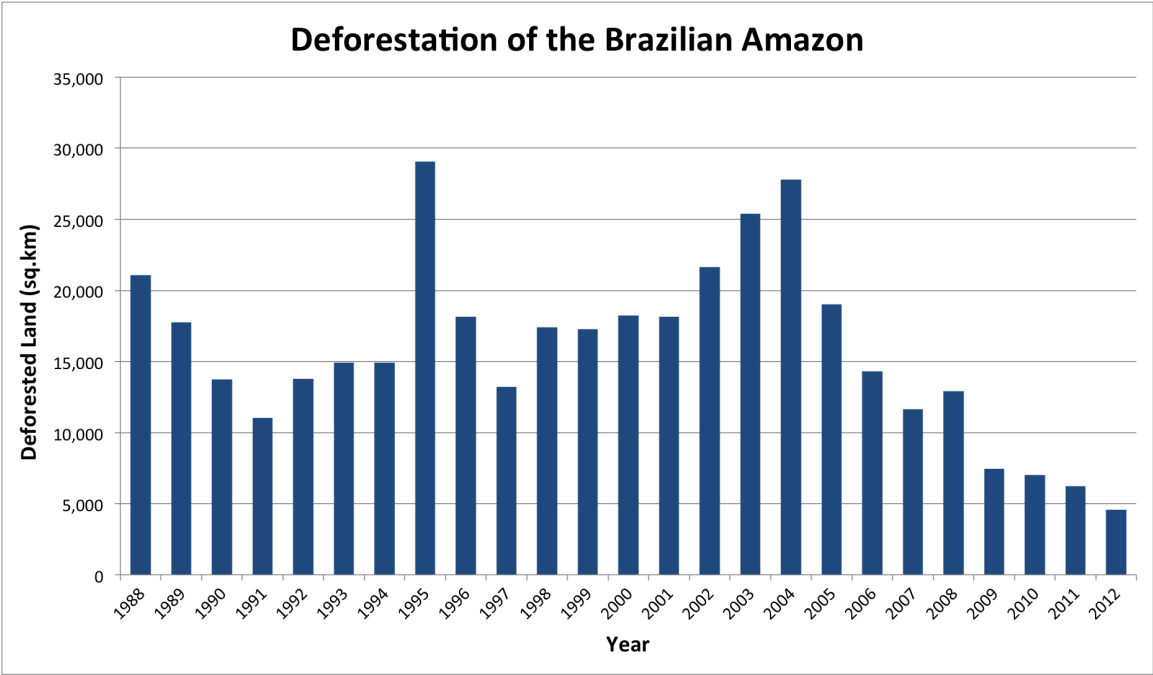


Figure 2.2: Annual deforestation rates of the Brazilian Amazon for the years 1988 through 2012. Data from National Institute of Space Research (INPE).

Table 2.1: Annual deforestation rates for the Brazilian Amazon for 1977 through 2012. For 1978 to 1987, figures represent the average annual loss. Data from the Brazil National Institute of Space Research (INPE).

Year	Estimated remaining forest in Brazilian Amazon (km²)	Annual forest loss (km²)	Percent of 1970 forest remaining
Pre-1970	4,100,000	–	–
1977	3,955,870	21,130	96.5%
1978-1987	3,744,570	21,130	91.3%
1988	3,723,520	21,050	90.8%
1989	3,705,750	17,770	90.4%
1990	3,692,020	13,730	90.0%
1991	3,680,990	11,030	89.8%
1992	3,667,204	13,786	89.4%
1993	3,652,308	14,896	89.1%
1994	3,637,412	14,896	88.7%
1995	3,608,353	29,059	88.0%
1996	3,590,192	18,161	87.6%
1997	3,576,965	13,227	87.2%
1998	3,559,582	17,383	86.8%
1999	3,542,323	17,259	86.4%
2000	3,524,097	18,226	86.0%
2001	3,505,932	18,165	85.5%
2002	3,484,538	21,651	85.0%
2003	3,459,291	25,396	84.4%
2004	3,431,868	27,772	83.7%
2005	3,413,022	19,014	83.2%
2006	3,398,913	14,286	82.9%
2007	3,387,381	11,651	82.6%
2008	3,375,413	12,911	82.3%
2009	3,367,949	7,464	82.2%
2010	3,360,949	7,000	82.0%
2011	3,354,711	6,238	81.8%
2012	3,350,140	4,571	81.7%

The last five years have seen a significant decrease in deforestation, with the amount of 2009 the lowest since these records have been kept. There are several likely reasons for why Brazil's efforts have been effective. In 2004, the Brazilian government released the Action Plan for Prevention and Control of Deforestation in the Amazon. A significant part of the plan included the remote sensing-based monitoring systems PRODES, DETER, etc... (as described above) and it also included new legislation for land tenure and territory planning as well as incentives for sustainable development. In 2008, both National and State plans to combat deforestation were in place, including financial reforms and investments in activities that promote forest conservation, restoration and sustainable agriculture. The combination of enhanced monitoring, increased law enforcement, financial incentives, and the global financial recession likely all contributed to the decrease of forest loss.

It is an arduous task to measure the amount of deforestation and degradation occurring in the Amazon region, primarily due to size and remoteness of the region and the dearth of data available. The new remote sensing monitoring systems and accepted method for analyzing the imagery is a favorable step. However, land degradation, forest fragmentation and selective logging are more difficult to measure than deforestation since the changes are gradual and ambiguous when interpreting satellite images, yet may exhibit similar effects on the surroundings (Skole and Tucker, 1993). These practices also degrade the rich biodiversity of the area, and impossible to estimate that loss due to the restrictions on information, nor are there are statistics or maps that illustrates the effect on this ecosystem (UNEP, 2008). Although the past drivers of Amazonia deforestation in the 1970s and 1980s are still active (largely induced by government policies and subsidies supporting local economic development), the current and future global marketplace will play a significant factor in Brazil's future activities related to deforestation (Margulis, 2004; Lindsey, 2007; Rust, 2011).

2.3 Regional Field Campaigns

There have been several regional (large-scale) field experiments, usually involving numerous research groups and multiple institutions, directed at studying the hydrologic characteristics of the Amazon River Basin during the past 20 years, usually within a meteorological and biological context. An abbreviated list of them is included in Table 2.2. The primary objective of many of these experiments was two-fold: 1) to obtain a comprehensive base-line of data in which to measure future environmental change due to deforestation or anthropogenic activities, and 2) to calibrate and validate current and future GCM simulations, remote sensing algorithms, or numeric models.

One of the first intensive and well documented campaigns is the Anglo-Brazilian Amazonian Climate Observation Study (ABRACOS) from 1990 to 1994. ABRACOS had the ambitious objective of discovering how the soil and vegetation of Amazonia interact with the atmosphere to affect climate, prompted by the need of ground-truth data for post-deforestation numerical studies (Gash et al., 1996). As with the other campaigns, ABRACOS paid little attention to upper air moisture content, though depth of the atmospheric boundary layer was thoroughly examined in the Amazonian Boundary Layer Experiment (ABLE) (Harriss et al., 1988; Ferreira, 1987) in the mid-1980s and the Rondônia Boundary Layer Experiment (RBLE) in the early 1990s (Gash et al., 1996). Any upper air measurements made during these campaigns were limited to 1 km to 3 km and were short-lived, extending up to a month at most.

Working within the framework of the International Geosphere/Biosphere Programme (IGBP), the Large-Scale Biosphere-Atmosphere Experiment in Amazonia, or LBA, was an international research initiative conducted from 1995 to 2005. LBA was the world's largest environmental science experiment, encompassing an intensive, multi-disciplinary set of campaigns that took place across the entire Amazon Region (Keller et al., 2009; NASA, 2004). Figure 2.3 illustrates the widespread coverage and cooperation of LBA. The mission of LBA was "to study how Amazonia currently functions as a regional entity within the larger Earth system, and how changes in land use and climate will affect the biological, physical, and chemical functioning of the region's

ecosystem.” (Lindsey, 2002). Numerous projects and experiments took place within the LBA context, including nearly 2000 scientists and producing at least 1300 scientific papers (Keller et al., 2009). LBA has proven beneficial in upper air studies since its goal is to better understand temporal variations of water and energy fluxes and to improve dynamical processes in numerical models (as part of LBA’s Physical Climate component).

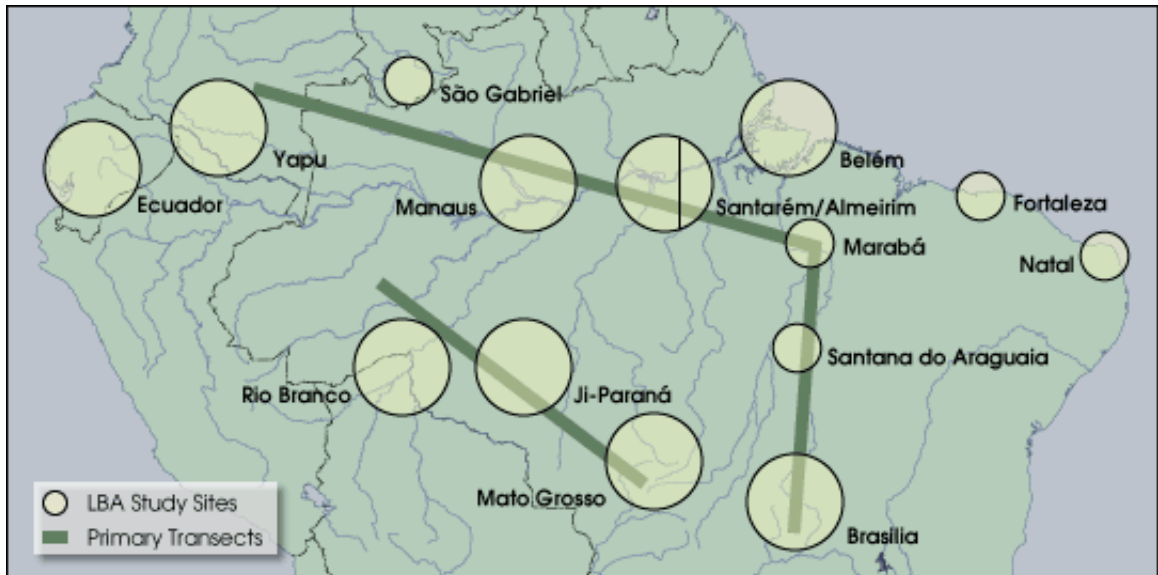


Figure 2.3: Large-scale Biosphere-Atmosphere (LBA) experiment sites. These sites span the Amazon from the headwaters in the Andes, along the river and its tributaries in the Amazon Basin, to the River’s mouth in coastal Brazil. Figure taken from (Lindsey, 2002).

Within the LBA, the first major atmospheric mesoscale campaign was the Wet Season Atmospheric Campaign (WETAMC). WETAMC took place in January and February of 1999 within the State of Rondônia in southwest Amazonia (Silva Dias et al., 2002; Betts and Jakob, 2002). The main focus points of WETAMC/LBA was on understanding the coupling between biosphere and atmosphere processes in the wet season in the Amazon region related to the energy and hydrological cycles, and on the impacts of local convection and deforestation on the larger scale circulation. Surface and upper-air measurements were made (including both meteorological and chemical)

at a few select sites. Colocated with the WETAMC was the validation experiment of the Tropical Rainfall Measuring Mission (TRMM) satellite program (Silva Dias et al., 2002; Betts and Jakob, 2002). The major objectives of TRMM/LBA were to validate the kinematic, microphysical and diabatic heating fields and satellite algorithms obtained by the TRMM satellite in the context of tropical continental convection. These campaigns together allowed for an extensive study of atmospheric moisture and tropical convection (1 to 8 soundings per day) in forested and non-forested areas to the larger region (Silva Dias et al., 2002).

Also within the scope of the LBA, two additional experiments took place during the transition from the dry to wet seasons, September to November in 2002. The Radiation, Cloud, and Climate Interactions in the Amazon (RACCI/LBA) experiment included an intensive collection of physical and chemical atmospheric information to understand the physical processes that control the seasonal transition (Sapucci et al., 2007; Betts et al., 2009). The other experiment, Smoke, Aerosols, Clouds, Rainfall and Climate (SMOCC/LBA) experiment, focused on detailed surface and airborne aerosol measurements to better understand the influences and regional effects of biomass burning particulates on large-scale circulation, radiation and energy budgets (Chand et al., 2006; Soto-Garcia et al., 2011).

Several intensive field campaigns were conducted that focused primarily on geochemistry. Although they recorded hydrologic data such as precipitation, river discharge, water quality, evapotranspiration, and similar variables, these campaigns did not specifically study the atmospheric water budget. One project was the Carbon in the Amazon River Experiment (CAMREX), conducted from 1982 to 1991, to define by mass balances and direct measurements those processes which control the distribution of bioactive elements (C, N, P and O) in the main stem of the Amazon River in Brazil. Another was the regional Andean Amazon Rivers Analysis and Management (AARAM) project conducted from 1996 to 2001, to understand the effects of land use change in the Andean Amazon region on water quality in the lower basin and thus contribute to effective natural resource management (Galárraga and Torres, 2001).

As well, the Hydrology and Geodynamics in the Amazon Basin (HiBAm) project conducted from 1994 to 1999, aimed to document and forecast the variability of surface hydrology and sediment transport through the Amazon Basin ([Ronchail et al., 2002](#)). GEOMA (Environmental Modeling of the Amazon) is a more recent program (established in 2002) aimed to facilitate the approach to extensive environmental problems in the Amazon and the spread of the scientific knowledge among different research institutes. It is a cooperative network of researchers whose objective is to develop models capable of predicting the dynamics of ecological systems and socio-economics in different geographical scales, within the concept of sustainability, in the Amazonian Region ([INPA, 2011](#)).

Three campaigns were focused on atmospheric chemical composition and processes, as part of the LBA atmospheric chemistry component, over the Amazon Basin through heavily instrumented aircraft. In February to March 1998, CLAIRE-1 (the Cooperative LBA Airborne Regional Experiment) conducted atmospheric observations in the Southern part of the Amazon Basin, centered in the Alta Floresta - Porto Velho - Brasilia region. The CLAIRE-2 experiment took place in September to October 2001 with basically the same instrumentation as in CLAIRE-1, but measured atmospheric properties in the region between Manaus - Paramaribo - Bélem - Boa Vista during the dry season. The CLAIRE project flights were designed to investigate the biosphere-atmosphere exchanges of natural trace gases and aerosol particles and to quantify chemical processes in the atmosphere. Data analyses focused on the composition of the air entering the Amazon Basin along one of the major input routes and of the high-altitude outflow towards the northeast ([Andreae et al., 1997](#); [Thielmann et al., 2003](#)). GABRIEL (Guyanas Atmosphere-Biosphere exchange and Radicals Intensive Experiment with the Lear-Jet) took place in October 2005 as a follow-up to CLAIRE-1. The main purposes of GABRIEL was to observe and quantify detailed atmospheric OH/HO₂ formation and destruction chemistry during the dry season as a function of the atmosphere-biosphere exchange and to study the role of convective transport in the vertical redistribution of primary and secondary gases.

The South American Low-level Jet Experiment (SALLJEX) field campaign was carried out during November 2002 through February 2003 in the southwestern part of Amazonia and into the Antiplano region in the central Andes and northern Argentina (Vera et al., 2006). SALLJEX focused on the low level jet carrying moisture and energy exchanges between the tropics and extratropics, and to related hydrometeorological aspects of the South American Monsoon. A wide assortment of surface and upper-air measurements took place during this experiment, including 22 new upper-air launch stations (most twice daily but some operated at 4x daily); precipitable water estimates from GPS techniques, MODIS imagery (aboard both the NASA AQUA and TERRA satellites), and microwave radiometers; infrared imagery from GOES-8; 13 flights from the NOAA P-3 aircraft, one of the two world's premier research aircrafts; and installation of approximately 1200 simple rain gauges (Vera et al., 2006; Falvey and Garreaud, 2005; Herdies et al., 2006). Although for a short time period, SALLJEX is an excellent source of atmospheric moisture data and information, in conjunction with colocated surface observations, for the southwestern Amazonian region.

Table 2.2: Summary of intensive field campaigns in the Amazon. For definitions of the acronyms, refer to the appendix.

Name	Dates	Location
CAMREX	1982 - 1991	Amazon River System
ARME	Sep 1983 - Sep 1985	Manaus (forest)
ABLE-2A	July - Aug 1985	Manaus (forest)
ABLE-2B	Apr - May 1987	4 forest sites, 2 mato grosso sites
FLUAMAZON	Nov - Dec 1989	5 sites in East Brazil
RBLE-1	Aug - Sep 1992	R�ndonia (forest and pasture)
RBLE-2	July 1993	R�ndonia (forest and pasture)
RBLE-3	Aug 1994	R�ndonia (forest and pasture)
SCAR-B	Aug/Sep 1995	Brazil
ABRACOS	Sep 1990 - Sep 1994	Marab�, Manaus, and Rod�nia (forest and pasture)
HiBAm	1994 - 1999	Amazon Basin Region
LBA	1995 - 2005	Amazon Basin Region
AARAM	1996 - 2001	Andean Amazon Region
CLAIRE-1/LBA	Feb - Mar, 1998	Southern/Southeastern Amazon
WETAMC/LBA	Jan - Feb 1999	Rond�nia (forest and pasture)
TRMM/LBA	Jan - Feb 1999	Rond�nia (forest and pasture)
CLAIRE-2/LBA	Sep - Oct 2001	Northern Amazon
RACCI/LBA	Sep - Nov 2002	R�ndonia (forest and pasture)
SMOCC/LBA	Sep - Nov 2002	R�ndonia (forest and pasture)
SALLJEX	Nov 2002 - Feb 2003	West and South Amazonia
GEOMA	2002 - 2004	Amazon Basin Region
GABRIEL	Oct 2005	Northern Amazonia

2.4 Local Hydrometeorological Studies

In June 1970, the Brazilian government implemented the "National Integration Plan of the Amazonas Region" which planned to increase colonization of Brazilian Amazonas. This would be accomplished by developing a large network of roads (≈ 1200 km) and establishing 100 km strips of land on each side of the highways for settlement (Molion, 1975), possibly resulting in deforesting approximately one-half of the Brazilian Amazon. With the massive development plan in place, many studies began to focus on understanding tropical circulations and predicting possible climatic deforestation impacts on the Amazon region. A focus of many early experiments was precipitation recycling. Precipitation recycling, labeled as ρ in most studies, is defined as the proportion of local precipitation that originated as local evapotranspiration (local meaning confined to specific geographic boundaries.) Prior to the late 1970s, this parameter was not deemed important to the hydrometeorology of the region (Lettau et al., 1979), although later studies have found it to be extremely important in estimating the role of land surface in local weather/climate. (It is important to note here that regional ρ estimation is dependent upon evapotranspiration and water vapor transport tracking and hence, upon the accuracy of precipitable water estimates.)

An early analytic experiment was carried out by Molion (1975) where he attempted to find the mean water and energy balance of the Amazon watershed using evapo- and thermo-climatology (i.e., through field-based measurements of moisture and heat fluxes.) Data from three radiosonde stations (0700 LST launches) and monthly climatologies from 40 surface stations were interpolated to a $5^\circ \times 5^\circ$ grid across the basin. These data were then input to the climatonic energy balance formulations. Most of the study was limited to six grid boxes that lined the main Amazon River and the moisture fluxes through them. In this cross-section, precipitable water was found to increase from east to west with a maximum of about 5 mm in the west-central part of the basin. Molion also estimated by climatonic methods that local evaporation contributed to about 56% of local precipitation ($\rho = 0.56$), though large errors may exist due to the limited upper-air data.

Marques et al. (1977) estimated the annual and monthly variation of precipitable water and water vapor flux between Manaus and Belém for 1972. Data were obtained from 658 upper-air observations and monthly surface measurements of precipitation and air temperature at these two cities. The study region was defined by a box with Manaus and Belém as its opposite vertices, measuring 178 km longitudinally by 1272 km latitudinally. Monthly water vapor available for precipitation was found by subtracting the zonal water vapor flux in Belém from Manaus, i.e.,

$$\Delta Q_\lambda = \left[\frac{1}{g} \int_{p_o}^p \overline{qu} dp \right]_{\text{Manaus}} - \left[\frac{1}{g} \int_{p_o}^p \overline{qu} dp \right]_{\text{Belém}}, \quad (2.1)$$

where q is the specific humidity, u and v are the zonal and meridional wind speeds, respectively, p is the pressure level, and the over-bar represents averages for the month. The meridional flux approximately canceled throughout the seasonal cycle. From this analysis, they found precipitation recycling (ρ) of 0.48, which is in relative agreement with the sparse earlier estimates. In analyzing the radiosonde data, monthly values of precipitable water at Manaus ($\text{pw}_{\text{avg}} = 43$ mm) were consistently higher (5-35%) than those at Belém ($\text{pw}_{\text{avg}} = 38$ mm) with the smallest differences occurring during the dry season, June through September. Peak precipitable water values at the Manaus station (November through February) occurred earlier in the year than at the Belém station (February through May). They also observed that in at least two months, October and November, the central basin served as a source of water vapor to the western basin. These results, however, must be viewed with caution since they represent only one year of measurements and do not include observations inside the study region.

In another early effort to assess the hydroclimate of the region, Lettau et al. (1979) used climatological methods to quantify Amazonia's hydrologic cycle. In their study, as with Molion (1975), they found that ρ does play a large role in local precipitation, increasing from east to west, with 88% of the water precipitating on the westernmost region falls at least a second time from the air. Salati et al. (1979) also

analyzed O^{18} concentrations in precipitation at different stations throughout the Amazon Basin. They found a small inland gradient and thus concluded that local evaporation significantly contributes to atmospheric water vapor though the amount may vary spatially and seasonally (Salati et al., 1979).

Ferreira (1987) attempted to identify large-scale features of atmospheric water vapor transport in the Amazon Basin. His method analyzed moisture retrievals through GOES satellite imagery during a few days in the dry season, as well as from the First Global Atmospheric Research Program (GARP) Global Experiment (FGGE) III-b dataset comprised of ECMWF global analyses for 1979. The FGGE III-b data depicts the Amazon Basin as a sink of water vapor in the Southern Hemisphere (SH) summer (wet season) and a source during the SH winter (dry season). Generally, there is a westward transport of water vapor near the equator and an eastward transport in the sub-tropics, the transition zone of these two being the South Atlantic Convergence Zone (SACZ.)

Moisture transport fields during July 8 - 14, 1985, which coincided with the Global Tropospheric Experiment (GTE)/ABLE-2A experiment, were derived from satellite estimates of precipitable water and wind fields from National Centers for Environmental Prediction (NCEP) National Meteorological Center (NMC) analyses. Retrievals were made over a large portion of the basin at roughly 80 km spatial resolution at various times throughout each day. Westward propagation of convective activity and high moisture values were observed as were fluctuations in the low-level flow. These observations also support the FGGE results that the basin acts as a source of water vapor during the dry season.

Brueske (1990) used satellite data to derive daily values of evapotranspiration throughout the Amazon Basin. These measurements were made at 1048Z and 1648Z on May 5 - 7, 1987 to coincide with the GTE/ABLE-2B field campaign. The retrieval algorithm was applied to GOES VAS dwell soundings and resulted in profiles of temperature and moisture. NMC analyses provided all first guess fields except winds, which were derived through tracking of visible objects in consecutive satellite images,

unlike Ferreira (1987). Retrievals could not be made over cloudy regions, which were prevalent on all three days in the western portion of the basin. Therefore, data were interpolated to a uniform $110\text{ km} \times 110\text{ km}$ grid using a 3-D recursive filter objective analysis system to achieve continuous fields. When VAS retrievals were compared to radiosonde data by averaging all retrievals within 150 km of the radiosonde site, broad agreement was found. Brueske (1990) observed much higher precipitable water values in the west than in the east by approximately 200% and the values at 1648Z (48 mm to 66 mm) were slightly higher than at 1048Z (42 mm to 62 mm). Results from both Brueske (1990) and Ferreira (1987) reflect that local evapotranspiration is a significant contributor to local precipitation. Also, the spatial distribution of precipitable water closely followed that of dewpoint temperature in the low and mid troposphere. This makes sense since water vapor is vertically stratified, decreasing exponentially with height.

Using the same GOES data and satellite retrieval algorithm as as Brueske (1990), Schmit et al. (1990) concentrated on water vapor and wind fields rather than daily evapotranspiration values. As would be expected, their results were very similar with minimum values of water vapor found in northeast Brazil and maximum values in central and western Amazonia. Water vapor gradients and trends were similar to that as provided by radiosondes as precipitable water tended to increase throughout the day with a late afternoon maximum.

Brubaker et al. (1993) and Eltahir and Bras (1993) focused on precipitation recycling measurements in the Amazon Basin. Both studies found that ρ is seasonally and spatially dependent. Maximum values occur in the southwestern/western portion of the basin during months with high precipitation and evapotranspiration, corresponding to the wet season. Using observed radiosonde data for 1963 to 1973 interpolated to a 2.5° grid, Brubaker et al. (1993) found estimates of basin-wide ρ ranging from 0.14 in June to 0.32 in December, with values above 0.4 observed in some months at some locations. Eltahir and Bras (1993), using 6 years of 2.5° gridded ECMWF data, determined a basin averaged value of ρ equal to 0.25. They emphasized that many

earlier precipitation recycling studies overestimate ρ by inappropriately assuming the Amazon Basin behaves as a closed system with respect to water vapor transport.

Costa and Foley (1999) examines the full hydrologic water budget for the Amazon Basin using 20 years of data from the National Centers for Environmental Prediction (NCEP) National Center for Atmospheric Research (NCAR) model reanalysis project during 1976 through 1996. The authors constructed annual averaged water budget parameters, from September through August of each year, so that the rainy season is not divided in two. Average precipitation recycling ratio was found to be 30%, similar to other estimates based on a well-mixed water vapor but smaller than the $\approx 50\%$ found from studies that did not assume as well mixed water vapor. Average evapotranspiration was found to be about 3.8 mm day^{-1} . A decrease in the water vapor transport into the basin (due to a decrease in the easterly flow trade winds) and out of the basin was found during this time period. However, no significant trend was found for precipitation, runoff, or precipitable water for most of the basin, coinciding with a significant increase of the recycling ratio.

Werth and Avissar (2004) evaluated two independent methods to produce annual cycles of evapotranspiration at the Amazon Basin scale. The Net Radiation Method measures a low (3.0 mm day^{-1}) in evapotranspiration in the summer (rainy season, December through February) and a high (4.0 mm day^{-1}) in the winter (dry season, July through September.) This is highly correlated with net radiation (due to cloud cover) and implies the evapotranspiration is minimally controlled by the vegetation. The Global Climate Modeling Method measured a high in summer (3.5 mm day^{-1}) and a low in late winter (1.5 mm day^{-1}). This method depicts a much stronger annual cycle, coinciding with precipitation, and decreasing ET with the natural decrease in soil moisture. The primary difference in the GCM model is how the vegetation regulates transpiration through its stomata. Their conclusion is that there is not enough ground observation to accurately understand regional evapotranspiration in the Amazon.

Da Rocha et al. (2004) measured fluxes of sensible heat, water vapor, and CO_2 between an old-growth tropical forest in eastern Amazonia and the atmosphere in July

2000 through July 2001. Average evapotranspiration was 3.96 mm day^{-1} during the dry season and 3.18 mm day^{-1} during the wet season. The evaporative fraction of the energy fluxes did not decrease in the dry season, implying the vegetation did not experience water stress. This would therefore imply deep rooting and possibly vertical water movement, allowing trees access to water year round.

Karam and Bras (2008) analyze basin-averaged evapotranspiration through a water budget analysis in the Amazon. Monthly averages were calculated as the residual of the water balance for the period 1988 to 2001. Precipitable water and water vapor flux in and out of the basin were computed using a weighted average of three model reanalysis products, based on the random error attributed to each of the source models. Based on Karam (2006) and other previous studies, this study focuses on the uncertainty in the annual cycle of evapotranspiration and its relation to soil moisture and net radiation. Although their estimates are lower than most studies (2.1 mm day^{-1} , mostly due to fitting water vapor convergence to local rainfall and discharge values), the research supports that evapotranspiration is controlled mostly by net radiation and the vegetation has access to deep water storage, which is contrary to most land surface model results which are in phase with rainfall. After the rainy season peaks in February, precipitable water and precipitation begin to decrease. However, precipitable water increases late in the dry season, a couple of months before precipitation begins to rise. This supports an argument that perhaps the transition to the wet season begins with increases in atmospheric water vapor. Lastly, the authors note the importance of increased observations to test and revise models in the Amazon as uncertainty exists in the land surface processes.

Sapucci et al. (2007) compared precipitable water measurements among four separate techniques: GPS, radiosondes, solar radiometer, and the Humidity Sounder for Brazil (HSB) aboard NASA's Aqua satellite. The analysis was part of the RACCI/DRY-TO-WET experiment carried out in three sites within southwestern Amazonia (State of R ndonia) from September through early November 2002. Radiosonde measurements were used as the reference observation method, even though the radiosondes have

a dry bias when compared to other techniques. Precipitable water slightly increased during the months of the experiment at all sites with the largest values (45 mm to 55 mm) in the northern forest region.

Da Rocha et al. (2009) performed similar measurements as in 2004 but this time used a network of stations, operated as part of the LBA experiment, to form a gradient from forest to savannah. Their work modified the result of recent previous studies that evapotranspiration had a diminished annual cycle (compared to earlier thinking) and soil moisture/vegetation had minimal control. At sites with annual precipitation over 1900 mm and a dry season of less than four months, evapotranspiration rates increased in the dry season, coincident with net radiation, up to 4.0 mm day^{-1} . Those sites with annual precipitation of less than 1700 mm and a longer dry season showed clear evidence of decreased evapotranspiration during the dry season, as low as 2.5 mm day^{-1} . Therefore, in thick forested biomes, evapotranspiration was mostly dependent upon net radiation, contrasted with the savannah biomes where soil moisture plays a more important role.

In the previous studies of precipitable water and water vapor transport in the Amazon Basin, it is difficult to summarize the results due to the paucity of consistent radiosonde observations, short time periods of experiments, varying methods of measurement, and coarse spatial resolution throughout the region. Both local and regional scale studies need to be performed at longer time periods, including across large-scale phenomena such as ENSO events, to assess the true nature of atmospheric water vapor in a region as large and complex as the Amazon Basin. Since too few upper-air soundings will continue to be available, it is important for satellite data and numerical models to contribute significantly to the environmental monitoring of the Amazon (although validation of these products remains a daunting task.)

Chapter 3

REVIEW OF PRECIPITABLE WATER MEASUREMENT TECHNIQUES

This background chapter describes current and past methods of estimating precipitable water in the absence of regional geographic coverage of continuous upper-air humidity observations. The first section emphasizes satellite-based remote sensing techniques, as they hold the most promise for continuous observation over large geographic areas, such as the Amazon Basin. Following sections discuss a variety of techniques that use statistical or numerical modeling methods to correlate easily observed environmental variables (usually made at the surface) to precipitable water amounts. Lastly, existing global precipitable water datasets are summarized, which typically integrate multiple sources of data, such as in situ observations, satellite measurements and modeling reanalyses.

3.1 Satellite-based Remote Sensing Methods

As mentioned in Chapter 1, remote sensing, particularly from satellites, has been used quite extensively for meteorological monitoring. Satellite remote sensing is essentially based upon measuring the amount of electromagnetic radiation received at the satellite. In Earth-observing satellite remote sensing, the source of the radiation is primarily the Earth's surface. The sensor (or camera) is mounted on the satellite and aimed directly at the Earth below. Radiation leaving the Earth's surface travels through the Earth's atmosphere before it reaches the sensor orbiting the Earth. With that in mind, the basic premise for measuring the amount of water vapor in the atmosphere using remote sensing is relatively simple.

Water vapor molecules absorb radiation at many different naturally occurring wavelengths within the electromagnetic spectrum. By measuring the intensity of radiation from the Earth's surface within a wavelength region (also called a wavelength band) that water vapor does not absorb (typically labeled a "clean" band) and comparing that to the measured intensity within a wavelength band water vapor does absorb (labeled a "dirty" band), the amount of water vapor in the atmosphere can be estimated. Figure 3.1 shows the various absorption spectra (and the transmittance windows in between) within the electromagnetic spectrum for common types of atmospheric gases, including water vapor.

Earth's surface naturally emits radiation very closely to that of a blackbody at a temperature approximately at 288 Kelvin, as shown in figure 3.1, where most of the energy emitted at this temperature is in the mid- to far-infrared parts of the spectrum. Radiation coming from Earth's surface in the ultraviolet and visible parts of the spectrum is reflected radiation from the sun. The general rule of thumb is that radiation at wavelengths under $4 \mu\text{m}$ is reflected or scattered radiation from the sun, and over $4 \mu\text{m}$ is emitted from the Earth's surface or absorbed and re-radiated from the atmosphere. It is difficult to ascertain the source of the radiation near the $4 \mu\text{m}$ band, where factors such as time of day, cloud cover, land surface characteristics, and others must be taken into account.

Fortunately, water vapor is an extremely efficient absorber of radiation at several different bands within the infrared part of the spectrum, most notably near the $0.74 \mu\text{m}$, $0.94 \mu\text{m}$, $2.4 \mu\text{m}$ to $3.3 \mu\text{m}$, $5 \mu\text{m}$ to $7 \mu\text{m}$, and above $11 \mu\text{m}$ bands. Therefore, many satellites incorporate sensors that record data in both clean and dirty bands within this region specifically to monitor atmospheric characteristics.

There are primarily two types of satellites (based on their orbital configurations) that are used for environmental monitoring from space: geostationary satellites and polar orbiting satellites.

Geostationary satellites have the ability to image large areas (up to one-third of the Earth's surface) every 15 to 30 minutes and are ideal for analysis of phenomena that

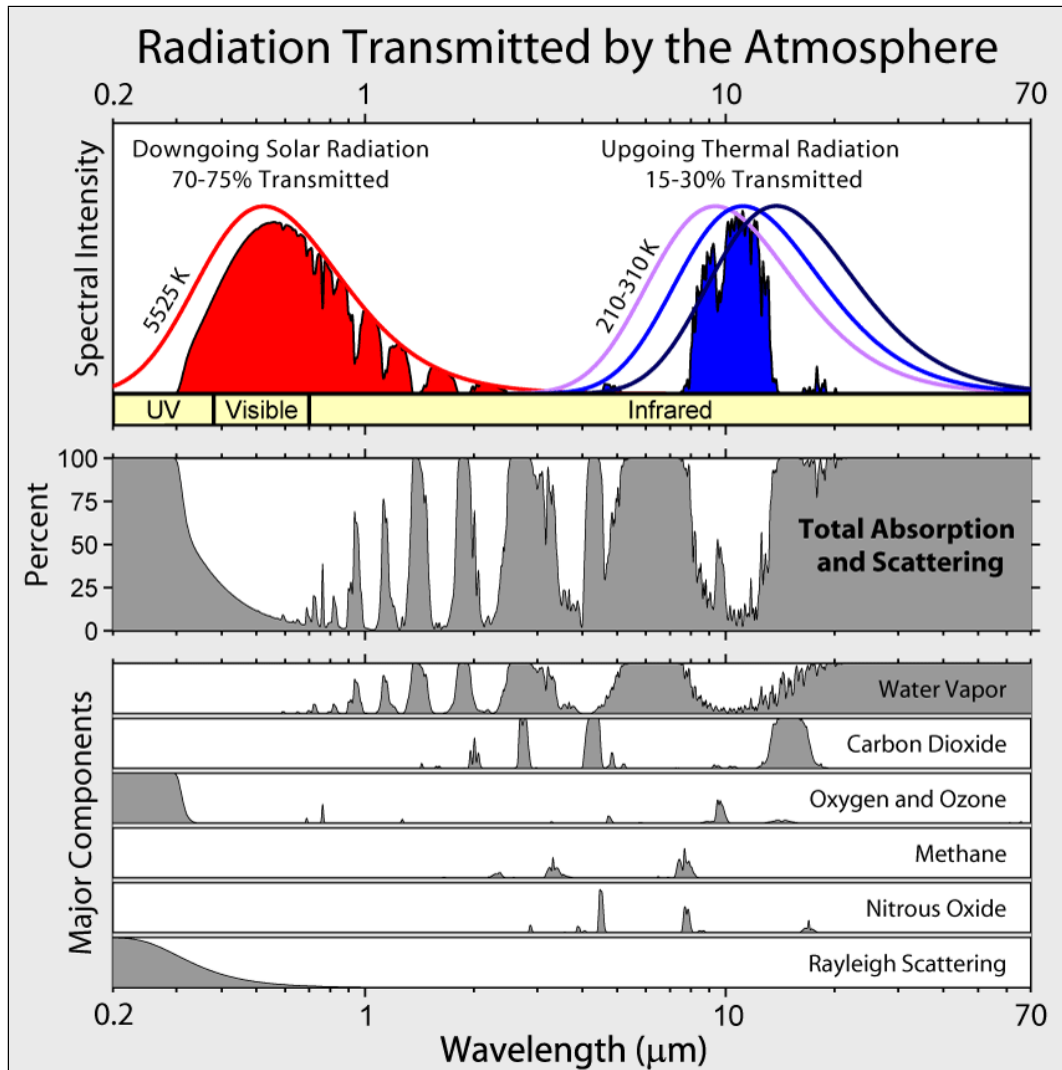


Figure 3.1: Atmospheric radiation transmittance/absorption spectrum for $0.2 \mu\text{m}$ to $70 \mu\text{m}$. The top panel shows blackbody emission spectra for typical temperatures for the sun (left) and Earth (right.) Image created by Robert A. Rohde / Global Warming Art.

operate at small time scales. Their orbital period is equal to the rotation of the earth (about 24 hours) with altitudes of approximately 36,000 km, located directly above the Earth's equator at 0° latitude. Geostationary satellites have been orbiting Earth since the launch of the first Application Technology Satellite (ATS-I) on December 7, 1966 (NASA, 2011a). The ATS program was initiated to "determine the feasibility and capability of placing a satellite in geostationary orbit over a fixed location on the

Earth's surface." Once this capability was established with the success of ATS, the Synchronous Meteorological Satellite (SMS) series was launched in 1974. SMS was the first geostationary satellites devoted to 24-hour tracking of weather patterns. With increasing technology and significant improvements in weather forecast models, NOAA commissioned a series of satellites capable of operating in real-time mode to replace the SMS series, which had operated only in research mode. Thus, the Geostationary Operational Environmental Satellite (GOES) program was born with the launch of GOES-1, October 16, 1975 ([NASA, 2011b](#)).

The United States National Oceanic and Atmospheric Administration (NOAA) National Environmental Satellite, Data, and Information Service (NESDIS) operates the GOES series of satellites, the longest running geostationary program. NOAA NESDIS has always deployed at least two satellites in order to monitor the entire Western Hemisphere. The primary mission of the two operational GOES satellites, termed GOES-East (75°W) and GOES-West (125°W), are to support weather forecasting, severe-storm tracking, and meteorological research. At their high altitude, spatial resolution of GOES satellites are approximately 4 km to 8 km. Because GOES continuously monitors the same region of earth, they can provide high temporal resolution of moisture content, cloud movement, and other atmospheric conditions over large areas, and can observe triggers for significant meteorological events, such as flash floods, tornadoes, heavy snowfall or rain, thunderstorms and hurricanes ([NESDIS Office of Satellite Operations, 2011](#)). Other geostationary satellite platforms from outside the US include the European Space Agency (ESA) Meteosat, the Indian INSAT, the Chinese Feng-Yun, the Japanese MTSAT, and the Russian Elektro.

For GOES satellites up to and including GOES-7, the primary instrument was the Visible Infrared Spin-Scan Radiometer (VISSR) Atmospheric Sounder (VAS). VAS was primarily an infrared instrument capable of operating in imaging mode (to produce frequent static images at high spatial resolution in one of several wavelength bands) as well as sounding mode (to produce less frequent, more coarse spatial resolution multi-channel although better quality vertical atmospheric profiles of temperature, moisture,

and other constituents.) Unfortunately, both modes could not operate simultaneously. GOES satellites after GOES-7 carried separate instruments to perform the imaging and sounding tasks: the GOES Imager and GOES Sounder. (The Imager supplies most of the US meteorological satellite imagery seen on TV weather forecasts.)

Polar orbiting satellites are another suite of satellites that carry sensors capable of monitoring meteorological variables. NOAA NESDIS operates both the Polar-Orbiting Operational Environmental Satellites (POES) program and the GOES program. These satellites orbit the earth with altitudes typically less than 1000 km, much less than geostationary satellites, and cross close to the poles with each orbit. Orbital periods are on the order of approximately 100 minutes, capable of generating global coverage maps from once or twice daily to weekly or monthly composites. Many polar orbiting satellites fly over the same area on earth at nearly the same local time each day, termed a sun-synchronous orbit, causing similar lighting conditions within each image. The low altitude orbit allows polar orbiting sensors to capture high spatial resolution images, on the order of 1 m up to 1 km.

Precipitable water retrievals have been operationally collected and continuously archived since late 1978 with the launch of the Television Infrared Operational Satellite - Next Generation (TIROS-N). Though TIROS-N carried several instruments, the sensor responsible for measuring total column ozone and atmospheric profiles of temperature and water content was the TIROS Operational Vertical Sounder (TOVS). The TOVS package consisted of three individual sensors: the Microwave Sounding Unit (MSU), the Stratospheric Sounding Unit (SSU), and the High-Resolution Infrared Radiation Sounder (HIRS). Most of the information needed to make successful water vapor retrievals comes from three channels on HIRS, namely, channels 10 ($8.2 \mu\text{m}$), 11 ($7.3 \mu\text{m}$), and 12 ($6.7 \mu\text{m}$). These channels are very close to the $6.5 \mu\text{m}$ strong water absorption band and are sensitive to water vapor in the lower, middle, and upper troposphere, respectively (Wu et al., 1993).

The Advanced Very High Resolution Radiometer (AVHRR), which also began operation in the late 1970s aboard the TIROS-N satellites and continues to be carried

on the NOAA satellites, measures wavelengths in 5 channels (6 channels on the Enhanced AVHRR beginning in the late 1990s) in the visible, near and thermal infrared regions. AVHRR is ideal for monitoring land surface (surface temperature, vegetation health, snow and ice monitoring) and atmospheric (moisture content, cloud mapping) characteristics. Several weekly and monthly data products are produced at 1 km spatial resolution. The Moderate Resolution Imaging Spectroradiometer (MODIS) sensor is a more advanced version of the AVHRR and sits aboard the NASA Terra (launched in 1999) and Aqua (launched in 2002) satellites. MODIS is similar to the AVHRR and GOES Imager in terms of the spectral regions it monitors (visible and infrared), however, it carries many more channels (36) and includes a finer spatial resolution, down to 250 m for some channels. Table 3.1 shows the relevant infrared wavelength bands on common satellite sensors used for water vapor estimation.

Table 3.1: Relevant infrared wavelength bands on common satellite sensors for monitoring atmospheric water vapor. Channel numbers labeled in parenthesis (channel 3A on Enhanced AVHRR only.) Wavelengths are in μm .

Band	GOES VAS	GOES Imager	AVHRR	MODIS
VIS/Near-IR	0.55 - 0.75	0.52 - 0.72(1)	0.58 - 0.68(1)	0.89 - 0.92(17)
			0.72 - 1.10(2)	0.93 - 0.94(18)
				0.92 - 0.97(19)
Mid-IR	3.84 - 4.06(12)	3.78 - 4.03(2)	1.58 - 1.64(3A)	1.36 - 1.39(26)
	6.40 - 7.08(10)	6.47 - 7.02(3)	3.55 - 3.93(3)	6.56 - 6.90(27)
				7.17 - 7.48(28)
Thermal-IR	10.4 - 12.1(8)	10.2 - 11.2(4)	10.3 - 11.3(4)	10.78 - 11.28(31)
	12.5 - 12.8(7)	11.5 - 12.5(5)	11.5 - 12.5(5)	11.77 - 12.27(32)

In addition to visible and infrared sensors, polar orbiting satellites also carry microwave sensors. The amount of microwave radiation reflected or emitted from Earth is relatively small and requires the lower altitude of polar orbiters to measure. Microwave sensors are significant because radiation in the microwave bands can penetrate through

clouds whereas visible and infrared radiation are scattered or absorbed by clouds. Microwave sensors are ideal in regions with consistent precipitation or cloud cover, such as tropical areas influenced by the ITCZ or convection. This is contrary to visible and infrared imagery, which are limited to observations in only cloud-free areas, leading to a dry-bias in their atmospheric moisture data.

Historically, the most common microwave sensor to collect precipitable water data is the Special Sensor Microwave Imager (SSM/I) aboard the NOAA Defense Meteorological Satellite Program (DMSP) satellites F8 to present. Spatial resolution for SSM/I images at nadir (from directly overhead) is roughly 25 km at 19 GHz, 22 GHz and 37 GHz and 12.5 km at 85 GHz. Unfortunately, microwave observations are best suited for observations over the oceans due to the highly varying emissivity of land surfaces and relatively constant emissivity over water surfaces in the microwave water vapor absorbing frequencies. As with other sensors aboard polar orbiters, regional and global composites of water vapor, temperature, and other parameters from microwave sensors are generated on weekly or monthly time scales.

Due to the high temporal frequency of geostationary satellites, GOES is commonly used for diurnal studies of surface and atmospheric hydrometeorological variables, such as surface temperature, precipitable water, and moisture advection. Global composites of water vapor are available on a hourly basis given the current configuration of the geostationary constellation, which are aligned along the equator roughly 75° longitude apart from each other. Since many polar orbiters are in sun-synchronous orbits, and may take several days to achieve global coverage, polar orbiter data are usually reserved for weekly or monthly aggregates.

Satellite data have recently become of primary use in climate change studies. The longest time-series comes from the NOAA POES and GOES satellite programs, which has recorded air temperature from the Microwave Sounding Unit (MSU) dating back to 1979, sea surface temperatures from the AVHRR since 1982, outgoing long wave radiation (OLR) from radiometers on the NOAA POES satellites back to 1974, and precipitable water vapor over the oceans from the SSM/I since 1987. Wentz

(2000) analyzed trends from these three datasets and found very high correlations. Although the techniques to merge information across multiple satellites and sensor technologies is difficult, these datasets give a significant baseline of surface and atmospheric temperature and moisture data to analyze trends and compare with other data sources.

Tropospheric warming rates since 1979 until near present have been calculated by NOAA based on satellite observations with high confidence (Karl et al., 2006; Fu et al., 2004; Church, 2009; Christy et al., 2007). The IPCC (2007) reported that the average atmospheric water vapor has increased since at least the 1980s over land and ocean as well as in the upper troposphere, and was broadly consistent with the increased saturation vapor pressure of the warmer air. Data were largely based on satellite observations (Trenberth et al., 2007b). In addition to surface temperature and atmospheric moisture, satellite data has also been used for climate change studies in describing sea-surface temperatures and ENSO, snow cover extent, Arctic and Antarctic sea ice extent, radiative forcing constituents (aerosols and greenhouse gases), severe storm frequency, clouds, and sea level rise (Solomon et al., 2007; Arrigo, 2010; NOAA National Climatic Data Center, 2011; NASA, 2011, 2007).

Satellite data are also used as an observational reference for comparison to model estimates of climate change (Christy et al., 2007; Christy and Norris, 2009; Spencer and Braswell, 2008). John Christy, Alabama's State Climatologist and Distinguished Professor of Atmospheric Science at the University of Alabama in Huntsville, testified before the US Federal House Ways and Means Committee in February 2009 and demonstrated a disagreement between satellite derived surface temperatures with those of past and current climate prediction models, such as those used in the 2007 IPCC Fourth Assessment Report. The disagreement was the climate models are overshooting climate warming. His hypothesis was that the satellites were recording a "real-world" response by the climate system to the warming through an increased cooling effect by clouds, something that the models poorly represent (Christy, 2009).

However, a major obstacle for remote sensing, particularly satellite remote sensing, to be used in climate change studies is that each new generation of satellite sensors also brings new technology and sensor materials, product generation algorithms, wavelength weighting functions, etc..., causing temporal continuity to be difficult to maintain in long-term monitoring programs. Lack of a priori knowledge of the land surface emissivity and amount of bidirectional reflectance for each wavelength band adds uncertainty to derived products. The most important error sources for determining long-term trends are: (1) offsets in calibration between satellites; (2) orbital decay and drift and associated long-term changes in the time of day that the measurements are made producing diurnal drifts in temperature; and (3) drifts in satellite calibration that are correlated with the temperature of the onboard calibration target, intricately coupled together with the diurnal drift ([Trenberth et al., 2007b](#)).

Another obstacle for the remote sensing community is the uncertainty in water vapor algorithm validation. Satellite sensors measure incoming radiation from an area on the top of the earth's atmosphere, which is a combination of radiation emitted from the ground and all levels in the atmosphere. This is dependent upon surface type, surface emissivity, and atmospheric carbon dioxide, aerosols, and water vapor, all which need to be known or estimated a priori. Additionally, physical quantities derived from radiation measured at the sensor are representative of areas and not exact locations. To calibrate and validate the algorithms, these area-weighted values must be compared to point data observations. Christy and Norris (2004) found considerable scatter when comparing tropospheric radiosonde station data with collocated satellite data. Despite this calibration problem, satellite algorithms perform well for moderate resolution scenes (over 1 km^2) and are often used in operational forecasting with satisfactory results.

3.1.1 Thermal-IR Studies

Chesters (1983) developed a precipitable water retrieval algorithm specifically applied to GOES VAS data. He estimated precipitable water from an abbreviated

version of the radiative transfer equation (RTE), treating the lower troposphere as a single thick layer with precipitable water PW and air temperature T_{air} overlying a surface with skin temperature T_{sfc} ;

$$\begin{aligned} T_v^B &= T_{sfc} \tau_v + T_{air} (1 - \tau_v), \\ \tau_v &= \exp \left[- (\kappa_v + \alpha_v PW + \beta_v PW^2) \sec \Theta \right], \end{aligned} \quad (3.1)$$

where PW is the precipitable water, T_{air} is the surface air temperature and is found from interpolation of surface observations, v is the sensor channel, τ_v and T_v^B are the total atmospheric transmittance and brightness temperature (i.e., temperature derived solely based on radiation received at the sensor) of that channel, respectively, and Θ is the zenith angle at time of observation. Parameters κ_v , α_v and β_v are representative of CO_2 absorptance and the first- and second-order water vapor transmittance coefficients, respectively, determined from a radiative transfer model applied to a diverse radiosonde profile data set. By applying equation 3.1 to the thermal infrared channels 11 and 12 on VAS and subtracting the air temperature, the expression now takes the form of

$$\frac{T_{11}^B - T_{air}}{T_{12}^B - T_{air}} = \exp \left[(\Delta\kappa + \Delta\alpha PW + \Delta\beta PW^2) \sec \Theta \right]. \quad (3.2)$$

This technique is sensitive to low-contrast conditions and to the estimates of T_{air} . Chesters (1983) notes that the algorithm clearly delineates low-level precipitable water gradients and extremes with excellent spatial resolution and temporal consistency but significant residual errors remain with respect to radiosonde sites.

In a follow-on study, Chesters et al. (1987) linearized equation 3.2 by setting $\Delta\beta$ to zero. They applied a least-squares minimization procedure to 135 radiosonde observations to determine $\Delta\kappa$ and $\Delta\alpha$ and found them to be less than those proposed in Chesters (1983). As would be expected, lower residuals were found when applied to 7 days of VAS images of the central US in June, 1981.

Dalu (1986) compared two techniques for deriving precipitable water over the oceans. Observed precipitable water was calculated from about 40 ship-borne radiosonde launches. Each technique was compared to values generated from a radiative transfer model and from the Infrared Interferometer Spectrometer (IRIS) sensor database. (IRIS was flown on Nimbus-4 satellite and measured wavelengths from $5 \mu\text{m}$ to $25 \mu\text{m}$.) The first method used was the $9 \mu\text{m}$ mean line amplitude (9MLA) technique. The weighting function of the $9 \mu\text{m}$ absorption lines has the same scale height (general height the wavelength band is sensitive too) as the vertical distribution of water vapor. 9MLA was calculated as $T_p - T_v$, where T_p is the average brightness temperature of the most transparent wavelength intervals from $7.7 \mu\text{m}$ to $9.1 \mu\text{m}$, and T_v is the average brightness temperature of the least transparent intervals in the same spectral region. The result was a non-linear functional relationship between 9MLA and observed precipitable water. Errors were about $\pm 2 \text{ mm}$ when fit against modeled profiles and $\pm 3 \text{ mm}$ when fit against the IRIS data.

Dalu (1986) compared these results to results from a second algorithm utilizing the split-window channels on the AVHRR. The same 40 ship-borne profiles, radiative transfer model, and IRIS data were incorporated. The expression takes the form

$$\begin{aligned}
 PW &= A \cos \Theta (T_{4B} - T_{5B}), \\
 A &= \frac{g(pw)}{k(T_s - \bar{T}_{4B})}, \\
 g(PW) &= \frac{1 - \tau_4}{C(1 - \tau_5)(1 - \tau_4)},
 \end{aligned} \tag{3.3}$$

where $C = (T_s - \bar{T}_{4B})/(T_s - \bar{T}_{5B})$, Θ is the scanning angle set to zero for nadir viewing, T_s is the surface temperature, and $\tau_4, T_{4B}, \tau_5, T_{5B}$ are the total atmospheric transmittances and brightness temperatures for channels 4 and 5, respectively. A and C were found to remain relatively constant under most atmospheric conditions, even though $g(pw)$ and the denominator of A are dependent upon the amount of water vapor. When the 40 observed values were regressed against the modeled $T_4 - T_5$, the

error was ± 4 mm; likewise, the error was ± 5 mm when IRIS $T_4 - T_5$ data was used. Dalu (1986) adds that the AVHRR algorithm did not perform as well as 9MLA because the AVHRR split-window channels are not optimized for water vapor retrieval since the channel 4 weighting function does not reach the surface while the channel 5 weighting function lies below the water vapor scale height.

Hayden (1988) developed a physical technique utilizing several of the channels on GOES-7 VAS, the Simultaneous Temperature-Moisture Retrieval Algorithm. This technique is very similar to that developed by Smith et al. (1985) using channels 7, 9, and 10 to retrieve three levels of water vapor and channels 2, 3, 4, 5, and 7 to retrieve 5 levels of temperature, simultaneously. When clouds are present, retrievals are only made from the cloud top to TOA, with profiles below the cloud linearly interpolated from surface observations.

A revised version as applied to the GOES-8 Sounder is described, as well as much of the derived product imagery (DPI), in Hayden et al. (1995). Both versions are highly dependent on the temperature and moisture first guess profiles (the accuracy of the DPI is almost entirely dependent on the quality of the first guess field) and are designed to be used with as many channels as possible.

Kleespies and McMillin (1990) applied a statistical technique based on the fact that land surface temperature varies much more significantly than air temperature. Their algorithm is applied to the split-window channels on GOES VAS (channels 11 and 12) and on the AVHRR (channels 4 and 5). When two scenes are assumed identical except for the surface temperature (such as two nearby locations, one over land and the other over water, or the same location with two images taken a few hours apart when the surface temperature is rapidly changing), Kleespies and McMillin (1990) derive the following relationship (as applied to GOES VAS, similar equation not shown here also derived for AVHRR):

$$\frac{\tau_{s12}}{\tau_{s11}} = \frac{T_{12B}^a - T_{12B}^b}{T_{11B}^a - T_{11B}^b}. \quad (3.4)$$

The superscripts a and b refer to the two different observing conditions. T_s is assumed the only parameter changing, and τ_{s11} and τ_{s12} are the total atmospheric transmittances in VAS channels 11 and 12, respectively. The left-hand side of equation 3.4 is linearly fit to the slant path precipitable water using a training set comprised of radiosonde data and a radiative transfer model to simulate VAS/AVHRR radiances. For AVHRR, retrievals were made in nighttime to avoid convection over a body of water and a nearby land surface. A correlation of $r = 0.85$ and a standard difference of 4.4 mm were found when comparing against $2^\circ \times 2^\circ$ gridded radiosonde data. VAS data performed slightly better when compared to individual station observations ($r = 0.92$ and standard difference of 3.9 mm.)

Jedlovec (1990) modifies the methods of Kleespies and McMillin (1990) by extending the use of the transmittance ratio to the Split Window Variance Ratio (SWVR) technique:

$$\frac{\tau_{s12}^2}{\tau_{s11}^2} = \frac{\sigma_{12}^2}{\sigma_{11}^2}, \quad \text{where} \quad \sigma^2 = \frac{\sum_{i=1}^N \delta T(i)^2}{N-1}. \quad (3.5)$$

σ^2 is the variance for each channel and δT is the difference between the individual cell and the average of the rectangular surrounding neighbors. The SWVR is then fit to precipitable water data via a linear or a log-linear transform, which resulted in a slightly better fit:

$$PW = A0 + A1 \times SWVR \quad \text{or} \quad PW = A2 - A3 \ln(SWVR). \quad (3.6)$$

From simulated transmittances, $A2 = -3.585$ and $A3 = 35.13$ with a standard error of less than 2.0 mm and $r = 0.96$. When applied to scenes from the Multi-spectral

Atmospheric Mapping Sensor (MAMS) instrument during Cooperative Huntsville Meteorological Experiment (COHMEX) for two days in June 1986, a standard error of 4.85 mm was achieved. The authors also discuss how the effects of random noise can be estimated and removed. An advantage of this technique is that inaccuracies in absolute measurements of emissivity and radiances are minimized through comparing ratios.

Harris and Mason (1992) developed a semi-empirical technique applied to the AVHRR split-window channels to determine the atmospheric correction term in sea-surface temperature (SST) algorithms. It makes use of the fact that SST is slightly more spatially variable than air temperature. Precipitable water values calculated from 56 seasonally and geographically diverse ocean radiosonde profiles were fit using the form

$$\frac{\Delta T_5}{\Delta T_4} = K PW + Constant. \quad (3.7)$$

ΔT represents a change in surface temperature occurring under identical atmospheric conditions as measured by channels 4 and 5, respectively. Therefore, any changes in radiance received at the sensor are assumed to be solely due to changing SSTs. This can be accomplished (with some assumptions) by imaging the same scene at two times or by imaging two geographically close, homogeneous scenes simultaneously. Performance was value dependent, with larger errors occurring at high precipitable water values. Overall root-mean-square deviation was 3.1 mm using equation 3.7. A second order polynomial fit was also tried reducing the RMS deviation to 2.6 mm.

Eck and Holben (1994) developed a statistical split-window technique to estimate precipitable water and applied it to the AVHRR to correct for atmospheric absorption in the calculation of Normalized Difference Vegetation Index (NDVI). Based on the difference between channel 4 (the clean channel representative of the surface) and channel 5 (the dirty channel affected by atmospheric absorption) on the NOAA-9

AVHRR, they derived a linear expression for precipitable water:

$$PW = C_1(T_4 - T_5) + C_2. \quad (3.8)$$

Data from 7 radiosonde stations, 3 in the Sahel region of Africa and 5 in the continental US, were colocated with several AVHRR images. Images were first aggregated into 3 x 3 pixel grids and those taken within 4 hours of the radiosonde launch were kept. Brightness temperature differences for grid cells that were cloudless and within 40 km of the radiosonde site were regressed with the observed precipitable water. Among the 7 stations, parameters C_1 and C_2 ranged from 0.8 to 1.2 and 0.04 to 1.5, respectively, and resulted in correlations of r^2 of 0.82 to 0.96 with standard errors of 2.2 mm to 4.8 mm. Three particular sources of error are inherent in their methods and include an unknown (and therefore assumed to be 1.0) surface emissivity, mis-alignment in time/space of AVHRR-derived precipitable water locations and radiosonde stations, and large aerosol loadings that may decrease the temperature difference ($T_4 - T_5$) to mask the precipitable water signal.

Lee and Park (2007) applied the Split-Window Logarithm Ratio (SWLR) method to the thermal-IR channels (11 and 12 μm bands) aboard the GOES-9 and Japan's MTSAT-1R geostationary satellites to compute total precipitable water. The formulation is a modified version of 3.2, a simple and fast method for operational purposes. Formula coefficients were computed using integrated radiosonde data and first guess estimates (calculated from the Radiative Transfer for Tiros Operational Vertical Sounder model using 43 atmospheric pressure levels) for data in 2002 and 2003. The algorithm was then applied to imagery from GOES-9 in 2004 and MTSAT-1R in 2006. Brightness temperatures were averaged within 40 km to 45 km of the radiosonde station (approximately 19 x 19 pixels) and data were carefully chosen to represent cloud-free images. RMSE was 7.2 mm for GOES-9 data and 9.4 mm for MTSAT-1R. Similarly, the correlation coefficient was 0.76 for GOES-9 data and 0.78 for MTSAT-1R.

Bedka et al. (2007) calculates precipitable water for three sites in Oklahoma, US, during the Department of Energy's Atmospheric Radiation Measurement (ARM) experiment from 2005 to 2007. They performed single field of view (SFOV) retrievals at $10\text{ km} \times 10\text{ km}$, and a 3x3 pixel-averaged field of view at $30\text{ km} \times 45\text{ km}$. The 3x3 FOV retrievals performed better (RMSE from 2.5 mm to 3.0 mm) than the SFOV retrievals (3.0 mm to 3.8 mm) across all three sites. They also note that the 3x3 FOV retrievals show the least improvement over the first guess during the afternoon, at a time where cloud contamination could be present.

3.1.2 Near-IR Studies

Atmospheric water vapor measurements using remote sensing have historically been done by observing the Earth's emission of radiation in the thermal-IR portion of the electromagnetic spectrum. As seen in the previous chapter, results vary depending upon the first guess estimates but also on the fact that surface brightness temperatures are different than the overlying atmosphere. When the surface temperature, a function of surface emissivity and skin temperature, is about equal to the average temperature of the boundary layer (where most of the water vapor resides) observations in the thermal bands will not be sensitive to the atmospheric water vapor (Gao and Kaufman, 2003). Recently, sensors have been launched to take advantage of the water vapor absorption bands in the near-IR portion of the spectrum. Near-IR radiation received at the satellite sensor is primarily composed of reflected solar radiation after it has traversed the atmosphere toward the surface, been reflected by the surface, and then transmitted back through the atmosphere. By comparing the radiances of a water vapor absorption band with that of a water vapor transmittance band, the total columnar precipitable water can be determined (Kaufman and Gao, 1992; Vesperini et al., 1999).

Gao and Kaufman (2003) describes a near-IR method implemented using the Moderate Resolution Imaging Spectrometer (MODIS) sensor aboard NASA's Terra and Aqua satellites. MODIS has five channels in the near-IR portion of the spectrum focused on water vapor absorption, aerosol scattering, and surface reflection, centered

at $0.865 \mu\text{m}$, $0.905 \mu\text{m}$, $0.936 \mu\text{m}$, $0.940 \mu\text{m}$ and $1.240 \mu\text{m}$. If surface reflectance is constant with wavelength, the a ratio of the radiances in an absorption (dirty) channel (such as the $0.94 \mu\text{m}$ wavelength) to a window (clean) channel within this near-IR region can give the transmittance in the absorption channel:

$$\tau_{obs}(0.94\mu m) = \frac{Ref(0.94\mu m)}{Ref(0.865\mu m)}, \quad (3.9)$$

where τ refers to the transmittance and Ref refers to the reflectance. If the surface reflectance varies linearly with wavelength, a three-channel ratio of an absorption channel with window channels on either side can give the transmittance in the absorption channel:

$$\tau_{obs}(0.94\mu m) = \frac{Ref(0.94\mu m)}{C_1 * Ref(0.865\mu m) + C_2 * Ref(1.24\mu m)}, \quad (3.10)$$

where C_1 is equal to 0.8 and C_2 is equal to 0.2. The two-channel ratio is used over water bodies (oceanic) with sun glint and three-channel ratio over land pixels with clear sky. Lookup values of the total amount of water vapor are generated using the HITRAN2000 atmospheric transmittance code. The total water vapor content can then be converted to precipitable water using

$$PW = \frac{WV_{total}}{\frac{1}{\cos(\theta_s)} + \frac{1}{\cos(\theta_v)}}, \quad (3.11)$$

where WV_{total} is the total water vapor content, θ_s is the solar zenith angle, and θ_v is the viewing zenith angle. (Note that for areas above clouds, a different algorithm is used, incorporating wavelength bands from $0.8 \mu\text{m}$ to $2.5 \mu\text{m}$.) The authors note that typical errors in precipitable water are in the range of 5-10% where the largest sources of error are the uncertainty in spectral reflectance in the surface targets and the amount of

haze for dark surfaces.

Falvey and Garreaud (2005) applied the MODIS precipitable water product to the Brazilian altiplano region during the SALLJEX experiment. Data were obtained from November 2002 to April 2003 at 1.0 km spatial resolution. Precipitable water was also computed using a permanent GPS receiving station and used as ground truth when evaluating the MODIS-PW data. A strong linear relationship was found between MODIS-PW and GPS-PW values:

$$PW_{GPS} = 2.08 + 1.06 * PW_{MODIS}, \quad (3.12)$$

with differences approximately 5%. The authors note that this regression was computed using data for only one location but does give credence to MODIS derived precipitable water over large areas.

3.1.3 Optical Methods

There have been several algorithms developed to retrieve atmospheric water vapor from the visible part of the electromagnetic spectrum, the most widely used methods are the classical Differential Optical Absorption Spectroscopy (DOAS) and the Air Mass Corrected version of DOAS (AMC-DOAS) (Slijkhuis et al., 2010). The concept was initially developed for sun photometry in the late 1970s, but was modified for satellite retrieval of various atmospheric constituents, focusing on water vapor, in the late 1990s and early 2000s (Noël et al., 1999, 2004).

These techniques have been primarily developed for and applied to the Global Ozone Monitoring Experiment (GOME) instrument aboard the European Research Satellite ERS-2, a polar orbiting satellite at an altitude of 780 km and crossing time of approximately 10:30 am local time. GOME measures radiation in 4096 channels from 0.24 μm to 0.79 μm . GOME was followed by two very similar, albeit higher spatial resolution, instruments: the SCanning Imaging Absorption spectroMeter for Atmospheric Chartography (SCIAMACHY) aboard the European satellite ENVISAT, and

the GOME-2 aboard EUMETSAT’s MetOp series of satellites. Noel et al. (2007) describes developing a combined precipitable water dataset from all three sensors, beginning with GOME 1997 and continuing until the projected lifespan of the GOME-2 on MetOp ends near 2020.

The basic principle of DOAS is to calculate the difference among the Earthshine radiance (including all radiation reflected and scattered) and solar irradiance at water vapor absorption wavelengths in the visible spectrum. For all three instruments, the wavelength bands incorporated are centered from $0.688 \mu\text{m}$ to $0.700 \mu\text{m}$, which overlaps with the molecular oxygen (O_2) absorption bands. With this approach, certain assumptions are made, namely no surface elevation, surface albedo of 0.05, a tropical atmosphere, and absence of clouds. An Air Mass Correction Factor (AMCF) is applied to account for differences from the actual conditions, at least to some degree. The AMCF is scaled to achieve the correct O_2 optical depth. If the AMCF deviates too much from unity, the water vapor measurements are discarded (Mieruch et al., 2008).

The central equation of the AMC-DOAS method is given by:

$$\ln \left(\frac{I}{I_0} \right) = P - AMCF \times \left(\tau_{O_2} + c PW^b \right), \quad (3.13)$$

where I and I_0 are the Earthshine radiance and solar irradiance measurements, respectively. P is a polynomial that represents all broadband contributions, such as from atmospheric scattering or surface reflection. τ_{O_2} is the O_2 optical depth and PW is the total columnar precipitable water. The spectral quantities b and c describe the saturation effect and the absorption, and are determined through radiative transfer calculations (Mieruch et al., 2008).

An advantage of DOAS is that it does not require a priori information, reducing the uncertainty in the input requirements and providing an independent dataset to compare against other methods. Another advantage is that it is sensitive to relative or differential absorptions, keeping consistent as the instrument degrades over

time (Wagner et al., 2006). A disadvantage, such as with any optical method, is that each scene must be nearly cloud-free, thereby limiting the amount of data able to be captured (and allowing cloud fringes to contaminate the signals) and inability to capture diurnal phenomena due to one measurement per day under dry conditions.

Slijkhuis et al. (2010) compared AMC-DOAS method derived precipitable water from GOME-2 with radiosonde and SSM/I data over the period May 2007 through August 2009. Collocations were taken within 60 minutes of GOME-2 retrievals with cloud fractions less than 20%. On average, GOME-2 values are about 2 mm higher than for radiosondes with a standard deviation of around 6 mm (larger deviations with higher precipitable values.) The authors note a residual albedo effect, based on solar zenith angle, with larger values occurring for lower albedos. In the comparison with SSM/I in January 2008, GOME-2 was found to be about 5% higher.

3.1.4 Microwave Studies

Alishouse (1990) developed an empirical relationship between the brightness temperatures of the SSM/I and observed oceanic moisture profiles, primarily over small island clusters. Although the SSM/I is a 7-channel, 4-frequency instrument, the authors fit a non-linear algorithm based upon only the vertical polarization of the 19 GHz, 22 GHz and 37 GHz brightness temperatures. The expression takes the form of

$$PW = a_0 + a_1 T_B^{19V} + a_2 T_B^{22V} + a_3 T_B^{37V} + a_4 (T_B^{22V})^2, \quad (3.14)$$

where,

$$\begin{aligned} a_0 &= 232.89393, & a_1 &= -0.148596, & a_2 &= -1.829125, \\ a_3 &= -0.36954, & a_4 &= -0.006193. \end{aligned}$$

Validation was performed by matching the single image pixels to the closest radiosonde station, within 2° of latitude and longitude and within 2 hours of launch. Summarizing

by latitudinal zone, the RMSE values fell within 1.9 mm to 4.3 mm with below average values in the tropics. Globally, there was no bias and few boundary discontinuities as were present in earlier versions of the SSM/I algorithms.

Jackson and Stephens (1995) perform an evaluation of four microwave algorithms applied to monthly mean SSM/I data. Two are statistical, one is semi-statistical, and the other algorithm is physically based. Land areas and scenes contaminated by precipitating clouds were eliminated from their analysis. Though no attempt will be made to describe each of these methods, a few general comments can be mentioned. Temporally, all four methods behaved similarly with respect to seasonal variability. All methods overestimated precipitable water in dry, cold conditions and underestimated it in very moist conditions with respect to radiosonde data. The physical method maintained the least bias among them all but maintained the largest RMSE and most scatter, whereas the statistical methods contained the most bias, especially in the mid-range values.

Wimmers and Velden (2011) describe microwave methods used to blend (and visualize) total precipitable water retrievals from polar orbiting satellites to develop the Cooperative Institute for Meteorological Satellite Studies (CIMSS) Morphed Integrated Microwave Imagery TPW product (MIMIC-TPW). They include only microwave-based retrievals over ocean regions from the SSM/I and SSMI/S aboard the NOAA Defense Meteorological Satellite Programs (DMSP) satellites, and AMSR-E aboard NASA Aqua satellite. They used methods as described above from Alihouse (1990) across all three satellites with very little intercalibration changes.

3.2 Global Positioning System (GPS) Technique

Estimation of precipitable water utilizing the Global Positioning System (GPS) network is a method that has gained recent interest. The method makes use of the constellation of nearly 30 GPS satellites, orbiting the Earth at 20,200 km at an orbital inclination of 55° . The design allows for approximately 12 satellites to be viewable from anywhere on the Earth at any one time. (Of course, this is dependent upon local

obstructions, such as buildings or trees. Fortunately, only 3 satellites are necessary to compute an accurate GPS measurement.) As the L-band microwave signals transmitted by the GPS satellites and received by the GPS receiver on Earth, the signal becomes refracted (delayed) by the ionosphere as well as within the troposphere. The ionospheric dispersion can be accounted for by using dual-frequency observations (Bock et al., 2007; Bevis et al., 1992). The tropospheric delay, called the "wet" delay, is nearly proportional to the amount of water vapor integrated along the signal's slant path. The zenith wet delay (in the vertical direction directly above the receiver) and total column precipitable water can be estimated with little additional uncertainty (Duan et al., 1996).

One of the benefits of GPS-derived precipitable water data is high temporal resolution. A fixed station can produce time steps of a few minutes to 2 hours of precipitable water indefinitely, as long as the receiving station keeps recording. Calculations can be made in nearly all types of weather conditions, due to the microwave-based GPS signals penetrative ability through clouds. As well, accuracy and precision are very high as compared to other in situ observations (Tregoning et al., 1998; Bevis et al., 1994; Sapucci et al., 2007; Wang and Zhang, 2008; Vey et al., 2010; Adams et al., 2011). Unfortunately, data received at a GPS receiver represents a single point and difficult to compare against areal averaged data. Several locations are necessary to perform a regional study. The GPS receiving station must also be referenced to a high degree of accuracy and infrastructure must be maintained throughout the observations. To compensate for this last point, many studies use permanent stations of the International Global Navigation Satellite Systems (GNSS) Service (IGS) network (i.e., Wang (2007)) of which there are nearly 400 active stations globally (Dow et al., 2009).

Bevis et al. (1994) describes the method for determining precipitable water from GPS signal delays. It is a two step process. First, the zenith wet delay (ZWD) is computed by subtracting the zenith hydrostatic delay (ZHD, calculated below) from

the zenith tropospheric delay (ZTD, estimated through processing of the GPS signals.)

$$ZWD = ZTD - ZHD \quad (3.15)$$

The ZHD is dependent upon air pressure and elevation at the GPS antenna height. ZHD can be modeled as

$$ZHD = 2.2779 \text{ (mm hPa}^{-1}\text{)} \times \frac{P_s}{f(\phi_{station}, h_{station})}, \quad (3.16)$$

with

$$f(\phi_{station}, h_{station}) = 1 - 0.0026 \cos(2\phi) - 0.0028 \text{ km}^{-1} \times h_{station}, \quad (3.17)$$

where $f(\phi_{station}, h_{station})$ is a correction of the mean gravity depending on the latitude (ϕ) and altitude (h) of the GPS station. The second step in the process is to convert the zenith wet delay into the amount of water vapor in the atmospheric column above the GPS receiver. Bevis et al. (1994) models this as

$$PW = ZWD \times \frac{10^6}{\rho_w R_v \left(\frac{k_3}{T_m} + k_2 \right)} \quad (3.18)$$

where ρ_w is the density of liquid water (1025 kg m^{-3}), R_v is the specific gas constant for water vapor ($461.51 \text{ J K}^{-1} \text{ kg}^{-1}$), and k_2 and k_3 are atmospheric refraction constants (22.1 K hpa^{-1} and $373900 \text{ K}^{-2} \text{ hpa}^{-1}$, respectively.) T_m is the mean temperature of the atmosphere directly above the GPS receiver. T_m can be modeled linearly, as in Bevis et al. (1994),

$$T_m = aT_{sfc} + b, \quad (3.19)$$

where $a = 0.72$ and $b = 70.2$ K (as derived from a set of radiosonde data in the United States) and T_{sfc} is the surface air temperature. Or, T_m can be computed from model reanalyses. Wang et al. (2007) and Vey et al. (2010) found that the NCEP and ECMWF reanalyses represented the mean temperature of the atmosphere very well.

Wang et al. (2007) developed a GPS-derived precipitable water dataset for 80 to 268 IGS stations (depending on the year) globally at 2-hourly time steps from 1997 to 2004. When compared against data for 98 radiosonde stations that match in launch time (within one hour) and location (within 50 miles horizontally and 100 m vertically), and which include observations at the surface up to at least 300 hPa, the mean difference was 1.08 mm, with a dry bias in the radiosonde observations. The RMSE for all data points at all the selected stations was 2.83 m. When compared against three near-surface microwave radiometers and corrected for elevation differences, mean biases ranged from 0.03 mm to 1.66 mm. The authors note errors in the GPS-derived values may be due to estimates of T_m , ZPD errors (receiver noise, antenna phase delays), GPS satellite orbit error, ionospheric corrections, surface pressure estimates, mapping functions that model ZTD based on signal path length, and others. The comparisons illustrate the usefulness of evaluating the quality of GPS-derived precipitable water with measurements from other devices.

Sapucci et al. (2007) compared integrated water vapor measurements from GPS stations to radiosondes (as well as to an Aerosol Robotic Network (AERONET) solar radiometer and the Humidity Sounder for Brazil (HSB) aboard the NASA's Aqua satellite.) The analysis was part of the RACCI/DRY-TO-WET experiment carried out in southwestern Amazonia in 2002. When GPS derived values were compared against the radiosonde data, the mean observed biases were from 1.7 mm to 3.3 mm, and RMSE within 2.9 mm to 4.0 mm. This result was in agreement with many other similar studies, although biases were slightly larger than in previous work, with the radiosonde precipitable water values lower (drier) than values derived using GPS, particularly for daytime measurements. Two possible causes for the errors are the tendency for

radiosondes to be drier during daytime observations and ionospheric interference, due to its location near the geomagnetic equator and enhanced sunspot activity. However, the bias between the GPS and radiosonde data were much lower for higher water vapor amounts (45 mm to 55 mm) than for lower amounts (35 mm to 45 mm.)

Vey et al. (2010) used GPS-derived precipitable water values as validation for model reanalyses. They note accuracy strongly depends on the estimates of ZTD values, whose sources of error are most notably the modeling of the location of the phase center of the satellite and receiver antenna relative to their geometrical reference point, and the mapping functions of the elevation dependence on path length. Due to some recent advances in processing to improve estimates of ZTD, systematic errors of precipitable water to 0.7 mm to 1.7 mm.

Adams et al. (2011) collected precipitable water values from a non-idealized rainforest tower, part of the LBA experiment in central Amazonia near Manaus in the State of Amazonas. Forest canopy at this site was ≈ 40 m and the tower reached up to 55 m. Two different quality-level GPS receivers were used with two different processing algorithms. Radiosondes were launched twice daily at a location within 5 km distance. Overall, errors relating to specifically GPS received quality or processing methods, were on the order of 1.0 mm (2-3%). Biases when compared to radiosondes were from 2.2 mm to 3.7 mm with GNSS slightly overestimating precipitable water in respect to the radiosondes. The results of this study supports the plausibility of developing a GNSS network within the Amazon forests with high accuracy precipitable water measurements taking place in adverse site and weather conditions.

3.3 Surface-based and Other Methods

Historically, the most popular method for estimating the amount of water vapor contained in an atmospheric column of air was by inference from meteorological surface measurements, dating back to the beginning of the century ([Reber and Swope, 1972](#)). Although many techniques exist, the most common are equations relating precipitable

water to surface dewpoint through a linear fit or to surface water vapor density through a log-linear fit.

$$\begin{aligned}
 PW &= a + b \rho_w, \quad \text{or} \\
 \ln PW &= a + b T_d,
 \end{aligned}
 \tag{3.20}$$

where T_d is the dewpoint temperature, a and b are statistically derived constants, and ρ_w is the water vapor density, usually substituted by water vapor pressure, e_w , or absolute humidity, χ . It is also very common to use monthly mean data to reduce random error and increase correlation.

Not only are near-surface measurements obviously much easier to obtain than measurements in the upper-air, humidity measurements at the surface may be less prone to errors. Many of the long-term changes and device improvements in the radiosonde history are related to the sensor's response in cold temperatures (Elliott, 1995; Ross and Elliott, 2001). This affects observations above 700 mb more than closer to the surface and cause biases in atmospheric integrated humidity derived products.

Reitan (1963), using equation 3.20, found $a = -0.981$ and $b = 0.0341$ with errors approximately 10% of the observed mean precipitable water. Using mean monthly values of precipitable water and T_d data from 1954 to 1956 for 15 U.S. stations, the correlation coefficient was 0.98, however, he notes the degree of relationship is less for daily data.

Reber (1972) examined the relationship of precipitable water to surface absolute humidity for soundings at three stations in California. Monthly correlation coefficients varied widely ranging from -0.29 to 0.83 . However, Reber (1972) assessed the validity of determining precipitable water from χ and notes, "...on an individual observational basis, at any time during day or night as required when conducting scientific measurements, that computation of total precipitable water from the absolute humidity at the surface results in large errors and, therefore, is not a valid experimental procedure."

Garrison and Adler (1990) also used equation 3.20 but regressed $\ln(pw)$ with

pressure corrected e_w and χ and found a to be 2.1 and 2.0, respectively, and b to be 1.4 and 1.9, respectively. They also examined methods that incorporate interpolated values of precipitable water from nearby stations as well as multiplying by adjustment factors based upon geographic location. Generally good agreement was found with monthly mean data for 82 stations in the contiguous U.S. and Alaska. In a follow-up study, Garrison (1992) fit a quadratic function to χ for 26 stations in Australia. Mean monthly data again was used and results very similar to Garrison and Adler (1990) were obtained.

Gueymard (1994) estimates precipitable water as a function of absolute humidity and water vapor scale height, H_v .

$$\begin{aligned}
 PW &= 10 H_v \rho_v \\
 \rho_v &= 216.7 \frac{e}{T} \\
 H_v &= 0.4976 + 1.5265 \frac{T}{T_o} + \exp \left[13.6897 \frac{T}{T_o} - 14.9188 \left(\frac{T}{T_o} \right)^3 \right]
 \end{aligned} \tag{3.21}$$

where T is the surface temperature in Kelvin and T_o is 273.15 K. Generally good agreement was found when comparing long term average data for 46 Canadian and Northern U.S. stations. Wahab et al. (1995) merged the precipitable water dependence on H_v and T_d . For 6 stations distributed globally, they derived the following expressions for the terms in equation 3.20:

$$\begin{aligned}
 a &= 4.8705 - \ln(273.16 + T_o) + \ln H_v \\
 b &= 0.068,
 \end{aligned} \tag{3.22}$$

where H_v is derived physically from measured wet and dry lapse rates, p and e . Regressions were performed for instantaneous soundings, daily, and monthly data and $r > 0.95$ was found at all time scales.

Choudbury (1996) conducted a review of many past articles concerning equations 3.20. Based on mean monthly data for 45 global stations representing very different climate regimes, he found very little difference between the two equations. The correlation coefficient r^2 was greater than 0.85 for 82% of the stations.

Ross and Elliott (2001) investigated the correlations between numerous surface and near-surface humidity variables and the surface-to-500-mb precipitable water. They looked at monthly means of temperature T , dewpoint temperature T_d , relative humidity RH and specific humidity q at the surface, 850-mb and 750-mb levels. The analysis covered 1973 to 1995 based on humidity data derived from the NCAR radiosonde archives, with their analysis only covering the Northern Hemisphere due to the paucity of upper-air observations in the Southern Hemisphere.

They found the strongest correlation with precipitable water to be the 850 mb specific humidity, with mean correlations (according to the Spearman Rank method) among the radiosonde observations of 0.92 to 0.94 for all four seasons, although correlations with 850 mb dew point temperature were nearly as high at 0.85 to 0.92. A small spread of correlations existed about the median, which is a favorable characteristic for a surrogate variable. The authors also note a similar conclusion was found by Sinha and Sinha (1981) for India and by Gaffen (1992) for a 63-station global network.

Though spaceborne remote sensing, GPS-based, and surface-based regression are the most common and conventional means for estimating precipitable water, there also exists many other techniques. Some examples include: ground-based near-IR ($0.94\ \mu\text{m}$) radiometers (Reagan et al., 1995; Mattioli et al., 2005), ground-based microwave (20 GHz to 90 GHz) radiometers (Gao and Kaufman, 2003; Li et al., 2008; Cady-Pereira et al., 2008), aircraft-based millimeter-wave imaging radiometer (Wang et al., 1995b, 2002), measuring the molecular backscattering from lasers such as lidar and Raman scattering techniques (Wang et al., 1995a; Renault et al., 1980), ground-based sun photometers (Bock et al., 2007; Campanelli et al., 2010), modified optical techniques to use other parts of the visible spectrum (Maurellis et al., 2000), and those that integrate several different methods (Westwater, 1997).

3.4 Global Water Vapor Data Inventories

Additionally, many datasets currently exist that include atmospheric precipitable water. Some of these datasets come from a single source or measurement technique while others integrate information from multiple sources. This section summarizes the availability and resolution of precipitable water within several commonly used datasets.

3.4.1 Satellite-based

TOVS

From the archived Television Infrared Operational Satellite - Next Generation (TIROS-N) Operational Vertical Sounder (TOVS) soundings, Wittmeyer and Vonder Haar (1994) developed the Global International Satellite Cloud Climatology Project (ISCCP) Water Vapor Climatology (Rossow et al., 1991). The water vapor retrieval scheme (which resolves three vertical layers of water vapor) was performed by the National Environmental Satellite Data and Information Service (NESDIS) and sent to ISCCP as an ancillary dataset to the cloud data (Wittmeyer and Vonder Haar, 1994). This dataset covers $6\frac{1}{2}$ years from July 1983 to December 1989. Precipitable water values were fit to a $2.5^\circ \times 2.5^\circ$ grid and interpolated to three vertical levels, to match cloud data from the ISCCP project. Though this dataset demonstrates some of the basic features in global water vapor, such as accurate placement of the ITCZ and South Pacific Convergence Zone (SPCZ) and lower values at higher elevations, the TOVS dataset fails to depict the spatial and temporal variability of water vapor (Wittmeyer and Vonder Haar, 1994). Missing data may be the result of gaps between individual image scans, between scans, or areas of cloudiness (Wittmeyer and Vonder Haar, 1994). Despite these shortcomings, the TOVS Initial Guess Retrieval (TIGR) dataset was also created to provide remote sensing algorithms with an approximate atmospheric profile of temperature and humidity (Wu et al., 1993).

SSM/I

The SSM/I, aboard the NOAA polar orbiting DMSP satellites, has been collecting meteorological data over the oceans since 1987. (As stated previously, the highly variable emissivity over land surfaces in the microwave regions prevents accurate atmospheric measurements over land.) The SSM/I dataset as described by Ferraro et al. (1996) includes precipitable water along with precipitation, sea ice, snow cover and clouds. NESDIS receives the SSM/I data at roughly 25 km resolution and composites of daily grids of $\frac{1}{3}^\circ \times \frac{1}{3}^\circ$. The authors then aggregated the data to monthly means of $1^\circ \times 1^\circ$ and $2.5^\circ \times 2.5^\circ$ grids for 1987 to 1994, then extended through 2007 (Ferraro et al., 2007). Two benefits of this dataset are: 1) several products derived from the same sensor with identical temporal and spatial resolutions, and 2) microwave imagery is unaffected by non-precipitating clouds and can capture data in more atmospheric conditions (Ferraro et al., 1996). A negative characteristic, other than data not being available over land, is data are taken once daily, hence, unresolving diurnal variability and possibly biasing longer-term averages. A similar dataset was created for 1978 through 1987, just previous to the SSM/I dataset. This data comes from the Seasat Scanning Multichannel Microwave Radiometers (SMMR) on the Nimbus-7 satellite. SMMR utilizes the 22.235 GHz weak water vapor absorption band, identical to the SSM/I (Carleton, 1991).

The Morphed Integrated Microwave Imagery at CIMSS - Total Precipitable Water (MIMIC-TPW) product incorporates real-time precipitable water globally over the oceans from various microwave sensors, however, it is unique in the blending the different data at different times throughout the day. It is based on advection of the moisture field using observed or forecasted winds to cover the regions that precipitable water is not directly measured. The dataset is gridded at $0.25^\circ \times 0.25^\circ$ spatial resolution at 1-hour temporal resolution. (The frequency of the DMSP or NASA Aqua satellites allow for such high temporal frequency; the typical gap between satellite passes is approximately 1 to 14 hours.) Mean average error of a global gridded product at 1-hour resolution is from 0.5 mm to 2.0 mm. (Wimmers and Velden, 2011). These data can be

accessed from <http://tropic.ssec.wisc.edu/real-time/mimic-tpw/global/main.html>.

NVAP

The NASA Water Vapor Project (NVAP) dataset is a global product from 1988 to 1999, produced by blending multiple data sources, such as radiosonde soundings, microwave data from SSM/I over the oceans, and infrared data from TOVS over land (Randel et al., 1996) and has been used in hundreds of studies regarding atmospheric water vapor (Vonder Haar et al., 2012). Each of those components carried different weights when merging the three datasets, with the surface-based radiosondes carrying the most weight. NVAP contains daily average total columnar and layered precipitable water values for each $1^\circ \times 1^\circ$ cell covering the globe.

The NASA Making Earth Science Data Records for Use in Research Environments (MEaSUREs) (NVAP-M) program, which began in 2008 to create stable, community accepted Earth system datasets available, has re-evaluated and extended the original NVAP dataset through to 2010 (Vonder Haar et al., 2012). NVAP-M incorporated more data sources and produces water vapor data as three separate products: NVAP Climate, NVAP Weather, and NVAP Ocean. The NVAP Weather is the highest resolution product at global $0.5^\circ \times 0.5^\circ$ total columnar and layered precipitable water for weather studies of time scales from a few days to weeks. Much more information can be found, along with sample graphics and downloadable datasets, on the NVAP-MeaSUREs website: <http://nvap.stcnet.com/>.

MODIS

The MODIS operational precipitable water product uses the near-IR techniques described in Gao (1998) and Gao (2003). The MODIS Level 2 product provides daily water vapor fields at 1 km spatial resolution. The MODIS level 3 products provide daily, 8-day and monthly composites at $1^\circ \times 1^\circ$ grids globally. Section 3.1.2 describes the algorithms used to generate the datasets and these are available for download at http://modis-atmos.gsfc.nasa.gov/MOD05_L2/.

GlobVapour

The GlobVapour project, funded by the European Space Agency (ESA) produces total column water vapor on a global basis. A combined data product was produced from the sensors SSM/I (0.5° over ocean) and Moderate Resolution Imaging Spectrometer (MERIS) aboard the ENVISAT satellite (0.05° over land) was derived for the time period 2003 - 2008. As well, data of the sensors GOME, SCIAMACHY and GOME-2 have been standardized into a $0.5^\circ \times 0.5^\circ$ monthly dataset for the time period 1996 to 2008 with data downloadable from <http://www.globvapour.info/>.

3.4.2 Radiosondes

The primary source for atmospheric water vapor data for the past 50 years has been vertical moisture and temperature profiles as measured from radiosondes. They are considered ground-truth and used for calibration and validation in statistical and remote sensing studies. Precipitable water is easily computed by vertically integrating the moisture profile. Therefore, any database of radiosonde profiles with measurements from the surface up to at least 300 mb can also be considered a database of precipitable water.

Trenberth (2005) explains that advancing our understanding of the variability and change in water vapor is vital, but knowledge is limited by inadequate observations. Several studies have examined the spatial and temporal water vapor patterns through radiosonde measurements over the United States (Reitan, 1960; Lott, 1976; Garrison and Adler, 1990; Maxwell et al., 1995), the Northern Hemisphere (Crutcher and Meserve, 1970; Ross and Elliott, 1996; Durre et al., 2006, 2009; Ross and Elliott, 2001), Canada (Hay, 1971), China (Zhai and Eskridge, 1997), tropical Western Pacific (Wang and Manning, 2001), and globally (Peixoto and Oort, 1992; Elliott et al., 1991; Eskridge et al., 1995; Sun and Oort, 1995; Trenberth et al., 2005). Regional and global studies using radiosonde data are difficult because of the paucity of data, especially over the oceans, tropics and Southern Hemisphere. Geographic spacing of soundings is roughly 400 km in North America, slightly less in western Europe, but

significantly greater elsewhere (Starr and Melfi, 1991). Diurnal phenomena are also very difficult to extract due to limited launches twice daily (0Z and 12Z) in populated areas and less frequent (e.g., once daily) in underdeveloped areas. Not only is the temporal frequency insufficient to depict diurnal water vapor changes, the local times of observation are lagged across some time zones, leading to inconsistent comparisons of diurnal ranges or other daily statistics and can lead to biases in weekly or monthly aggregation (Wang and Zhang, 2008).

Radiosonde devices have limitations in various conditions and uses. Numerous papers have described their shortcomings (Elliott et al., 2002; Elliott, 1995; Pratt, 1985; Elliott and Gaffen, 1991; Ross and Elliott, 2001; Trenberth et al., 2007b, 2005; Seidel et al., 2011; Durre et al., 2009; Wang and Zhang, 2008; Miloshevich et al., 2006; Soden et al., 2004). Radiosondes suffer from numerous types of systematic errors, such as calibration, miscalculations, time lag, or hysteresis (Wang and Zhang, 2008). For example, hygrometers generally perform poorly in cold, dry conditions. It is for this reason, and that little water exists above 300 mb, that humidity data in some locations are not taken above 300 mb, or were not taken during extreme wet or dry events, or were reported as missing if the air temperature was below -40°C , although these practices have gradually been eliminated over the years (Elliott and Gaffen, 1991; Durre et al., 2009). Radiosondes also drift horizontally during its ascent, therefore measuring a different region of the atmosphere than from where it was launched and recorded. Drift distances vary widely, from a few km in the lower troposphere to approximately 20 km in the upper troposphere and 50 km in the lower stratosphere (Seidel et al., 2011).

One significant complicating matter is that the primary purpose of the radiosonde network is short-term, local weather forecasts for populated regions and not necessarily for long-term, global climate studies (Elliott, 1995; Elliott et al., 2002). However, they have received increased attention in climate research due to their long period of record from a consistent source (Wang and Zhang, 2008). Elliott (2002) and Trenberth (2007) summarize the many efforts to resolve the inhomogeneities among

various radiosonde networks, device types and non-standard reporting practices around the world with the aim of improving the quality of radiosonde information for climate change studies. Although efforts have been made to normalize long-term records, such as through various physical and statistical approaches, it was found that significant problems remain.

Despite the deficiencies, radiosonde data are still used as reference for comparing against many other techniques, especially remotely sensed observations (Miloshevich et al., 2006; Soden et al., 2004; Reale et al., 2008; Seidel et al., 2011; Seidel and Coauthors, 2004; Angell, 2003) as well as to numerical models (McGrath et al., 2006) although many scale problems arise when comparing point data, such as radiosondes, to gridded data, such as models or remotely sensed products. They also provide first guess or initial condition fields for many satellite-based algorithms (Guillory et al., 1993) by interpolating the data points to provide approximate conditions. To date, no new system has proved to be comparable with the radiosonde system with regard to in situ accuracy and consistency (WMO, 2010).

There are two primary inventories of global radiosonde data currently available: the Integrated Global Radiosonde Archive (IGRA) and the Global Climate Observing System (GCOS) Upper Air Network (GUAN). (Note that some locations and records from GUAN may be subsumed by IGRA.)

IGRA consists of radiosonde and balloon observations at over 1500 globally distributed stations (Durre et al., 2006). Observations are available for standard, surface, tropopause and significant levels within the atmosphere. Variables include pressure, temperature, exponential height, dewpoint depression, wind direction, and wind speed. IGRA was compiled by merging 11 source datasets from the US and around the world. Although vigorous quality control was performed on all ingested data to develop a homogeneous and robust dataset (McCarthy et al., 2009; Durre et al., 2006), no adjustments were made for biases resulting from historical changes in instrumentation and observing practices (NOAA NESDIS, 2011).

Unfortunately, the period of record and percentage of completeness varies from

station to station. Figure 3.2 shows the count density of IGRA radiosondes over time. Even though many stations have recorded data since the 1950s, they have numerous missing or incomplete months, numerous levels missing on any given day, or include only one launch per day. The percentage (ratio) of stations with at least 80% days with valid data to the total number of stations was significantly less after 1973 than before that time. Figure 3.3 displays the IGRA stations used in Wang (2008) that matched their study criteria. McCarthy (2009) notes that the Comprehensive Aerological Reference Data Set (CARDS) inventory, a precursor dataset to IGRA maintained by NOAA National Climatic Data Center (NCDC) for radiosonde data from 1940 to 2000 (Eskridge et al., 1995), was found to be significantly more complete for some stations, with the difference being some CARDS records were rejected by IGRA due to its vigorous quality control procedures. IGRA station records are continuously quality controlled and updated daily and are available online at no charge (NOAA NESDIS, 2011).

The World Meteorological Organization (WMO) co-sponsors and coordinates the Global Climate Observing System (GCOS), established in 1992, whose goal is to provide comprehensive information on the total climate system, involving a multidisciplinary range of physical, chemical and biological properties, and atmospheric, oceanic, hydrological, cryospheric and terrestrial processes (WMO, 2011). The Atmospheric Observation Panel for Climate (AOPC) was established to define the requirements for meteorological observations for GCOS.

Data obtained from GCOS is valuable for weather forecasting and climate change studies. For a station to participate in GCOS, several requirements must be met to help ensure data homogeneity and representativeness, including a written statement of commitment by the responsible WMO member to operate the station on a long-term basis, and to provide data and metadata as documented. Two networks of observing stations have been established to support GCOS: the GCOS Surface Network (GSN) and the GCOS Upper-Air Network (GUAN) (1018 and 172 stations as of January 2013, respectively.) AOPC is responsible for the planning and implementation of GUAN in

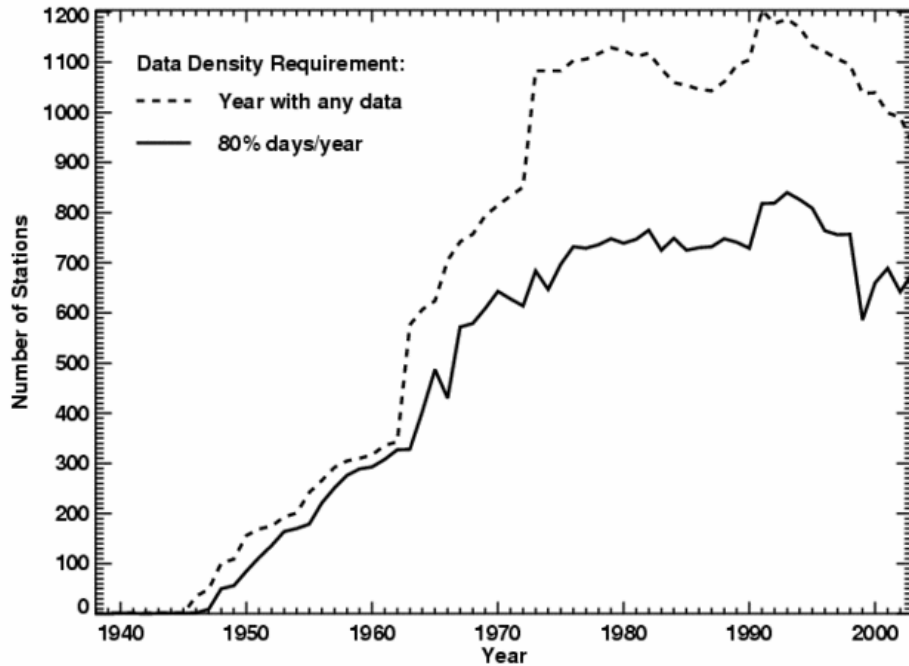


Figure 3.2: IGRA annual global radiosonde station density from 1940 through 2003. Number of stations where data are available on at least one day of the year (dashed line) and at least 80% of the days in the year (solid line).

cooperation with the World Weather Watch of the WMO ([GCOS, 2013](#)).

Radiosondes part of the GUAN are designed to collect a required set of essential data in a standardized, consistent manner. These data may be distributed globally without formal restrictions. Geographic spacing is approximately 5 to 10 degrees latitude, sufficient to resolve synoptic-scale weather patterns ([WMO, 2010](#)) as shown in Figure 3.4. Furthermore, the GCOS Reference Upper-Air Network (GRUAN), approximately 30 to 40 stations, was established to provide high-quality long-term climate records as well as to calibrate more spatially-comprehensive global observing systems, such as remote sensing and other in situ networks ([WMO, 2007](#)). Unlike the GUAN, GRUAN is not conceived to provide globally complete and spatially homogeneous coverage.

Due to the complexity of analyzing climate trends from historical radiosonde

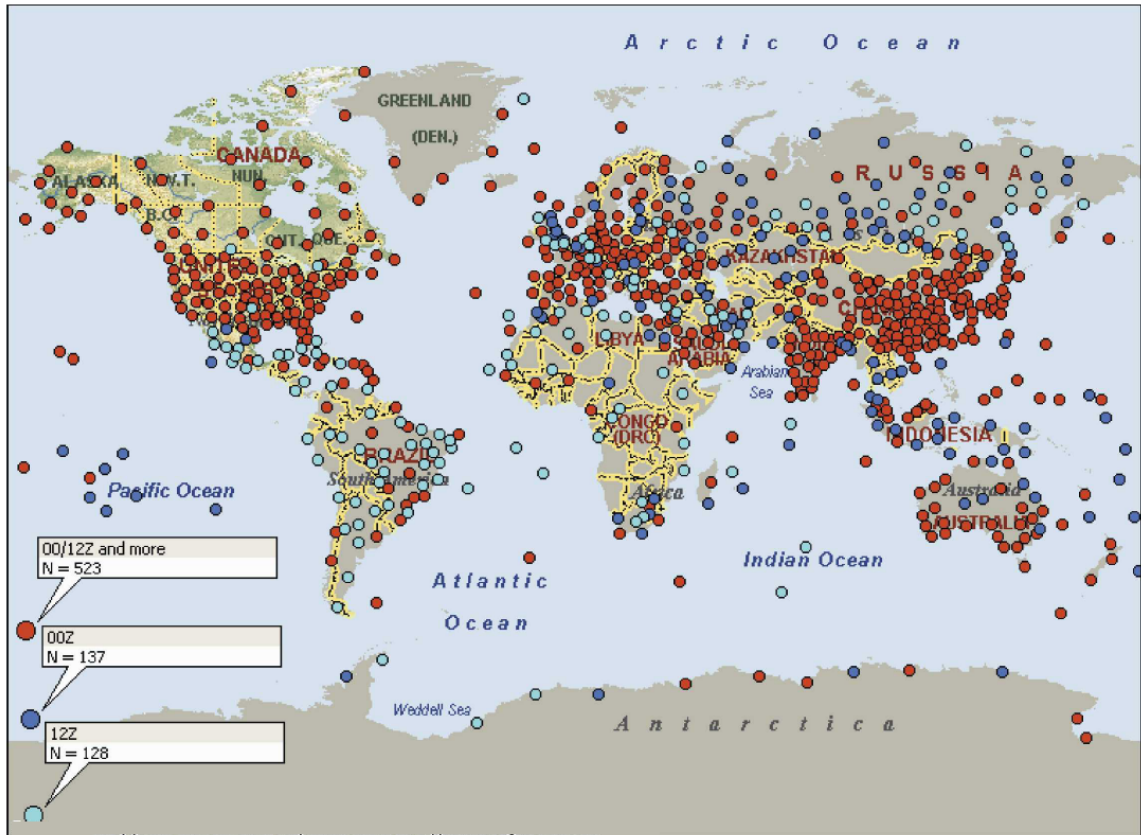


Figure 3.3: IGRA global radiosonde network map. Stations launching radiosondes at 00Z and 12Z are colored dark and light blue, respectively. Dark red represents stations with launch times at 00Z, 12Z and other times. Image taken from Wang (2008). Background data copyright of Microsoft Corp 2011.

data, the WMO datasets have been developed that preprocess radiosonde temperature data using various methods. They include temperature data and anomalies for the surface and the standard reporting pressure levels, and include gridded and time series products, monthly means, and zonal averages. Two to note are the Hadley Centre Atmospheric Temperature Data Set Version 2 (HadAT2, <http://www.metoffice.gov.uk/hadobs/hadat/index.html>) and the Radiosonde Atmospheric Temperature Products for Assessing Climate (RATPAC, <http://www.ncdc.noaa.gov/oa/climate/ratpac/>). Both of these datasets include global data from 1958 through present and are updated monthly using data from IGRA stations.

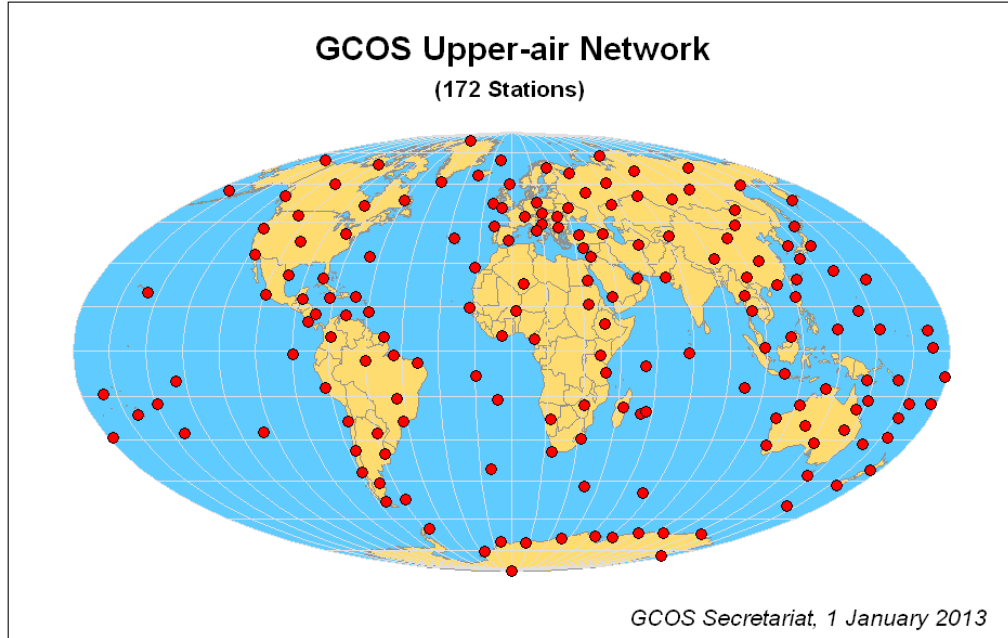


Figure 3.4: Global Climate Observing System (GCOS) Upper-Air Network (GUAN) global map as of January 2013.

Ross and Elliot (2001) collected radiosonde data from various sources and developed 0Z and 12Z monthly mean precipitable water values for the years 1973 - 1995. These included approximately 200 stations whose records were considered to be homogeneous by the authors based upon a combination of station history information and statistically identified change points. These were used to fill gaps in the IGRA archive or monthly precipitable water, resulting in an 8.6% increase in the total number of station months. Durre et al. (2009) extended the time period to 2006 by combining the Ross and Elliott (2001) dataset with the IGRA dataset and re-evaluated the stations for homogeneity and temporal completeness (no more than 60 missing months and no gap larger than 36 months). A trend analysis was performed on the integrated monthly mean precipitable water values. However, since only a handful of stations in the Southern Hemisphere satisfied the criteria, the trend analysis was restricted to 300 Northern Hemisphere stations only and results are not reported here.

3.4.3 Others

Global Positioning Systems

Using ground-based GPS permanent stations, Wang et. al (2007) produced a global, 2 hourly dataset of total precipitable water. Data are available every 2 hours from 1997 to 2004 for 80 to 268 individual locations. Each site is an International Global Navigation Satellite Systems (GNSS) Service (IGS) ground station. Computation of precipitable water values are based on surface pressure from 3-hourly, synoptic observation network, and mean temperature of the atmosphere by interpolating the NCEP/NCAR Reanalysis model dataset. Accuracy of the product is roughly 4 mm. Wang and Zhang (2008) then extended the dataset through 2006 and increasing the number of GPS stations to 350.

National Solar Radiation Database

The U.S. National Renewable Energy Laboratory (NREL) maintains the National Solar Radiation Data Base (NSRDB) (Maxwell et al., 1995). The NSRDB contains solar radiation and supplementary meteorological data for 1961 to 1990 from 237 NWS sites in the U.S., plus sites in Guam and Puerto Rico. They derived empirical equations based upon observations of 50 sounding stations to produce hourly total column water vapor based upon the methods of Garrison and Adler (1990) to develop hourly estimates. It was also updated to include 1991 to 2010 for 1454 stations. Data is accessible from http://rredc.nrel.gov/solar/old_data/nsrdb/.

Numerical Models

In addition to the in situ and remotely sensed datasets described, precipitable water data can be obtained through model reanalysis projects. These projects couple meteorological observations (including radiosonde profiles and satellite data for upper-air observations) with forecast (short-term) mesoscale atmospheric physical models for a selected time periods in the past. Many of the higher resolution, mesoscale models, such as the European Center for Meteorological Weather Forecast (ECMWF)

and National Centers for Environmental Prediction (NCEP) National Meteorological Center (NMC) models, are designed for short-term weather forecasting and analysis procedures which change over time. The goal of these projects is to produce consistent analyses using the same data assimilation procedures on an archived dataset (Elliott, 1995) and to include data that were not available for the operational runs.

However, like large-scale radiosonde studies, models provide only an estimate of the general overlying patterns. They generally involve very coarse spatial resolution (typically 1.0° to 2.5°) and perform poorly in data sparse areas, such as the remote tropical regions or over oceans. Mesoscale models generally do very well in data-rich areas, where they are forced by the observations (Soden and Bretherton, 1994; Trenberth and Guillemot, 1995). Often, mesoscale models are optimized for specific regions (ECMWF in Europe, NCEP in the US). These types of datasets are then problematic in climate studies (Trenberth and Olson, 1988; Trenberth et al., 2005). Reanalyses are designed to prevent changes in the analysis system from contaminating the climate record (as may occur with global analyses from operational weather prediction models), and they compensate for some but not all of the effects of changes in the observing system (Trenberth et al., 2007b).

It is beyond the scope of this thesis to describe the treatment of atmospheric moisture in the many reanalysis projects that exist. However, references for the more common reanalyses that contain precipitable water data are listed below. Additionally, a more comprehensive list of reanalysis projects are listed in Table 3.2.

- ECMWF Reanalysis Versions 1 and 2 (ERA-15 and ERA-40, respectively) - Upala et al (2005) and Kallberg et al. (2005) .
- NCEP Reanalysis Version 1 (R1) by the National Center for Atmospheric Research (NCAR) - Kalnay et al. (1996) and Kistler et al. (2001)
- NCEP Reanalysis Version 2 (R2) by the US Department of Energy (DOE) for the Atmospheric Model Intercomparison Project (AMIP) - Kanamitsu et al. (2002) and Amenu and Kumar (2005)

Table 3.2: Summary of global data inventories containing precipitable water. All datasets are global in coverage except NSRDB which is US only. For meanings of the acronyms, refer to the appendix.

Name	Dates	Source	Resolution
ISCCP/TOVS	1983 - 1989	Satellite	2.5° x 2.5° Grid
SSMI	1987 - present	Satellite	1° x 1° Grid
NVAP	1988 - 1999	Satellite, Radiosonde	1° x 1° Grid
NVAP-M	1987 - 2010	Satellite, Radiosonde, GPS	1° x 1° Grid
MODIS	2003 - present	Satellite	1 km x 1 km Grid
GlobVapor	1996 - 2008	Satellite	1° x 1° Grid
GPS-based	1997 - 2006	GPS	IGS Ground Stations
NSRDB	1961 - 2010	Surface Meteorological Stations	NWS plus other sites
IGRA	1960s - present	Radiosonde	1500+ Radiosonde Stations
GUAN	1950 - present	Radiosonde	172 Radiosonde Stations
GRUAN	In development	Radiosonde	30 - 40 Radiosonde Stations
Japanese Reanalysis (JRA-25)	1979 - 2004	Modeled	2.5° x 2.5° Grid
Japanese Reanalysis (JRA-55)	1958 - 2012	Modeled	1.25° x 1.25° Grid
ECMWF Reanalysis (ERA-15)	1979 - 1994	Modeled	2.5° x 2.5° Grid
ECMWF Reanalysis (ERA-40)	1957 - 2002	Modeled	2.5° x 2.5° Grid
NASA/DAO (GEOS-1)	1980 - 1996	Modeled	2.5° x 2.5° Grid
NASA MERRA (GEOS-5)	1979 - present	Modeled	0.5° x 0.67° Grid
NCEP/NCAR Reanalysis R1	1957 - 1996	Modeled	2.5° x 2.5° Grid
NCEP/DOE Reanalysis R2	1979 - present	Modeled	2.5° x 2.5° Grid

Chapter 4

STUDY DATA

This study makes use primarily of three types of ancillary data: infrared imagery from the GOES satellite, the National Center for Atmospheric Research/National Center for Environmental Prediction (NCAR/NCEP) model reanalysis, and radiosonde data. The GOES imagery is used as the source radiance data, and the NCAR/NCEP model reanalysis (simply called Reanalysis data) to provide first guess conditions, to the precipitable water remote sensing retrieval algorithm (the Physical Split Window technique.) The radiosonde data include atmospheric temperature and moisture vertical profiles obtained from six stations in the Amazon Basin and serve as ground truth. Additionally, the NASA Water Vapor Project (NVAP) data is used to analyze the generated water vapor fields. This chapter describes each of these datasets and their role in this study.

4.1 GOES Imagery

Multi-band imagery was obtained from the GOES-East satellite for the months of June and October during the years 1988 and 1995. The months were chosen to represent the time period between the wet season and dry season in the Amazon, which should result in relatively less cloud coverage due to the consistent precipitation occurring during the wet season and burning activities causing smoke and haze in the dry season. The years were chosen due to the availability of the data. For each month/year, the images were collected at 3-hourly intervals for daytime hours only: 12Z, 15Z, 18Z, 21Z, and 00Z, accounting for five images per day. Daytime-only images were chosen based on data availability to have a consistent set of data for all four

months. Unfortunately, no 21Z images were available for October 1988, and no 00Z images were available for June 1995.

Images for 1995 were obtained from the Cooperative Institute for Meteorological Space Studies (CIMSS) at the University of Wisconsin. In that year, GOES-8 was occupying the GOES-East position, and the sensor used for operational imaging was the GOES Imager. A limited amount of preprocessing had been applied to these images, such as geometric and radiometric corrections. Image coverage from CIMSS data extends to just beyond the boundaries of the Amazon Basin from 5°N to 24°S and 80°W to 32.5°W.

Images for 1988 were obtained from the GOES Pathfinder archive through cooperation from NASA Marshall Space Flight Center (MSFC). The sensor used was the GOES Visible Infrared Spin Scan Radiometer (VISSR) Atmospheric Sounder (VAS). At that time, VAS was the only sensor measuring in the thermal infrared wavelength region for the needed time and space scales. These images had a higher degree of preprocessing applied (Anthony Guillory, personal communication, 1997) and covered most of the Western Hemisphere. The GOES Pathfinder dataset did not contain images for the last 8 days in June 1988. Therefore, images for this 8-day period were extracted from the CIMSS archive and were geonavigated to the Pathfinder images.

Both satellites used in this study, GOES-7 in 1988 and GOES-8 in 1995, had the same sub-nadir geographic location at 0° latitude (the Equator) and 75°W longitude at the time the imagery was acquired.

4.1.1 GOES-7 VAS and GOES-8 Imager

GOES-7 was launched in February 1987 to replace GOES-5 as the new GOES-East satellite. It would occasionally be positioned at 105°W longitude, approximately midway between the GOES-East and GOES-West, to cover for GOES-West malfunctions. During these times, the METEOSAT geostationary satellite would be leased from the European Space Agency for coverage of the US East Coast. Ultimately, soon

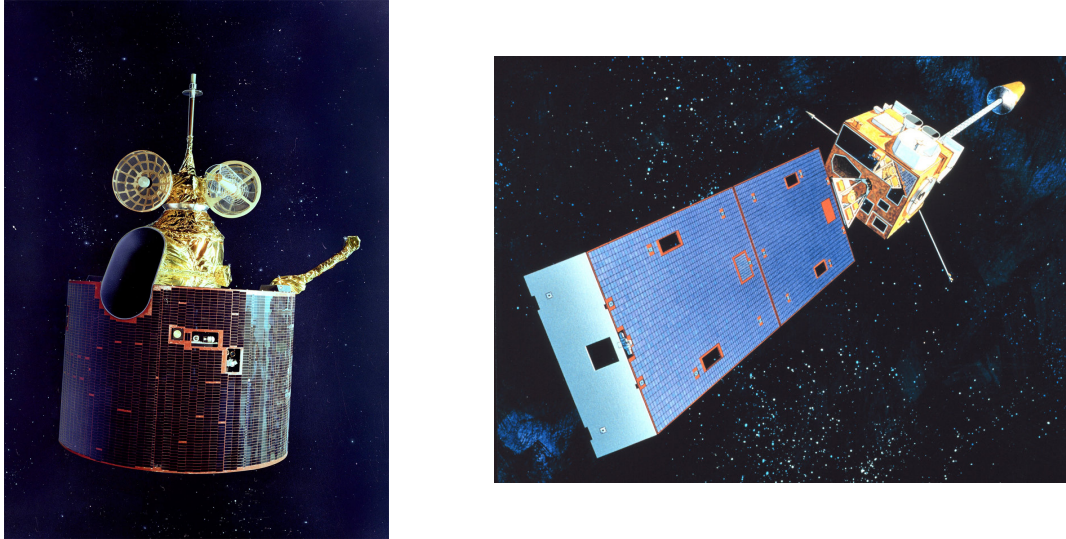


Figure 4.1: Images of the GOES-7 (left) and GOES-8 (right) satellites.

after it was replaced by GOES-8 in 1994, GOES-7 remained in orbit near 105°W longitude as a communications satellite for the Pan-Pacific Education and Communication Experiments by Satellite (PEACESAT) program ([NOAA NESDIS, 2012](#)).

The primary instrument on GOES-7 was the VAS sensor. VAS was originally launched aboard GOES-4 in September 1980, and continued with little modification through GOES-7. It was the first geostationary satellite sensor to provide multi-spectral imagery (MSI) and dwell soundings (DS, vertical atmospheric profiles of temperature and moisture.) Unfortunately, the dwell times of the sounding versus imaging operations on VAS did not allow for both modes to be performed simultaneously ([NASA, 2011b](#)). Only a single spin was required for taking snapshots in MSI mode whereas in DS mode, each channel had its own spin budgets with several channels taking up to 7 and 9 spins to achieve the required signal-to-noise ratio of the DS ([Hayden, 1988](#)). The spinning GOES-7 viewed the earth only 5% of the time during its spins, causing higher instrument signal-to-noise ratios ([Menzel and Purdom, 1994](#)) although the imagery provided researchers movies of water vapor advection through time, a technique pioneered by ESA's METEOSAT in the late 1970s.

GOES-8 was the first satellite of the next-generation GOES series, termed GOES-Next (GOES-8/9/10), and was launched in April, 1994, replacing GOES-7 as the new GOES-East in November later that same year (Menzel and Purdom, 1994). Instrumentation aboard the GOES-Next series of satellites were a dramatic improvement over those on GOES-7. In addition to higher spatial resolutions, a distinct advantage of GOES-8 is that multi-spectral images and the dwell soundings are recorded by completely separate instrument systems, namely the GOES Imager and GOES Sounder sensors. GOES-8 is three-axis stabilized allowing the Earth-atmosphere to be nearly continuously observed and thereby enabling a higher signal-to-noise ratio; noise levels were improved two to three times over the GOES VAS. Additionally, GOES-8 provided better storm and cloud tracking, a new data format was devised for retransmission of raw data to direct-receive users, a new ground processing system was developed to handle the high data volume, a more precise image frame-to-frame registration, and more stable long-term calibration and stabilization to reduce orbital drift throughout its lifetime.

VAS measured radiation in the visible spectrum using 8 identical channels simultaneously for higher resolution imaging as well as in the infrared spectrum using 12 different infrared bands, ranging from $3.95\ \mu\text{m}$ to $14.7\ \mu\text{m}$. Sub-nadir spatial resolutions were about 1 km for the visible band to 14 km for the thermal-IR bands (Montgomery and Uccellini, 1985). The 18 spectral channels and the spatial resolutions of the GOES-8 Sounder closely matched those of GOES-7 VAS-DS mode. The GOES-8 Imager channels aligned not as closely, but could easily be associated with GOES-7 VAS-MSI mode channels. Original designs of the GOES-8 Sounder and Imager were taken from popular polar-orbiting sensors in operation at that time, namely the High-resolution Radiation Sounder (HIRS) and Advanced Very High-resolution Radiometer (AVHRR), respectively (Menzel and Purdom, 1994). Table 4.1 lists the channels and nadir ground spatial resolution of GOES VAS vs GOES-8 Imager. Menzel and Purdom (1994) provide an excellent discussion of GOES-8 vs. GOES-7 features. Table 4.2 lists a brief summary of the differences between each.

Table 4.1: Bandwidths and IGFOV spatial resolution for comparable channels on GOES-7 VAS-MSI mode and GOES-8 Imager. IGFOV is the instantaneous geometric field of view whose directions are E/W \times N/S. Data from Menzel (1994).

GOES-7 VAS		GOES-8 Imager	
bandwidth	IGFOV	bandwidth	IGFOV
(μm)	(km)	(μm)	(km)
0.55 – 0.75	0.75×0.86	0.52 – 0.72	1.0×1.0
3.84 – 4.06	13.8×13.8	3.78 – 4.03	4.0×4.0
6.40 – 7.08	13.8×13.8	6.47 – 7.02	8.0×8.0
10.4 – 12.1	6.9×6.9	10.2 – 11.2	4.0×4.0
12.5 – 12.8	13.8×13.8	11.5 – 12.5	4.0×4.0

Figure 4.2 shows more clearly the differences in the width of the wavelength bands of the thermal infrared channels of the GOES-7 VAS and GOES-8 Imager. The data for this study focuses on the $10\ \mu\text{m}$ to $13\ \mu\text{m}$ region of the electromagnetic spectrum and shows the thermal split window channels of each sensor. On the GOES-8 Imager, channels 4 and 5 were moved spectrally closer together than the comparative channels on the GOES-7 VAS. Although this was to improve the fidelity of the split window approximations, so that the two bands measure more closely the same mean atmospheric conditions, it was at the cost of reduced moisture absorption, which essentially increased the noise in the signal (Hayden et al., 1996). Suggs and Jedlovec (1996) compared precipitable water retrievals from the two sensors using the Physical Split Window (PSW) technique (the same technique used in the current study) for a region in the western US in June 1995. Precipitable water estimates from both sensors were extremely close to each other, with the correlation coefficient and standard deviation being 0.93 mm and 3.2 mm, respectively. GOES-8 Imager seemed to be less sensitive to first guess estimates and were slightly wet biased when compared to both VAS and GOES-8 Sounder.

Imagery from GOES-8 Imager were chosen as opposed to the Sounder for this

Table 4.2: Sensor characteristics of GOES-7 VAS and GOES-8 Imager.

	VAS	Imager
Satellites	GOES 4 - 7	GOES 8 - 10
Operating Mode	Imaging/Sounding	Imaging Only
No. of Channels	13	5
Visible/IR Channels	1/12	1/4
No. of Bands Used in Imaging Mode	2 or 3	5
Spatial Resolution	1 km (visible) - 13.8 km (infrared)	1 km (visible) - 8 km (infrared)
Earth Navigation Error	3 - 10 km	2 - 4 km
Visible Data Precision	6-bit (1 in 64)	10-bit (1 in 1024)
Accuracy in Channel 4	0.10K @ 300K, 0.20K @ 230K	0.20K @ 300K, 0.40K @ 230K
Accuracy in Channel 5	0.40K @ 300K, 0.80K @ 230K	0.20K @ 300K, 0.40K @ 230K

study because: 1) it covers most of the Western Hemisphere whereas the Sounder’s coverage is much smaller and usually limited to the contiguous United States (Suggs et al., 1998), 2) Imager data has better temporal and spatial resolution than the Sounder data, and 3) the GOES-8 Sounder scans at numerous wavelengths irrelevant for precipitable water determination.

4.2 NCEP/NCAR Reanalysis Model

The National Centers for Environmental Prediction (NCEP) and the National Center for Atmospheric Research (NCAR) re-analyzed over 40 years of weather forecast model output from 1957 to 1996. This undertaking, known as the NCEP/NCAR Reanalysis Project or more simply the R1 Project, includes running a revised operational model incorporating additional observational data that were not available at the time of the initial operational run. A 4-dimensional data assimilation (4DDA) scheme is used consistently throughout the entire time period. Modeled fields are global, continuous in time and space, and are available at 6 hour time intervals: 00Z, 06Z, 12Z, and 18Z. Resolution of the raw model runs at the surface is T62, which is $1.875^\circ \times 1.905^\circ$

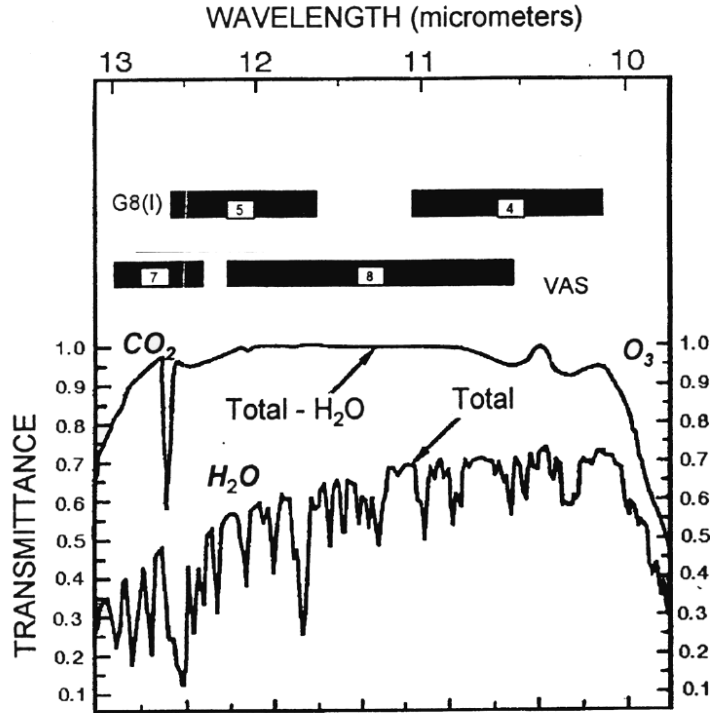


Figure 4.2: Atmospheric transmittance focused on the thermal infrared split window region, $10\ \mu\text{m}$ to $13\ \mu\text{m}$. GOES-7 VAS, GOES-8 Imager, and GOES-8 Sounder channel bandwidths are shown, with channel numbers labeled in the boxes. (Data was simulated through a spectroscopy method as described by Weinrab et al, 1991 in (Suggs et al., 1998).)

or equivalent to about 210 km horizontal resolution, with 28 vertical sigma layers (i.e., pressure levels). The actual model is identical to the global operational model used by NCEP beginning on January 10, 1995, except the operational model is run at T126, horizontal resolution of about 105 km (Kalnay et al., 1996).

This dataset does a good job on monthly mean fields of basic variables and at depicting synoptic features, such as the influence of 1997/98 El Niño and the Mt. Pinatubo eruption in 1991 (Marengo et al., 1997; Sudradjat et al., 2005), but has some problems with the diurnal cycle and small-scale events. Some variables in the model output are well defined by the observations, such as upper-air mass and temperature

fields, and the modeled spatial interpolations provide a better estimate than the observations alone. Other variables are more closely linked to the model, such as the precipitation and atmospheric moisture, since they strongly depend on the parameterization of the particular convective scheme being used, and therefore have difficulty capturing convective events (and the diurnal cycle) in the tropical atmosphere (Kalnay et al., 1996). Allan (2007) also mentions that the models appear to severely underestimate the observed precipitation response in the ascending and descending branches of the tropical atmosphere.

Several studies have found inconsistencies with regard to moisture variables in the tropics. Paltridge et al. (2009) found a negative trend in upper tropospheric humidity from the R1 data. However, Dessler and Davis (2010) analyzed the same dataset, compared it with other model reanalyses, and concluded the negative trend from the R1 was invalid. Sudrajat et al. (2005) found substantial dryness in the total precipitable water values in convective regions with R1. Trenberth et al. (2005) found the R1 analyses of precipitable water to be deficient over the oceans in terms of the mean, variability, and trends, likely due to the lack of satellite results fed into the data assimilation. The authors also found inconsistencies with water vapor surface pressure, particularly for years up to 1979.

Accuracy of the NCEP/NCAR Reanalysis in the Amazon is difficult to determine because of the paucity of observations. For precipitable water, the model is forced with the few observations that do exist, thereby creating an abnormally high correlation when the model is compared against integrated radiosonde profiles. Costa and Foley (1999) used R1 monthly data averaged over the entire Amazon Basin for a water budget analysis. They note that the R1 numerically restored soil moisture values toward a climatological mean, which would likely affect surface-based water vapor flux and may have caused the imbalance in the long-term water budget they observed.

For this study, data were obtained from the equal-angular grid produced by NCEP, 2.5° horizontal resolution and 17 vertical levels. Variables used were air temperature and relative humidity at the surface and all vertical levels, and total columnar

precipitable water. Air temperature is available at all 17 levels while relative humidity is available only up to 300 mb corresponding to about 6 levels. Each 6-hourly global grid was clipped to the Amazon Basin region, 80°W to 33°W and 5°N to 20°S. 15Z and 21Z fields were then created by averaging 12Z and 18, and 18Z and 00Z, respectively, in order to match the time acquisition of the GOES imagery.

In the PSW technique used in this study, utilization of the Reanalysis data is three-fold: 1) in determining first approximations to 11 μm and 12 μm channel radiances measured by the satellite sensors, 2) in calculating atmospheric transmittance dependence of thermal infrared radiation on water vapor, surface air temperature, and precipitable water, and 3) in providing "first guess" estimates of land surface temperature and precipitable water.

NCEP/NCAR's Reanalysis was chosen over other reanalysis projects, such as the ECMWF and NASA/Goddard, due to its consistency over such a long time period in accordance with future research plans, its continuously updated archive, its inclusion of a wide variety of global observational databases, and its public availability (Kalnay et al., 1996). Although many studies highlight the problems and inconsistencies with using model reanalyses to detect climate trends (Bengtsson et al., 2004; Trenberth et al., 2005), it is reasonable to believe, especially as compared to lack of observational data in this region, the reanalysis data provides the "best" overall description of realistic large-scale features present throughout the day and therefore suitable for providing first guess fields into remote sensing algorithms. Fortunately, the PSW method is a perturbation technique, attempting to calculate the difference from the first guess estimates to actual conditions, and minimizing inaccuracies of the first guess fields.

Note that due to the complexity of the R1 reanalysis, which included numerous staff and a complex system of programs, libraries, scripts, and datasets, some human errors were found in the processing steps. Some of these errors were found too late to be fixed through reprocessing, although for most studies these errors would be a minor consequence (Kanamitsu et al., 2002). A second reanalysis project began with NCEP

cooperating with the Lawrence Livermore National Laboratory, who provided the supercomputing time at the National Energy Research Supercomputing Center (NERSC) of the US Department of Energy. In addition to fixing the human errors found in the R1 process, this second Reanalysis project (referred to as NCEP/DOE or R2) incorporated upgrades to the forecast model for the Atmospheric Model Intercomparison Project (AMIP-II) (Kanamitsu et al., 2002). The R2 Reanalysis was not available to use at the time the current study was performed. Even if it was, it is difficult to ascertain if any improvements would be realized in the Amazon Basin atmospheric profiles as no new observational data were available. Some studies have shown that the spatial inconsistencies of water vapor in the tropics in R1 are still present in R2 (Trenberth et al., 2005; Sudradjat et al., 2005).

4.3 Radiosonde Observations in the Amazon

Radiosonde data for six stations located within the study area were used to calculate precipitable water to serve as ground truth for comparing against the remote sensing retrievals. The data are from the NOAA Comprehensive Aerological Reference Data Set (CARDS) database, an initial effort began by NOAA in 1991 to collect radiosonde data from multiple sources into a common data format and repository. CARDS includes global radiosonde data from over 20 different sources from 1940 to 2000 (Eskridge et al., 1995). (The IGRA dataset, described in section 3.4.2, eventually superseded CARDS and is the appropriate dataset for more recent data.) Table 4.3 lists the names, locations, and elevations for each of the stations.

Station data included temperature and moisture profiles for October and June in 1988 and 1995. Figure 4.3 show a map of the location of each station along with the Amazon Basin boundary outline. These were the only six stations available in the CARDS database located within the Amazon Basin for the study time period.

Although the collected upper-air data were run through quality control testing prior to being integrated into the CARDS dataset, additional issues, such as incomplete documentation, unreadable sections of old tape recordings, and limitations in storage

Table 4.3: Radiosonde sites in and around the Amazon Basin obtained from the NOAA CARDS network for the present study.

Station	Latitude	Longitude	Elevation(m)
1, Belém	-1.383	-48.483	16
2, Manaus	-3.15	-59.983	84
3, Recife	-8.067	-34.883	19
4, Vilhena Airport	-12.73	-60.133	652
5, Brasilia Airport	-15.86	-47.933	1061
6, Campo Grande Airport	-20.46	54.667	567

capacity, resulted in inconsistencies in station numbering, undocumented or unreadable variations in the data format, and duplicate records of various types for some stations and/or time periods (Durre et al., 2006). Therefore, for this study, a few additional quality control procedures were applied to the soundings.

Once the radiosonde data were obtained, the first step was to remove records where the air temperature or relative humidity was labeled as missing data. Next, all soundings that consisted of less than five vertical levels were removed. Each sounding was also required to have at least one measurement near the surface and one near the 500 mb layer. The definition of "near" was determined by the author on a case-by-case basis. Finally, each temperature and humidity profile was vertically plotted and visually inspected. Any problems encountered were investigated further and appropriate action taken, usually by removing the suspicious data values. Tables 4.4 through 4.7 reflect the number of soundings and levels remaining for each station for each month and year after these quality control procedures were performed.

4.4 NVAP Data

In late 1990, a workshop entitled "The Role of Water Vapor in Climate Processes" was held under the auspices of the Global Energy and Water Cycle Experiment (GEWEX) Science Steering Group. The primary goal of this workshop was to bring

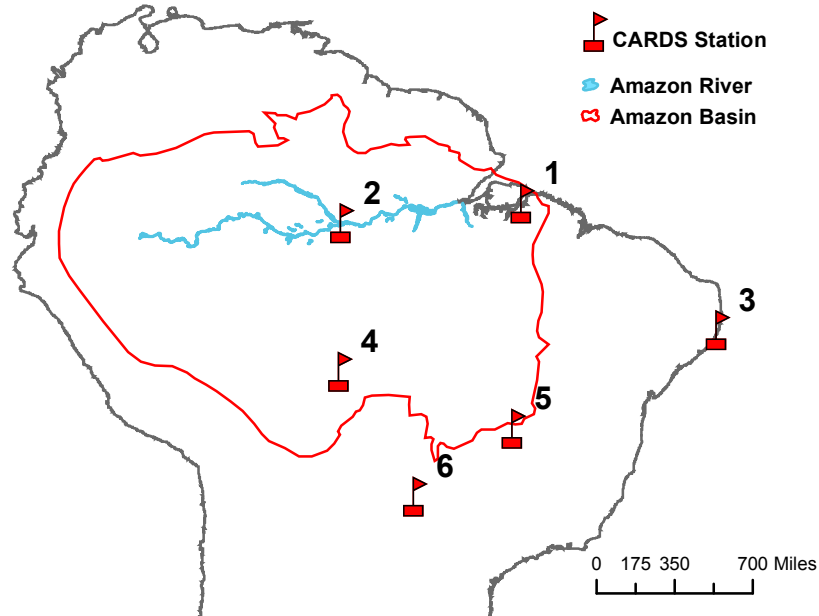


Figure 4.3: Map of the radiosonde sites, listed in table 4.3, in and around the Amazon Basin obtained from the NOAA CARDS network for the present study.

Table 4.4: Radiosonde data report for each station for June 1988.

Station	Number of Soundings	Number of Levels		
		Mean	Minimum	Maximum
1. Belém	31	30	19	40
2. Manaus	32	30	8	41
3. Recife	15	18	6	28
4. Vilhena Airport	23	27	15	41
5. Brasilia Airport	0	-	-	-
6. Campo Grande Airport	40	31	21	40

together interested members of the scientific community to discuss the needs and direction for a research program designed to increase our knowledge of atmospheric water vapor and our understanding of moist processes (Starr and Melfi, 1991). They identified an urgent need for a comprehensive and accurate data set of atmospheric moisture

Table 4.5: Radiosonde data report for each station for October 1988.

Station	Number of Soundings	Number of Levels		
		Mean	Minimum	Maximum
1, Belém	45	32	22	41
2, Manaus	38	27	8	37
3, Recife	17	16	5	25
4, Vilhena Airport	19	24	8	42
5, Brasilia Airport	53	29	16	39
6, Campo Grande Airport	52	27	7	41

Table 4.6: Radiosonde data report for each station for June 1995.

Station	Number of Soundings	Number of Levels		
		Mean	Minimum	Maximum
1, Belém	52	28	8	39
2, Manaus	39	27	12	41
3, Recife	0	-	-	-
4, Vilhena Airport	8	28	24	32
5, Brasilia Airport	9	30	25	34
6, Campo Grande Airport	32	30	19	38

information. What developed was the GEWEX Water Vapor Project (GVaP), eventually becoming the NASA Water Vapor Project (NVAP).

The initial version of the NVAP dataset, termed "heritage NVAP," is a blend of three different sources of data: radiosonde soundings, microwave data from SSM/I, and infrared data from TOVS. Radiosonde data were received from Ross and Elliott (1996) at five atmospheric levels, up to 300 mb. A description of the quality control procedures may be found in Ross and Elliot (1996). Daily, near-global TOVS data were received from NOAA/NESDIS as measured from the NOAA-9, -10, -11, and -12 satellites with ascending equatorial local times of 14:20, 19:30, 13:40, and 19:30,

Table 4.7: Radiosonde data report for each station for October 1995.

Station	Number of Soundings	Number of Levels		
		Mean	Minimum	Maximum
1, Belém	53	30	7	41
2, Manaus	29	29	14	39
3, Recife	16	16	6	33
4, Vilhena Airport	29	25	9	36
5, Brasilia Airport	46	28	20	39
6, Campo Grande Airport	43	30	21	39

respectively (Randel et al., 1996). Water vapor amounts were retrieved at three atmospheric levels using the algorithm of Smith and Wolf (1984) and modified versions by Fleming et al. (1986) and Reale et al. (1989). SSM/I data, derived from the DMSP F-8 and F-11 satellites (ascending local times of 06:15 and 17:04, respectively) using the algorithm of Greenwald et al. (1993). These data were total column water vapor only and limited to ocean scenes (Randel et al., 1996).

A blending process was then performed to create daily global $1^\circ \times 1^\circ$ grids of total columnar precipitable water as well as cloud liquid water and precipitable water at three atmospheric levels: 1000 - 700 mb, 700 - 500 mb, 500 - 300 mb. Radiosonde data were considered ground-truth whereas the SSM/I carried a weighting of 90% and TOVS carried 10%. Prevailing data gaps were filled by spatial and temporal interpolation. Hemispherical and global averages show reasonable agreement with other global studies as does the interannual variability (Randel et al., 1996).

The heritage release of NVAP covered 1988 to 1999. The next generation dataset, NVAP-NG, extended the time period through 2003. NVAP-NG also brought in more data sources, such as Advanced Microwave Sounding Unit (AMSU-A/B) on the NOAA satellites, the SSM/T2 on the DMSP satellites, and MODIS on the NASA Terra satellite. Processing methods also changed when developing NVAP-NG.

NVAP was originally designed to be model-independent and for weather studies

as it's primary purpose. It was determined that it should not be used for analyzing water vapor climate trends (Vonder Haar et al., 2005; Trenberth et al., 2005; Vonder Haar et al., 2012). This is due to: 1) the short time span of the dataset, the number of natural events occurring during this time span (ENSO of 1987-1998, Mt. Pinatubo eruption in 1991, ENSO again in 1998), the changes in the algorithms of both TOVS and SSM/I, and the changes in the processing practices when merging the data sources to develop NVAP.

The NASA Making Earth Science Data Records for Use in Research Environments (MEaSUREs) program began in 2006 to provide Earth Systems Science data records from multiple sources into stable, consistent data records. NVAP was selected as one of the initial proposals under MEaSUREs, to completely reprocess heritage NVAP, extend the time period to 2010, and incorporate new data sources (including those used by NVAP-NG) (Vonder Haar et al., 2012). The resultant dataset, NVAP-M, distributes global precipitable water as three distinct products: NVAP Climate, NVAP Weather, and NVAP Ocean, each with its own data sources, weighting functions, and target audience. NVAP Climate produces daily average total columnar and layered precipitable water as a global $1.0^\circ \times 1.0^\circ$ grid. NVAP Ocean is the same as NVAP Climate, except it does not include layered products and covers the ocean only. NVAP Weather produces global $0.5^\circ \times 0.5^\circ$ grids of total columnar and layered precipitable water for weather studies of time scales from a few days to weeks.

NVAP-M Climate data are used to assist with the analysis of the precipitable water fields generated in this study. Global total columnar precipitable water fields from the NVAP dataset were clipped to the extent of the study area and subsets within various analysis zones were extracted for comparison as described in Chapter 7.

Chapter 5

METHODOLOGY

As stated in section 1.3, the objectives of this study are as follows: 1) to apply a remote sensing technique that can measure atmospheric water vapor in regions with sparse in situ observational data to the Amazon River Basin region, and 2) analyze the diurnal signal and mesoscale spatial distribution of atmospheric total columnar precipitable water in the Amazon region for months June and October. Figure 5.1 shows the outline of the Amazon River Basin and surrounding countries. This chapter will describe the methodology used to accomplish these objectives.

In order to measure atmospheric conditions from such a large, remote area as the Amazon, remote sensing techniques were the obvious method to explore. Remote sensing can capture large regions with a single snapshot, record radiation in multiple wavelength bands simultaneously, are nearly completely automated, have a high statistical precision (based the sheer number of observations), data can be quickly compared from different parts of the world using the same sensor and techniques, and provides a rather unique perspective of measuring energy contributions from the full Earth system rather than just one component (although this does make it difficult to tease out the contributions of any one component.) Remote sensing techniques also have the promise of more future applications, such that imagery can be reprocessed in the future using new algorithms or previously unavailable data, and the research can be used to contribute to new sensors or platforms. Chapter 3 describes the physical basis of monitoring Earth through remote sensing and highlights numerous studies that have specifically measured precipitable water.

To achieve time scales appropriate for daily and diurnal analysis, geostationary satellites were the most appropriate as they continuously look down on the Earth and

are able to provide hourly (or more frequent) images. This high temporal resolution of geostationary satellites was therefore a priority over the high spatial resolution of sensors on polar orbiting satellites. GOES East maintains a sub-nadir point located on the equator at 75°W longitude, immediately above Northwest Amazonia, making this satellite an obvious choice. GOES data were also available for use at no cost through both the CIMSS and NASA Pathfinder data archives.

For the current study, several techniques for estimating atmospheric moisture through remote sensing were reviewed in Chapter 3. The Physical Split Window (PSW) (Guillory et al., 1993) algorithm, optimized for determining atmospheric total columnar precipitable water using GOES infrared channels, was applied in this study and is described in more detail below. In addition, the developers of PSW, Mr. Anthony Guillory, Dr. Gary Jedlovec, and Mr. Ron Suggs, provided the PSW code at no cost and (more importantly) made themselves available for technical support.

Due to data availability and computer speed/memory considerations, only a few selected months were used in this study. Months of June and October were selected for several reasons: 1) to avoid excessive smoke from burning activities that take place during the dry season in July and August, 2) to avoid excessive cloudiness during the wet season from December through March, 3) to compare the derived precipitable fields just prior to and after peak burning season, and 4) to coincide with previous studies on biomass burning by Prins and Menzel (1995). Two distinct years were also selected to represent different climatic conditions and different satellite sensors. 1988 was considered as a relatively dry year (imagery taken by GOES-7 VAS) whereas 1995 was a relatively wet year (imagery taken by GOES-8 Imager.)

5.1 Geographic Extent of Study Area

The region of interest for this study is the Amazon River Basin and the immediately surrounding area. Figure 5.2 shows the geographic bounding box of the GOES satellite image used as input to the PSW algorithm. It covers an area bounded by 5°N to 24°S and 80° to 32.5°W, nearly completely encompassing the Amazon Basin

(except for a very small portion in the northern central basin) and covers an area of about $1.617 \times 10^7 \text{ km}^2$. PSW-derived precipitable water values are then resampled to a slightly smaller, interior grid of 55 rows by 85 columns at $0.5^\circ \times 0.5^\circ$ resolution to remove edge effects of the retrieval algorithm yet preserving as much data as possible. The first guess fields derived from the NCEP/NCAR Reanalysis model has global extent and complete coverage of this region for all months of the study.



Figure 5.1: Outline of the Amazon River Basin and surrounding South American countries.

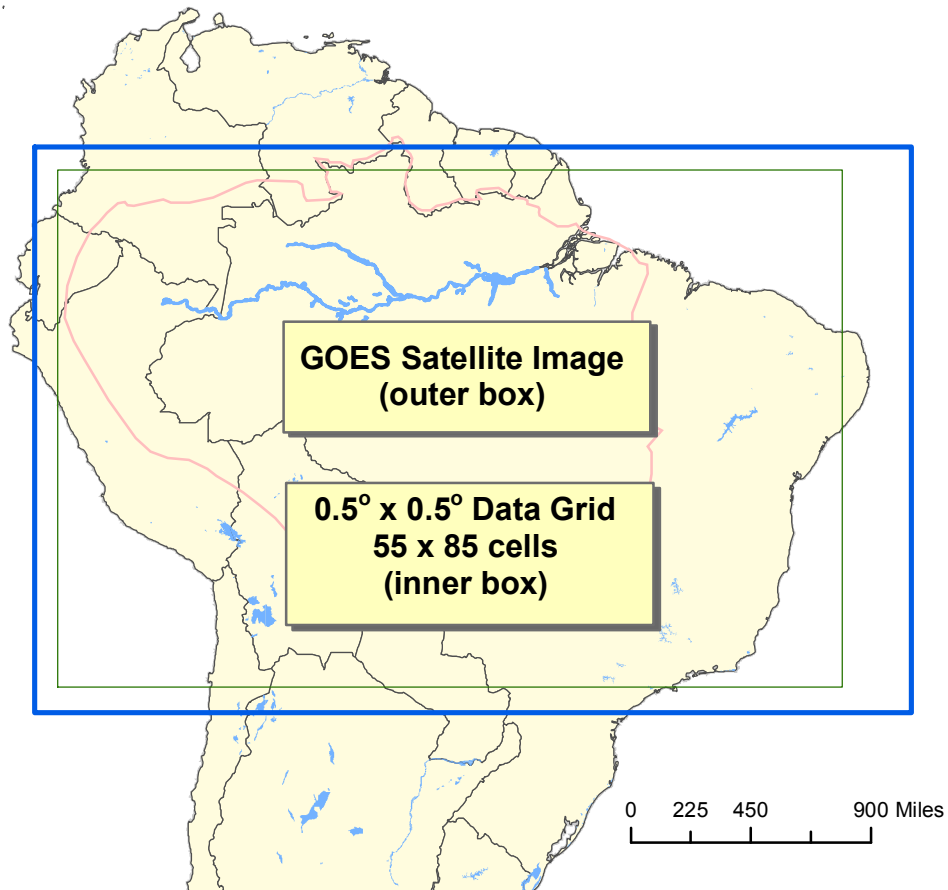


Figure 5.2: Geographic extent of the GOES satellite imagery and output (0.5° data grid for the present study).

5.2 Calculation of Precipitable Water from Radiosondes

To compare precipitable water retrieved from the GOES imagery to in situ observations, total columnar precipitable water must first be integrated from the vertical profiles of temperature and humidity as measured from a radiosonde. Note that additional quality control was performed on the radiosonde profile data before the precipitable water calculations took place, as described in section 4.3. The section below outlines the calculations following the equations defined in Buck (1981). The saturation

vapor pressure, e_s , in millibars (mb), at each level is first calculated using

$$e_s = f 6.1121 \exp \left(\frac{(18.729 - \frac{T_{air}}{227.3}) T_{air}}{T_{air} + 257.87} \right), \quad (5.1)$$

where T_{air} is the air temperature in degrees Celsius and f is a correction factor to account for the inclusion of water vapor in the air, expressed as

$$f = 1.0007 + 3.46 p (10^{-6}). \quad (5.2)$$

The units of p , the atmospheric pressure at which the measurements were taken, are millibars (mb).

Actual vapor pressure, e_a , also in mb, is then determined from e_s and the observed relative humidity, RH , as

$$e_a = e_s \frac{RH}{100}. \quad (5.3)$$

The specific humidity (defined as the mass of water vapor per kilogram of mixed air in units of $\text{kg}_{\text{H}_2\text{O}}/\text{kg}_{\text{air}}$), q , can easily be found from

$$q = \frac{0.622e_a}{p - 0.378e_a}. \quad (5.4)$$

Once q is found for each level, precipitable water is then computed by vertically integrating q throughout the atmosphere. In theory, this integration should be from the surface to the top of the atmosphere (TOA), but due to the very low RH values in the upper troposphere, typical radiosonde data report RH only to about 300 mb (Elliott and Gaffen, 1991; Pratt, 1985). For the present study, RH values above this level were simply reported as "missing data". It is assumed here that q decreases linearly

to zero from the highest RH reported level to the first missing RH level above it. Mathematically,

$$\begin{aligned}
 PW &= \frac{1}{g\rho} \int_{sfc}^{TOA} q dp \\
 &= \frac{1}{g\rho} \sum_{i=sfc}^n \left(\frac{q_i + q_{i+1}}{2} \right) 100 (p_i - p_{i+1}),
 \end{aligned}
 \tag{5.5}$$

where g is gravity (9.807 m s^{-2}), ρ is the density of liquid water of 1000 kg m^3 , n is the first level RH reported missing, and the factor of 100 is for converting the units of pressure from mb to pascals. Following the above formulation, PW will be in meters and must be divided by 1000 to obtain millimeters as used throughout this paper.

5.3 Preparation of First Guess Estimates

Before precipitable water retrievals can be made from the GOES images, the NCEP/NCAR Reanalysis data must be processed into estimates of atmospheric conditions to provide as input to the PSW algorithm. The algorithm will then modify the initial values of precipitable water and land surface temperature, based on measured radiances of the GOES bands, to more closely match the true conditions. This initial estimate of atmosphere is termed as a "first guess" when in context of satellite remote sensing retrievals.

The NCEP/NCAR Reanalysis model data provides a reasonably accurate spatially and temporally continuous measure of atmospheric conditions at 17 vertical pressure levels and at a $2.5^\circ \times 2.5^\circ$ degree horizontal grid. Three dimensional data were extracted for the study region, extending slightly larger than the GOES imagery bounding box in all directions, into GIS-formatted GRID files. Variables that were extracted included air temperature, relative humidity, and pressure at the surface, as well as air temperature and relative humidity at all 17 pressure levels. These variables were composited to form a complete atmospheric profile of temperature and mixing ratio, from the surface to TOA. The profiles were then sent to NASA Marshall Space Flight

Center (MSFC) and run through a line-by-line atmospheric transmittance code called SIMRAD (SIMulated RADiance).

Several parameters were derived from SIMRAD, while maintaining the same spatial resolution of the original Reanalysis grids. For inclusion to the PSW algorithm, SIMRAD generated estimated precipitable water, estimated skin temperature, estimated atmospheric outgoing radiances in the thermal infrared split windows bands for the sensor used (channels 4 and 5 for GOES-8 Imager and channels 8 and 7 for GOES-7 VAS), a 40-layer profile of air temperature and moisture, and an estimated transmittance for each layer of the atmosphere (also for the thermal infrared split windows bands for the sensor used.) SIMRAD is then run again with a 20% decrease in moisture at each layer. In this way, an estimated dependence of atmospheric transmittance upon water vapor can be achieved. Each of the above parameters were incorporated into a Man-computer Interactive Data Access System (McIDAS) language MD file, which is the same language of the PSW algorithm. These fields are then available to provide a first guess of the atmospheric conditions to the PSW algorithm.

5.4 Performing the Precipitable Water Retrievals

The PSW algorithm was run on each GOES image twice. The first time was to generate spatially continuous fields of precipitable water across the region. However, even at the spatial resolutions of GOES-7 VAS and GOES-8 Imager, retrievals may not be exactly collocated with the validation locations. Therefore, the retrievals were run again but only at specific locations to match the validation spots (6 radiosonde locations as mapped in fig 4.3.) This section describes the process of both types of retrieval runs and data post-processing.

5.4.1 Regional Field Retrievals

To obtain continuous precipitable water fields across the basin, retrievals are made at 5 pixel increments in longitude and latitude directions throughout the GOES image but leaving a 10 pixel buffer around the edge. At nadir, this is equivalent to 40 km

resolution for GOES-7 VAS and 20 km resolution for GOES-8 Imager. Since PSW uses an average radiance from the 5x5 template, no pixel is used more than once. This is essentially a moving window technique and is employed to reduce instrument noise at the expense of spatial resolution (which is acceptable since 20 km to 40 km resolution is still fine enough to support the objective to look at regional variations.) The size of the moving window, 5 pixels on a side, was chosen to balance noise reduction and spatial resolution. Figure 5.3 from Guillory (1993) shows that a 4x4 moving window was the optimal size for compromise but due to software constraints, a box with an odd-number of pixels per side, such as 5x5, was required.

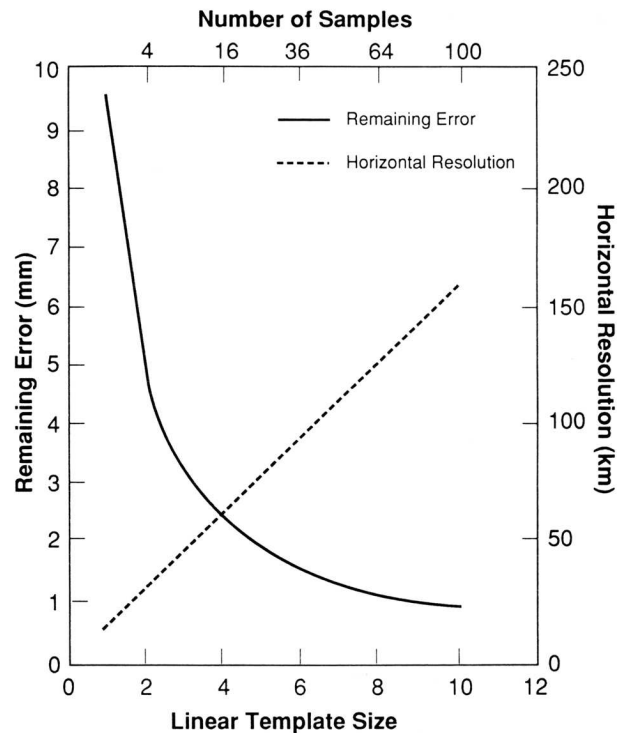


Figure 5.3: The expected random noise (in mm) in the PSW-derived precipitable water (solid line) and the horizontal resolution (dashed line) versus the linear template size used for neighborhood averaging during retrievals, where 4 represents a 4x4 pixel template. (Guillory et al., 1993)

Some assumptions were required during the PSW retrievals, including the following:

- Land surface emissivities in the thermal wavelength channels at $11\ \mu\text{m}$ and $12\ \mu\text{m}$, for both satellite sensors, are assumed to be constant throughout the region and for all times at 0.98. Typically, emissivity in the thermal-IR bands for water surfaces is 1.0 (i.e., behaves as a blackbody) and land surfaces between 0.85 (for arid lands) to 0.99 (for vegetated and moist land cover). Factors that influence thermal emissivity include characteristics of land-cover and vegetation type, density and structure of vegetation, organic composition, and soil moisture content. Hayden (1988), using GOES-7 VAS for retrieval of temperature and moisture for a region around Texas in the south-central US, found significant improvements when using 0.96 rather than 1.0 for thermal infrared emissivity. Zhang (1990) found through atmospheric transmittance code simulations and field observations that values for emissivities in this spectral region for deciduous forests hovered around 0.98 varying slightly. Menzel et al. (1991) found 0.97 to be an appropriate value for forests in the $11\ \mu\text{m}$ channel on GOES VAS during their investigations into biomass burning activities in the Amazon. Jin and Liang (2006) found that broadband emissivity in the thermal infrared bands ($8\ \mu\text{m}$ to $13\ \mu\text{m}$) to be 0.96 to 0.98 for densely vegetated areas with leaf area index greater than 2. In the Soil Erosion, Land Use and Vegetation Analysis of the Amazon Basin from a Space-based Rapid Exploration Platform (SELVA-RX) mission proposal, the authors estimate a typical value of infrared emissivity of 0.99 (Allende and Others, 2011).

Through discussions with MSFC staff, it was felt that keeping the same emissivity value for both split window bands would minimize the noise when computing the radiance differences between them. For a region as densely vegetated and moist as the Amazon Rainforest, a value of 0.98 was a compromise based on the land surface types within the retrieval study area. Guillory (1993) estimates that, on average, an emissivity change of 0.01 results in a change of retrieved precipitable water by 0.30 mm, which is minimal when compared to the values in the Amazon region.

- A terrain tolerance factor of 50 m was set for all retrievals. This is the maximum difference allowed between the elevation of the retrieval location and the first guess location. Significant changes in elevation will infer changes in the pressure, temperature and moisture profiles, thereby affecting the first guess fields and radiance generated by SIMRAD. If the difference is larger, the first guess is adjusted based on the elevation difference.
- A simple cloud mask was set at 290 K. Pixels with brightness temperatures smaller than this value in the 11 μm channel are considered to be clouds. Clouds can significantly impact the retrieval of precipitable water although automatic detection algorithms are difficult to implement in a robust manner. At the time these retrievals were run, a more sophisticated cloud detection scheme was not incorporated into the PSW.
- Cloud flag of 50 was set for all retrievals. The cloud flag represents the maximum percentage of cloud pixels allowed in the 5x5 pixel template used for the retrievals. A cloud flag of 50 correlates to at least 13 cloud-free pixels within the 25 pixel neighborhood for a precipitable water retrieval to take place. In the validation analysis of this study described in Chapter 6, only retrievals with over 80% cloud free pixels were used.

First guess fields were available at six hourly intervals from the reanalysis data: 0Z, 6Z, 12Z, and 18Z. Retrievals were processed based on the availability of three-hourly GOES imagery: 12Z, 15Z, 18Z, 21Z, and 24Z (24Z is technically 0Z on the following day.) Therefore, retrievals made at 15Z and 21Z had two possible guess files 3 hours off to choose from, the 12Z and 18Z first guess fields for the 15Z retrieval time, and the 18Z and 24Z first guess fields for the 21Z retrieval time. Due to the fact that the PSW algorithm performs better when 1) the temperature contrast between the surface and the near-surface air is at its greatest, and 2) no temperature inversions exist ([Suggs](#)

et al., 1998), retrievals at both the 15Z and 21Z times used the same 18Z first guess field, which represents the afternoon hours (2-3:00 pm) in the Amazon.

Many pixels were cloud contaminated, as expected in this region. This left many retrievals invalid as greater than 50% of the pixels in the surrounding 5x5 window are flagged as cloud. Figure 5.4 shows an example field with solid dots representing valid retrievals (less than 50% of the pixels in the surrounding 5x5 window are flagged as cloud.). To keep track of this, two variables output from the PSW code were captured and stored for analysis: PW and UPX. PW is total column integrated precipitable water as derived by the PSW algorithm. UPX is the cloud flag, the percentage of pixels in the 5x5 template that passed the cloud threshold test. In other words, the fractional part of the 5x5 template with an $11\ \mu\text{m}$ brightness temperature of greater than 290 K. For example, for one particular retrieval attempt, if 15 pixels passed the cloud threshold test, then $\text{UPX} = 60$ ($\frac{15}{25} = 60\%$). UPX will always be greater than 50% as values less than that would prevent a value of precipitable water from being returned.

To generate continuous fields of precipitable water covering the region, both PW and UPX were interpolated to a uniform grid with spacing of $0.5^\circ \times 0.5^\circ$, resulting in a grid 58 by 92 cells, as shown in figure 5.2. A half-degree grid was optimal because it is slightly larger than the most coarse resolution retrievals (that from GOES-7 VAS at 40 km) yet finer than most other large scale precipitable water fields currently in use (model grids at 2.5° , NVAP at 1.0° .) Ease of comparison is also favorable since 0.5 divides evenly into the common grid spacing of 1.0 and 2.5 degrees.

Interpolations were performed using SPHEREMAP, which is essentially Shepard's 1968 algorithm on a spherical surface (Shephard, 1968) and has been used extensively in the Department of Geography, University of Delaware for interpolating climate data. Shepard's algorithm is based upon an inverse distance weighting function utilizing between 4 and 10 nearest neighbors. It contains a directional algorithm (to prevent a bias from station clusters) and has an extrapolation capability. It is assumed that the variations in PW and UPX, either through natural variability or random error of

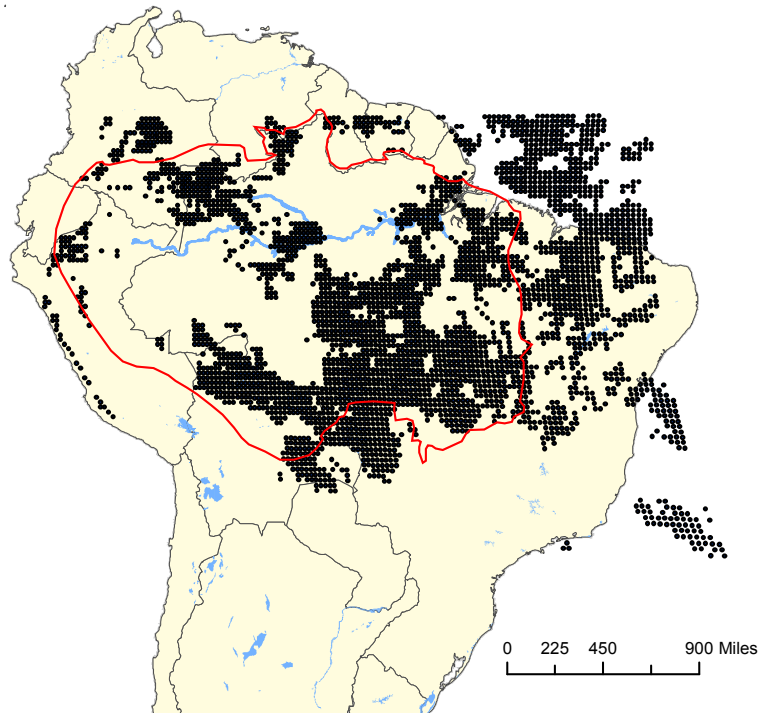


Figure 5.4: Example PSW retrieval field for June 6, 1988 at 21Z. Dots represent valid precipitable water retrievals. Blank areas represent where the percentage of clouds in the surrounding 5x5 window was greater than 50. For this image, 2061 valid points were obtained from a possible 3559 attempted within the GOES image.

the retrieval methods, are much larger than those caused by the interpolation method. Therefore, errors involved with the interpolation procedure will not likely play an important role in the analysis. SPHEREMAP and its companion, SPHERECROSS (to perform cross-validation), are freely available through the Department of Geography, University of Delaware.

Ultimately, to create smooth fields of precipitable water throughout the basin, areas where no retrievals could be performed, primarily due to cloud cover, are filled by precipitable water values from the Reanalysis fields. To accomplish this, the Reanalysis data is resampled to the $0.5^\circ \times 0.5^\circ$ grid with the same geographic boundaries as the PW and UPX grids. Once all grids are aligned, a composite precipitable water grid

is formed based upon the UPX value. At each 0.5° grid cell, if $UPX \geq 80$, then the resulting grid cell obtains the PSW-derived value of PW. Otherwise the resulting grid cell will inherit the Reanalysis data value. Once the resulting grid is complete, a moving window is then applied to smooth out any discontinuities that may exist between adjacent PSW-derived and Reanalysis precipitable water data. The kernel window is a 5×5 rectangular box with each cell weighted equally (the dimensions of the moving window is therefore equal to the resolution of the Reanalysis data at 2.5° .)

This process is optimal for obtaining the "best estimate" of the precipitable water field. As stated in section 3.1.1, infrared radiation cannot penetrate through clouds. Therefore, IR-only techniques are of limited use at times dominated by cloud cover. Merging reanalysis model and satellite data circumvents the cloud problem while maintaining relatively high spatial and temporal resolution and incorporating as much observational data as possible.

Analysis of the resultant precipitable water fields is described in Chapter 7. Several $5^\circ \times 5^\circ$ square regions or "analysis zones", each equivalent to 10×10 grid cells, are used in the analysis and are distributed evenly throughout northern South America as mapped in figure 7.1; four lie within the basin boundary, two in the less forested (cerrado) region to the east, and one to the far northwest. Averaging of data within each zone will aid in further removing some of the discontinuities from merging disparate datasets, as well as errors in the PSW retrieval process. All of the geospatial processing and map generation was performed by ESRI's ArcGIS and QGIS software packages. Pre-processing and analysis of the data, including statistics generation, was accomplished through programming written in several languages, including Fortran, Python, Interactive Data Language (IDL), and R. R was also used to generate all of the the graphs and plots.

The process to generate precipitable water fields can be summarized as follows:

1. Clip Reanalysis data to study region at 2.5° grid resolution.

2. Run Reanalysis data through SIMRAD atmospheric transmittance code to generate values of total columnar precipitable water, land surface temperature, profiles of moisture and temperature from the surface to the TOA, and estimated radiances in the $11\ \mu\text{m}$ and $12\ \mu\text{m}$ bands.
3. Run PSW algorithm on GOES images using 5x5 window average and processed Reanalysis data as first guess to a 20 km (GOES-7) or 40 km (GOES-8) grid.
4. Interpolate PW and UPX (percentage of cloud-free pixels) values at each retrieval point to a 0.5° grid.
5. Interpolate original Reanalysis precipitable water values to same 0.5° grid.
6. For grid cells where $UPX \geq 0.80$, use the PSW-derived precipitable water. Otherwise, use the Reanalysis value.
7. Perform a 5x5 moving window filter on resulting grid to smooth out differences.

5.4.2 Individual Location Retrievals

In order to assess the validity of using the PSW algorithm in the Amazon Basin, retrievals must be run again, but this time only at the specified sites with in situ radiosonde data, depicted in figure 4.3. Six locations were found within the GOES imagery boundaries and contain sounding data (temperature and moisture profiles) for 0Z and 12Z. These stations were obtained through the NOAA/NCDC CARDS network. This data is described further in section 4.3.

The same basic assumptions that were applied to the field retrievals are also applied here (i.e., cloud threshold, emissivity, terrain tolerance.) Each individual location retrieval used the GOES imagery pixel closest to each radiosonde location and the nearest center grid point of the Reanalysis field was used as the first guess. As with the field retrievals, individual location retrievals made at 15Z and 21Z both used the the same 18Z first guess values. One difference is that retrievals were allowed for any UPX value, i.e., for any percentage of cloud contaminated pixels found within the

5x5 window. Retrievals with significant amount of cloud contamination were simply excluded from the validation statistical comparison.

Once the PSW retrievals were made for each month and year at each of the six locations, statistics were computed against the integrated 0Z and 12Z radiosonde profiles, as well as against the first guess estimates of precipitable water. Chapter 6 describes the results of that analysis.

5.5 The Physical Split Window (PSW) Technique

The Physical Split Window (PSW) Technique is a physically based approach that estimates total columnar precipitable and land surface temperature simultaneously. It was originally developed by Dr. Gary Jedlovec in his PhD dissertation applied to high spatial resolution Multispectral Atmospheric Mapping Sensor (MAMS) data ([Jedlovec, 1987](#)). Guillory (1991, 1993) applied the PSW technique to the GOES-7 VAS sensor. The PSW code was later modified further to accommodate sensors on more recent GOES satellites (Anthony Guillory, personal communication, 1998.) The PSW technique has been applied for the retrieval of precipitable water and land surface temperature data in numerous applications, including in GOES operational products ([Haines et al., 2004](#); [Suggs et al., 1998](#)), Fengyun-2 series ([Shi, 2005](#); [Shi and Xie, 2005](#)), Fengyun-3A ([Zheng et al., 2010](#)), and MODIS.

The Physical Split Window (PSW) algorithm was chosen for several reasons: 1) it is optimized to work with the GOES satellite sensors to calculate precipitable water, and 2) it is a perturbation technique as it modifies an initial guess estimate of precipitable water requiring little a priori information, 3) being physically based, it does not depend on statistical procedures to relate a derived quantity, and 4) can be used for other atmospheric constituents that have differing absorption characteristics in thermal infrared split window wavelength bands, and 5) can be applied to other instruments that carry thermal infrared split window channels ([Guillory et al., 1993](#)).

Previous studies have shown applying PSW to GOES imagery has performed well. In Guillory (1993), the PSW was applied to the Alabama and Tennessee region

as part of the Cooperative Huntsville Meteorological Experiment (COHMEX) in June 1986 and several Florida NWS sites in the summers of 1989 and 1991. Mean absolute errors were around 4 mm (10% error) and RMSE was approximately 5 mm. Applied to a dense network of radiosondes had improved the first guess, with MAE and RMSE decreasing to 2.4 mm and 2.9 mm, respectively. Knabb and Fuelberg (1997) compared the PSW to the techniques of Chesters et al. (1983, 1987) and Hayden (1988) using simulated radiances (rather than actual satellite observations to more closely compare the algorithms) based on real radiosonde profiles across North America during June through October in 1979. The PSW technique exhibited the greatest correlation (0.92) and was least susceptible to systematic bias. Suggs et al. (1998) performed PSW retrievals using GOES images during the COHMEX experiment. They found that with ideal first guess (coincident in space and time, and with no temperature inversion), mean error was around 0.2 mm and standard deviation of errors was around 2.0 mm. As the first guess veered away from the retrieval time or if temperature inversions existed, mean errors were between 2.0 mm and 7.0 mm with standard deviation of errors also up to 7.0 mm.

5.5.1 Formulation of the PSW Technique

A detailed derivation of the PSW equations can be found in Guillory (1991) and Suggs et al. (1998). A summarized version of the formulation is presented here. It is applicable to thermal infrared bands in the $8\ \mu\text{m}$ to $13\ \mu\text{m}$ range for the retrieval of atmospheric trace gas constituents with absorption properties in this range, such as water vapor and ozone.

PSW's form derives from a perturbation of the radiative transfer equation (RTE), which for a non-scattering, plane-parallel atmosphere can be expressed as

$$I_\lambda = \epsilon B_\lambda(T_S)\tau_s - (1 - \epsilon)\tau_s \int_{P_S}^0 B_\lambda(T_P) \frac{d\tau}{dp} dp - \int_0^{P_S} B_\lambda(T_P) \frac{d\tau}{dp} dp, \quad (5.6)$$

where I denotes radiance at wavelength λ received at the sensor, subscripts S and P denote the surface or pressure level layer, ϵ and B_λ are the emissivity and Planck (blackbody) emission of the surface at wavelength λ , τ is the atmospheric transmittance from the TOA to a pressure layer (of thickness dp), and T and p are the temperature and pressure of that layer.

The RTE equates the radiance measured at the sensor to the sum of the contributing sources. This form is structured for application to a specific wavelength band. The three terms on the right-hand side of the RTE are the three primary contributing sources: 1) energy emitted from the Earth's surface, 2) energy reflected from the Earth's surface, and 3) the sum of upward emitted energy from the atmospheric layers.

For most surfaces in the thermal-IR bands, $\epsilon \approx 1.0$, particularly in a region such as the Amazon. Equation 5.6 then reduces to

$$I_\lambda = \epsilon B_\lambda(T_S)\tau_s - \int_0^{P_s} B_\lambda(T_P) \frac{d\tau}{dp} dp. \quad (5.7)$$

Substituting the following perturbations,

$$\begin{aligned} I &= \bar{I} + \delta I, \\ B &= \bar{B} + \delta B, \\ \tau &= \bar{\tau} + \delta\tau, \end{aligned} \quad (5.8)$$

where the overbar represents the mean, or initial guess value, of the variable and δ represents a departure from the mean, into equation 5.7, and then integrating by parts, results in the perturbation form of the thermal infrared RTE:

$$\delta I = \tau_\lambda \delta B_\lambda(T_S) - \int_0^{P_s} \delta B_\lambda(T_P) \frac{d\tau}{dp} dp + \int_0^{P_s} \delta\tau \frac{dB_\lambda(T_P)}{dp} dp. \quad (5.9)$$

Two assumptions can be made to remove the middle term in equation 5.9: 1) the Planck function and the vertical derivative of the transmittance at the TOA (the lower limit of the integral) is zero, and 2) the atmospheric profile is known (actual atmospheric profiles of temperature and moisture match the first guess profiles) and therefore, δB_λ at each level would also be zero. Equation 5.9 then reduces to

$$\delta I = \tau_\lambda \delta B_\lambda(T_S) + \int_0^{P_s} \delta \tau \frac{dB_\lambda(T_P)}{dp} dp. \quad (5.10)$$

Substituting the following expressions,

$$\begin{aligned} \delta \tau &= \frac{\partial \tau}{\partial \ln(U)} \delta \ln(U), \\ \delta B_\lambda(T_S) &= \frac{\partial B_\lambda(T_\lambda)}{\partial T_S} \delta T_S, \\ \delta I &= \frac{\partial B_\lambda(T_\lambda)}{\partial T_S} \delta T_\lambda. \end{aligned} \quad (5.11)$$

where U is the total columnar precipitable water, will lead to the following equations for the 11 μm and 12 μm channels:

$$\begin{aligned} \delta T_{11} &= \delta T_S C_{11} + \frac{\delta U}{U_o} D_{11}, \\ \delta T_{12} &= \delta T_S C_{12} + \frac{\delta U}{U_o} D_{12}. \end{aligned} \quad (5.12)$$

U_o is the initial guess of precipitable water and δU is the perturbation from that. C_{11} , C_{12} , D_{11} and D_{12} are values calculated from the first guess atmospheric profiles. δT_{11} and δT_{12} are calculated from the measured radiance at the satellite sensor and the simulated radiance from SIMRAD in each channel. Solving both equations simultaneously for δT_S and δU (2 equations, 2 unknowns), then adding back to the first guess estimates of each, will result in the final values for the land surface temperature and precipitable water. The process of simultaneously solving these two equations through

numerical methods in the code requires iterations until convergence of T_S is achieved. Convergence of 0.1 K is usually reached within 2 or 3 iterations (Anthony Guillory, personal communication, 1998).

Chapter 6

PSW TECHNIQUE PERFORMANCE

This chapter will compare precipitable water values derived from the PSW algorithm individual retrievals against values calculated from radiosonde vertical temperature and moisture profiles. Comparisons are made at all six radiosonde locations (described in section 4.3) for all four months of this study: June and October, 1988 and June and October, 1995. The analysis breaks down the comparisons by time of day (12Z vs 24Z), by month and year, and by location (different radiosonde stations.)

For model validation purposes, a suite of statistics are generated for each comparison. In particular, the mean (μ) and standard deviation (σ) of both the observed (radiosondes) and predicted (PSW-derived) precipitable water values, the Pearson correlation coefficient (r), the Modified Index of Agreements (d), the root mean square error ($RMSE$), the mean bias error (MBE), the mean absolute error (MAE), and the ratio of the MAE to observed mean (MAE/μ_x).

The mean bias error (MBE), the mean absolute error (MAE), and the error percentage (ratio of the MAE to the observed mean) are the primary statistics used in this discussion. Typically the most widely used measures of model performance are the Pearson correlation coefficient (r) (or its associated Coefficient of Determination, R^2) and the root mean square error ($RMSE$.) However, the $RMSE$ is widely misleading and misinterpreted as it is a function of three separate factors: the average error (MAE), the distribution of error magnitudes (due to square of the errors), and the \sqrt{N} (Willmott and Matsuura, 2005). The squaring of the error terms puts a unduly strong influence on the magnitudes of each error (e.g., a small number of large errors can significantly negatively influence the resultant $RMSE$). The Pearson correlation coefficient (r) focuses on the fit to a linear model. High values of r can be obtained

for a poorly performing model (with large absolute errors) if the linear relationship of the errors remains constant. It also standardizes the differences between the observed and predicted means and variances, meaning that the differences in the variances do not alter the value of the statistic (Legates and McCabe, 1999). Like the *RMSE*, *r* is sensitive to outliers as an extreme event can significantly alter the linear relationship. Both *RMSE* and *r* are reported in the tables below for comparison to other studies and familiarity to the reader.

The Modified Index of Agreement (*d*) was a modification on Willmott's original Index of Agreement, which was too sensitive to large magnitude errors due to the squaring of the error terms (Willmott et al., 1985). The modified version, also with boundaries of -1.0 (poor performance) to 1.0 (good performance), approaches 1.0 more slowly than the original, provides greater separation when comparing performance from different models, and is less sensitive to the shape of the error frequency distribution (since it is based on absolute error differences rather than the square of the difference.)

Throughout this section, two types of graphs accompany the summary statistics tables. Box plots are included to summarize the magnitude and spread of each data series. The central "box" in each box plot represents the first (Q1), second (Q2 or median), and third (Q3) quartiles. The length of the extending whiskers represents a measure of the interquartile range (IQR.) Hence, the top line of the whisker marks $Q3 + 1.5 \times IQR$ or the max value (whichever is smaller), and likewise, the bottom line marks $Q1 - 1.5 \times IQR$ or the min value (whichever is larger.) Data points beyond these are plotted as circles. The notches in each box represent a confidence interval about the median, $Q2 \pm 1.57 \times IQR / \sqrt{N}$. If two boxes' notches do not overlap, there is strong evidence, at 95% confidence, that their medians are different. Additionally, scatter plots with the linear regression line are shown for each breakdown. The equation of the line and number of data points is also displayed.

6.1 PSW-Derived Precipitable Water vs Radiosonde Observations

Individual location retrievals of precipitable water were made by averaging the observed radiances in a 5x5 pixel window for each band of the GOES imagery, centered on the locations of the six radiosonde stations. These values were compared to the precipitable water computed from the radiosonde temperature and moisture profiles. Computation of precipitable water from the radiosonde atmospheric profiles is described in section 5.2. Table 6.1 shows summary statistics for all retrievals during the time period, including retrievals made at all stations, for all months and years, and for both times of day radiosondes were launched.

There are two important aspects to note about the radiosonde launch times used in this study, particular to this region:

1. Radiosonde launch times of 0Z and 12Z correspond to local times of 8/9 pm (depending on the western/eastern part of the Amazon region) and 8/9 am, respectively. These times represent morning and late evening, neither time being ideal for precipitable water retrievals. In previous studies, the PSW algorithm performed best at times without temperature inversions and a contrast between temperatures of the surface and atmosphere, such as in mid-afternoon. There is potential for temperature inversions during these times, particularly for the stations not in the heart of the rainforest, which tend to stay more consistent.
2. Radiosonde data are typically recorded as date and time, starting from 0Z through to 23Z for a single day. For example, the two launches on June 15, 1988 would be labeled in the data records as: June 15, 1988 0Z and June 15, 1988 12Z. However, in the Amazon region, 12Z represents the morning time and 0Z represents the late evening of the previous day. Therefore, the analysis in this study labels all 0Z radiosonde data as 24Z of the previous day. Following the same previous example, this study would label those data points as June 14, 1988 24Z and June 15, 1988 12Z.

Table 6.1: Statistics for PSW-derived vs radiosonde precipitable water including observations from all months and stations. μ , σ , MBE , and MAE values are in mm. x represents radiosonde observations and y represents PSW-derived values.

	N	μ_x	μ_y	σ_x	σ_y	r	d	MBE	MAE	$\frac{MAE}{\mu_x}$
All Data	168	33.4	39.0	10.4	11.7	0.72	0.60	5.6	8.0	0.24

Data were only included in the statistical comparison if valid precipitable water values were achieved by both the PSW-algorithm and the radiosonde observations at the same time of day for the same location. For the PSW-algorithm, a valid precipitable water data point consisted of a clear sky ($UPX = 100$ in the 5x5 pixel retrieval window) and passed all flags (such as the first guess location and retrieval location ground-surface elevations within the terrain tolerance, the matrix calculations in the code converged to a single answer, etc...) For the radiosonde-derived precipitable water, vertical profiles of temperature and moisture must exist with at least 5 measured levels, one of them being near the surface, and passed manual inspection (as described in section 4.3.)

A total of 168 data pairs were found to compare, accounting for less than 12% of the total number of possible data pairs. (By calculation of six stations, launching radiosondes twice per day, for the four months of June and October, 1988 and 1995, the total maximum possible number of data points is approximately 1440.) There are two primary reasons for the low number of valid data pairs. First, many radiosonde launches did not take place at each station twice per day. Reviewing tables 4.4 to 4.7, the number of launches fell well below the maximum of 60 (June) and 63 (October) at each station. Second, on many occasions, clouds contaminated the retrieval. A relatively small number of data points were removed due to inconsistencies or missing data in the radiosonde atmospheric profiles, or due to the failing of the PSW retrieval from non-cloud contamination issues.

Overall, the MBE is 5.5 mm and the MAE is 8.0 mm, indicating a generally

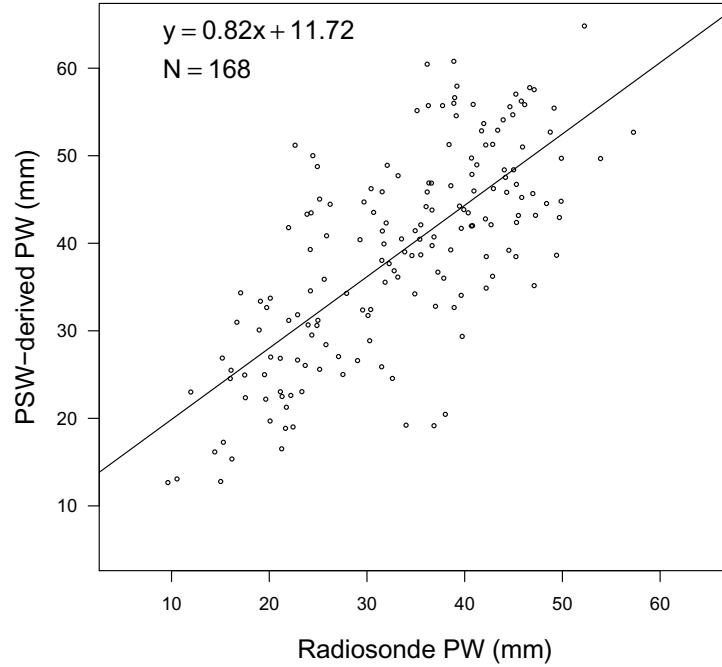


Figure 6.1: PSW-derived vs radiosonde precipitable water scatter plot and linear regression line of observations from all months and stations. $N = 68$.

consistent moist bias with an average percentage error of approximately 24%. A moist bias can be seen in nearly all breakdowns described in the following sections and common when comparing remote sensing techniques to radiosondes. Both $r = 0.72$ and $d = 0.60$ show relatively good fit with the linear trend of the predictions. Figure 6.1 shows all of the data points with the regression line plotted. Figure 6.2 displays a histogram of the residuals (differences between radiosonde and PSW-derived values) in a nearly normal distribution centered on the *MBE* of 5.5 mm. The overall fit seems reasonable considering the simple cloud filtering technique employed in a region dominated by cloud cover, the mixture of land cover types, different local times across all stations, the Amazonian local times being analyzed, the 5x5 pixel averaging within the PSW retrieval process, and the potential inaccuracies in the radiosonde profiles.

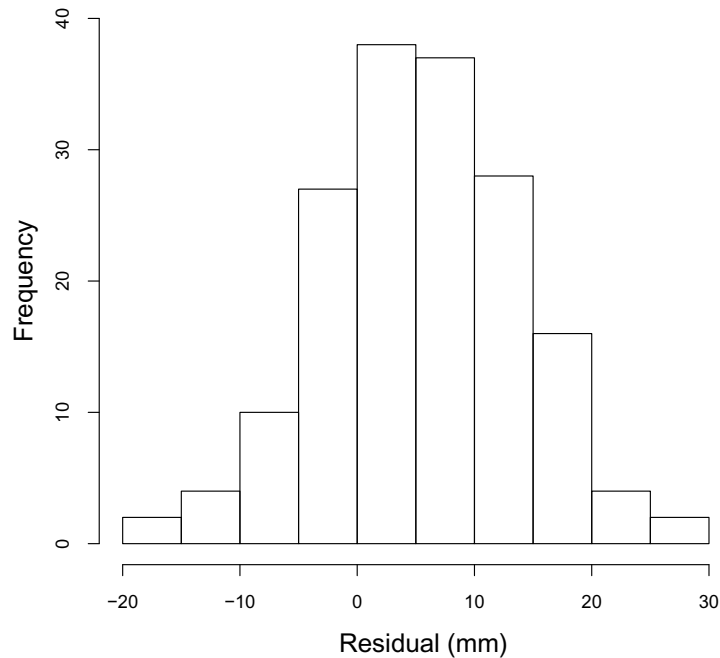


Figure 6.2: PSW-derived vs radiosonde precipitable water histogram of residuals for all months and stations. $N = 168$.

6.1.1 Comparison by Time of Day

Statistics are divided separately for comparisons with radiosonde launches at each time of day, 12Z and 24Z. These represent local times of 8:00 am and 8:00 pm, respectively, for stations in the western half of the region (Manaus, Vilhena, and Campo Grande) and local times of 9:00 am and 9:00 pm, respectively, for stations in the eastern half (Belém, Recife, and Brasilia.) Table 6.2 includes the same summary statistics as in the previous section for both 12Z and 24Z. Likewise, Figure 6.3 displays the scatter plot and linear regression line and Figure 6.4 shows box plots for both the PSW-derived and radiosonde observed precipitable water values.

Note that there is a overwhelming difference in the number of paired observations used in the statistics. 86% (145 out of 168) of the paired data points were from 12Z observations. This is primarily due to the following reasons.

Table 6.2: Statistics for PSW-derived vs radiosonde precipitable water observations for 12Z and 24Z, including data from all months and stations. μ , σ , MBE , and MAE values are in mm. x represents radiosonde observations and y represents PSW-derived values.

	N	μ_x	μ_y	σ_x	σ_y	r	d	MBE	MAE	$\frac{MAE}{\mu_x}$
12Z	145	32.8	38.7	10.3	11.8	0.73	0.59	6.0	8.1	0.25
24Z	23	37.6	40.5	9.8	11.0	0.66	0.59	2.9	7.0	0.19

- First, there were significantly more radiosonde launches at 12Z than at 24Z. From looking at solely radiosonde launches at all stations for all months, about 64% were launched at 12Z. Station 3, in Recife, did not include any launches at 24Z. (Station 5, at the Brasilia Airport, was the only station to have approximately equal launches at both times with 52% at 12Z and 48% at 24Z.)
- Second, there were more GOES images for 12Z. No 24Z GOES imagery was available for June 1995.
- Third, a larger percentage of successful PSW retrievals were obtained from the 12Z imagery than for 24Z. About 62% of all attempted retrievals at 12Z were considered valid as opposed to 40% for 24Z. This is most notably due to increased average cloud contamination at 24Z. The average UPX value (the percentage of pixels passing cloud threshold test in the 5x5 pixel window centered on retrieval location) for all attempted 12Z retrievals was about 49%. For all attempted 24Z retrievals, the average UPX value was 28%.

However, retrievals at 24Z generally performed better than those at 12Z. For 24Z performance statistics, the MBE is 2.9 mm, MAE is 7.0 mm and percentage error is 18.6%. Conversely, for 12Z, the MBE is 6.0 mm, MAE is 8.1 mm and percentage error is 24.8%. Two possibilities contribute to this result. By examining the atmospheric profiles, more inversions seem to occur in the morning hours (12Z) than in the late afternoon hours (24Z), which is expected. Also, the Reanalysis model first

guess estimates are closer to the radiosonde observations during 24Z retrievals than 12Z retrievals, influencing a better performance during those times. The scatter plots in Figure 6.3 do not show a general bias for large or small values of precipitable water. Although the *MAE* and *MBE* are larger for 12Z, the slope of the regression line is closer to 1.0 than for the 24Z data. The box plots in Figure 6.4 depict very similar data distributions for both radiosonde and PSW-derived 12Z values (too few valid data points exist at 24Z to make a good comparisons of the distributions.)

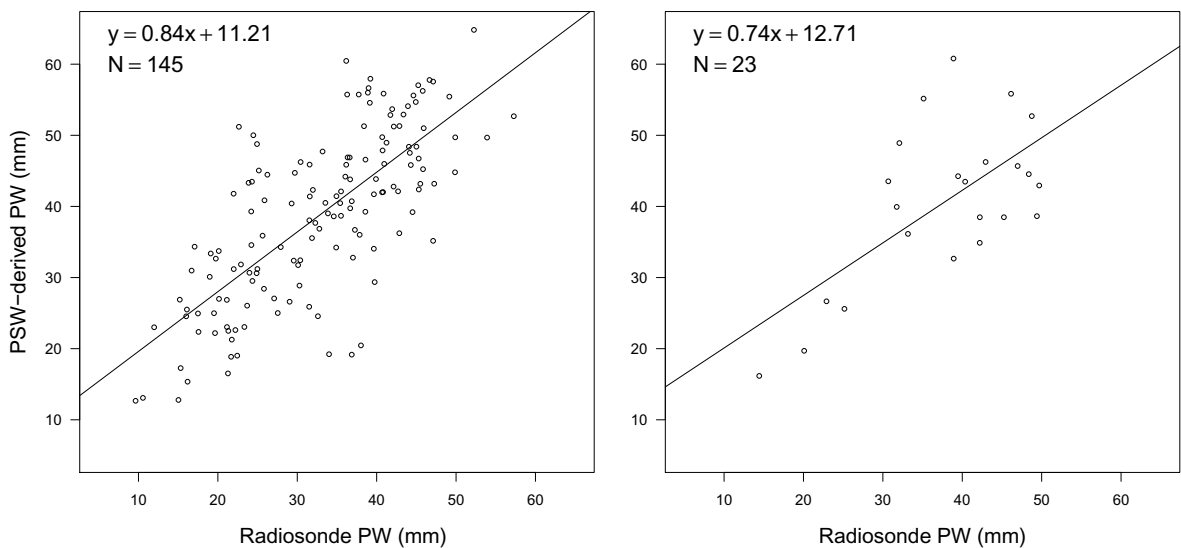


Figure 6.3: PSW-derived vs radiosonde precipitable water scatter plots and linear regression line based on time of day, 12Z (left) and 24Z (right).

6.1.2 Comparison by Month and Year

Statistics are divided separately for comparisons among the various months and years, namely June and October for 1988 and 1995. Table 6.3 provides summary statistics for all of the time periods. Likewise, Figure 6.5 shows separate box plots and Figures 6.6 and 6.6 show the scatter plots and regression lines for the same set of data.

Of all four months, June 1988 performed the best, with $MBE = -1.9$ mm, $MAE = 5.0$ mm and percentage of error = 16%. October 1995 performed the worst

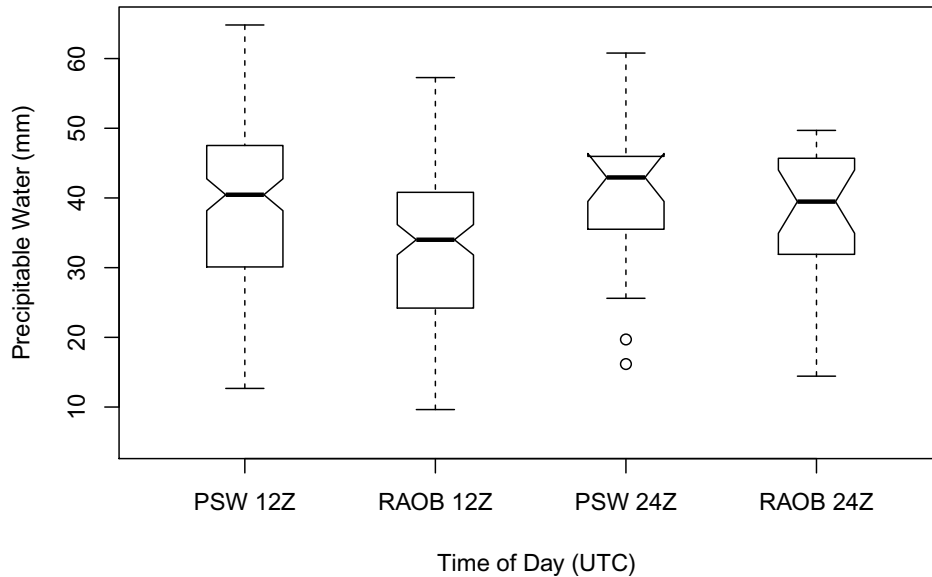


Figure 6.4: PSW-derived vs radiosonde precipitable water box plots based on time of day of radiosonde launch, 12Z and 24Z. (PSW = PSW-derived, RAOB = Radiosonde observed.)

of the four, with $MBE = 10.2$ mm, $MAE = 10.9$ mm and percentage of error = 34%. Overall, June retrievals performed better than October retrievals, with percentage errors of 18% to 27%, respectively. Similarly, 1988 retrievals performed better than 1995 retrievals, with percentage errors of 19% to 29%, respectively. Aside from June 1988, which had a negative MBE , the PSW-technique consistently overestimated precipitable water, as can be seen on the scatter plots and box plots, and the fact that both MBE and MAE was of the same sign (positive) and similar magnitude. Box plots show similar distributions of all the 1988 data, with a larger range of data in October. The 1995 data for October also showed similar distributions for the radiosonde observed and PSW-derived values albeit with a shift to lower values for the observed data, as indicated by large MAE and MBE values. The 1995 June data show more extreme toward the minimum for the PSW-derived data. Scatter plots for both months

Table 6.3: Statistics for PSW-derived vs radiosonde precipitable water observations for each month and year combination, including data from both times and all stations. μ , σ , MBE , and MAE values are in mm. x represents radiosonde observations and y represents PSW-derived values.

	N	μ_x	μ_y	σ_x	σ_y	r	d	MBE	MAE	$\frac{MAE}{\mu_x}$
Jun1988	29	31.6	29.7	10.2	9.1	0.79	0.71	-1.9	5.0	0.16
Oct1988	56	34.6	38.6	9.7	9.9	0.72	0.58	4.1	6.9	0.20
Jun1995	26	37.0	43.9	11.5	12.2	0.88	0.68	6.9	7.3	0.20
Oct1995	57	31.7	41.8	9.9	11.7	0.73	0.51	10.2	10.9	0.34
1988	85	33.5	35.6	10.0	10.5	0.73	0.64	2.1	6.2	0.19
1995	83	33.3	42.5	10.7	11.9	0.78	0.57	9.1	9.8	0.29
June	55	34.2	36.4	11.2	12.8	0.82	0.72	2.3	6.1	0.18
October	113	33.1	40.2	9.9	11.0	0.69	0.53	7.1	8.9	0.27

of 1995 show a moist bias, particularly for higher values of precipitable water.

There were twice as many valid data pairs found for October (113) than for June (55.) Although October retrievals did experience a slight decrease in cloud contamination (average UPX for all attempted retrievals was 74% in June and 77% in October), the main reason for the discrepancy was that June had less potential valid data pairs. The radiosonde station at Brasilia did not include data for June 1988, and the station at Recife did not have data for June 1995. Additionally, no GOES images were available at all for 24Z in June 1995 to perform retrievals.

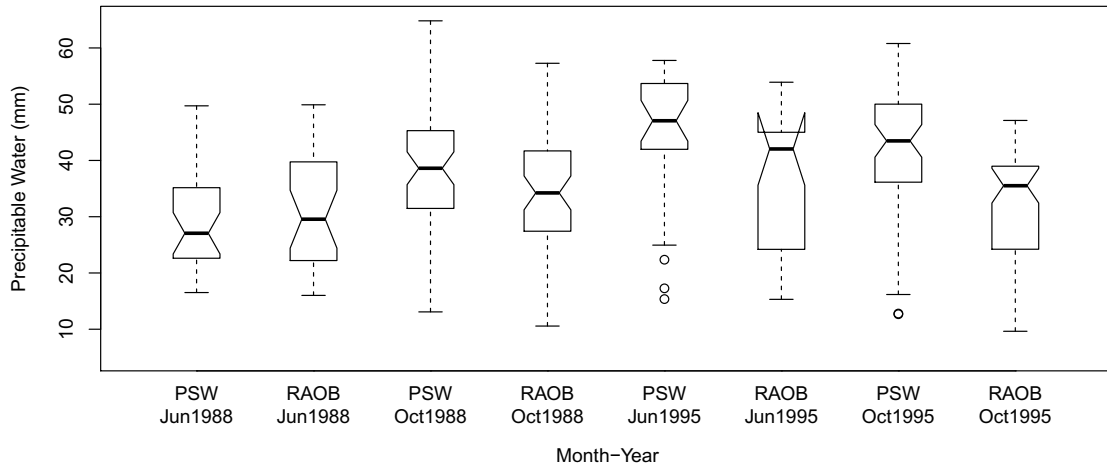


Figure 6.5: PSW-derived vs radiosonde precipitable water box plots of observations in October and June, 1988 and 1995. (PSW = PSW-derived, RAOB = Radiosonde observed.)

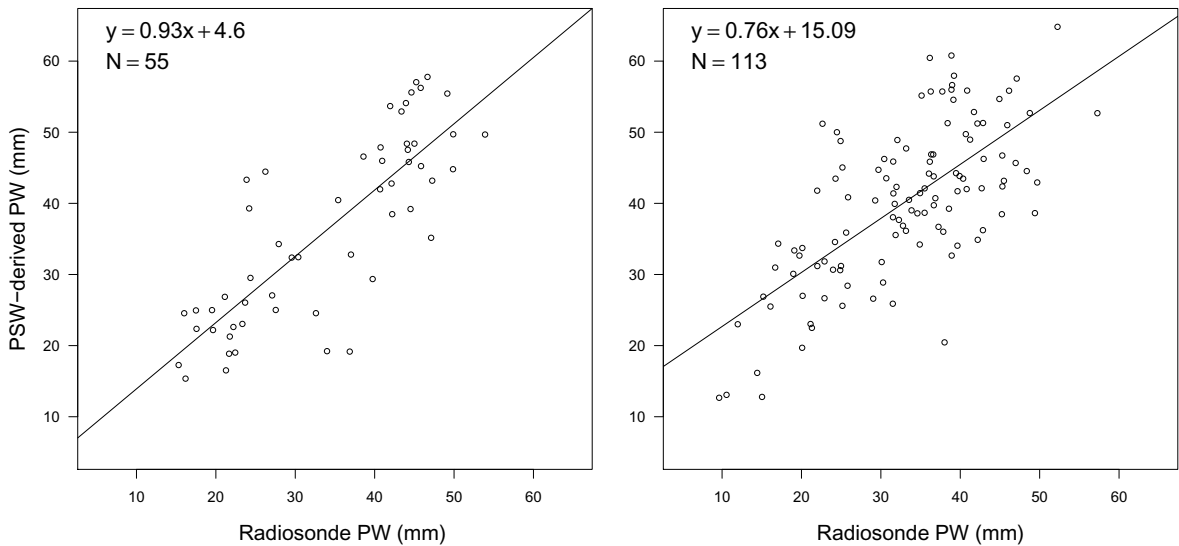


Figure 6.6: PSW-derived vs radiosonde precipitable water scatter plots and linear regression line based on month of observation, June (left) and October (right), for both 1988 and 1995 data combined.

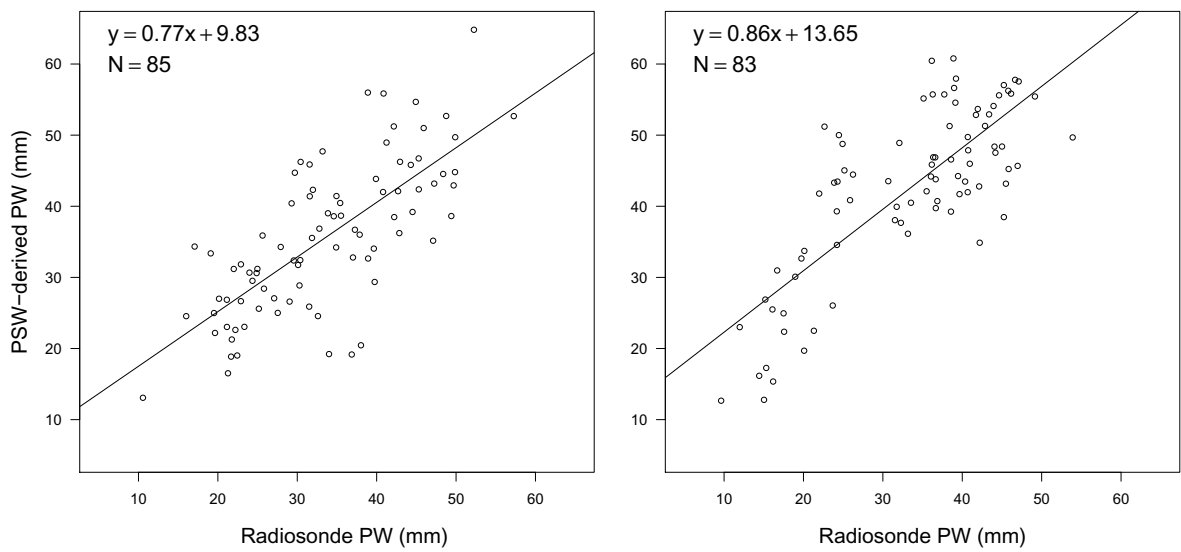


Figure 6.7: PSW-derived vs radiosonde precipitable water scatter plots and linear regression line based on year of observation, 1988 (left) and 1995 (right), for both June and October month data combined.

6.1.3 Comparison by Location

Statistics are also divided geographically for comparisons among the various radiosonde stations throughout the study area. Table 6.4 provides summary statistics for each of the radiosonde stations across all years, months, and daily launch times. Likewise, Figure 6.8 shows separate box plots and Figures 6.9, 6.10, and 6.11 show the scatter plots and regression lines for the same set of data. Figure 6.12 shows the stations in reference to regional land cover.

Table 6.4: Statistics for PSW-derived vs radiosonde precipitable water observations for each station, including data from both 0Z and 12Z launch times and all months. μ , σ , MBE , and MAE values are in mm. x represents radiosonde observations and y represents PSW-derived values.

Station	N	μ_x	μ_y	σ_x	σ_y	r	d	MBE	MAE	$\frac{MAE}{\mu_x}$
1. Belém	60	40.5	45.1	5.2	7.1	0.39	0.39	4.6	6.8	0.17
2. Manaus	23	44.6	47.4	5.4	8.4	0.51	0.40	2.9	6.9	0.15
3. Recife	11	32.9	28.4	6.0	6.6	-0.15	0.22	-4.5	8.7	0.26
4. Vilhena	23	29.9	38.5	6.1	13.2	0.87	0.48	8.6	9.4	0.31
5. Brasilia	14	22.7	35.1	4.0	8.8	0.53	0.21	12.4	12.4	0.55
6. C. Grande	37	21.5	28.8	5.9	10.2	0.75	0.47	7.3	7.8	0.36

Both stations that fall within the tropical rainforest, Station 1 in Belém and Station 2 in Manaus, performed similarly well, with MBE values around 2.8 mm to 4.6 mm, MAE values under 7.0 mm and percentage errors of 17% and 15% respectively. These stations constituted the largest values of precipitable water among all stations, with values over 40 mm. This is expected since very few inversions were noted in these areas, for either the 12Z or 24Z radiosonde launch times, and elevations of both stations were near sea-level, improving the accuracy of the first guess atmospheric profiles. Additionally, the assumed emissivity value of 0.98 in the 11 and 12 μm channels is likely appropriate for the forest land cover type surrounding these stations, although it is difficult to ascertain if these stations may be located in urban areas large enough

to influence the radiance received by GOES. Data from these two stations also account for one-half (83 out of 168) of all paired data points used in the comparison.

Stations at the Vilhena Airport (Station 4), Brasilia Airport (Station 5), and Campo Grande Airport (Station 6) performed similarly although with relatively larger errors, with *MBE* and *MAE* values above 7.0 mm and percentage errors over 30%. Precipitable water at these stations were the lowest of the group, with values in the 20 mm to 30 mm range. The PSW algorithm consistently overestimated precipitable water at all three stations as compared to the radiosondes.

One likely cause of the poor performance is the land cover near these stations. These stations are in regions of mixed savannah, grasslands, shrublands, urban, and forest ([European Commission, 2003](#)). Not only are these areas more susceptible to temperature inversions, particularly at the radiosonde launch time of 12Z and 24Z, but it is very difficult to ascertain the appropriate emissivity to use for the 5x5 pixel neighborhood around the station. Other possible contributing factors are the relatively high elevations above sea level, approximately 600 m for Vilhena and Campo Grande and over 1000 m at Brasilia, and the latitudinal distance away from the equator, increasing uncertainty from the slant path correction from the satellite.

Comparisons at Recife (Station 3) were interesting for several reasons. Precipitable water values were around 30 mm, midway between the other stations to the north and those to the south. The *MBE* is -4.5 mm, the only station with a negative bias (i.e., an underestimate). The Pearson r was also negative albeit with a low magnitude, indicating little correlation. This station also had a large *MAE* of 8.7 mm. Individual residuals either had large errors of over 10 mm or smaller errors under 6 mm. Very few radiosondes were launched from this station, located on the eastern coast of Brazil, in an urban setting surrounded by agriculture ([European Commission, 2003](#)). As with the other southern stations, an inappropriate emissivity is a likely cause of error. The easterly trade winds could also influence the results since the overlying water vapor comes from the Atlantic Ocean and little is recycled from the region.

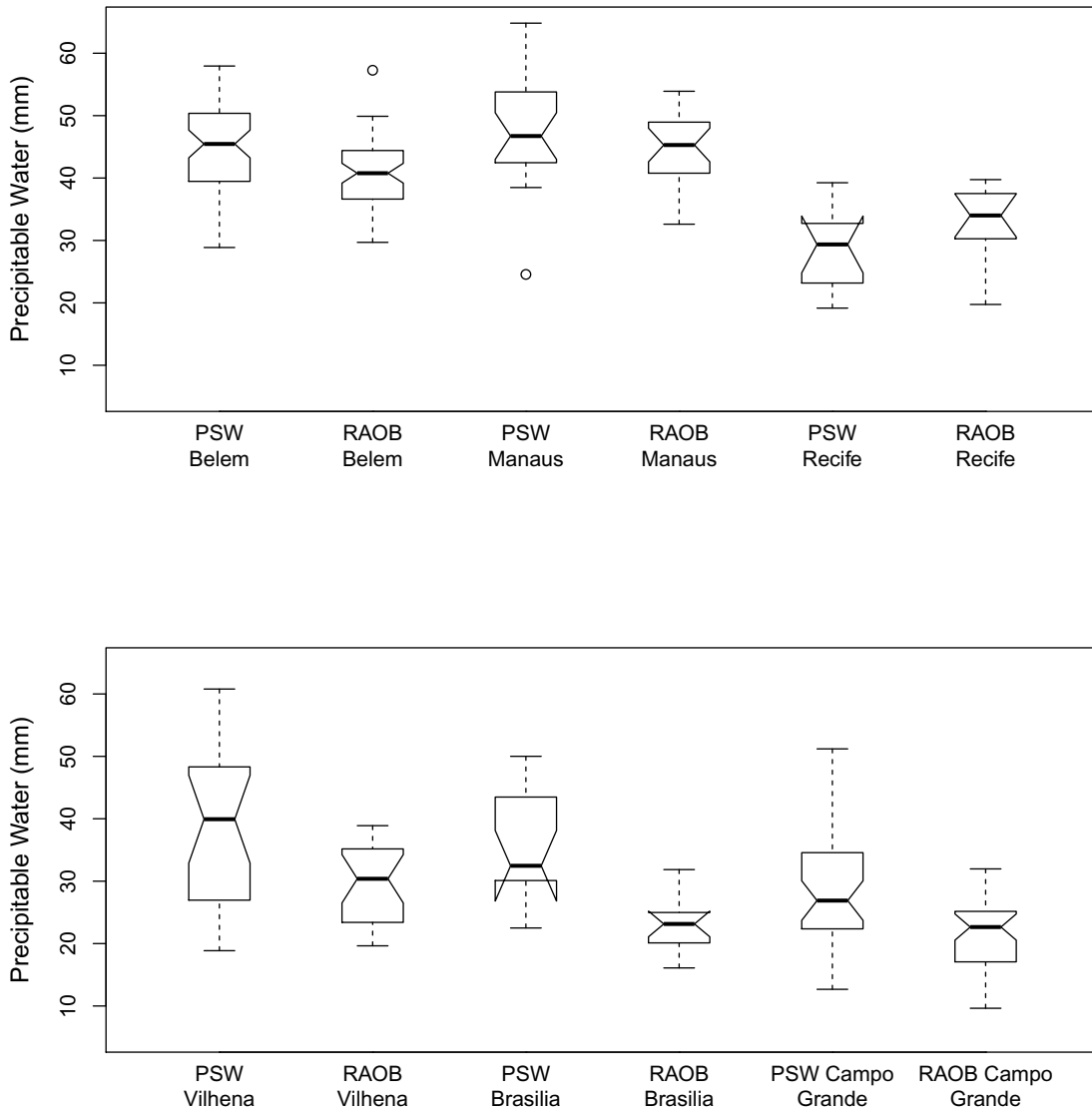


Figure 6.8: PSW-derived vs radiosonde precipitable water box plots based on radiosonde stations 1 - 3 (top) and 4 - 6 (bottom), including data from both launch times and months. (PSW = PSW-derived, RAOB = Radiosonde observed.)

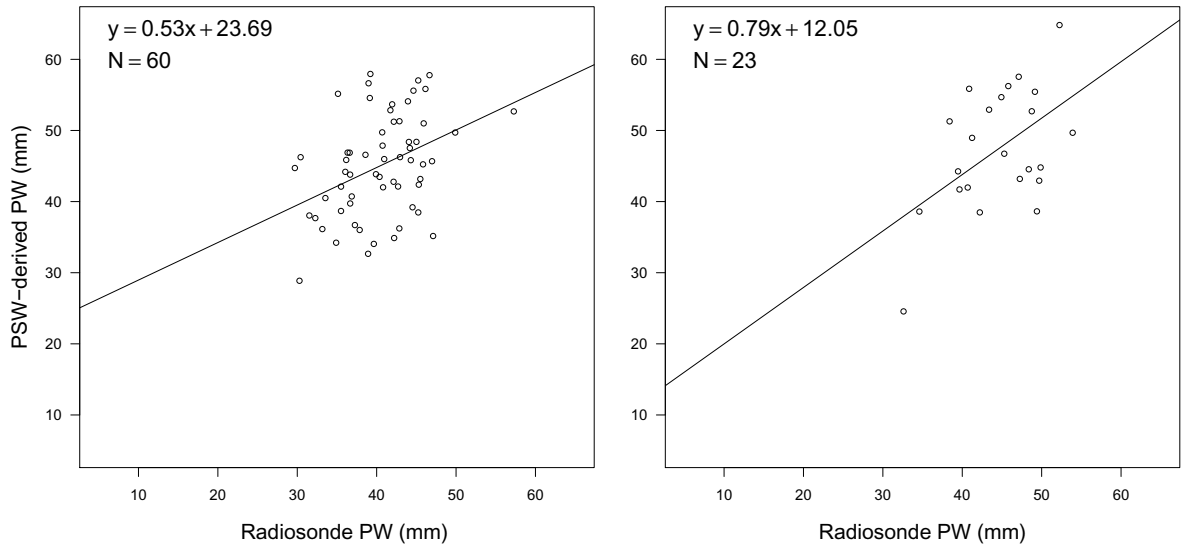


Figure 6.9: PSW-derived vs radiosonde precipitable water scatter plots and linear regression line of all observations for stations 1 and 2.

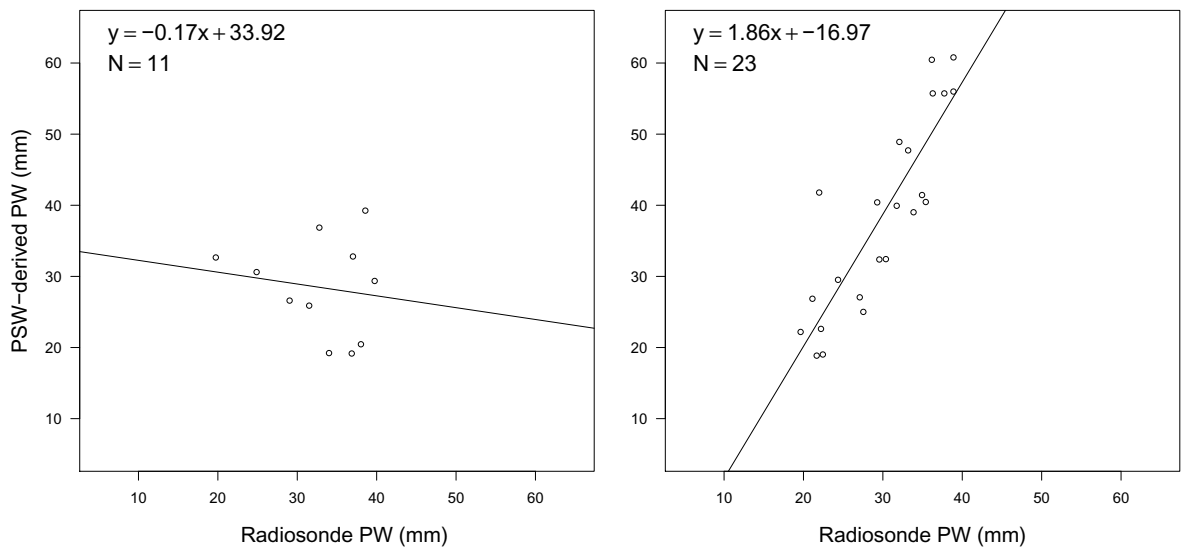


Figure 6.10: PSW-derived vs radiosonde precipitable water scatter plots and linear regression line of all observations for stations 3 and 4.

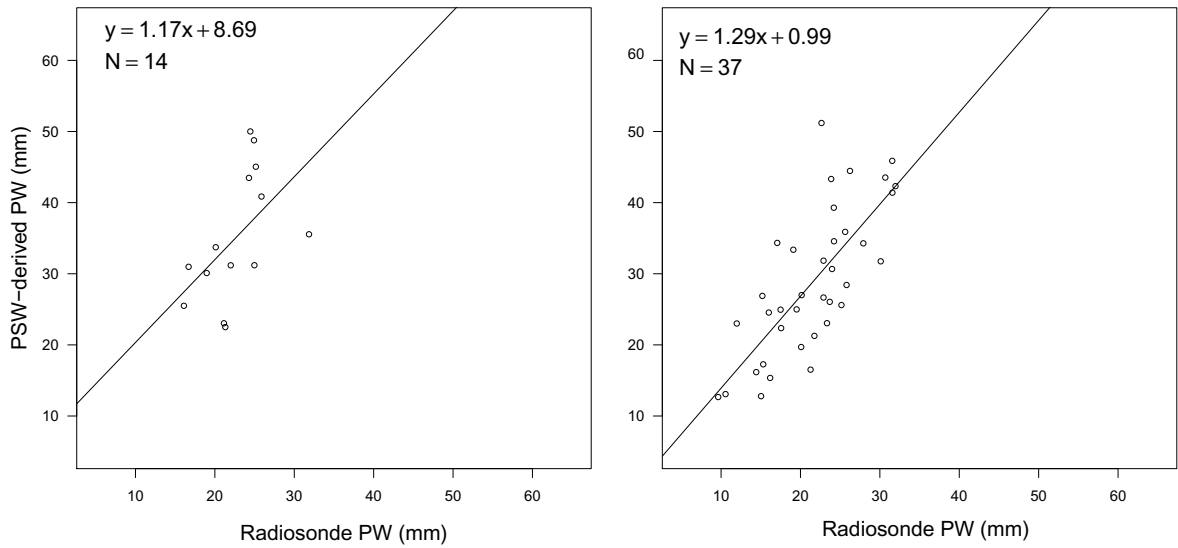


Figure 6.11: PSW-derived vs radiosonde precipitable water scatter plots and linear regression line of all observations for stations 5 and 6.

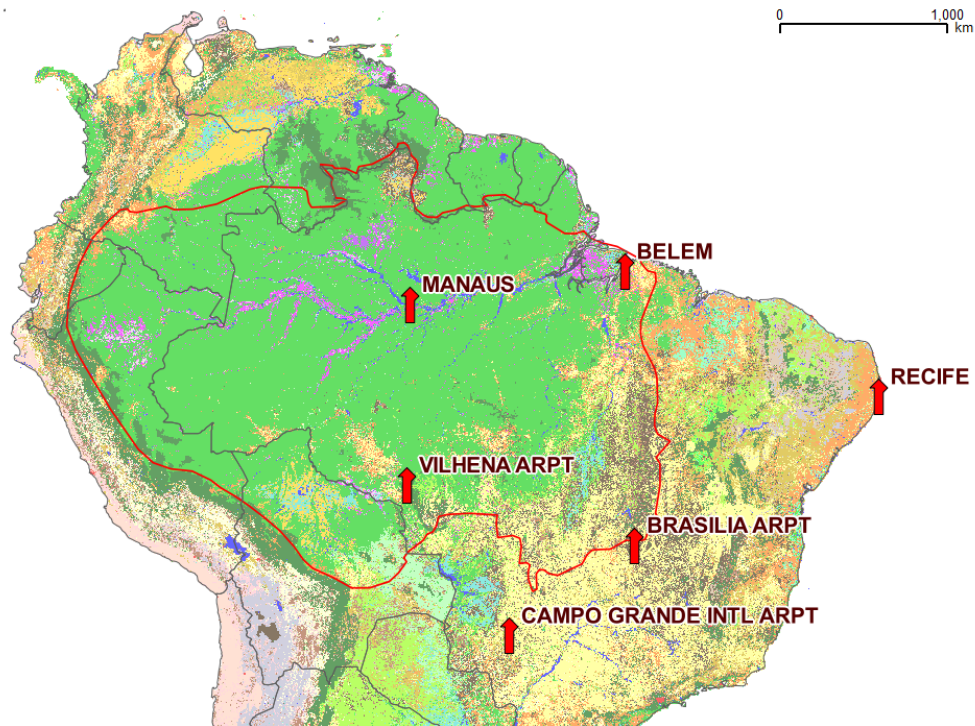


Figure 6.12: Land cover map with radiosonde stations. Source: European Commission Global Land Cover 2000 database ([European Commission, 2003](#)).

Chapter 7

ANALYSIS OF PRECIPITABLE WATER FIELDS

This chapter will analyze the spatial and diurnal distribution of precipitable water throughout the Amazon Basin as derived by applying the Physical Split Window (PSW) technique to GOES imagery. The first section will review the regional monthly climatology of precipitable water, as calculated from analyzing 20 years of daily grids from the NVAP-M Climate dataset from 1988 through 2009. Results from the PSW-derived precipitable water field retrievals for June and October, 1988 and 1995, are then explored by comparing the monthly average and daily values in each of seven "zones", located uniformly throughout the region. As well, diurnal variations of precipitable water are also described by looking at the water vapor peak time of day and diurnal range within each zone, for each month and year.

Figure 7.1 shows the seven zones used for the analysis in this study plotted on a vegetation/land cover map. The zones measure $5^{\circ} \times 5^{\circ}$ each and are located uniformly throughout the Amazon Basin. Zones 2, 3, and 5 lie entirely within the basin, with low elevations, and with land cover mostly dominated by closed evergreen forest, with the slight exception of zone 2 that also includes some of the Amazon River itself and mangrove and swamp forests along the river banks (European Commission, 2003). Land cover for zone 1, in the upper northwest portion of the basin is a mix of evergreen forests and savannah. Zone 6, in the southern basin, is similar to zone 1 in that it contains about half evergreen forests although it contains a much smaller amount of savannah and larger amount of agricultural fields and forest plantations. Both zones 4 and 7 lie mostly outside the Amazon Basin to the east and south, and have high elevations, averaging approximately 400 m and 675 m, respectively. Zone 4 is a mix of numerous land cover types, including a large section of deciduous forests,

shrublands, savannah and agricultural fields. Zone 7 is nearly all agricultural fields and shrublands with very little forest.

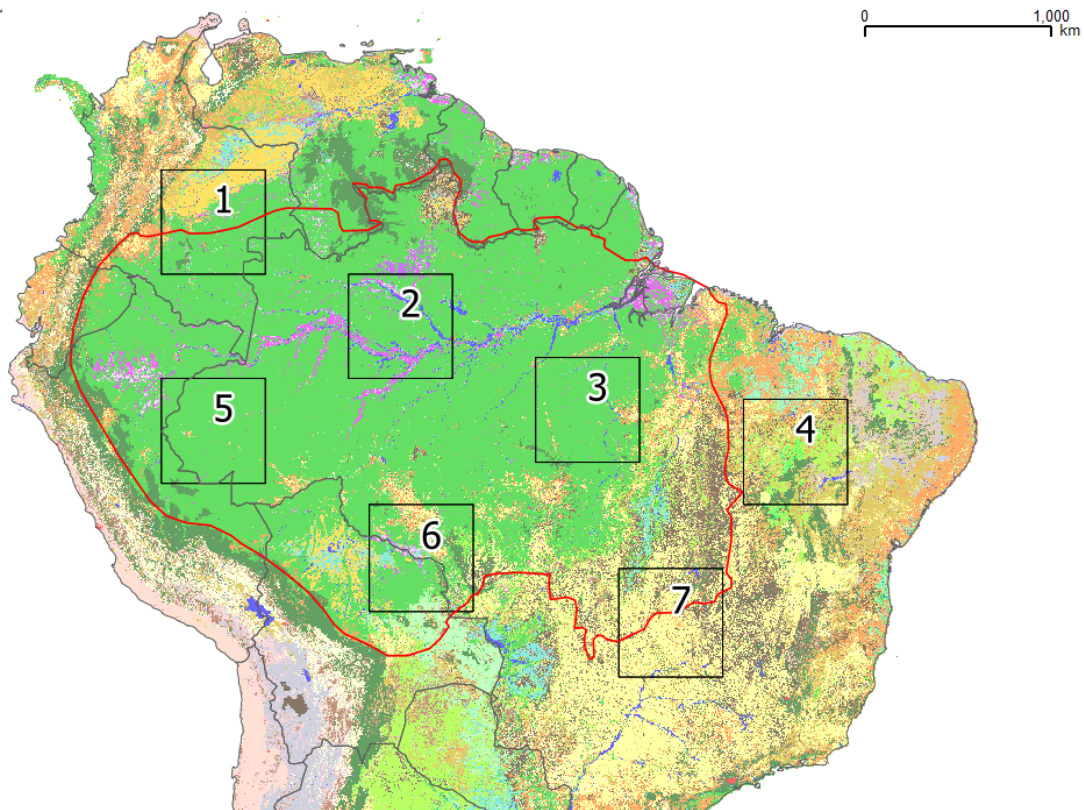


Figure 7.1: Local zones used in the analysis of precipitable water fields. Each of the seven zones measure $5^\circ \times 5^\circ$ and located uniformly throughout the Amazon Basin.

For the zone statistics listed in the tables and figures below, values of precipitable water were averaged for all grid cells that fall within each zone. Grid cells with null values were also not an issue since the analysis was performed on the final output of the PSW-derived fields (described in section 5.4), all grid cells contain valid precipitable water values.

It is important to recall that only daytime GOES imagery were used, beginning at 12Z (local time of 8:00 am for western basin; 9:00 am for the eastern basin) through 24Z (local time of 8:00 and 9:00 pm) at 3-hour intervals. Daily precipitable water was determined by averaging all available data for that day, typically being five times per

day. For the diurnal analysis, determination of peak time of day for precipitable water is not affected as water vapor is usually larger during the daytime hours than night time (Dai et al., 2002; Wu et al., 2003). However, for determining the diurnal range of precipitable water, only a portion of the range is being captured as the overnight minimum values are not included. Also note that imagery for 21Z in October 1988 and 24Z in June 1995 were not available for retrievals. Therefore, following the same thinking as replacing retrievals that did not pass the cloud threshold with Reanalysis data for that location, precipitable water fields during times of missing imagery were produced by using the Reanalysis data only.

7.1 Regional Precipitable Water Climatology

Daily total columnar precipitable water grids were obtained from the NVAP-M Climate dataset at $1.0^\circ \times 1.0^\circ$ spatial resolution. Details of the dataset are described in section 4.4. Daily grids were averaged on a cell-by-cell basis for each day to determine an average for each month for each of the 20 years, then clipped to an extent just outside the boundaries of the study area. Each month was then averaged across all years to determine a monthly climatology. For example, all of the January monthly grids for all of the years were averaged together for the January climatology. The same was done for each month of the year. Figure 7.2 shows the resultant monthly climatology of precipitable water for the study area.

Additionally, figure 7.3 shows the average monthly cloud coverage for the northern South America region. These data were obtained from the NASA Langley Distributed Active Archive Center, collected as part of the International Satellite Cloud Climatology Project (ISCCP) through the World Climate Research Program (WCRP). ISCCP cloud coverage grids were obtained at $2.5^\circ \times 2.5^\circ$ spatial resolution.

Water vapor for this region rises quickly from a minimum near July to its peak near November with max values over 60 mm. Moisture remains high through January and then a steady decrease until July with min values in the 20 mm range and most of the basin in the 30 mm range. The largest values correspond to areas over the

closed evergreen forests of the Amazon Rainforest, which makes sense due to enormous amounts of vegetation transpiring. Areas of savannah, shrubland, and agriculture with much less vegetation also have much smaller values of precipitable water and less pronounced seasonal cycle.

Based on precipitation, the typical peak of the wet season in southern Amazonia is around December through February, central Amazonia around March through May, and the northwestern region receiving significant rainfall throughout the year (Marengo, 2007). This corresponds to the movement of the ITCZ, at its southern most extent (covering central/southern Amazonia) near the southern hemisphere summer solstice in January, and reaching its peak northern position (just north of Amazonia) near the southern hemisphere winter solstice in July. The ISCCP cloud cover data strongly corresponds to the seasonal cycle of ITCZ position and precipitation, with peak cloud cover from January through March and a minimum from June through August.

While the ITCZ is in its southern position, it brings strong, consistent east winds from the Atlantic ocean and therefore significant moisture advection, causing high precipitable water for the region. Evapotranspiration has been found to be relatively consistent throughout the year, even during the dry season due to the deep rooting of the vegetation and large amounts of soil moisture available down to several meters (da Rocha et al., 2004; Bruno et al., 2006; Karam and Bras, 2008). Huerte et al. (2006) found an increase in the MODIS Enhanced Vegetative Index (EVI) during the dry season. Water vapor tends to increase before the heavy precipitation months, supporting the argument made by Karam and Bras (2008) and others that the transition to the wet season begins with increases in precipitable water rather than precipitation.

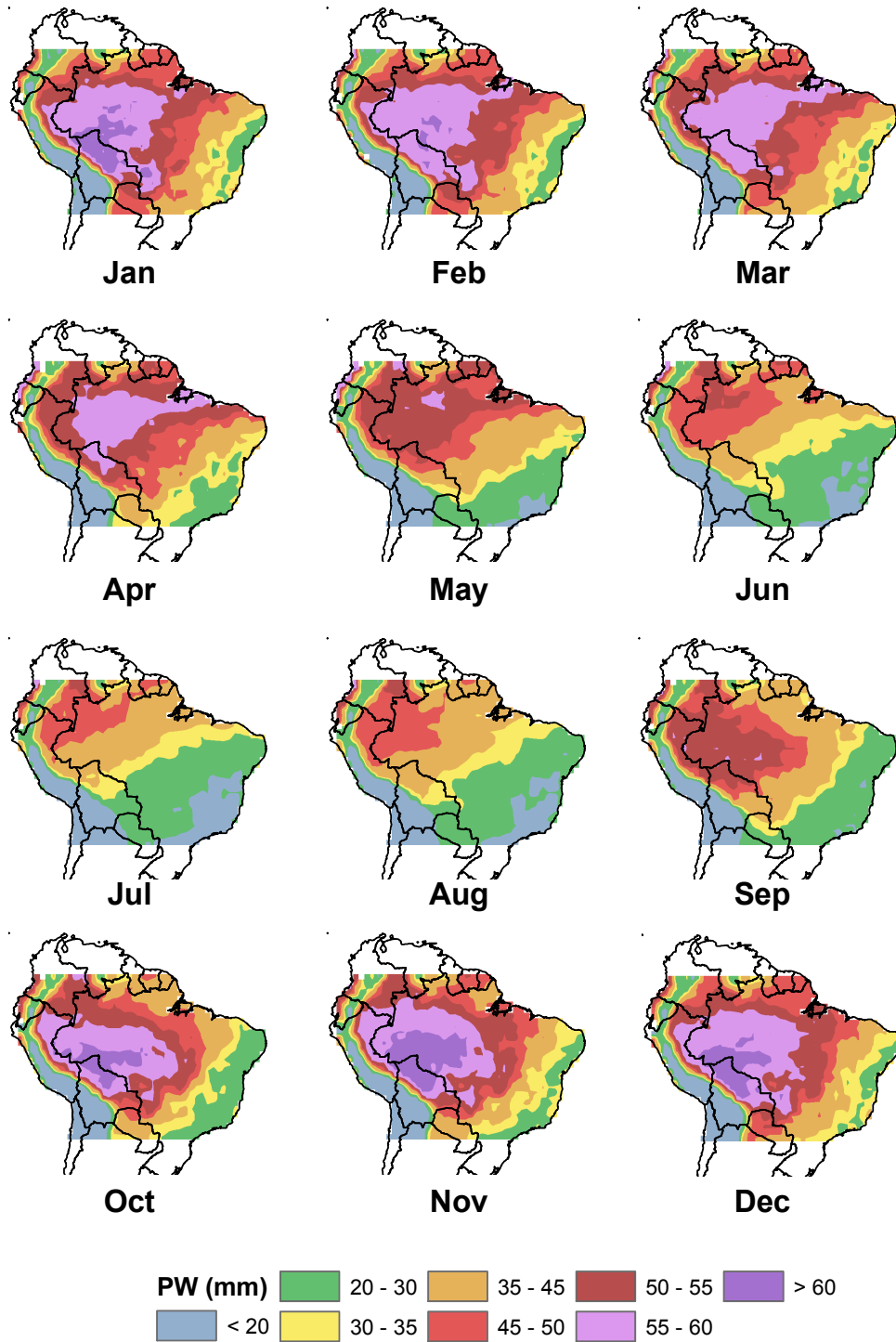


Figure 7.2: Monthly climatology of precipitable water in the Amazon from the NASA Water Vapor Project (NVAP).

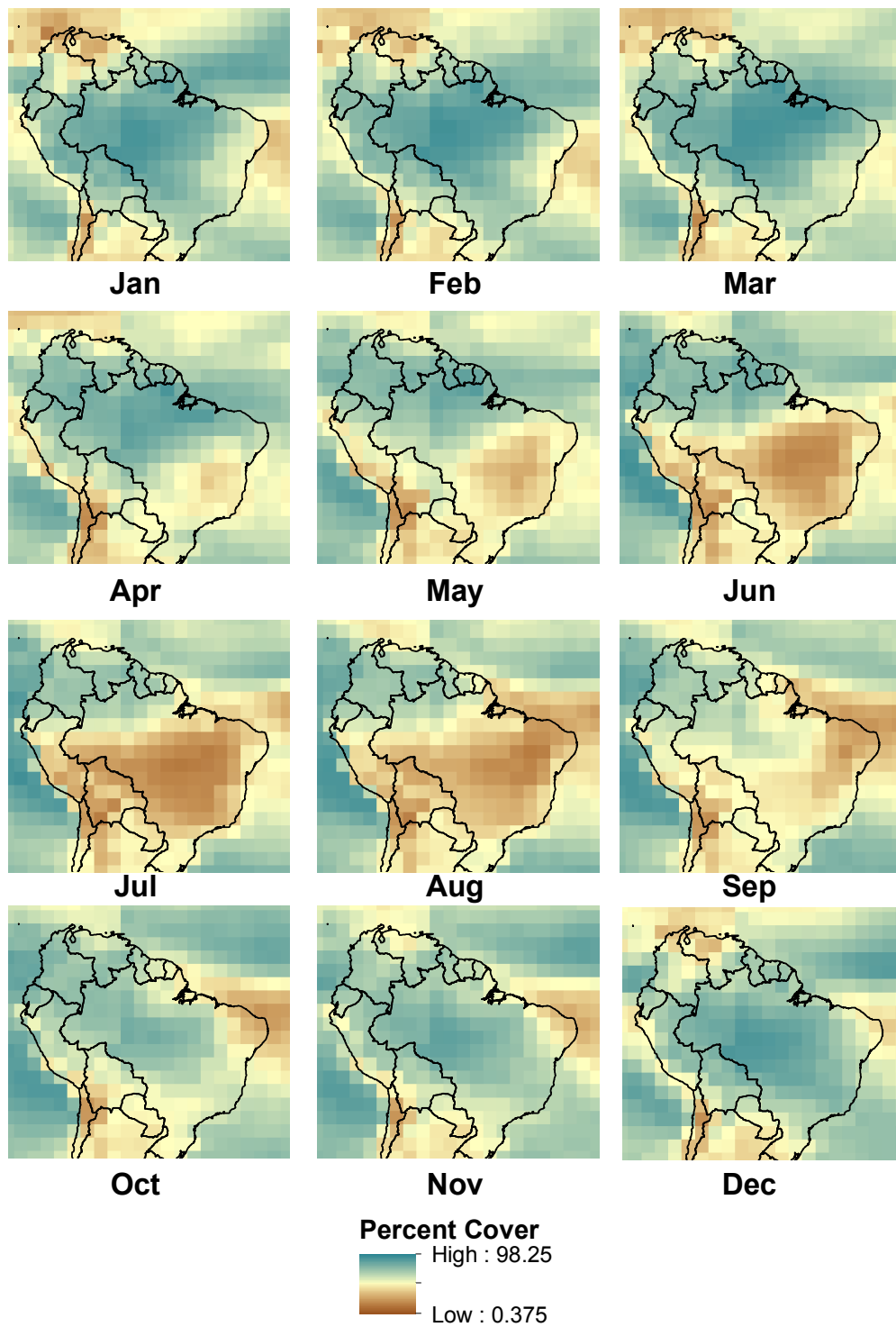


Figure 7.3: Monthly climatology of cloud cover in the Amazon from International Satellite Cloud Climatology Program (ISCCP).

7.2 PSW-Derived Precipitable Water Monthly Fields

7.2.1 Spatial Distribution of PSW-Derived Precipitable Water

PSW-derived precipitable water fields were generated by averaging, on a cell by cell basis, all fields retrieved for that month, typically five times per day (12Z through 24Z) for 30 (June) or 31 (October) days, totaling about 130 to 135 fields per month. (The last 24Z GOES image on the last day for each month was not available since it was labeled as 0Z for the following day/month.) Output grid spatial resolution is $0.5^\circ \times 0.5^\circ$. Details of the methodology are explained in section 5.4. Since daytime-only fields are used in the analysis, the resultant grid would be wet-biased compared to the true average conditions for that month. The NVAP dataset incorporates radiosondes launched at 12Z and 24Z as well as daytime-only thermal infrared imagery and would therefore suffer from similar biases as the PSW-derived data. Figures 7.4 and 7.5 show the PSW-derived precipitable water fields and differences from NVAP for all four months of this study, June and October, 1988 and 1995.

The pattern of precipitable water in all months of the PSW-derived fields is similar to what is seen in the NVAP data: highest values in the northwest at 45 mm to 50 mm with a decreasing gradient toward the southeast at 20 mm to 30 mm. Both June maps exhibit a strong north to south gradient whereas the October maps exhibit the typical northwest to southeast gradient. In both 1988 and 1995, the maps show significantly higher precipitable water in October than in June in central and south/southeast Amazonia, except in the northwest region where June and October have similar peak values. This is to be expected based on the NVAP climatology and the fact that the rainy season is about to begin.

Table 7.1 shows the precipitable water averages for both PSW-derived and NVAP in each zone for all four months. In all zones, the PSW-derived values in June are less in 1988 than 1995. NVAP shows a more drastic difference. This is an interesting case since a strong La Niña was present in 1988-1989, resulting in increased precipitation in northern Amazonia (zones 1-3) and decreased precipitation in central and southern regions (zones 4-7), a typical response to La Niña for the region (Ronchail

et al., 2002). The fact that PSW-derived precipitable water does not show an increase in the northern zones could be due to the inability for thermal radiation to penetrate the increased cloud cover, thereby resulting in invalid retrieval attempts and defaulting to the Reanalysis value, which may not do a good job capturing heavy convection.

For October, values in 1988 were very similar to 1995, except in zones 5 and 6 where values were 3 mm to 4 mm higher. This seems reasonable since the impacts of ENSO are less noticeable due to the very high transpiration and moisture advection from the ITCZ winds.

Although the maps in figure 7.4 show more water vapor in October than in June, this is not necessarily true for zones 1 and 2, both in the northwest. Precipitable water values are very similar in June and October, similar to the precipitation in the region. The zones further to the south and east, with mixed land cover characteristics and further away from the influence of the trade winds, show a significantly more pronounced seasonal change.

Table 7.1: Monthly averages of PSW-derived and NVAP precipitable water in each zone for each month and year. No valid NVAP data were available for Zone 1 in June 1995. All data values are in mm.

	Zone1	Zone2	Zone3	Zone4	Zone5	Zone6	Zone7
June 1988							
PSW-derived	45.3	46.5	38.0	31.4	40.4	29.9	22.1
NVAP	32.6	41.6	27.7	25.5	44.4	35.8	24.0
October 1988							
PSW-derived	44.1	46.3	43.0	38.0	42.1	39.1	34.4
NVAP	38.6	46.0	48.4	33.5	59.7	59.6	37.3
June 1995							
PSW-derived	46.4	48.0	40.2	35.4	42.7	33.4	26.2
NVAP	–	53.3	39.3	31.1	48.5	33.0	22.1
October 1995							
PSW-derived	45.4	46.2	43.7	36.5	45.9	42.7	34.7
NVAP	45.7	55.7	55.8	37.9	67.1	62.1	37.5

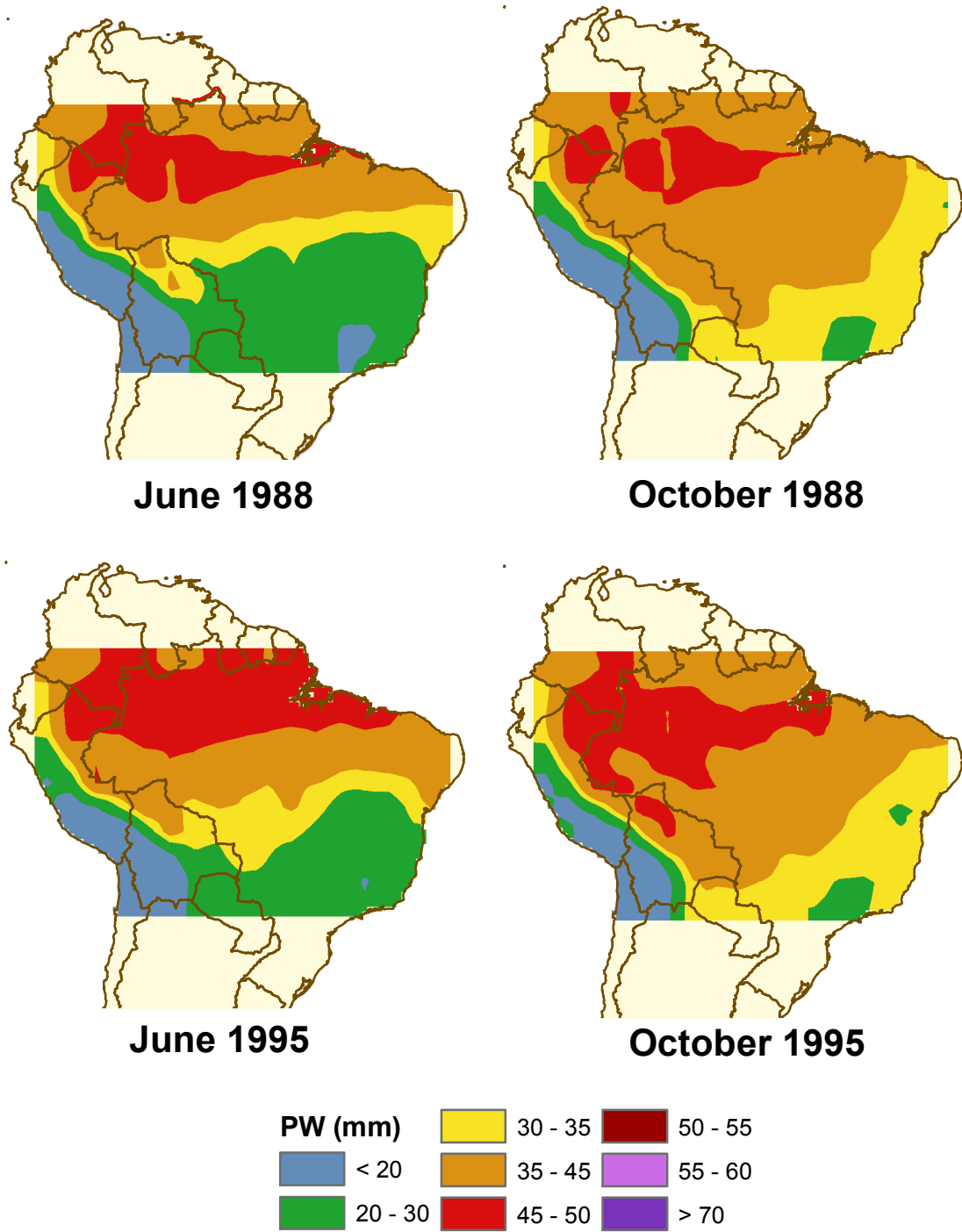


Figure 7.4: PSW-derived precipitable water fields for June and October, 1988 and 1995. Red and purple colors represent higher values of precipitable water; blue and green colors represent lower values.

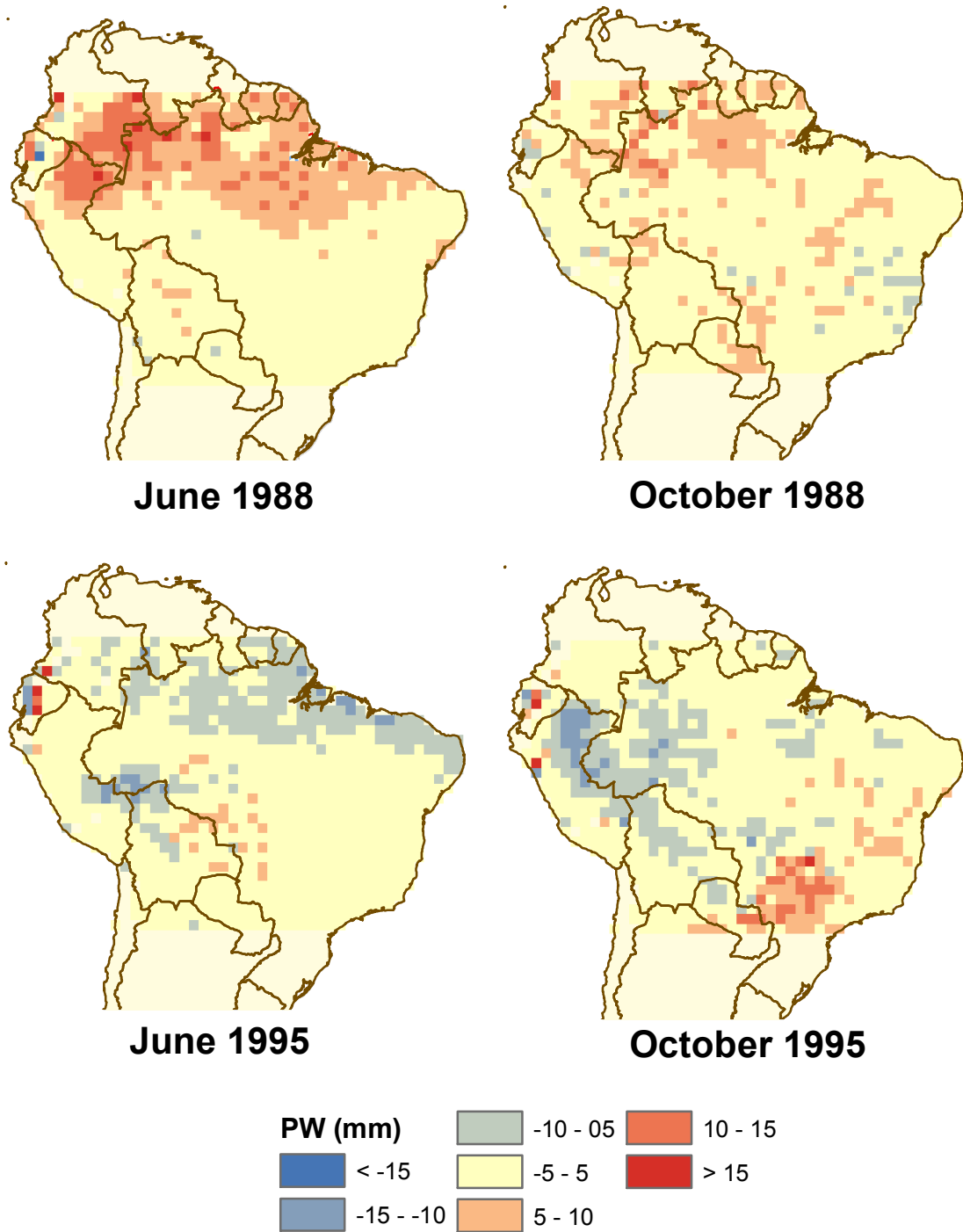


Figure 7.5: Difference maps between PSW-derived and NVAP precipitable water fields for June and October, 1988 and 1995. Positive numbers (red) represent areas where PSW-derived values are greater than NVAP.

7.2.2 PSW-Derived Precipitable Water Daily Timeseries

Figures 7.6 through 7.9 show daily mean PSW-derived and NVAP precipitable water for each zone for each month. Note that table 7.1 from the previous section shows monthly averages for the same data. Zones 1 and 2 in the north are relatively constant across all months, with values near 50 mm, consistent with its relative location and land cover continuously providing moisture.

Zones 3 shows slightly more variability and precipitable water values about 5 mm to 10 mm less than zones 1 and 2. Both PSW-derived and NVAP data follow similar daily changes throughout each month. Zones 5 matches the variability and quantity of zone 3 (similar locations) while zone 6 also matches the variability with quantities less by about 10 mm. For all three zones, values are higher in October than June by a few mm. NVAP seems to match the same daily pattern changes in June for these zones but is very inconsistent in October, usually with high values. NVAP values near 65 mm seem suspicious in October 1995, leading to the thought of cloud contamination.

Zones 4 and 7, located in the south and east (closest to the Atlantic Ocean coast) with similar land cover characteristics and elevations, have similar variability to zones 3, 4, and 6, and in general the lowest values of precipitable water. NVAP matches the total amount of precipitable water and the daily changes well in these two zones, in all months, likely due to mostly clear skies (the least amount of cloud contamination.)

In general, for the zones that experience significant precipitation and cloud cover (all zones except for 4 and 7), NVAP data exhibit a larger variation and many days without valid data points (not displayed). This is due to the limited radiosonde availability and the thermal infrared imagery used by NVAP being unable to see through clouds. Although the current PSW technique also uses thermal infrared imagery (from the GOES satellite), filling in the gaps of missing data with the Reanalysis model provides a smooth continuous record of precipitable water otherwise not available.

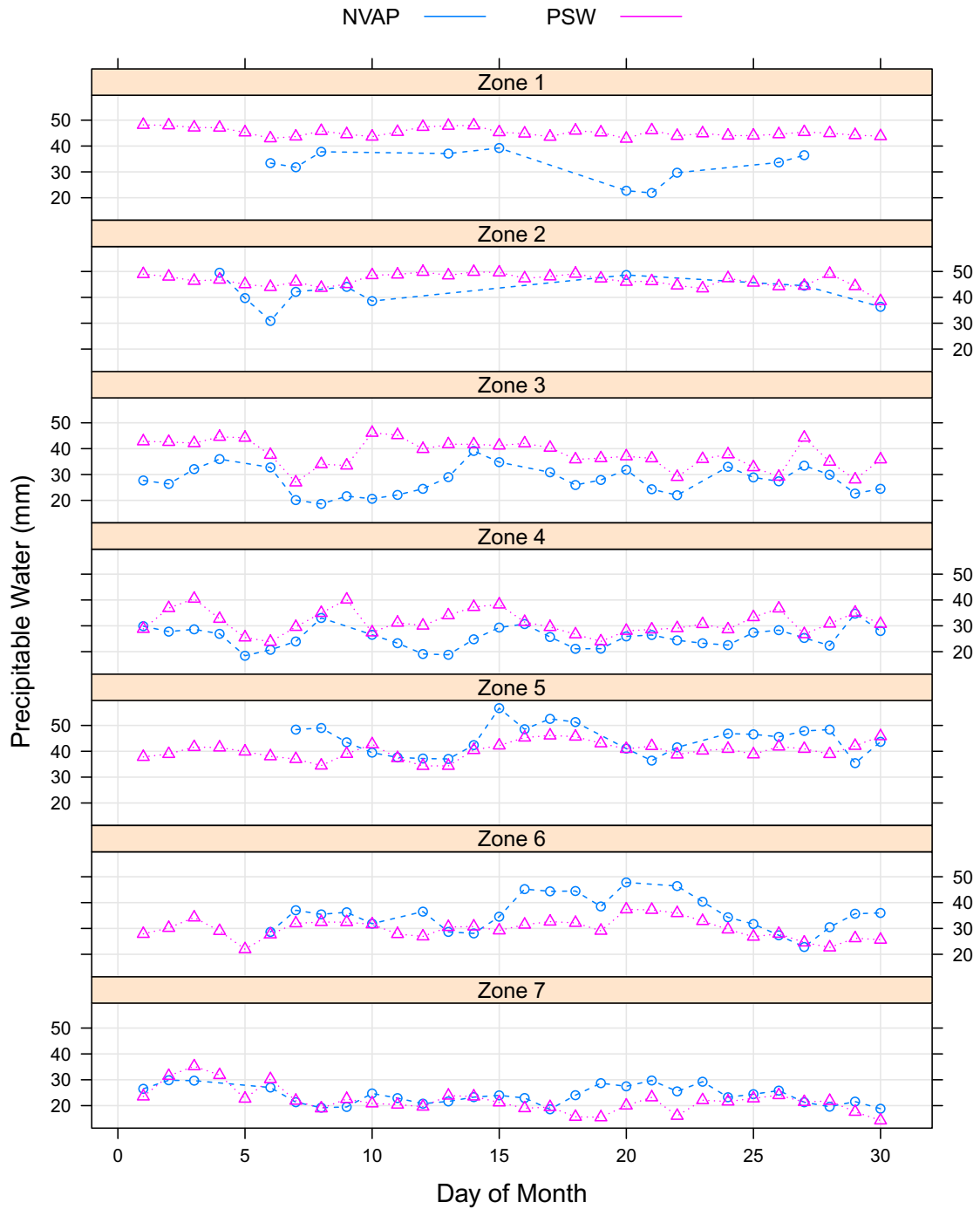


Figure 7.6: Daily mean PSW-derived and NVAP precipitable water in each zone for June 1988. Values for NVAP included only if valid data existed in over 50% of the zone. Pink triangles represent PSW-derived data; blue circles represent NVAP.

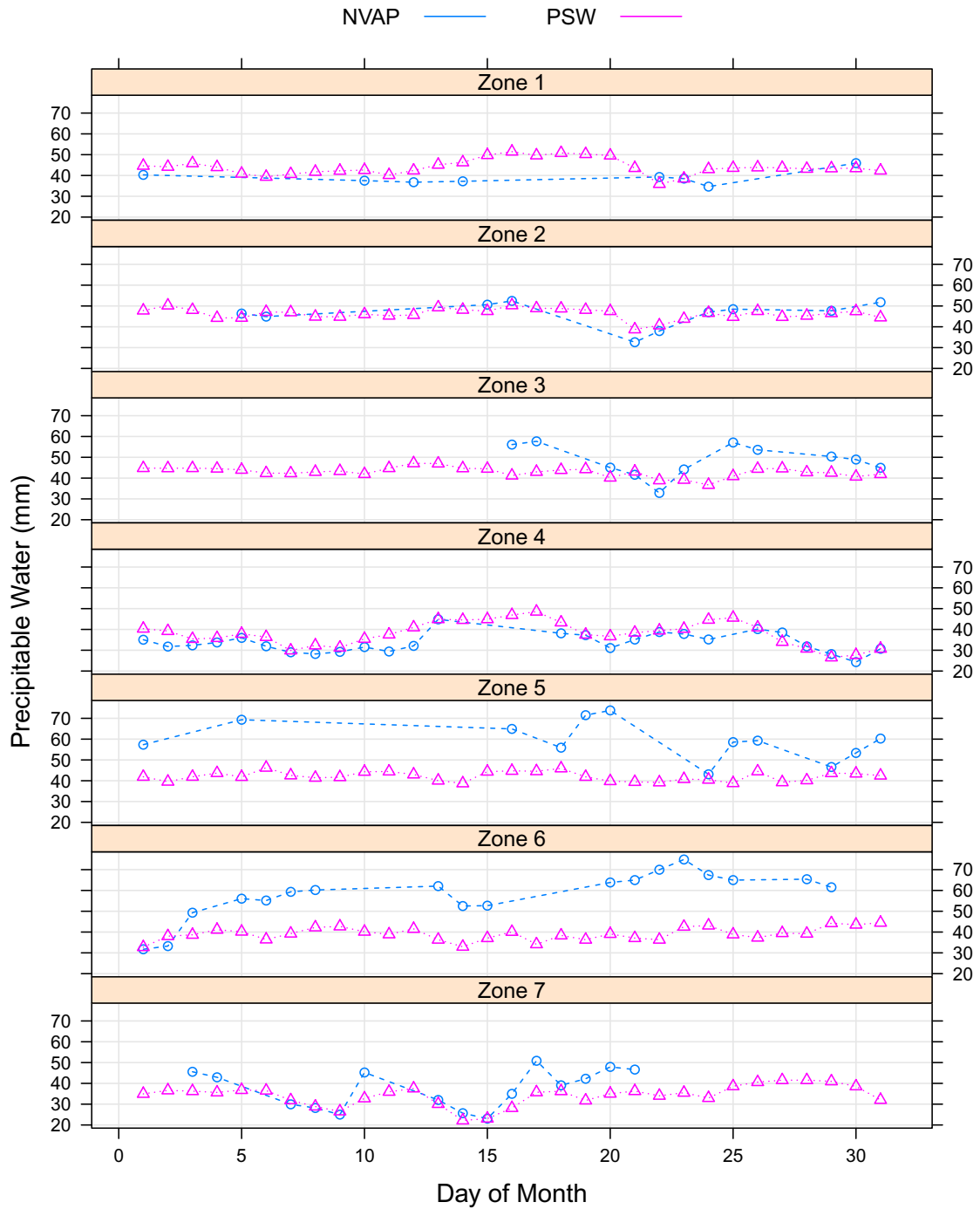


Figure 7.7: Daily mean PSW-derived and NVAP precipitable water in each zone for October 1988. Values for NVAP included only if valid data existed in over 50% of the zone. Pink triangles represent PSW-derived data; blue circles represent NVAP.

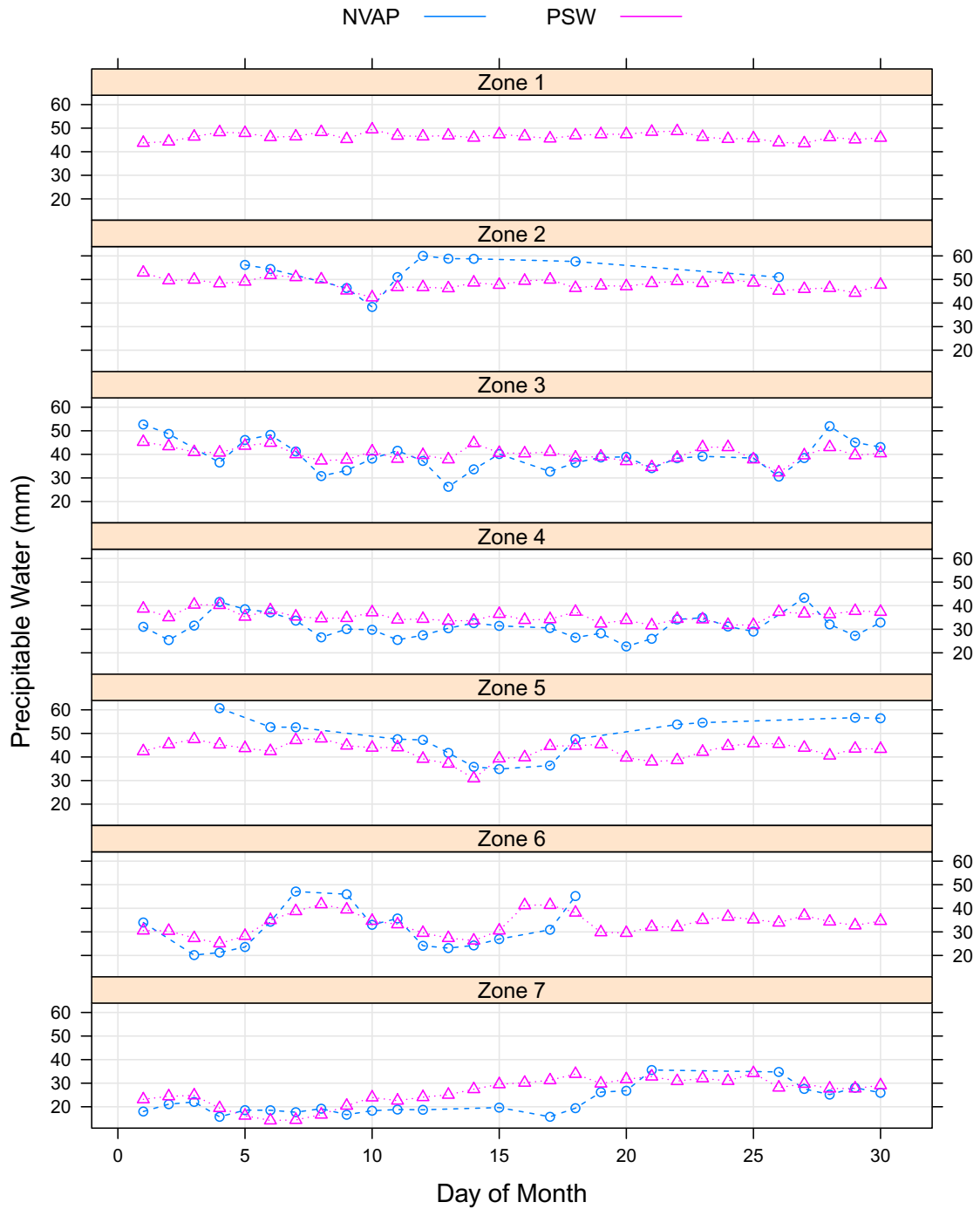


Figure 7.8: Daily mean PSW-derived and NVAP precipitable water in each zone for June 1995. Values for NVAP included only if valid data existed in over 50% of the zone. Pink triangles represent PSW-derived data; blue circles represent NVAP.

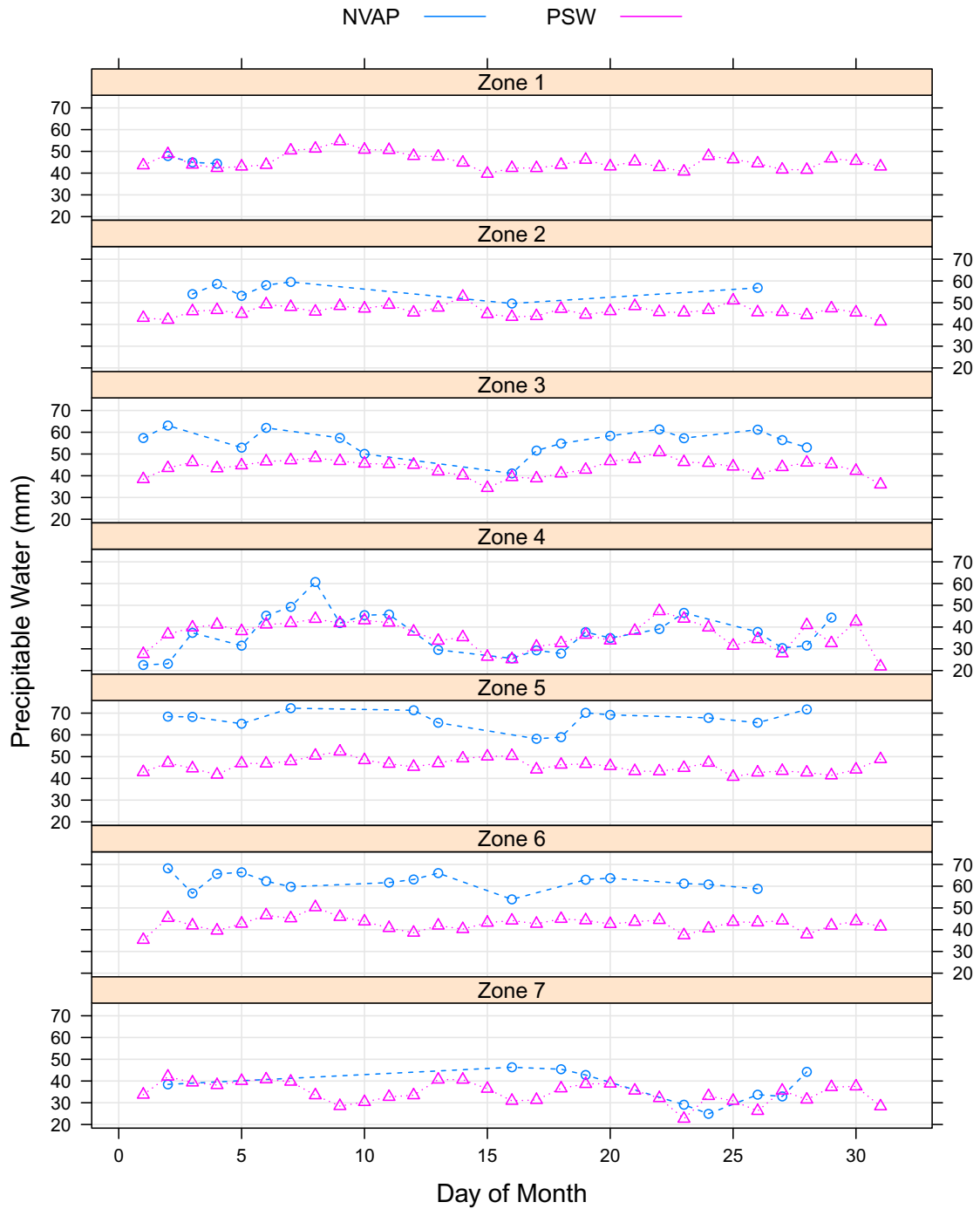


Figure 7.9: Daily mean PSW-derived and NVAP precipitable water in each zone for October 1995. Values for NVAP included only if valid data existed in over 50% of the zone. Pink triangles represent PSW-derived data; blue circles represent NVAP.

7.3 Diurnal Behavior of Precipitable Water

7.3.1 Diurnal Variations

Mean precipitable water fields were calculated for each time of day for each zone during all four months. As mentioned previously, only daytime images were used in this study for deriving precipitable water fields, namely images at 12Z (representing 8:00 am for western Amazonia and 9:00 am for eastern Amazonia local time), 15Z, 18Z, 21Z, and 24Z. All fields for a given time were averaged on a grid cell by cell basis. Figures 7.10 through 7.13 show the average value for each zone throughout the day for each month. Table 7.2 identifies the peak time of day for precipitable water within each zone.

Atmospheric water vapor may change for many reasons: evaporation from standing water, vegetative transpiration (dependent upon available water storage for the plant and incident solar radiation), condensation (cloud/fog or dew formation), moisture convergence, and moisture advection. Although all of these factors could contribute to diurnal changes at any one place and time, this study does not attempt to identify the principle causes of each change.

Table 7.2: Average peak time of day for precipitable water in each zone for each month and year. Multiple times are given when differences between times were difficult to distinguish, for example, less than 0.4 mm difference.

	Zone 1	Zone 2	Zone 3	Zone 4	Zone 5	Zone 6	Zone 7
June 1988	21-24Z	15Z	18Z	18-24Z	18Z	18Z	18Z
October 1988	15Z	15Z	15Z	21Z	15-18Z	15Z	12Z
June 1995	21Z	15-18Z	24Z	24Z	18Z	18Z	18Z
October 1995	15Z	15Z	15-18Z	15Z	15Z	12Z	15Z

Overall, water vapor peaks during the day between 15Z and 21Z, representing local times of approximately 12:00 noon through 7:00 pm. This is expected since the afternoon is the time of day with greatest temperature, solar radiation, evapotranspiration, trade winds (due to thermal differences among the ocean and other land cover

types), and latent heat flux (convective activity.) Wu et al. (2003) found a water vapor peak of 17:00 local time and a minimum at 06:00 local time when studying the tropical region of Sumatra Island.

Differences between 1988 and 1995 were minimal. However, there existed consistent differences between June and October. In general, for all zones, precipitable water peaked earlier in October than in June, usually by one three-hour time step. Zone 1 is unique as water vapor peaks about six hours earlier in October than June. This could be due to the increased amount of water on the ground and solar radiation (higher sun angle) earlier in the day in October (beginning of wet season) than in June, causing earlier evapotranspiration and advection, and therefore convective activity, condensing much of the water vapor out for lower precipitable water values later in the afternoon.

Most zones peaked near the 15Z-18Z time on average. Zone 2, in the heart of the Amazon Rainforest, remained relatively constant with a 15Z peak time for all months, the earliest of all the zones. Zone 4, completely outside the rainforest region to the east, peaked around 21Z, the latest of all the zones, except in October 1995 when it peaked at 15Z. October 1995 had the earliest peak times across the zones and highest precipitable water amounts.

Figures 7.10 through 7.13 show graphs of the total valid number of retrievals within each zone for each time of day. Invalid retrievals are most often caused by clouds, where the percentage of pixels within each 5x5 retrieval window (UPX) is less than 50%. The number of valid retrievals reflects the atmospheric conditions at the time of retrieval. Due to the lower spatial resolution of GOES-7 VAS, the maximum number of retrievals within the zones for 1988 is between 210 and 290, dependent upon distance from GOES satellite nadir location of 75° West, whereas for 1995 it is between 800 and 1200. As would be expected, the number of valid retrievals for zones 1 and 2 were much less than all other zones. There exists a noticeable difference in the number of valid retrievals throughout the day, although a distinct pattern cannot be determined. Data for 21Z in October 1988 and for 24Z in June 1995 are blank since no GOES imagery were available to attempt retrievals.

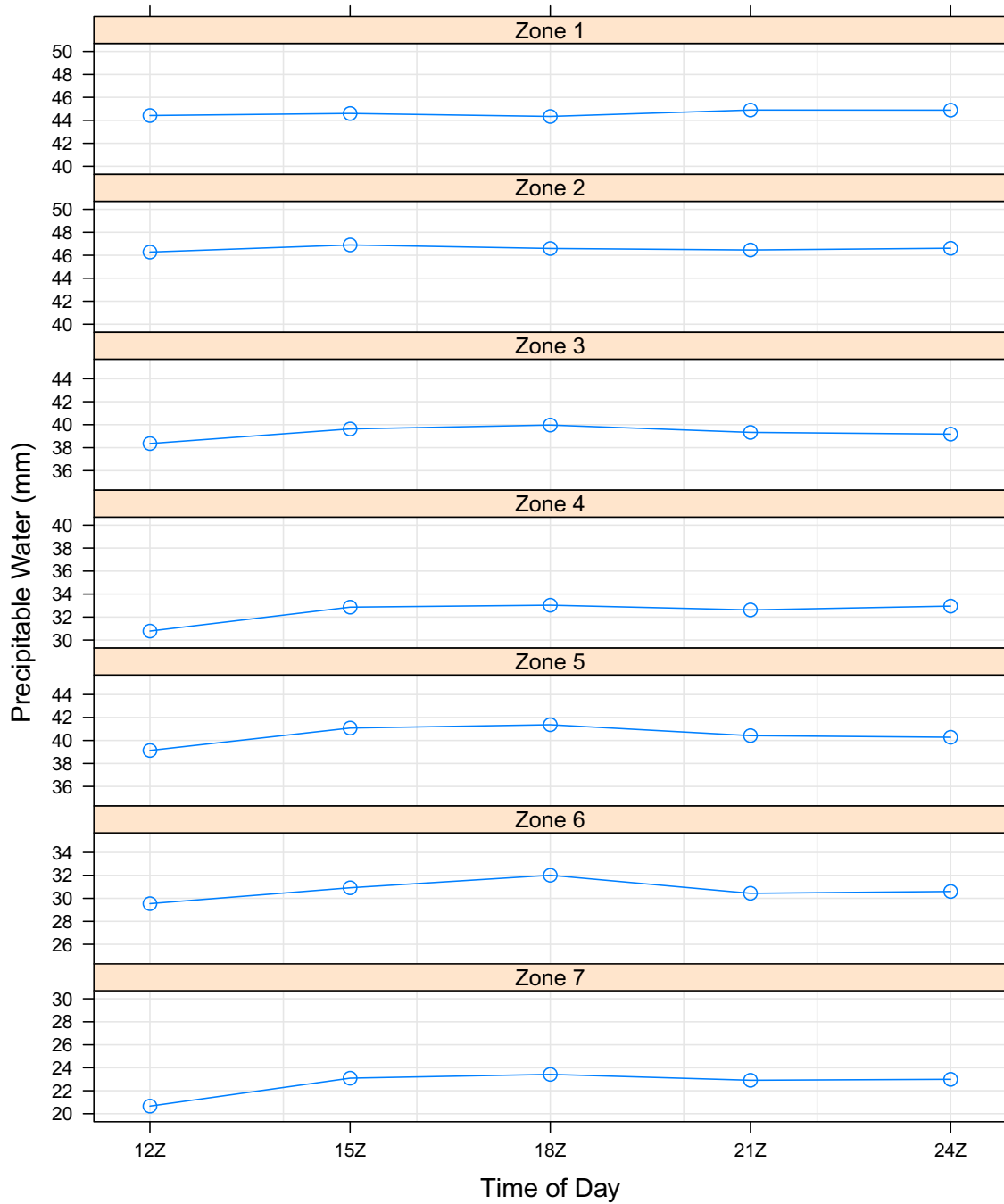


Figure 7.10: Monthly 3-hourly mean PSW-derived precipitable water in each zone for June 1988. Daylight hours only included, from 12Z through 24Z.

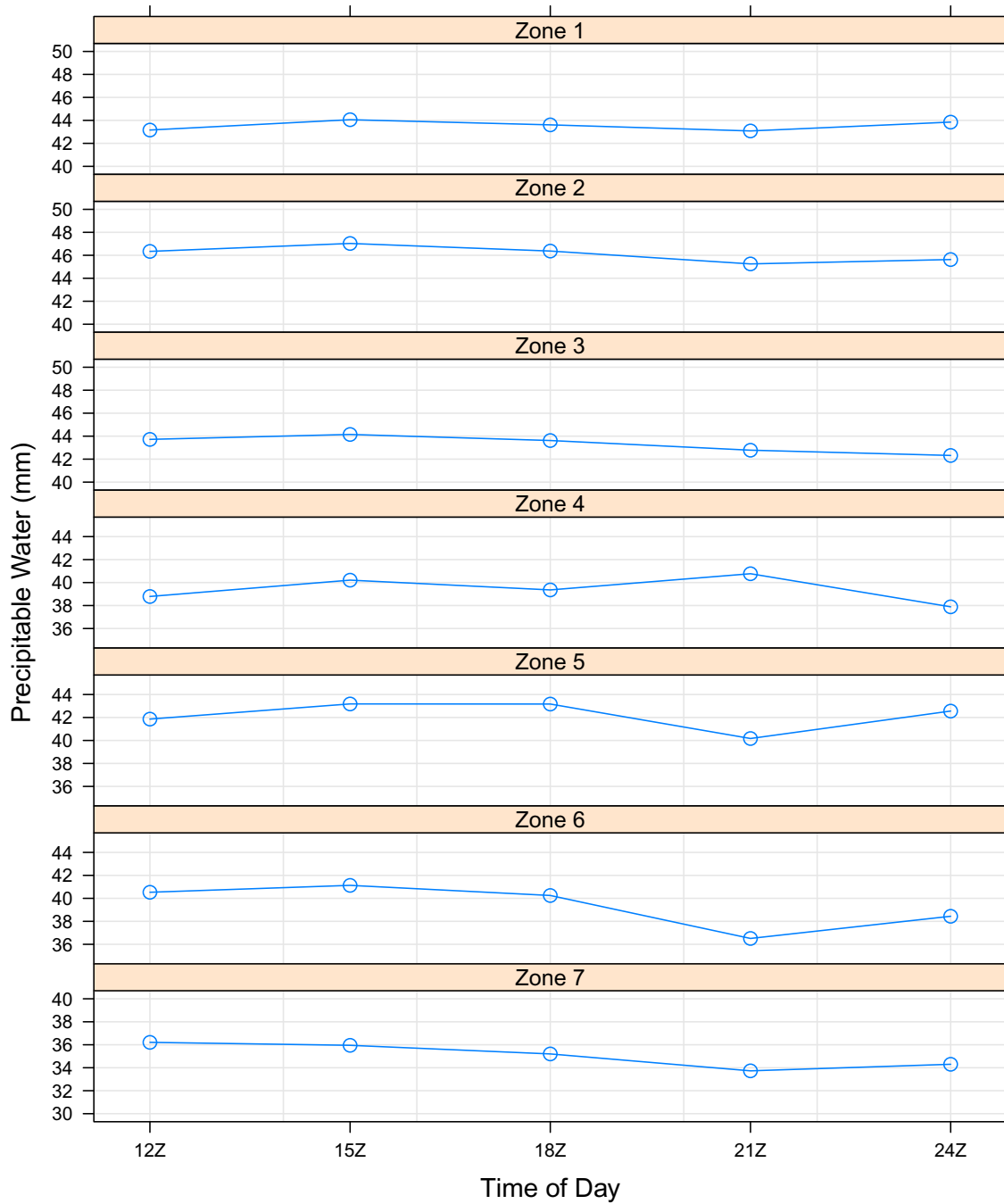


Figure 7.11: Monthly 3-hourly mean PSW-derived precipitable water in each zone for October 1988. Daylight hours only included, from 12Z through 24Z.

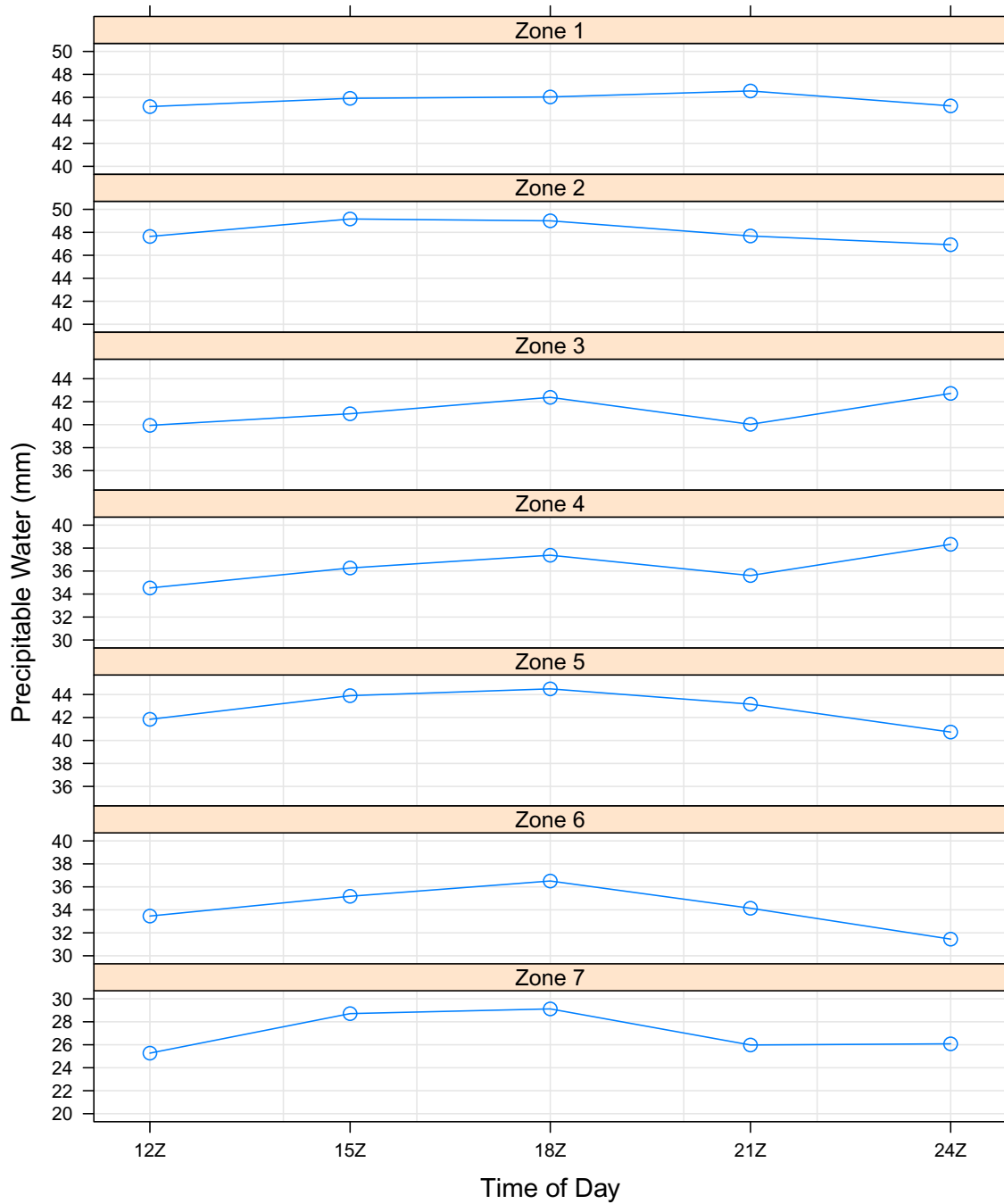


Figure 7.12: Monthly 3-hourly mean PSW-derived precipitable water in each zone for June 1995. Daylight hours only included, from 12Z through 24Z.

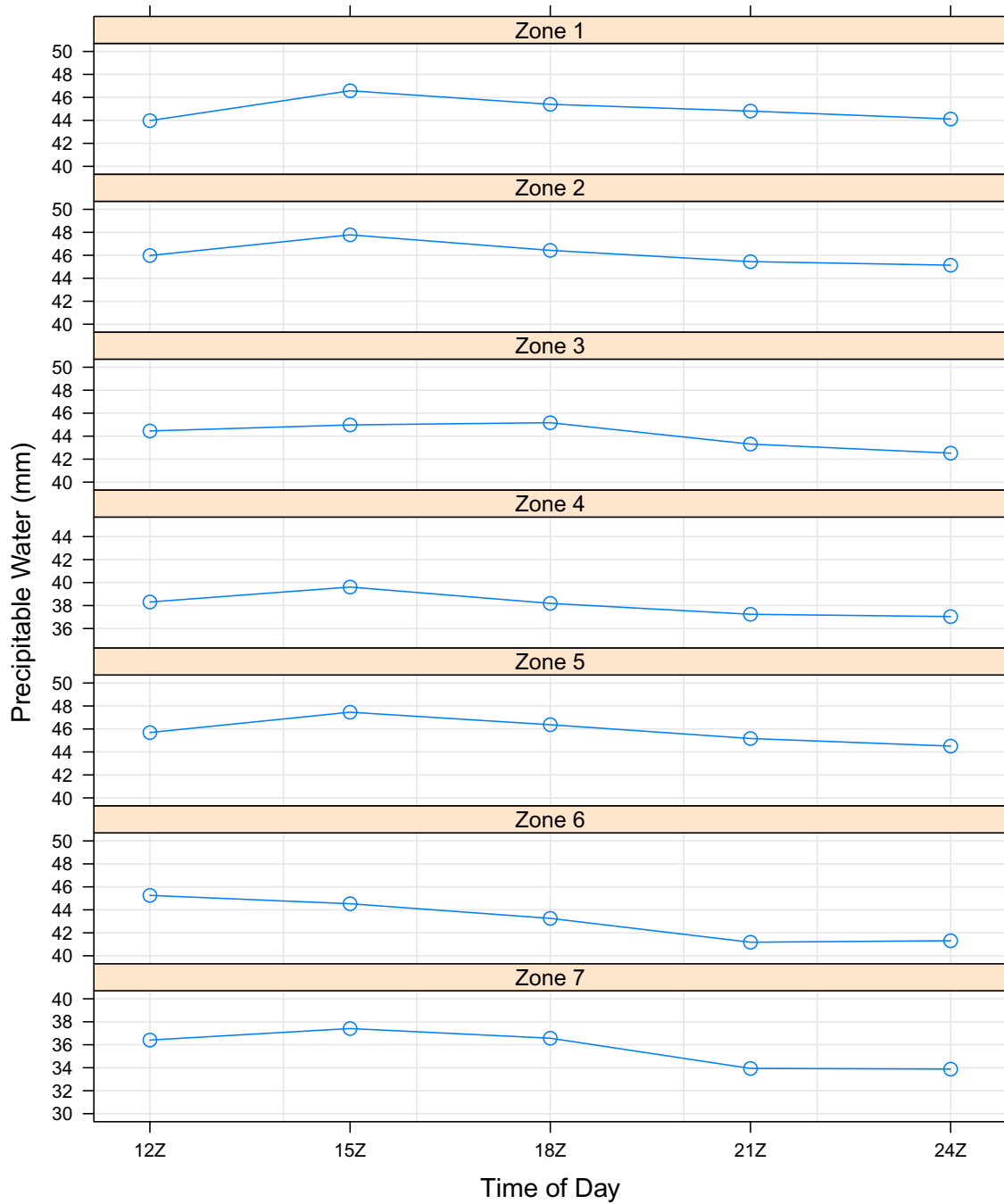


Figure 7.13: Monthly 3-hourly mean PSW-derived precipitable water in each zone for October 1995. Daylight hours only included, from 12Z through 24Z.

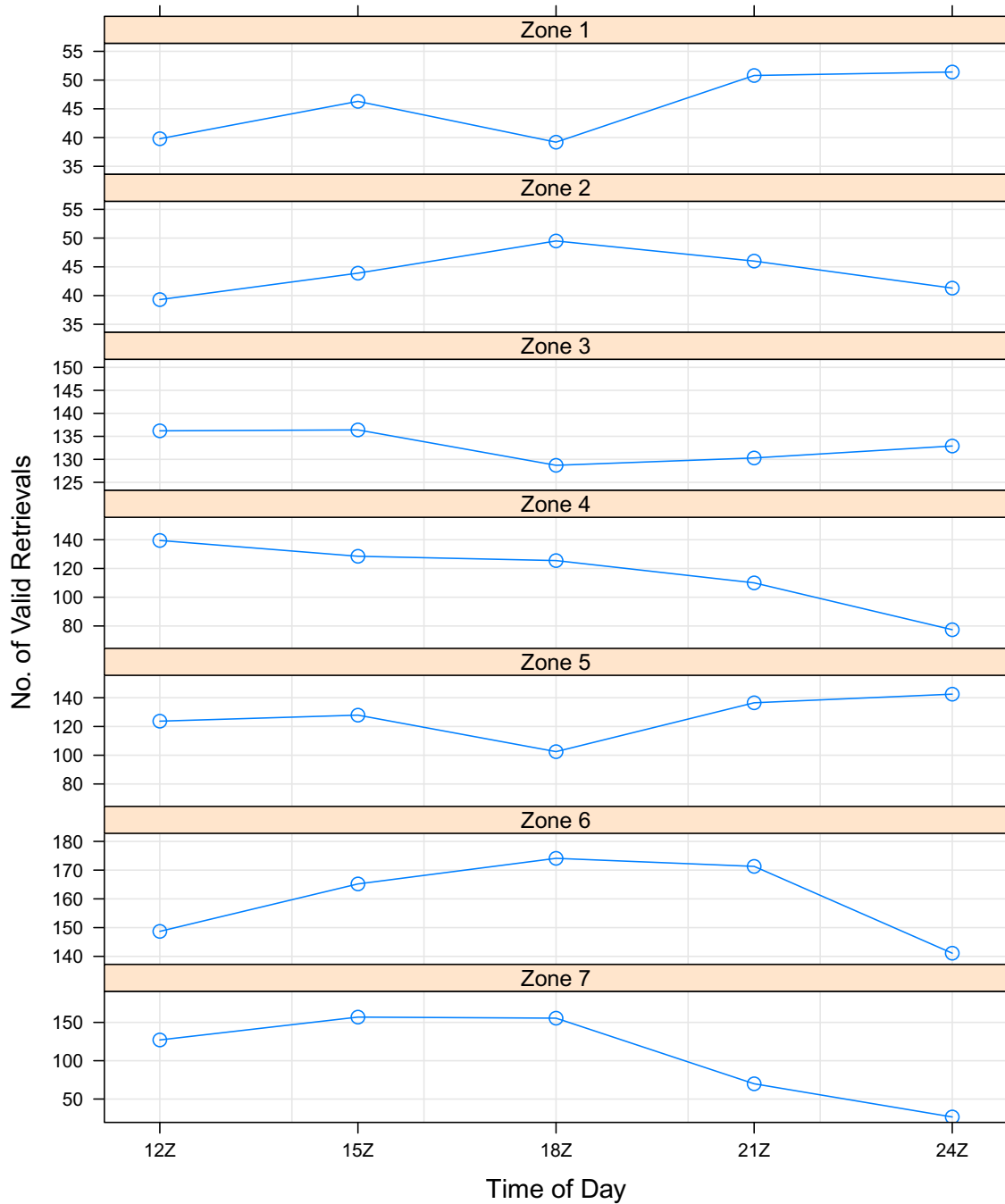


Figure 7.14: Monthly 3-hourly mean number of valid retrievals in each zone for June 1988. An attempted retrieval is considered valid if it passed all tests as described in section 5.4.

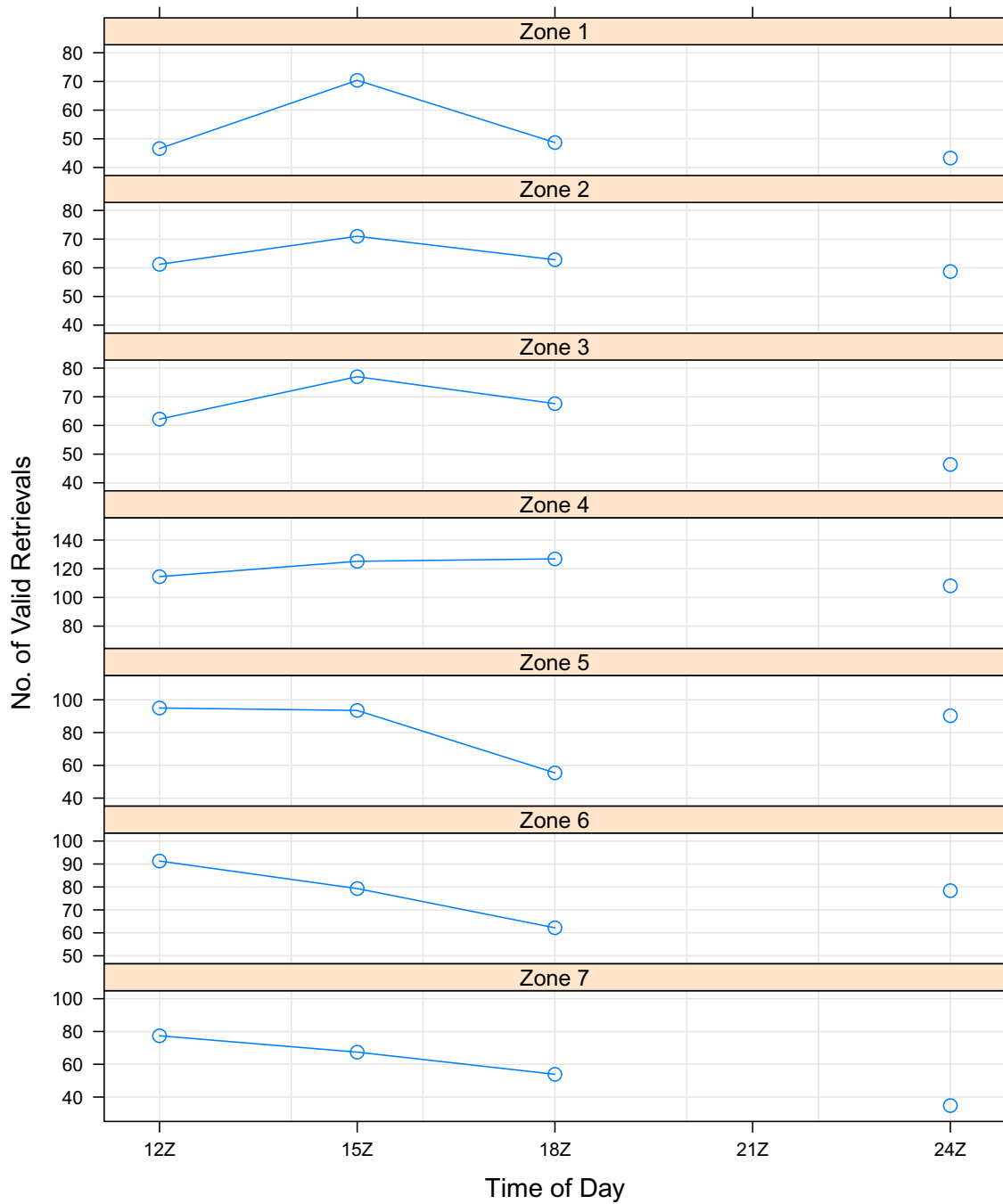


Figure 7.15: Monthly 3-hourly mean number of valid retrievals in each zone for October 1988. An attempted retrieval is considered valid if it passed all tests as described in section 5.4. GOES imagery not available for 21Z in October 1988.

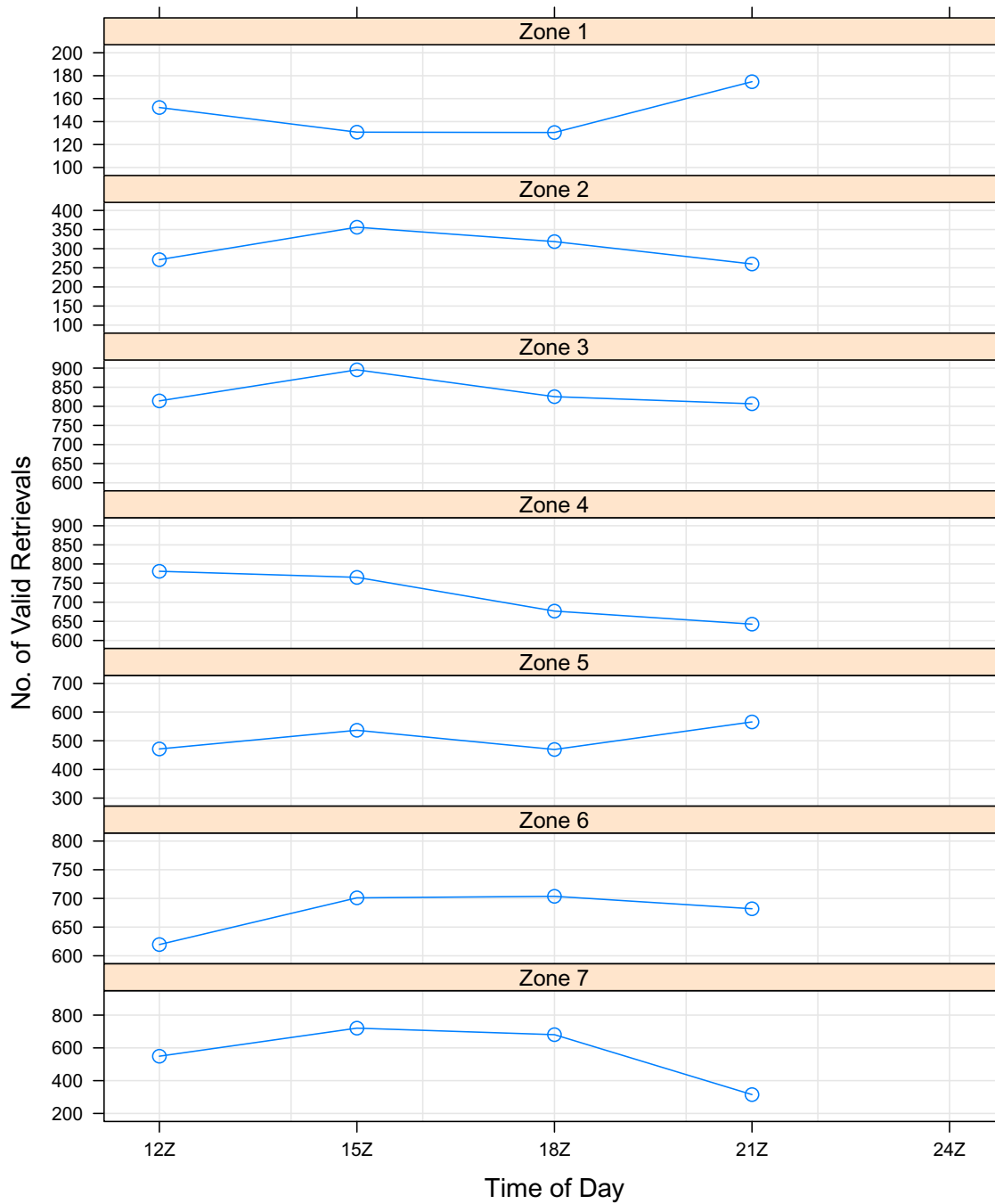


Figure 7.16: Monthly 3-hourly mean number of valid retrievals in each zone for June 1995. An attempted retrieval is considered valid if it passed all tests as described in section 5.4. GOES imagery not available for 24Z in June 1995.

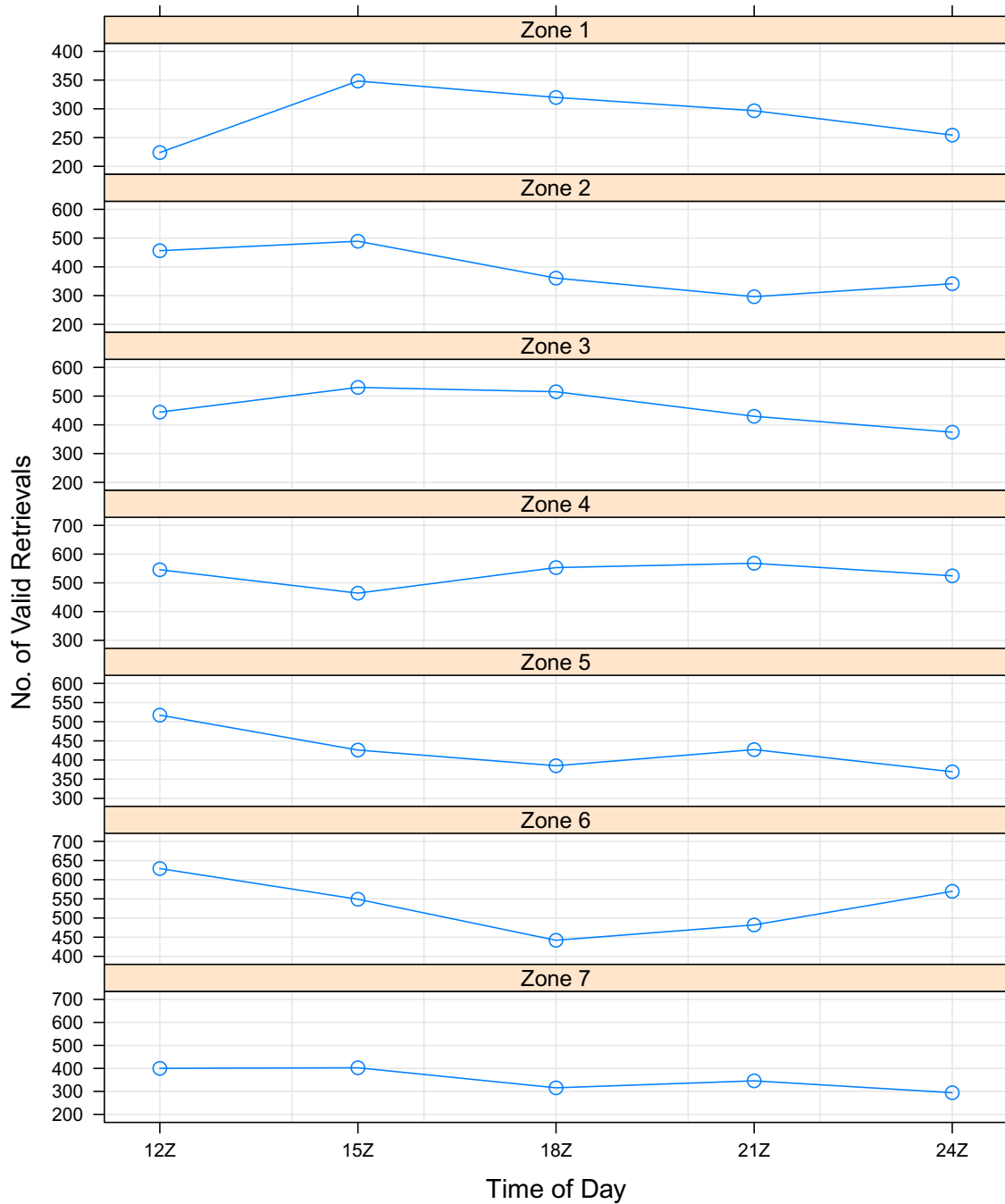


Figure 7.17: Monthly 3-hourly mean number of valid retrievals in each zone for October 1995. An attempted retrieval is considered valid if it passed all tests as described in section 5.4.

7.3.2 Diurnal Range Variations

The diurnal range of precipitable water was calculated for each day within each zone for each month. This was computed on a grid cell by cell basis as the maximum value for that cell at any time during the day minus the minimum value at any time during the day. Monthly means were also computed by simple averaging of the the daily diurnal range grids on a cell by cell basis. Table 7.3 shows the mean diurnal range of precipitable water within each zone for each month. Table 7.4 shows the same data as a percentage of daily mean precipitable water, essentially dividing table 7.3 by table 7.1. Additionally, figure 7.18 maps the monthly mean diurnal range for each month and figures 7.19 through 7.22 graphs the daily values from which the monthly means were calculated.

Table 7.3: Monthly mean diurnal range of PSW-derived precipitable water in each zone for each month and year. Calculation based on daylight precipitable water fields only, from 12Z through 24Z. All data values in in mm.

	Zone 1	Zone 2	Zone 3	Zone 4	Zone 5	Zone 6	Zone 7
June 1988	2.3	2.7	5.5	6.5	4.8	5.3	5.7
October 1988	3.5	4.3	3.8	6.5	5.4	6.7	5.4
June 1995	3.5	4.3	7.1	7.2	6.7	7.0	6.4
October 1995	6.7	6.4	6.1	8.7	7.5	10.1	8.8

Table 7.4: Monthly mean diurnal range of PSW-derived precipitable water in each zone for each month and year as percentage of zone mean.

	Zone 1	Zone 2	Zone 3	Zone 4	Zone 5	Zone 6	Zone 7
June 1988	4.97	5.87	14.45	20.71	11.79	17.56	25.59
October 1988	7.92	9.18	8.75	17.17	19.92	17.23	15.69
June 1995	7.63	8.85	17.75	20.37	15.66	21.05	24.25
October 1995	14.74	13.75	14.00	23.97	16.23	23.67	25.33

Diurnal range values are from 5% to 25% of the mean throughout the region. The smallest diurnal range throughout all months can be found in the northwest region. This region consistently maintains the largest amounts of precipitable water and least variability throughout the month. Each month also shows a slight path or channel of minimum diurnal range running from northwest to southeast through the basin. The existence of the channel is because a region of high diurnal range peaks in the northeast, likely due to advection from the trade winds, changing between seas breezes and land breezes. This channel is most pronounced in October 1988. High values of diurnal range are also found in a parallel pattern shifted to the southwest, just eastward of the Andes Mountains.

The analysis zones tend to fall into two groups. Zones 1 and 2 have the smallest diurnal range in magnitude and percent of mean. October diurnal ranges are greater in these zones than in June. Zones 4 through 7 have larger values of diurnal range, with all values for all months greater than 17% of the mean (except one: zone 5 in June 1988.) These areas have mixed land cover types and higher elevations, which typically show effects of varying incident solar radiation through the day. Zone 3 falls in the middle, siding with zones 1-2 in October and zones 4-7 in June. As stated in previous sections, zone 3 tends to mimic the behavior of the northwest zone 1 and in many cases, especially in October when the water vapor is high. For just about all zones, as with total amount of precipitable water, diurnal ranges during 1995 are higher than during 1988.

Figures 7.19 through 7.22 also include the daily diurnal range as shown in the Reanalysis model data. As would be expected, the PSW technique displays larger diurnal ranges than the Reanalysis. As with comparing the daily means to the NVAP data, the PSW-derived daily diurnal ranges match the model data very well for zones 1 and 2. All of the other zones exhibit short periods (few days) with significant differences in the ranges. These differences can be seen in multiple adjacent zones. It is likely that the Reanalysis model data, a smoothed data at 2.5° spatial resolution, does not properly capture diurnal heating, surface elevations, and afternoon convective activity

resulting in significant differences in atmospheric moisture. The Reanalysis model is forced by radiosonde observations for upper-air data, which unfortunately within the Amazon are launched at 12Z and 24Z, missing the peak afternoon activity. It could also be the case that the PSW-derived and Reanalysis values match during times of persistent (non-convective) cloud cover when PSW retrievals could not take place and the output grids default to the Reanalysis estimates.

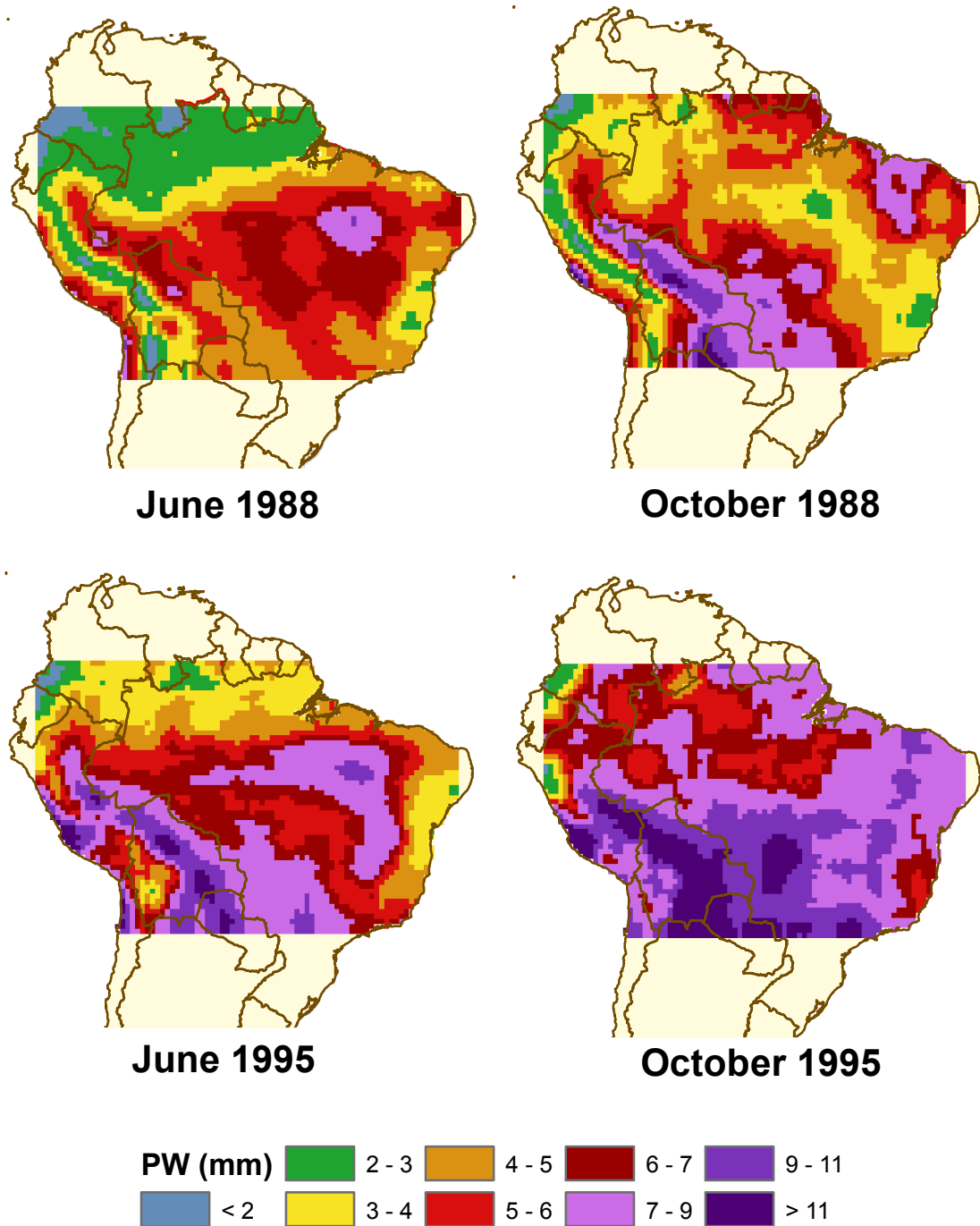


Figure 7.18: Monthly mean fields of the diurnal range of PSW-derived precipitable water for June and October, 1988 and 1995. Calculation based on daylight precipitable water fields only, from 12Z through 24Z.

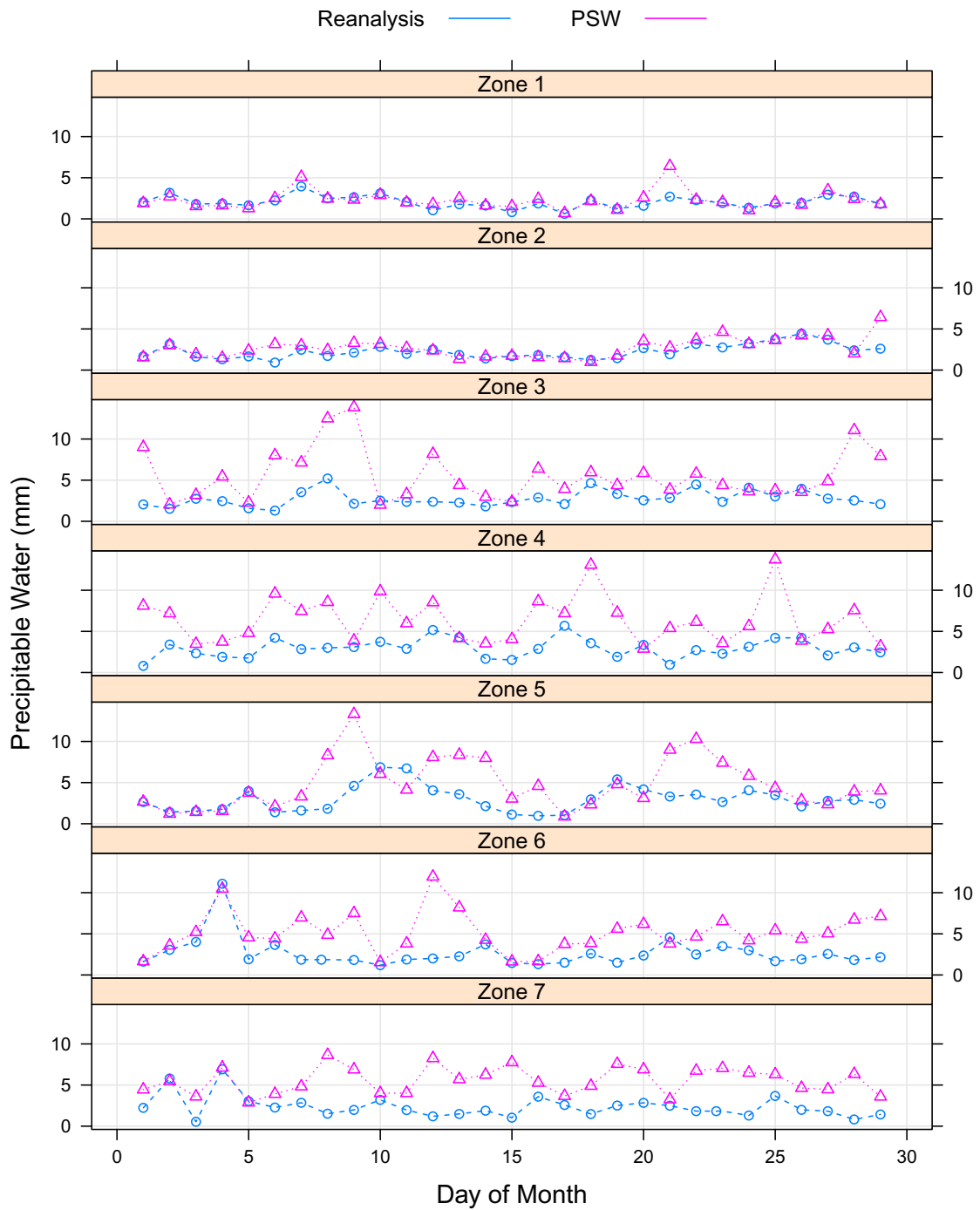


Figure 7.19: Daily mean diurnal range of PSW-derived precipitable water in each zone for June 1988. Pink triangles represent PSW-derived data; blue circles represent data from the Reanalysis model.

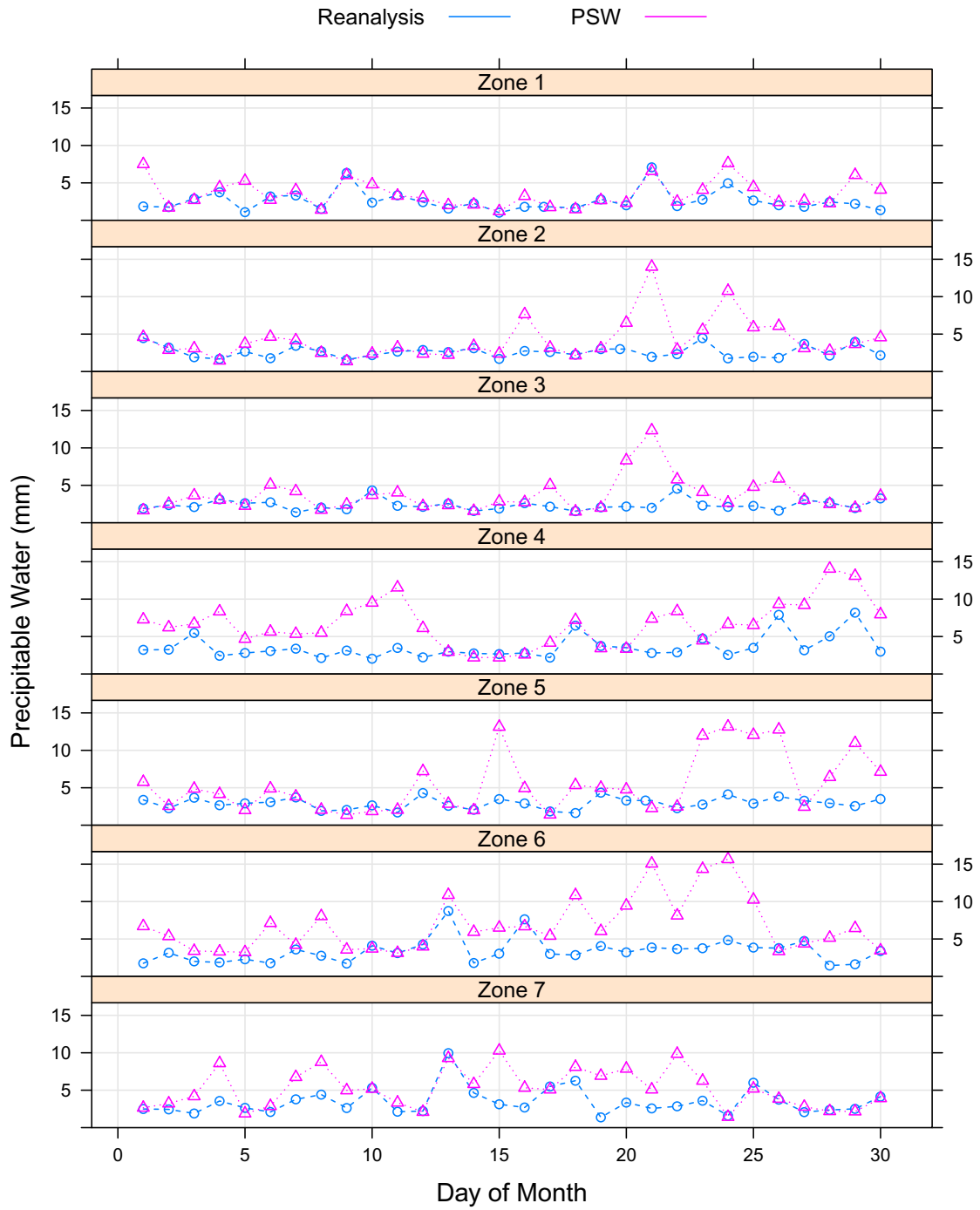


Figure 7.20: Daily mean diurnal range of PSW-derived precipitable water in each zone for October 1988. Pink triangles represent PSW-derived data; blue circles represent data from the Reanalysis model.

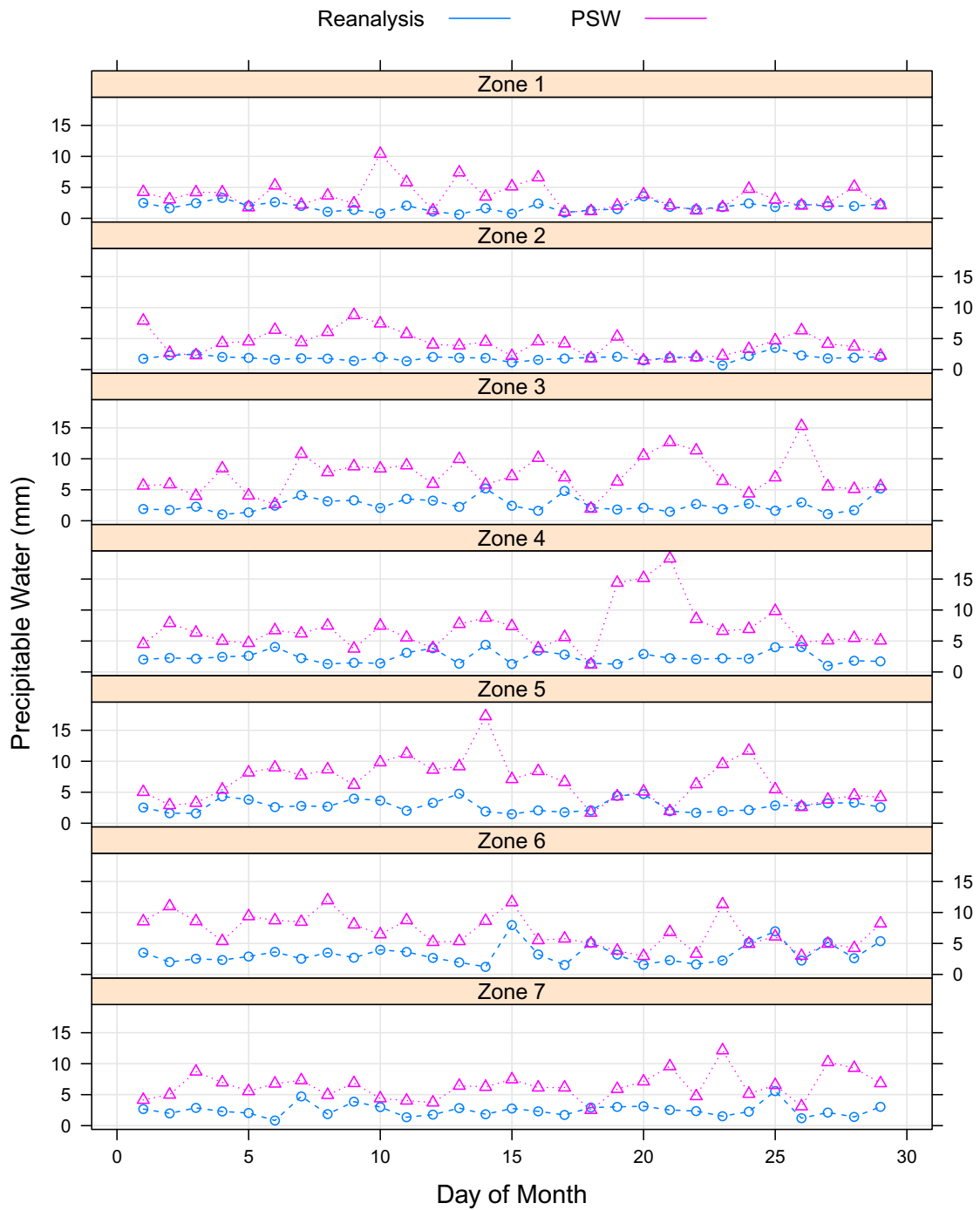


Figure 7.21: Daily mean diurnal range of PSW-derived precipitable water in each zone for June 1995. Pink triangles represent PSW-derived data; blue circles represent data from the Reanalysis model.

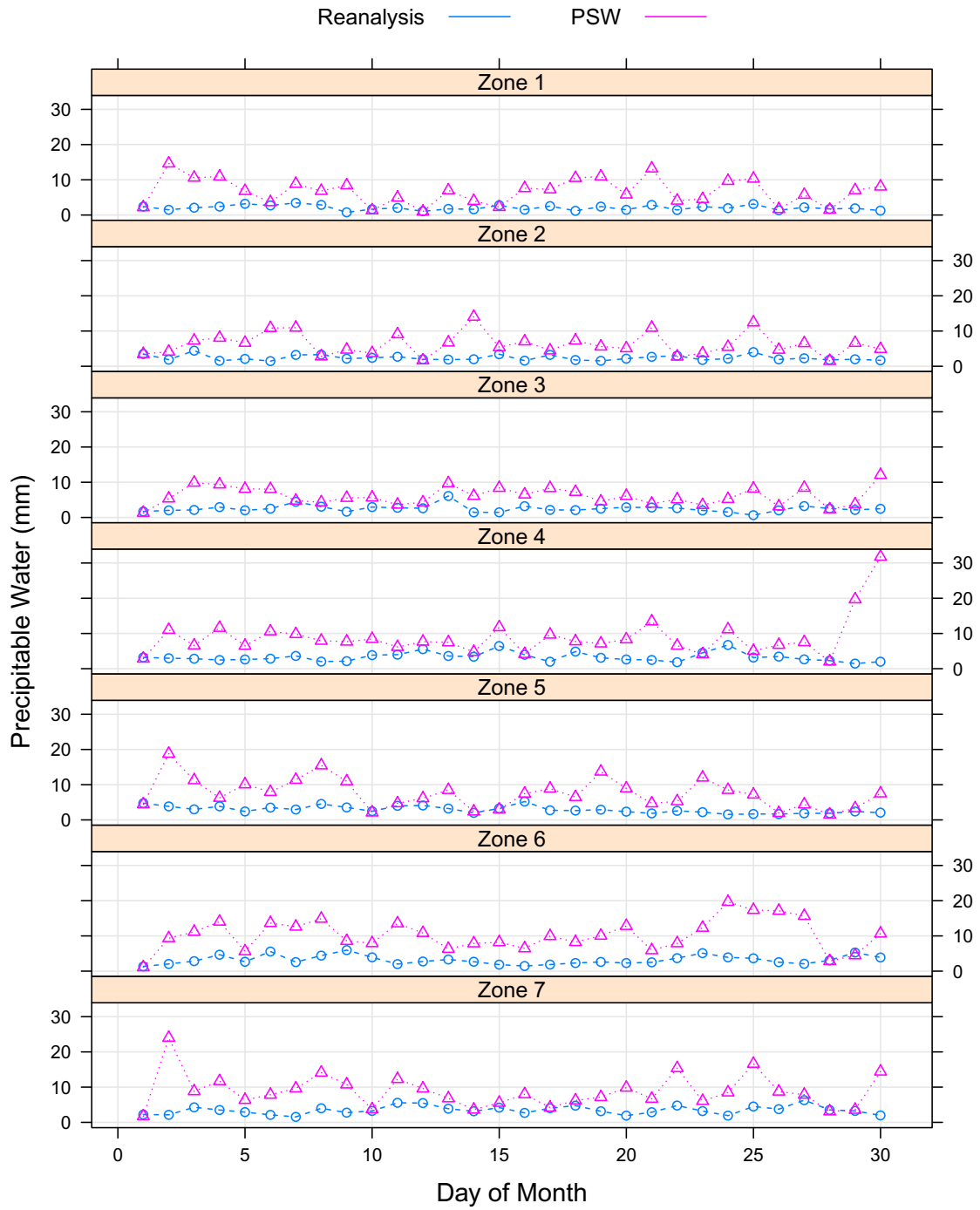


Figure 7.22: Daily mean diurnal range of PSW-derived precipitable water in each zone for October 1995. Pink triangles represent PSW-derived data; blue circles represent data from the Reanalysis model.

Chapter 8

CONCLUSION

This chapter summarizes the impetus and methodology of the current study and highlight significant findings. It concludes with a short discussion of ideas for future research that can build off the current study.

8.1 Summary and Discussion

The primary objective of this study is to apply a remote sensing technique that can measure atmospheric water vapor in regions with sparse in situ observational data to the Amazon River Basin region. Secondary objectives are to capture and analyze the diurnal signal and mesoscale spatial distribution of atmospheric total columnar precipitable water in the Amazon region for the months of June and October, just before and after the dry season.

The Amazon Basin is the world's largest hydrologic system, covering over 6.0 million km², containing over half of the world's rainforests and approximately 20% of all the fresh water that flows on the Earth. Precipitation is significant in the region, averaging approximately 2200 mm yr⁻¹ across the basin with areas in the northwest (thick rainforests) averaging 3600 mm yr⁻¹. The Amazon River itself is considered the world's largest, longest, and deepest river. The region's hydrologic cycle is a complex mixture of precipitation, evapotranspiration, soil moisture, and atmospheric water vapor and undergoes significant changes seasonally, due to the north-south movement of the ITCZ causing large-scale changes in moisture advection leading to pronounced wet and dry seasons throughout most of the region, as well as diurnally, due to high amounts of vegetative transpiration and changing sun angle causing afternoon convective storms.

Land cover also can play a significant role in the hydrologic cycle and climate within the Amazon Basin. The wide expanses of rainforests with broad deciduous leaves transpire large amounts of water vapor throughout the year, including during the dry season due to their deep rooting depth and the persistent water availability. Unfortunately, a significant amount of deforestation and land degradation has taken place in the region to make way for infrastructure development, sale of timber (logging), the establishment of cattle ranches, the development of commercial and subsistence agricultural farm fields (mostly soybean), and many other factors. Although rates of deforestation have continued to decrease since the approximately 27,000 km² of forest lost in 2004 to less than 5,000 km² lost in 2012, activities that degrade the forest cover commonly take place in and around the Amazon Basin (and is partly dependent upon the global economy and Brazil's role therein) and future consequences from past activities are yet unknown.

Land that has been changed to savannah, shrubland or farm fields contains much less vegetation than the native rainforests, resulting in less transpiration, less surface roughness, higher surface albedo and ambient temperatures, leading to a modification in the local circulation and convective activity cycles. The methods of deforestation and land degradation also have effects, such as large amounts of carbon released to the atmosphere through biomass burning, enhancing the greenhouse effect by increased atmospheric absorption. Changes in the water balance of the immense Amazon can significantly affect regional and global circulation and moisture patterns. Although large-scale and mesoscale GCM studies provide insight into the regional effects of land use changes on the environment, the actual long-term changes to precipitation, temperature, and components of the hydrologic cycle are extremely complex. Much more research is needed to assess the environmental effects of the activities that have been taking place in the Amazon, such as developing finer resolution models, improving diurnal processes in the models, a better understanding of the seasonal soil moisture capacity, sensitivity to the size, shape, and connectivity of land degradation, a better understanding of the differences of secondary vs primary growth forests, more analysis

on long-term global climate trends. Therefore, monitoring components of the hydrologic cycle in this rapidly changing, albeit influential, region remains quite critical.

However, monitoring of climatologic and hydrologic variables are difficult in the Amazon. Wide expanses of remote, difficult to manage terrain, especially during the wet season, make it difficult to establish and maintain operational, continuously monitoring stations. There have been numerous field campaigns (several are listed in table 2.2) that intensely studied selected aspects of the climate, although these on typically short time scales, small spatial scales, and a focused set of observations. Marengo (2004) echoes this sentiment, stating that in the Amazon Basin, hydrometeorological and upper-air variables are fragmentary: the sparse observations are often inaccurate, irregularly spaced, and there are very few long-term climate records. For example, radiosondes used for regular monitoring in the Amazon are launched at 12Z and 24Z, corresponding to 8:00/9:00 am and 8:00/9:00 pm local time, respectively, completely missing the peak times of water vapor and afternoon convective activity. It is therefore common to integrate the sparse observations with model reanalyses to generate spatially or temporally consistent fields, particularly over longer time periods. And although models do a good job depicting generalized behavior of the climate system, data inconsistencies exist when inaccurate observations are used to force them, and often have difficulties in capturing small time and spatial scale phenomena. Estimating climate trends from these models may not be reliable as once previously thought (WMO, 2007).

Spaceborne remote sensing is an ideal technology for monitoring environmental variables in the Amazon Basin. Satellites provide actual measurements, as opposed to models, and can be calibrated to more traditional land surface or upper-air observations. Since they are completely automated, most remote sensing algorithms can be corrected in real-time or reprocessed in batch mode afterward. Satellites can record the conditions of the wide expanses of the Amazon either continuously (3-hourly or better from geosynchronous satellites) or with high spatial resolution and less temporal resolution (daily or weekly from polar orbiting satellites.) Monitoring variables such

as water vapor, precipitation and temperature that change throughout the day would benefit from the geosynchronous satellites whereas variables such as land cover or vegetation health would be more appropriate from polar orbiters. In particular, based on the ground-breaking work of Skole and Tucker (1993) with Landsat data, the officially accepted method of monitoring deforestation in the Amazon is through remote sensing. The PRODES program incorporates imagery from several satellites once per year (after the wet season but before the start of the dry season to minimize cloud coverage) and calculates the land cover changes from the previous year. Additionally, since satellite data have been used for operational meteorologic (including water vapor as described in section 3.1) and land surface monitoring since the 1970s, they are now being used for deducing long-term climate change trends.

This study utilized the Physical Split Window (PSW) technique as applied to GOES imagery for the months of June and October, 1988 and 1995. Originally developed by Jedlovec (1987), it was optimized for the GOES satellite by Guillory et al. (1993). Data from the GOES satellite were chosen to simultaneously capture the spatial distribution and diurnal behavior of water vapor throughout the entire region. The GOES-East satellite also sits directly above the 75°W longitudinal meridian, located within the region. The years 1988 and 1995 were chosen because of data availability and to incorporate two separate years in the study. The months of June and October bookend the peak dry season and have fewer issues with cloud contamination as compared with most other months. Haze and smoke are common due to biomass burning in the middle of the dry season, and clouds due to afternoon convection and advection from the easterly trade winds are dominant in the rainy season.

The PSW technique is a physically based approach that estimates total columnar precipitable and land surface temperature simultaneously. It has been optimized for use with the thermal infrared channels on the VAS and Imager sensors aboard the GOES satellites as well as for sensors aboard the Chinese Fengyun geostationary satellites. Also, being a physically-based technique, it does not depend on statistical procedures to relate a derived quantity, such as water vapor. The PSW method works by first

starting with an estimated atmospheric profile of temperature and moisture, which will also give an estimated land surface temperature and precipitable water. For this study, these first guess profiles are extracted from the 6-hourly, $2.5^\circ \times 2.5^\circ$ NCEP/NCAR Reanalysis model. As well, an atmospheric radiation program, called SIMRAD, is run to calculate a simulated brightness temperature as would be sensed by the satellite under the assumed atmospheric profile. Based on the actual brightness temperatures sensed by the satellite sensor in the two split window thermal infrared channels, it is assumed the differences are caused by differences in the actual land surface temperature and precipitable water from the estimated values. Solving the equations for the two unknowns (perturbations of land surface temperature and precipitable water) using data from two thermal infrared channels, gives the final retrieved value.

Precipitable water retrievals are performed throughout each GOES image, at 3-hourly intervals from 12Z through 24Z for each month, by averaging the brightness temperatures measured in the neighboring 5×5 pixel window. If more than 50% of the pixels are determined to be clouds (based on a simple temperature threshold of 290 K), a retrieval could not be performed. Although the chosen months had relatively limited contamination from clouds or smoke, the Amazon is still a region of significant cloud cover year round and precipitable water could not be retrieved at many locations. To fill in the missing gaps, all valid retrievals and cloud percentage (of the 5×5 window) were interpolated to a $0.5^\circ \times 0.5^\circ$ grid throughout the region. For each grid point, if the cloud percentage was 80% or greater, the PSW-derived precipitable water was used, and if not, the first guess precipitable water was determined by the Reanalysis model. Lastly, a 5×5 moving window filter was applied to the entire region to smooth out any discontinuities.

An analysis was performed on the PSW-derived precipitable water field and also compared against the NASA Water Vapor (NVAP) dataset and radiosonde observations. Some interesting findings are listed below:

- There are very few radiosondes launched in this region and model validation is

difficult due to lack of quality data and neither 12Z or 24Z launch times are ideal for PSW retrievals. Comparing PSW-derived precipitable water to precipitable water computed from the few available radiosondes, the average $MBE = 5.5$ mm, average $MAE = 8.0$ mm, and $MAE/\mu_x = 24\%$ of the mean. Generally, data from 24Z (8:00/9:00 pm local time) performed better, with errors of 2.9 mm, 7.0 mm, 19%, respectively, than data from 0Z (8:00/9:00 am local time), with errors of 6.0 mm, 8.1 mm, 25%, respectively.

- Comparisons made for 1988 using the GOES-7 VAS sensor ($MBE = 2.0$ mm, $MAE = 6.2$ mm, $MAE/\mu_x = 19\%$) performed better than those for 1995 using the GOES-8 Imager sensor (9.1 mm, 9.8 mm, 29%). Likewise, comparisons made for June (2.3 mm, 6.1 mm, 18%) performed better than those for October (7.1 mm, 8.9 mm, 27%).
- Precipitable water is higher in October than in June throughout the Amazon Basin, which mimics that of precipitation. In particular, from analyzing the monthly NVAP data, precipitable water tends to peak about a month earlier than precipitation, supporting the argument that the start of the wet season is more appropriately defined as an increase in water vapor rather than rainfall.
- Precipitable water is higher and significantly more stable in the central and north-west portion of the Amazon, which also mimics the behavior of precipitation. Average values in this region (analysis zones 1 and 2) for both months June and October, in both years 1988 and 1995, are very similar, approximately 45 mm, with very little variation day to day, or hour-to-hour throughout the day.
- Precipitable water tends to correlate with land cover type, with the largest values over thick evergreen deciduous forests and lesser amounts and higher variability over agricultural fields and savannah.
- The diurnal range of precipitable water tends to inversely follow the land cover, with the smallest ranges of 2 mm to 4 mm over thick evergreen deciduous forests

(analysis zones 1 and 2), with larger diurnal ranges of 4 mm to 10 mm over agricultural fields and savannah.

- Atmospheric water vapor peaks during the day between 15Z and 21Z, representing local times of between 12:00 noon through 7:00 pm. Most zones peaked near 18Z. For all zones, on average, precipitable water peaked earlier in October than in June, usually by one three-hour time step, although zone 1 peaked six hours earlier.

As well, a few lessons were learned along the way:

- Radiosondes launched at 12Z (morning) and 24Z (evening) do not capture the diurnal cycle nor the afternoon peak of precipitable water. Analyses that utilize these observational data alone are likely to underestimate the amount of water vapor in the Amazon hydrologic cycle.
- Using a remote sensing algorithm on imagery from the GOES geostationary satellite covers the wide expanse of the Amazon in a similar fashion as a numerical model, but improves upon a model by more accurately capturing diurnal processes, resolving a higher spatial resolution, and not being restricted to calibration from poorly timed radiosonde launches.
- The method used in this study to fill-in missing data by interpolating valid data points and replacing them with first guess estimates if cloud coverage reaches a threshold (20%) seems to produce smooth fields of precipitable water in both time and space. This may be a more appropriate method to use in data sparse regions rather than leaving large data gaps, as in both NVAP and observational data. However, an improved cloud masking algorithm needs to be implemented.
- Clouds are a problem. Although thermal infrared radiation is sensitive to atmospheric water vapor, it cannot penetrate through clouds. Smoke, haze, cloud fringes may be present but undetected by a simple cloud threshold test, and can

significantly alter the brightness temperature derived from the radiation received at the satellite, therefore negatively influencing estimates of precipitable water. The same can be said for the presence of cirrus clouds, which may go undetected but have a lower emissivity in the thermal infrared wavelengths (Anthony Guillory, personal communication, 1999.)

8.2 Further Research

This study brought to light several modifications that may improve the performance of the PSW technique over regions such as the Amazon Basin. Future work may include the following:

- Performance of the PSW technique can be improved by implementing a spatially varying emissivity module. A drawback of the current code implementation is that a single emissivity must be used for each channel for the entire scene. GOES images of the Amazon region include numerous types of land cover, from the lush rainforests to shrublands to the Andes Mountains, where thermal emissivities can be different by 10% or more. Perhaps channel emissivity can be incorporated into the first guess estimates or read from a raster grid of the image.
- As mentioned earlier, a better cloud masking should be implemented. The current implementation uses a single temperature threshold. Although this values can be set for each run, a more statistical variance approach could be used to detect patterns or shape characteristics of clouds. As well, perhaps tests using a mixture of multi-band brightness temperatures vs land estimated surface temperature, or a set of hierarchal tests could be performed depending on the types of clouds expected (cirrus vs convective vs smoke/haze.)
- The PSW technique can be applied to other regions where GOES satellite imagery is available. Once configured, it is relatively easy to run and read the results within the McIDAS image processing software package. The simplicity of the

PSW technique allows for application to nearly any satellite sensor measuring in the thermal split window channels.

- Not only for support of studies involving the PSW-technique, it may be helpful for many research projects to develop an operational infrastructure for running a radiative transfer code. Although SIMRAD was used in the present study, other similar code packages exist, such as the Limited Area Mesoscale Prediction System (LAMPS), as used in Suggs et al. (1998).
- A much better measure of the PSW technique performance would compare retrievals against radiosonde-observed atmospheric profile data during the afternoon hours, instead of during times common to temperature inversions, such as the morning or late evening launches used in this study. Computing retrievals over areas with consistent land cover, with similar thermal emissivities in the split window channels, would also give a better measure of algorithm performance. This could be done by synchronizing imagery with proposed field campaigns, and plan upper-air flights with polar orbiting satellites passing overhead, if planning to optimize PSW for use with sensors aboard polar orbiters, such as MODIS.
- The diurnal behavior of water vapor in the Amazon should be further investigated. It could be a significant factor in the changing hydrologic cycle of the region. GPS techniques would be ideal for this purpose (as it could produce hourly data) and could be used as validation and calibration of remote sensing methods instead of radiosondes. A better understanding is needed of the relationship between diurnal variation and seasonal variations.
- A general approach needs to be developed on how to measure atmospheric water vapor during times of significant cloud cover, such as afternoon convective activity or nearly the entire wet season in the central and northwest Amazon. Thermal infrared techniques alone are not sufficient as they do not penetrate through clouds. Microwave techniques are possible but very difficult over land.

GPS stations are ideal, as they are ground based, but measure at a single point location and may be expensive or difficult to maintain. More radiosonde launches are also needed, especially near peak of precipitable water from 15 to 21Z. A combined approach will likely be necessary to give the most accurate results, with the least amount of missing data, and would aid greatly in better understanding the seasonality of atmospheric water vapor and its relationship with other components of the hydrologic cycle.

8.3 Conclusion

Overall, the remote sensing PSW technique applied to GOES imagery is a viable option for retrieving precipitable water in the Amazon Basin. The technique requires little a priori information, important for application in the Amazon, and can be modified to address some of the issues mentioned in the previous section. The method of replacing regions of missing data due to cloud contamination (some of these regions covering large areas) with precipitable water from the Reanalysis model produces smooth water vapor fields for analysis of the spatial distribution, which would not be possible from the PSW-derived retrievals alone. The GOES imagery provides a good balance between wide coverage and spatial resolution sufficient enough to capture the behavior of water vapor in the region. As well, GOES observations maintain a high enough temporal resolution to adequately capture water vapor diurnal processes. The results show a significant variation in the quantity and behavior of precipitable water in the Amazon, which is likely linked to the regional weather patterns and local land use changes, and demonstrate that more research on the hydrologic is needed in this complex and continuously changing region.

BIBLIOGRAPHY

- Adams, D. K., Fernandes, R. M. S., Maia, J. M. F., 2011. GNSS precipitable water vapor from an Amazonian rain forest flux tower. *Journal of Atmospheric and Oceanic Technology* 28, 1192–1198.
- Albert, J. S., Reis, R. E. (Eds.), 2011. *Historical Biogeography of Neotropical Freshwater Fishes*. University of California Press.
- Alishouse, J. C., Snyder, S. A., Vongsathorn, J., Ferraro, R. R., Sep. 1990. Determination of oceanic total precipitable water from the SSM/I. *IEEE Transactions on Geoscience and Remote Sensing* 28 (5), 811–816.
- Allan, R., 2007. Monitoring present day changes in water vapour and the radiative energy balance using satellite data, reanalyses and models. *Proceedings of the Joint 2007 EUMETSAT Meteorological Satellite Conference and the 15th Satellite Meteorology & Oceanography Conference of the American Meteorological Society*.
- Allende, G., Others, 2011. Soil erosion, land use and vegetation analysis of the Amazon Basin from a space-based rapid exploration platform - SELVA-RX: Satellite mission proposal. Tech. rep., Piranha Coporation and Technische Universitt Mnchen.
- Amaral, S., D’Alge, J. C. L., 2009. Spatial data availability and its implications for sustainable development of the Brazilian Amazon. *Earth Science Informatics* 2 (4), 193–203.
- Amenu, G. G., Kumar, P., February 2005. NVAP and reanalysis-2 global precipitable water products: Intercomparison and variability studies. *Bulletin of the American Meteorological Society* 86 (2), 245256.
- Anderson, L. O., Shimabukuro, Y. E., Defries, R. S., Morton, D., July 2005. Assessment of deforestation in near real time over the Brazilian Amazon using multitemporal fraction images derived from terra MODIS. *IEEE Geoscience and Remote Sensing Letters* 2 (3).
- Andreae, M. O., Artaxo, P., Crutzen, P. J., Lelieveld, J., March 1997. Science plan for the cooperative LBA airborne regional experiment (LBA-CLAIRE). Obtained from <http://lba.cptec.inpe.br/lba/eng/research/claire/claire1.htm> on June 25, 2011.

- Angell, J. K., 2003. Effect of exclusion of anomalous tropical stations on temperature trends from a 63-station radiosonde network, and comparison with other analyses. *Journal of Climate* 16, 2288–2295.
- Arrigo, K., July 2010. The role of satellite imagery in climate change research [ICESCAPE]. Obtained from <http://science.dodlive.mil/2010/07/09/the-role-of-satellite-imagery-in-climate-change-research-icescape/> on June 2, 2011.
- Avissar, R., Dias, P. L. S., Dias, M. A. F. S., Nobre, C., 2002. The large-scale biosphere-atmosphere experiment in Amazonia (LBA): Insights and future research needs. *Journal of Geophysical Research* 107 (8086), 6 pp.
- Avissar, R., Werth, D., 2005. Global hydroclimatological teleconnections resulting from tropical deforestation. *Journal of Hydrometeorology* 6, 134145.
- Bastable, H. G., Shuttleworth, W. J., Dallarosa, R. L. G., Fisch, G., Nobre, C. A., 1993. Observations of climate, albedo, and surface radiation over cleared and undisturbed Amazonian forest. *International Journal of Climatology* 13, 783–796.
- Bedka, S., Li, J., Feltz, W., Schreiner, A., Nelson, J., 2007. Evaluation of GOES-12 sounder single field of view and 3x3 retrievals of total precipitable water over the ARM SGP site. Proceedings of the Joint 2007 EUMETSAT Meteorological Satellite Conference and the 15th Satellite Meteorology & Oceanography Conference of the American Meteorological Society.
- Bengtsson, L., Hagemann, S., Hodges, K. I., June 2004. Can climate trends be calculated from reanalysis data? *Journal of Geophysical Research* 109 (D11).
- Betts, A. K., Fisch, G., von Randow, C., Dias, M. S., Cohen, J., da Silva, R., Fitzjarrald, D., 2009. Amazonia and Global Change. *Geophysical Monograph Series* 186. American Geophysical Union, Ch. The Amazonian Boundary Layer and Mesoscale Circulations, pp. 163–181, 576 pp., hardbound, ISBN 978-0-87590-476-4.
- Betts, A. K., Jakob, C., September 2002. Evaluation of the diurnal cycle of precipitation, surface thermodynamics, and surface fluxes in the ECMWF model using LBA data. *Journal of Geophysical Research* 107 (D20).
- Bevis, M., Businger, S., Chiswell, S., Herring, T. A., Anthes, R. A., Rocken, C., Ware, R. H., 1994. GPS meteorology: Mapping zenith wet delays onto precipitable water. *Journal of Applied Meteorology* 33, 379–386.
- Bevis, M., Businger, S., Herring, T. A., Rocken, C., Anthes, R. A., Ware, R. H., October 1992. GPS meteorology: Remote sensing of atmospheric water vapor using global positioning systems. *Journal of Geophysical Research* 97 (D14), 15787–15801.

- Bock, O., Bouin, M. N., Walpersdorf, A., Lafore, J. P., Janicot, S., Guichard, F., Agusti-Panareda, A., 2007. Comparison of ground-based GPS precipitable water vapour to independent observations and NWP model reanalyses over Africa. *Quarterly Journal of the Royal Meteorological Society* 133 (629), 2011–2027.
- Bonan, G. B., June 2008. Forests and climate change: Forcings, feedbacks, and the climate benefits of forests. *Science* 320 (5882), 1444–1449.
- Brubaker, K. L., Entekhabi, D., Eagleson, P. S., Jun. 1993. Estimation of continental precipitation recycling. *Journal of Climate* 6, 1077–1089.
- Brueske, K. F., 1990. Estimates of daily evapotranspiration over the Amazon Basin using Geostationary Environmental Satellite (GOES-7) Visible and Infrared Spin Scan Radiometer Atmospheric Sounder (VAS) data. Master's thesis, University of Wisconsin - Madison, 102 pages.
- Bruno, R. D., da Rocha, H. R., de Freitas, H. C., Goulden, M. L., Miller, S. D., August 2006. Soil moisture dynamics in an eastern Amazonian tropical forest. *Hydrological Processes* 20 (12), 2477–2489.
- Buck, A. L., 1981. New equations for computing vapor pressure and enhancement factor. *Journal of Applied Meteorology* 20, 1527–1532.
- Butler, R. A., July 2008. Future threats to the Amazon rainforest. Obtained from <http://news.mongabay.com/2008/0801-amazon.html> on July 20, 2011.
- Butler, R. A., October 2010. Brazil to launch new deforestation monitoring system that 'sees' through clouds. Obtained from http://news.mongabay.com/2010/1011-indicar_brazil.html on Aug 2, 2011.
- Cady-Pereira, K. E., Shephard, M. W., Turner, D. D., Mlawer, E. J., Clough, S. A., Wagner, T. J., June 2008. Improved daytime column-integrated precipitable water vapor from vaisala radiosonde humidity sensors. *Journal of Atmospheric and Oceanic Technology* 25 (6), 873883.
- Campanelli, M., Lupi, A., Nakajima, T., Malvestuto, V., Tomasi, C., Estelles, V., 2010. Summertime columnar content of atmospheric water vapor from ground-based sun-sky radiometer measurements through a new in situ procedure. *Journal of Geophysical Research* 115.
- Carleton, A. M., 1991. *Satellite Remote Sensing in Climatology*. CRC Press, Inc., 2000 Corporate Blvd., N. W., Boca Raton, Florida 33431.
- Chand, D., Guyon, P., Artaxo, P., Schmid, O., Frank, G. P., Rizzo, L. V., Mayol-Bracero, O. L., Gatti, L. V., , Andreae, M. O., 2006. Optical and physical properties of aerosols in the boundary layer and free troposphere over the Amazon basin during the biomass burning season. *Atmospheric Chemistry and Physics* 6, 2911–2925.

- Chen, T.-C., ho Yoon, J., Croix, K. J. S., , Takle, E. S., October 2001. Suppressing impacts of the Amazonian deforestation by the global circulation change. *Bulletin of the American Meteorological Society* 82 (10), 2209–2216.
- Chesters, D., Robinson, W. D., Uccellini, L. W., Aug. 1987. Optimized retrievals of precipitable water from the VAS ‘Split Window’. *Journal of Climate and Applied Meteorology* 26, 1059–1066.
- Chesters, D., Uccellini, L. W., Robinson, W. D., May 1983. Low-level water vapor fields from the VISSR Atmospheric Sounder (VAS) ‘Split Window’ channels. *Journal of Climate and Applied Meteorology* 22, 725–743.
- Chokkalingam, U., 2010. Design options for a forest carbon legal framework for lao PDR: Drawing lessons from across the globe. Tech. rep., Deutsche Gesellschaft fr Internationale Zusammenarbeit (GIZ) GmbH.
- Choudhury, B. J., 1996. Comparison of two models relating precipitable water to surface humidity using globally distributed radiosonde data over land surfaces. *International Journal of Climatology* 16, 663–675.
- Christy, J. R., 2009. Written testimony to house ways and means committee. Accessed on June 1, 2011.
- Christy, J. R., Norris, W. B., 2009. Discontinuity issues with radiosonde and satellite temperatures in the Australian region 1979 - 2006. *Journal of Atmospheric and Oceanic Technology* 26, 508–522.
- Christy, J. R., Norris, W. B., Spencer, R. W., Hnilo, J. J., 2007. Tropospheric temperature change since 1979 from tropical radiosonde and satellite measurements. *Journal of Geophysical Research* 112.
- Chu, P.-S., Yu, Z.-P., Hastenrath, S., Apr. 1994. Detecting climate change concurrent with deforestation in the Amazon Basin: Which way has it gone? *Bulletin of the American Meteorological Society* 75 (4), 579–583.
- Church, S., January 2009. Climate change & tropospheric temperature trends.
- Correia, F. W. S., Alval, R. C. S., Manzi, A. O., 2007. Modeling the impacts of land cover change in Amazonia: a regional climate model (RCM) simulation study. *Theoretical and Applied Climatology* 93 (3-4), 225–244.
- Costa, M. H., Foley, J. A., 1999. Trends in the hydrologic cycle of the Amazon Basin. *Journal of Geophysical Research* 104 (D12), 14,189–14,198.
- Crutcher, H. L., Meserve, J. M., 1970. Selected level heights, temperatures and dew points for the Northern Hemisphere. Tech. Rep. 50-1C-52, Naval Weather Service Command, NAVAIR, 406 pages. [Available from U. S. Govt. Printing Office, Washington, DC 20402].

- Cutrim, E., Martin, D. W., Rabin, R., Oct. 1995. Enhancement of cumulus clouds over deforested lands in Amazonia. *Bulletin of the American Meteorological Society* 76 (10), 1801–1805.
- da Rocha, H. R., Coauthors, January 2009. Patterns of water and heat flux across a biome gradient from tropical forest to savanna in Brazil. *Journal of Geophysical Research* 114 (G00B12).
- da Rocha, H. R., Goulden, M. L., Miller, S. D., Menton, M. C., Pinto, L. D. V. O., de Freitas, H. C., e Silva Figueira, A. M., 2004. Seasonality of water and heat fluxes over a tropical forest in Eastern Amazonia. *Ecological Applications* 14, 22–32.
- da Silva, R. R., Avissar, R., October 2006. The hydrometeorology of a deforested region of the Amazon Basin. *Journal of Hydrometeorology* 7, 1028–1042.
- Dai, A., Wang, J., Ware, R. H., van Hove, T., May 2002. Diurnal variation in water vapor over North America and its implications for sampling errors in radiosonde humidity. *Journal of Geophysical Research* 107 (D10).
- D’Almedia, C., Vorosmarty, C., Hurtt, G. C., Marengo, J., Dingman, S. L., Keim, B. D., 2007. The effects of deforestation on the hydrological cycle in Amazonia: a review on scale and resolution. *International Journal of Climatology* 27, 633–647.
- Dalu, G., Sep. 1986. Satellite remote sensing of atmospheric water vapor. *International Journal of Remote Sensing* 7 (9), 1089–1097.
- Dessler, A. E., Davis, S. M., 2010. Trends in tropospheric humidity from reanalysis systems. *Journal of Geophysical Research* 115 (D19127).
- Dow, J., Neilan, R. E., Rizos, C., 2009. The International GNSS service in a changing landscape of Global Navigation Satellite Systems. *Journal of Geodesy* 83, 191–198.
- Downton, M. W., 1995. Measuring tropical deforestation: Development of the methods. *Environmental Conservation* 22 (3), 229–240.
- Duan, J., Bevis, M., Fang, P., Bock, Y., Chiswell, S., and Christian Rocken, S. B., Solheim, F., van Hove, T., Ware, R., McClusky, S., Hering, T. A., King, R. W., Jun. 1996. GPS meteorology: Direct estimation of the absolute value of the precipitable water. *Journal of Applied Meteorology* 35, 830–838.
- DuBois, J. L., Multhauf, R. P., Ziegler, C. A., 2002. The invention and development of the radiosonde. *Tech. Rep. 53, Smithsonian Studies in History and Technology*, 78 pages.
- Duffy, G., June 2007. Amazon River 'longer than Nile'. BBC News, obtained from <http://news.bbc.co.uk/2/hi/6759291.stm> on July 25, 2011.

- Durre, I., Jr., C. N. W., Yin, X., Vose, R. S., 2009. Radiosonde-based trends in precipitable water over the Northern Hemisphere: An update. *Journal of Geophysical Research* 114 (D05112).
- Durre, I., Vose, R. S., Wuertz, D. B., January 2006. Overview of the Integrated Global Radiosonde Archive. *Journal of Climate* 19, 53–68.
- Eck, T. F., Holben, B. N., Mar. 1994. AVHRR split window temperature differences and total precipitable water over land surfaces. *International Journal of Remote Sensing* 15 (3), 567–582.
- Elliott, W. P., 1995. On detecting long-term changes in atmospheric moisture. *Climatic Change* 31, 349–367.
- Elliott, W. P., Gaffen, D. J., Oct. 1991. On the utility of using radiosonde humidity archives for climatic studies. *Bulletin of the American Meteorological Society* 72 (10), 1507–1520.
- Elliott, W. P., Ross, R. J., Blackmore, W. H., 2002. Recent changes in NWS upper-air observations with emphasis on changes from VIZ to Vaisala radiosondes. *Bulletin of the American Meteorological Society* 83, 1003–1017.
- Elliott, W. P., Smith, M. E., Angell, J. K., 1991. On monitoring tropospheric water vapor changes using radiosonde data. In: *Greenhouse-Gas-Induced Climate Change: A Critical Appraisal of Simulations and Observations*. Elsevier, pp. 311–328, m. Schlesinger.
- Eltahir, E. A. B., Bras, R. L., Jan. 1993. Precipitation recycling in the Amazon Basin. Tech. rep., Center for Global Change Science, Massachusetts Institute of Technology, report No. 20.
- Eltahir, E. A. B., Bras, R. L., 1994. Sensitivity of regional climate to deforestation in the Amazon Basin. *Advances in Water Resources* 17, 101–115.
- ESA, April 2010. DUE GlobVapour: Requirements baseline document. Tech. rep., ESA.
- Eskridge, R. E., Alduchov, O. A., Chernykh, I. V., Panamao, Z., Polansky, A. C., Doty, S. R., Oct. 1995. A comprehensive aerological data set (CARDS): Rough and systematic errors. *Bulletin of the American Meteorological Society* 76 (10), 1759–1775.
- European Commission, 2003. Global land cover 2000 database. Tech. rep., Joint Research Centre, GIS formatted datasets obtained from <http://bioval.jrc.ec.europa.eu/products/glc2000/glc2000.php>.

- Facility, U. G. E., 2006. Concept document for the integrated and sustainable management of transboundary water resources in the Amazon River Basin. Tech. rep., UNEP Global Environment Facility.
- Falvey, M., Garreaud, R. D., November 2005. Moisture variability over the South American altiplano during the South American low level jet experiment (SALLJEX) observing season. *Journal of Geophysical Research* 110 (D22105).
- Fearnside, P. M., 1989. Deforestation in Brazilian Amazonia: The rates and causes of forest destruction. *The Ecologist* 19 (6), 214–218.
- Ferraro, R., Weng, F., Meng, H., Vila, D., 2007. 20 years of hydrological products from the SSM/I: Status and future. Proceedings of the Joint 2007 EUMETSAT Meteorological Satellite Conference and the 15th Satellite Meteorology & Oceanography Conference of the American Meteorological Society.
- Ferraro, R. R., Weng, F., Grody, N. C., Basist, A., May 1996. An eight-year (1987 - 1984) time series of rainfall, clouds, water vapor, snow cover, and sea ice derived from SSM/I measurements. *Bulletin of the American Meteorological Society* 77 (5), 891–905.
- Ferreira, N. C., Ferreira, L. G., Miziara, F., January 2007. Deforestation hotspots in the Brazilian Amazon: Evidence and causes as assessed from remote sensing and census data. *Earth Interactions* 11 (1), 1–16.
- Ferreira, N. J., 1987. Large-scale features of the atmospheric water vapor transport over the Amazon region. Ph.D. dissertation, University of Wisconsin - Madison, 135 pages.
- Fleming, H. E., Goldberg, M. D., Crosby, D. S., 1986. Minimum variance simultaneous retrieval of temperature and water vapor from satellite radiance measurements. In: Proceedings of the 2nd Conference on Satellite Meteorology: Remote Sensing and Applications. Williamsburg, Virginia, pp. 20–23.
- Fu, Q., Johanson, C. M., Warren, S. G., Seibel, D. J., 2004. Contribution of stratospheric cooling to satellite-inferred tropospheric temperature trends. *Nature* 429 (6987), 55–58.
- Fund, W. W., January 2009. Amazon deforestation trend on the increase. ScienceDaily, obtained from [http://www.sciencedaily.com /releases/2009/01/090104093542.htm](http://www.sciencedaily.com/releases/2009/01/090104093542.htm) on July 24, 2011.
- Gaffen, D. J., Barnett, T. P., 1992. A comparison of observations and model simulations of tropospheric water vapor. *Journal of Geophysical Research* 97, 2775–2780.

- Galárraga, R., Torres, M. C., 2001. Water quality in the Napo River Basin (Ecuadorian Andean Amazonia): The Andean Amazon rivers analysis and management project (aaram). *Mountain Research and Development* 21 (3), 295–296.
- Gao, B.-C., Kaufman, Y. J., 2003. Water vapor retrievals using Moderate Resolution Imaging Spectroradiometer (MODIS) near-infrared channels. *Journal of Geophysical Research* 108 (D13), 4389.
- Garrison, J. D., 1992. Estimation of atmospheric precipitable water over australia for application to the division of solar radiation into its direct and diffuse components. *Solar Energy* 48 (2), 89–96.
- Garrison, J. D., Adler, G. P., 1990. Estimation of precipitable water over the United States for application to the division of solar radiation into its direct and diffuse components. *Solar Energy* 44, 225–241.
- Gash, J. H. C., Nobre, C. A., Roberts, J. M., Victoria, R. L. (Eds.), 1996. *Amazonian Deforestation and Climate*. John Wiley & Sons, Inc., 611 pages.
- GCOS, Jan 2013. Global Climate Observing System (GCOS). Obtained from <http://gosc.org/gcos> on June 13, 2013.
- Gibbs, H., Ruesch, A. S., Achard, F., Clayton, M. K., Holmgren, P., Ramankutty, N., Foley, J. A., August 2010. Tropical forests were the primary source of new agricultural land in the 1980s and 1990s. *Proceedings of the National Academy of Sciences* 107 (37).
- Greenwald, T. J., Stephens, G. L., Haar, T. H. V., Jackson, D. L., 1993. A physical retrieval of cloud liquid water over the global oceans using special sensor microwave/imager (SSM/I) observations. *Journal of Geophysical Research* 98 (D10), 1847118488.
- Gueymard, C., 1994. Analysis of monthly average precipitable water and turbidity in Canada and Northern United States. *Solar Energy* 53 (1), 57–71.
- Guillory, A. R., 1991. A physical split window technique for deriving precipitable water utilizing VAS data. Master's thesis, The Florida State University, 70 pgs.
- Guillory, A. R., Jedlovec, G. J., Fuelberg, H. E., Jul. 1993. A technique for deriving column-integrated water content using VAS split-window data. *Journal of Applied Meteorology* 32 (32), 1226–1241.
- Gullison, R. E., Frumhoff, P. C., Canadell, J. G., Field, C. B., Nepstad, D. C., Hayhoe, K., Avissar, R., Curran, L. M., Friedlingstein, P., Jones, C. D., Nobre, C., May 2007. Tropical forests and climate policy. *Science* 316 (5827), 985–986.

- Haines, S. L., Suggs, R. J., Jedlovec, G. J., 2004. The Geostationary Operational Environmental Satellite (GOES) product generation system. Tech. Rep. NASA/TM-2004-213286, NASA Marshall Space Flight Center, Huntsville, AL, 64 pp.
- Hansen, M. C., Shimabukurob, Y. E., Potapova, P., Pittmana, K., October 2008. Comparing annual MODIS and PRODES forest cover change data for advancing monitoring of Brazilian forest cover. *Remote Sensing of Environment* 112 (10), 3784–3793.
- Harris, A. R., Mason, I. M., May 1992. An extension to the split-window technique giving improved correction and total water vapor. *International Journal of Remote Sensing* 13 (5), 881–892.
- Harriss, R. C., Wofsy, S. C., Garstang, M., Browell, E. V., Molion, L. C. B., McNeal, R. J., Hoell, J. M., Bendura, R. J., Beck, S. M., Navaro, R. L., Riley, J. T., Snell, R. L., 1988. The Amazon Boundary Layer Experiment (ABLE-2A) dry season 1985. *Journal of Geophysical Research* 93 (D2), 1351–1360.
- Hastenrath, S., 1985. *Climate and Circulation in the Tropics*. D. Reidel, 455 pages.
- Hay, J. E., 1971. Precipitable water over Canada: li - distribution. *Atmosphere* 9, 101–111.
- Hayden, C. M., Jun. 1988. GOES-VAS simultaneous temperature-moisture retrieval algorithm. *Journal of Applied Meteorology* 27 (6), 705–733.
- Hayden, C. M., Wade, G. S., Schmit, T. J., Feb. 1996. Derived product imagery from GOES-8. *Journal of Applied Meteorology* 35, 153–162.
- Held, I. M., Soden, B. J., 2000. Water vapor feedback and global warming. *Annual Review of Energy and the Environment* (2000) 25, 441–475.
- Herdies, D. L., Kousky, V. E., Ebisuzaki, W., April 2006. The impact of high-resolution SALLJEX data on NCEP global analyses. *Proceedings of the 8th International Conference on Southern Hemisphere Meteorology and Oceanography*, 1105–1110 Foz do Iguau, Brazil.
- Huete, A. R., Coauthors, 2006. Amazon rainforests green-up with sunlight in dry season. *Geophysical Research Letters* 33 (L06405).
- INPA, July 2011. NETWORK GEOMA-introduction: The challenges of sustainability. Obtained from <http://www.geoma.lncc.br/introducao.htm> on July 5, 2011.
- Jackson, D. L., Stephens, G. L., Aug. 1995. A study of SSM/I-derived columnar water vapor over the global oceans. *Journal of Climate* 8, 2025–2038.

- Jedlovec, G. J., 1987. Determination of atmospheric moisture structure from high resolution MAMS data. Ph.D. dissertation, University of Wisconsin - Madison, 187 pages.
- Jedlovec, G. J., Sep. 1990. Precipitable water estimation from high-resolution split window radiance measurements. *Journal of Applied Meteorology* 29 (9), 863–877.
- Jin, M., Liang, S., June 2006. An improved land surface emissivity parameter for land surface models using global remote sensing observations. *Journal of Climate* 19, 2867–2881.
- Kallberg, P., Berrisford, P., Hoskins, B. J., Simmons, A., Uppala, S., Lamy-Thépaud, S., Hine, R., 2005. ERA-40 atlas. Tech. rep., ECMWF, see Official URL for a link to the Atlas paper and to the Atlas web version.
- Kalnay, E., Kanamitsu, M., Kistler, R., Collins, W., Deaven, D., Gandin, L., Iredell, M., Saha, S., White, G., Wollen, J., Zhu, Y., Chelliah, M., Ebisuzaki, W., Higgins, W., Janowiak, J., Mo, K. C., Ropelewski, C., Wang, J., Leetma, A., Reynolds, R., Jenne, R., Joseph, D., Mar. 1996. The NCEP/NCAR 40-year reanalysis project. *Bulletin of the American Meteorological Society* 77 (3), 437–471.
- Kanamitsu, M., Ebisuzaki, W., Woollen, J., Keng Yang, S., Hnilo, J. J., Fiorino, M., Potter, G. L., November 2002. NCEP/DOE AMIP-II reanalysis (r-2). *Bulletin of the American Meteorological Society* 83, 1631–1643.
- Karam, H. N., 2006. Estimating evapotranspiration from the Amazon Basin using atmospheric water balance. Master's thesis, MIT.
- Karam, H. N., Bras, R. L., 2008. Climatological basin-scale Amazonian evapotranspiration estimated through a water budget analysis. *Journal of Hydrometeorology* 9 (5), 1048–1060.
- Karl, T. R., Hassol, S. J., Miller, C. D., Murray, W. L., 2006. Temperature trends in the lower atmosphere: Steps for understanding and reconciling differences. Tech. rep., A Report by the Climate Change Science Program and the Subcommittee on Global Change Research.
- Kaufman, Y. J., Gao, B.-C., September 1992. Remote sensing of water vapor in the near ir from EOS/MODIS. *IEEE TRANSACTIONS ON GEOSCIENCE AND REMOTE SENSING*, 30, 871–884.
- Keller, M., Bustamante, M., Gash, J., Dias, P. S. (Eds.), 2009. Amazonia and Global Change. *Geophysical Monologue Series* 186. American Geophysical Union.
- Kiehl, J. T., Trenberth, K. E., February 1997. Earth's annual global mean energy budget. *Bulletin of the American Meteorological Society* 78 (2), 197–208.

- Kistler, R., Others, Feb 2001. The NCEPNCAR 50-year reanalysis: Monthly means CD-ROM and documentation. *Bulletin of the American Meteorological Society* 82 (2), 247–267, this article is accompanied by a CD-ROM that contains the complete documentation of the NCEPNCAR Reanalysis and all of the data analyses and forecasts. It is provided to members through the sponsorship of SAIC and GSC.
- Kleespies, T. J., McMillin, L. M., Sep. 1990. Retrieval of precipitable water from observations in the split window over varying surface temperatures. *Journal of Applied Meteorology* 29 (9), 851–862.
- Knabb, R. D., Fuelberg, H. E., 1997. A comparison of the first guess dependence of precipitable water estimates from three techniques using GOES data. *Journal of Applied Meteorology* 36 (5), 417–427.
- Laurance, W. F., Albernaz, A. K. M., Fearnside, P. M., Vasconcelos, H. L., Ferreira, L. V., May 2004. Deforestation in Amazonia. *Science* 304 (5674), 1109–1111.
- Laurance, W. F., Cochrane, M. A., Bergen, S., Fearnside, P. M., Delamnica, P., Barber, C., D'Angelo, S., Fernandes, T., January 2001. The future of the Brazilian Amazon. *Science* 291, 438–439.
- Lean, J., Rowntree, P. R., 1993. A GCM simulation of the impact of Amazonian deforestation on climate using an improved canopy representation. *Quarterly Journal of the Royal Meteorological Society* 119, 509–530.
- Lee, K.-M., Park, J.-H., 2007. Retrieval of total precipitable water from the split-window technique in the East Asian region. *Proceedings of the Joint 2007 EU-METSAT Meteorological Satellite Conference and the 15th Satellite Meteorology & Oceanography Conference of the American Meteorological Society*nce.
- Legates, D. R., McCabe, G. J., Jan. 1999. Evaluating the use of goodness-of-fit measures in hydrologic and hydroclimatic model validation. *Water Resources Research* 35 (1), 233–241.
- Lettau, H., Lettau, K., Molion, L. C. B., Mar. 1979. Amazonia's hydrologic cycle and the role of atmospheric recycling in assessing deforestation effects. *Monthly Weather Review* 107 (3), 227–238.
- Li, Z., Li, J., Menzel, P., Schmit, T., Nelson, H., Daniels, J., Ackerman, S. A., 2008. GOES sounding improvement and applications to severe storm nowcasting. *Geophysical Research Letters* 35 (L03806).
- Lindsey, R., December 2002. Introduction to the large-scale biosphere-atmosphere experiment in Amazonia. NASA Earth Observatory.
- Lindsey, R., March 2007. Tropical deforestation. NASA Earth Observatory.

- Liu, G., Curry, J. A., Clayson, C. A., 1995. Study of tropical cyclogenesis using satellite data. *Meteorology and Atmospheric Physics* 56, 111–123.
- Lott, G. A., 1976. Precipitable water over the United States, Volume 1. Technical report NWS 20, NOAA, 173 pages [Available from U.S. Govt. Printing Office, Washington, DC 20402].
- Mantovani, A. C. D. M., Setzer, A. W., 1997. Deforestation detection in the Amazon with an AVHRR-based system. *International Journal of Remote Sensing* 18 (2), 273–286.
- Marengo, J., Nobre, C. A., Betts, R. A., Cox, P. M., Sampaio, G., Salazar, L., 2009. Amazonia and Global Change. American Geophysical Union, Ch. Global Warming and Climate Changes in Amazonia: Climate-Vegetation Feedback and Impacts on Water Resources, pp. 273–292.
- Marengo, J. A., April 2004. Interdecadal variability and trends of rainfall across the Amazon Basin. *Theoretical and Applied Climatology* 78 (1-3), 79–96.
- Marengo, J. A., 2005. Characteristics and spatio-temporal variability of the Amazon River Basin water budget. *Climate Dynamics* 24 (1), 11–22.
- Marengo, J. A., 2007. Tropical Rainforest Responses to Climatic Change. Praxis Publishing, Ch. Climate change and hydrologic modes of the wet tropics, pp. 237–268.
- Marengo, J. A., Nobre, C. A., Clip, A. D., Nov. 1997. Climatic impacts of "Friagens" in forested and deforested areas of the Amazon Basin. *Journal of Applied Meteorology* 36, 1553–1566.
- Marengo, J. A., Sanches, M., Cunningham, C., Camargo, H., Nobre, C. A., 2002. Characteristics and variability of the atmospheric water balance in the Amazon basin. *Proceedings of the Sixth International Conference on Southern Hemisphere Meteorology and Oceanography*, 597–601 This entry could also be a later doc describing this - Marengo, J., Characteristics and variability of the atmospheric water balance of the Amazon Basin, in 6th International Conference on Southern Hemisphere Meteorology and Oceanography, Santiago, Chile, April 3 - 7, 2000, 284–285, AMS Publ.
- Margulis, S., 2004. Causes of deforestation of the Brazilian Amazon. Working Paper 22 22, The World Bank.
- Marques, J., dos Santos, J. M., Nova, N. A. V., Salati, E., 1977. Precipitable water and water vapor flux between Belém and Manaus. *Acta Amazonica* 7 (3), 355–362.
- Mattioli, V., Westwater, E. R., Gutman, S. I., Morris, V. R., 2005. Forward model studies of water vapor using scanning microwave radiometers, global positioning

- system, and radiosondes during the cloudiness inter-comparison experiment. *IEEE Transactions on Geoscience Remote Sensing* 43 (5), 10121021.
- Maurellis, A. N., Lang, R., van der Zande, W. J., Aben, I., Ubachs, W., March 2000. Precipitable water column retrieval from GOME data. *Geophysical Research Letters* 27 (6), 903–906.
- Maxwell, E. L., Marion, W. F., Myers, D. R., Rymes, M. D., Wilcox, S. M., Jan. 1995. Final technical report: National solar radiation data base (1961 - 1990). Tech. rep., National Renewable Energy Laboratory, Golden, Colorado, report Number TP-463-5784, 318 pages.
- McCarthy, M. P., Thorne, P. W., Titchner, H. A., 2009. An analysis of tropospheric humidity trends from radiosondes. *Journal of Climate* 22, 58205838.
- McGrath, R., Semmler, T., Sweeney, C., Wang, S., July 2006. Impact of balloon drift errors in radiosonde data on climate statistics. *Journal of Climate* 19, 34303442.
- Menzel, P. W., Cutrim, E. C., Prins, E. M., 1991. Geostationary satellite estimation of biomass burning in Amazonia during BASE-A. In: *Global biomass burning: Atmospheric, climatic and biospheric implications*. MIT Press, pp. 41–46.
- Menzel, W. P., Purdom, J. F. W., May 1994. Introducing GOES-I: The first of a new generation of geostationary operational environmental satellites. *Bulletin of the American Meteorological Society* 75 (5), 757–781.
- Mieruch, S., Noel, S., Bovensmann, H., Burrows, J. P., February 2008. Analysis of global water vapour trends from satellite measurements in the visible spectral range. *Atmospheric Chemistry and Physics* 8, 491–504.
- Millikan, B., 2009. Implementing REDD in the Brazilian Amazon: Contextualization, debates and challenges, background paper on the first REDD readiness field dialogue. Tech. rep., The Forests Dialogue, background paper for Field Dialogue in Brazil, October 28-29, 2009, Belem - PA.
- Miloshevich, L. M., Vmel, H., Whiteman, D. N., Lesht, B. M., Schmidlin, F. J., Russo, F., 2006. Absolute accuracy of water vapor measurements from six operational radiosonde types launched during AWEX-G and implications for AIRS validation. *Journal of Geophysical Research* 111 (D09S10).
- Molion, L. C. B., 1975. A climatonic study of the energy and moisture fluxes of the Amazonas Basin with considerations of deforestation effects. Ph.D. dissertation, University of Wisconsin - Madison, 133 pgs.
- Montgomery, H. E., Uccellini, L. W., 1985. VAS demonstration: (VISSR atmospheric sounder) description and final report. Tech. rep., NASA, NASA Reference Publication 1151, 33 pages.

- Morton, D. C., DeFries, R. S., Shimabukuro, Y. E., Anderson, L. O., Arai, E., del Bon Espirito-Santo, F., Freitas, R., Morisette, J., September 2006. Cropland expansion changes deforestation dynamics in the Southern Brazilian Amazon. *Proceedings of the National Academy of Sciences* 103 (39), 1463714641.
- NASA, July 2004. NASA plays a key role in largest environmental experiment in history. Obtained from <http://www.nasa.gov/centers/goddard/news/topstory/2004/0727lba.html> on July 3, 2011.
- NASA, December 2007. NASA satellites help lift cloud of uncertainty on climate change. NASA Press Release.
- NASA, 2011. The afternoon constellation. Obtained from <http://atrain.nasa.gov/> on May 25, 2011.
- NASA, September 2011a. NASA's application technology satellite (ATS) mission page. Obtained from <http://science.nasa.gov/missions/ats/> on Sept 12, 2011.
- NASA, September 2011b. NASA's Geostationary Operation Environmental Satellite (GOES) mission page. Obtained from <http://science.nasa.gov/missions/goes/> on Sept 12, 2011.
- Negri, A. J., Adler, R. F., Xu, L., Surratt, J., 2004. The impact of Amazonian deforestation on dry season rainfall. *Journal of Climate* 17, 1306–1319.
- NESDIS Office of Satellite Operations, May 2011. Geostationary operational environmental satellites. obtained May 30, 2011.
- NOAA National Climatic Data Center, 2011. State of the climate. Obtained from <http://www.ncdc.noaa.gov/sotc/> on May 20, 2011.
- NOAA NESDIS, 2011. Integrated global radiosonde archive (IGRA). Obtained from <http://www.ncdc.noaa.gov/oa/climate/igra/> on June 5, 2011.
- NOAA NESDIS, 2012. PEACESAT: A communication lifeline for the pacific. Obtained from http://www.nesdis.noaa.gov/news_archives/goes-7_deorbit.html on June 2, 2013.
- Nobre, C. A., Sellers, P. J., Shukla, J., 1991. Amazonian deforestation and regional climate change. *Journal of Climate* 4, 957–988.
- Nobre, P., Malagutti, M., Urbano, D. F., de Almeida, R. A. F., Giarolla, E., 2009. Amazon deforestation and climate change in a coupled model simulation. *Journal of Climate* 22, 56865697.

- Noël, S., Buchwitz, M., Bovensmann, H., Hoogen, R., Burrows, J. P., July 1999. Atmospheric water vapor amounts retrieved from GOME satellite data. *Geophysical Research Letters* 26 (13), 1841–1844.
- Noël, S., Buchwitz, M., Burrows, J. P., 2004. First retrieval of global water vapour column amounts from SCIAMACHY measurements. *Atmospheric Chemistry and Physics* 4, 111–125.
- Noël, S., Mieruch, S., Bovensmann, H., Burrows, J. P., 2007. Towards a combined GOME, SCIAMACHY and GOME-2 global total column water vapour data set. Proceedings of the Joint 2007 EUMETSAT Meteorological Satellite Conference and the 15th Satellite Meteorology & Oceanography Conference of the American Meteorological Society.
- NWS, June 2011. NOAA NWS radiosonde observations factsheet. Obtained from <http://www.ua.nws.noaa.gov/factsheet.htm> on June 1, 2011.
- O'Brien, K. L., 1995. Deforestation and climate change in the Selva Lacandona of Chiapas, Mexico: some preliminary results. *Norsk geogr. Tidsskr* 49, 105–122.
- O'Brien, K. L., September 1996. Tropical deforestation and climate change. *Progress in Physical Geography* 20 (3), 311–335.
- Olander, L. P., Gibbs, H. K., Steininger, M., Swenson, J. J., Murray, B. C., June 2008. Reference scenarios for deforestation and forest degradation in support of REDD: a review of data and methods. *Environmental Research Letters* 3, 11 pp.
- Paltridge, G., Arking, A., Pook, M., 2009. Trends in middle- and upper-level tropospheric humidity from NCEP reanalysis data. *Theoretical and Applied Climatology* 98, 351–359.
- Peixoto, J. P., Oort, A. H., 1992. *Physics of Climate*. American Institute of Physics, New York, New York, 520 pages.
- Phillips, O. L., Lewis, S. L., Baker, T. R., Malhi, Y., 2007. Tropical Rainforest Responses to Climatic Change. Praxis Publishing, Ch. The response of South American tropical forests to contemporary atmospheric change, pp. 317–332.
- Pratt, R. W., Sep. 1985. Review of radiosonde humidity and temperature errors. *Journal of Atmospheric and Oceanic Technology* 2, 404–407.
- Prins, E. M., Menzel, W. P., Aug. 1994. Trends in South American biomass burning detected with the GOES visible infrared spin scan radiometer atmospheric sounder from 1983 to 1991. *Journal of Geophysical Research* 99 (D8), 16719–16735.
- Raintree, July 2011. Rainforest facts. Obtained from <http://www.raintree.com/facts.htm> on July 14, 2011.

- Randall, D. A., Wood, R., Bony, S., Colman, R., Fichet, T., Fyfe, J., Kattsov, V., Pitman, A., Shukla, J., Srinivasan, J., Stouffer, R., Sumi, A., Taylor, K., 2007. *Climate Change 2007: The Physical Science Basis. Contribution of Working Group I to the Fourth Assessment Report of the Intergovernmental Panel on Climate Change.* Cambridge University Press, Ch. Climate Models and Their Evaluation, pp. 589–662.
- Randel, D. L., Haar, T. H. V., Ringerud, M. A., Stephens, G. L., Greenwald, T. J., Combs, C. L., 1996. A new global water vapor dataset. *Bulletin of the American Meteorological Society* 77, 1233–1246.
- Reagan, J., Thome, K., Herman, B., Stone, R., DeLuisi, J., Snider, J., Jun. 1995. A comparison of columnar water vapor retrievals obtained with near-IR solar radiometer and microwave radiometer measurements. *Journal of Applied Meteorology* 34, 1384–1391.
- Reale, A., Tilley, F., Ferguson, M., Allegrino, A., 2008. NOAA operational sounding products for ATOVS. *International Journal of Remote Sensing* 29 (29), 4615–4651.
- Reale, A. L., Goldberg, M. D., Daniels, J. M., 1989. Operational TOVS soundings using a physical approach. In: *Proceedings of the IGARRS '89 12th Canadian Symposium on Remote Sensing.* Vancouver, British Columbia, pp. 2653–2657.
- Reber, E. E., Swope, J. R., Dec. 1972. On the correlation of the total precipitable in a vertical column and absolute humidity at the surface. *Journal of Applied Meteorology* 11, 1322–1325.
- Reitan, C. H., 1960. Distribution of precipitable water vapor over the continental United States. *Bulletin of the American Meteorological Society* 41, 79–87.
- Reitan, C. H., 1963. Surface dew point and water vapor aloft. *Journal of Applied Meteorology* 20, 776–779.
- Renault, D., Pawny, J. C., Capitini, R., 1980. Daytime Raman lidar measurements of water vapor. *Optics Letters* 5, 223–235.
- Roach, J., June 2007. Amazon longer than Nile River, scientists say. *National Geographic News*, obtained from http://news.nationalgeographic.com/news/2007/06/070619-Amazon-river_2.html on July 25, 2011.
- Ronchail, J., Cochonneau, G., Molinier, M., Guyot, J.-L., De Miranda Chaves, A. G., Guimaraes, V., De Oliveira, E., 2002. Interannual rainfall variability in the Amazon basin and sea-surface temperatures in the equatorial Pacific and the tropical Atlantic Oceans. *International Journal of Climatology* 22 (13), 1663–1686.
- Ross, R. J., Elliott, W. P., Dec. 1996. Tropospheric water vapor climatology and trends over North America: 1973 - 1993. *Journal of Climate* 9 (12), 3561–3574.

- Ross, R. J., Elliott, W. P., 2001. Radiosonde-based Northern Hemisphere tropospheric water vapor trends. *Journal of Climate* 14, 16021611.
- Rossow, W. B., Gardner, L. C., Lu, P. J., Walker, A. W., 1991. International satellite cloud climatology project (ISSCP). Tech. rep., World Meteorological Organization, documentation of Cloud Data. WMO/TD-No. 266, 76 pgs.
- Rust, E., July 2011. Brazil's Amazon deforestation is protected and encouraged by the constitution. *Brazzil Magazine*.
- Saad, S. I., da Rocha, H. R., Dias, M. A. F. S., Rosolem, R., 2010. Can the deforestation breeze change the rainfall in Amazonia? a case study for the br-163 highway region. *Earth Interactions* 14 (18), 1–25.
- Salati, E., Dall'Olio, A., Matsui, E., Gat, J., 1979. Recycling of water in the Amazon Basin. *Water Resources Research* 15, 1250–1258.
- Sapucci, L. F., Machado, L. A. T., Monico, J. F. G., Plana-Fattori, A., November 2007. Intercomparison of integrated water vapor estimates from multisensors in the Amazonian region. *Journal of Atmospheric and Oceanic Technology* 24 (11), 18801894.
- Schmit, T. J., Brueske, F. F., Smith, W. L., Sep. 1990. Visible and Infrared Spin Scan Radiometer Atmospheric Sounder water vapor and wind fields over Amazonia. *Journal of Geophysical Research* 95 (D10), 17031–17038.
- Seidel, D. J., Coauthors, 2004. Uncertainty in signals of large-scale climate variations in radiosonde and satellite upper-air temperature datasets. *Journal of Climate* 17, 22252240.
- Seidel, D. J., Sun, B., Pettey, M., Reale, A., 2011. Global radiosonde balloon drift statistics. *Journal of Geophysical Research* 116 (D07102).
- Shephard, D., 1968. A two-dimensional interpolation function for irregularly-spaced data. In: *Proceedings of the 1968 23rd ACM national conference*. ACM 1968, New York, NY, pp. 517–524.
- Shi, C.-X., 2005. The operational products of Fengyun-2C. chapter 11: Clear-sky total precipitable water from FY-2C. Tech. rep., National Satellite Meteorological Center, Beijing, 77-82.
- Shi, C.-X., Xie, Z.-H., 2005. Operational method of total precipitable water retrieved from satellite multi-channel's infrared data. *Journal of Infrared and Millimeter Waves* 24 (4), 304–308, (in Chinese).
- Shimabukuro, Y., Duarte, V., Anderson, L., Valeriano, D., Arai, E., Freitas, R., Rudorff, B. F., Moreira, M., 2006. Near real time detection of deforestation in the Brazilian Amazon using MODIS imagery. *Ambiente & Água - An Interdisciplinary Journal of Applied Science* 1 (1).

- Short, N. M., 2009. The remote sensing tutorial. NASA Reference Publication 1078 and Library of Congress Catalog Card No. 81-600117.
- Shukla, J., Mintz, Y., Mar. 1982. Influence of land-surface evapotranspiration on the Earth's climate. *Science* 215, 1498–1501.
- Shuttleworth, W. J., 1988. Evaporation from Amazonian rainforest. *Proceedings of the Royal Society of London B* 233, 321–346.
- Shuttleworth, W. J., Gash, J. C., Roberts, J. M., Nobre, C. A., Molion, L. C. B., de Nazare GOES Ribeiro, M., 1991. Post-deforestation Amazonian climate: Anglo-Brazilian research to improve prediction. *Journal of Hydrology* 129, 71–85.
- Silva Dias, M. A. F., Rutledge, S., Kabat, P., Dias, P. L. S., Nobre, C., Fisch, G., Dolman, A. J., Zipser, E., Garstang, M., Manzi, A. O., Fuentes, J. D., Rocha, H. R., Marengo, J., Plana-Fattori, A., Sa, L. D. A., Alvala, R. C. S., Andreae, M. O., Artaxo, P., Gielow, R., Gatti, L., September 2002. Cloud and rain processes in a biosphere-atmosphere interaction context in the Amazon region. *Journal of Geophysical Research* 107 (D20).
- Sinha, S., Sinha, S. K., 1981. Precipitable water and dew point temperature relationship during the Indian summer monsoon. *Pure and Applied Geophysics* 119 (5), 913–921.
- Skole, D., Tucker, C., Jun. 1993. Tropical deforestation and habitat fragmentation in the Amazon: Satellite data from 1979 to 1988. *Science* 260, 1905–1910.
- Skole, D. L., Chomentowski, W. H., Salas, W. A., Nobre, A. D., May 1994. Physical and human dimensions of deforestation in Amazonia. *BioScience* 44 (5), 314–322.
- Slijkhuis, S., Beirle, S., Mies, K., Wagner, T., Emmadi, S., Loyola, D., Zimmer, W., Kalakoski, N., 2010. Water vapour: A new operational O3M-SAF trace gas total column product. *Proceedings of the 2010 EUMETSAT Meteorological Satellite Conference*.
- Smith, W. L., Woolf, H. M., 1984. Improved vertical sounding from amalgamation of polar and geostationary radiance observations. In: *Proceedings of the Conference on Satellite Meteorology: Remote Sensing and Applications*. Clearwater, Florida, pp. 45 – 48.
- Smith, W. L., Woolf, H. M., Schreiner, A. J., 1985. Simultaneous retrieval of surface atmospheric parameters: A physical and analytically direct approach. *Advances in Remote Sensing*, 221–230.
- Soden, B. J., Bretherton, F. P., Jan. 1994. Evaluation of water vapor distribution in general circulation models using satellite observations. *Journal of Geophysical Research* 99 (D1), 1187–1210.

- Soden, B. J., Turner, D. D., Lesht, B. M., Miloshevich, L. M., 2004. An analysis of satellite, radiosonde, and lidar observations of upper tropospheric water vapor from the atmospheric radiation measurement program. *Journal of Geophysical Research* 109 (D04105).
- Solomon, S., Qin, D., Manning, M., Chen, Z., Marquis, M., Averyt, K., M.Tignor, Miller, H. (Eds.), 2007. *Climate Change 2007: The Physical Science Basis. Contribution of Working Group I to the Fourth Assessment Report of the Intergovernmental Panel on Climate Change*. Cambridge University Press, United Kingdom and New York, NY, USA., Ch. Summary for Policymakers, p. 996.
- Sombroek, W., November 2001. Spatial and temporal patterns of Amazon rainfall. *AMBIO: A Journal of Human Environment* 30 (7), 388–396.
- Soto-Garcia, L. L., Andreae, M. O., Andreae, T. W., Artaxo, P., Maenhaut, W., Kirchstetter, T., Novakov, T., Chow, J. C., Mayol-Bracero, O. L., 2011. Evaluation of the carbon content of aerosols from the burning of biomass in the Brazilian Amazon using thermal, optical and thermal-optical analysis methods. *Atmospheric Chemistry and Physics* 11, 4425–4444.
- Spencer, R. W., Braswell, W. D., 2008. Potential biases in feedback diagnosis from observational data: A simple model demonstration. *Journal of Climate* 21, 5624–5628.
- Starr, D. O., Melfi, S. H., 1991. The role of water vapor in climate. NASA Conference Publication 3120, NASA, 45 pages.
- Sud, Y. C., Yang, R., Walker, G. K., Mar. 1996. Impact of in-situ deforestation in Amazonia on the regional climate: General circulation model simulation study. *Journal of Geophysical Research* 101 (D3), 7095–7109.
- Sudradjat, A., Ferraro, R. R., Fiorino, M., June 2005. A comparison of total precipitable water between reanalyses and NVAP. *Journal of Climate* 18 (11), 1790–1807.
- Suggs, R. J., Jedlovec, G. J., 1996. A comparison of total integrated water content retrieved from GOES-7 and GOES-8. In: *Proceedings of the Eighth Conference on Satellite Meteorology and Oceanography*. American Meteorological Society, pp. 30–34.
- Suggs, R. J., Jedlovec, G. J., Guillory, A. R., October 1998. Retrieval of geophysical parameters from GOES: Evaluation of a split window technique. *Journal of Applied Meteorology* 37, 1205–1227.
- Sun, D.-Z., Held, I. M., Apr. 1996. A comparison of modeled and observed relationships between interannual variations of water vapor and temperature. *Journal of Climate* 9, 665–675.

- Sun, D.-Z., Oort, A. H., Aug. 1995. Humidity-temperature relationships in the tropical troposphere. *Journal of Climate* 8, 1974–1987.
- Taylor, L., 2004. *The Healing Power of Rainforest Herbs*. Square One Publishers, Inc., Garden City Park, NY 11040.
- The Guardian, July 2010. First Amazon bridge to open world's greatest rainforest to development. Obtained from <http://www.theguardian.com/environment/2010/jul/29/manaus-bridge-amazon-rainforest> on November 1, 2013.
- The World Bank, July 2011. Brazilian Amazon rain forest fact sheet. Obtained from <http://go.worldbank.org/6U24IFID10> on July 14, 2011, page updated December 2005.
- Thielmann, A., Kolle, O., Lloyd, J., Meixner, F., Andreae, M. O., Apr. 2003. Convective boundary layer budget of NO_x during LBA-CLAIRE 2001. In: EGS - AGU - EUG Joint Assembly. pp. 11831–+.
- Tregoning, P., Boers, R., O'Brien, D., Hendy, M., November 1998. Accuracy of absolute precipitable water vapor estimates from GPS observations. *Journal of Geophysical Research* 103 (D22), 28,701–28,710.
- Trenberth, K. E., 2011. Changes in precipitation with climate change. *Climate Research* 47.
- Trenberth, K. E., Fasullo, J., Smith, L., 2005. Trends and variability in column-integrated atmospheric water vapor. *Climate Dynamics* 24 (7-8), 741–758.
- Trenberth, K. E., Guillemot, C. J., Sep. 1995. Evaluation of the global atmospheric moisture budget as seen from analyses. *Journal of Climate* 8 (9), 2255–2272.
- Trenberth, K. E., Guillemot, C. J., 1998. Evaluation of the atmospheric moisture and hydrological cycle in the NCEP/NCAR reanalyses. *Climate Dynamics* 14, 213–231.
- Trenberth, K. E., Olson, J. G., Sep. 1988. An evaluation and intercomparison of global analyses from the national meteorological center and the European Centre for Medium Range Forecasting. *Bulletin of the American Meteorological Society* 69 (9), 1047–1057.
- Trenberth, K. E., Smith, L., Qian, T., Dai, A., Fasullo, J., August 2007a. Estimates of the global water budget and its annual cycle using observational and model data. *Journal of Hydrometeorology* 8, 758–769.
- Trenberth, K. E., et al., 2007b. *Climate Change 2007: The Physical Science Basis*. Contribution of Working Group I to the Fourth Assessment Report of the Intergovernmental Panel on Climate Change. Cambridge University Press, Ch. Observations: Surface and Atmospheric Climate Change, pp. 235–336.

- UNEP, 2008. Environment Outlook in the Amazonia - GEO Amazonia. United Nations Environment Programme (UNEP) and the Amazon Cooperation Treaty Organization (ACTO).
- UNFCCC, June 2009. Information on experiences and views on needs for technical and institutional. Tech. rep., United Nations Framework Convention on Climate Change, fCCC/SBSTA/2009/MISC.2/Add.1.
- Uppala, S. M., Coauthors, October 2005. The ERA-40 re-analysis. *Quarterly Journal of the Royal Meteorological Society* 131 (612), 2961–3012.
- Vera, C., Baez, J., Douglas, M., Emmanuel, C. B., Marengo, J., Meitin, J., Nicolini, M., Nogues-Paegle, J., Paegle, J., Penalba, O., Salio, P., Saulo, C., Dias, M. A. S., Dias, P. S., Zipser, E., January 2006. The south american low-level jet experiment. *Bulletin of the American Meteorological Society* 87 (1), 63–77.
- Vesperini, M., Breon, F.-M., Tanre, D., May 1999. Atmospheric water vapor content from spaceborne POLDER measurements. *IEEE Transactions on Geoscience and Remote Sensing* 37, 1613–1619.
- Vey, S., Dietrich, R., Rlke, A., Fritsche, M., 2010. Validation of precipitable water vapor within the NCEP/DOE reanalysis using global GPS observations from one decade. *Journal of Climate* 23, 16751695.
- Vonder Haar, T. H., Bytheway, J., Forsythe, J. M., August 2012. Weather and climate analyses using improved global water vapor observations. *Geophysical Research Letters* 39.
- Vonder Haar, T. H., Forsythe, J. M., Luo, J., Randel, D. L., Woo, S., 2005. Water vapor trends and variability from the global NVAP dataset. *Proceedings of 16th Symposium on Global Change and Climate Variations*.
- Wagner, T., Beirle, S., Grzegorski, M., Platt, U., June 2006. Global trends (19962003) of total column precipitable water observed by global ozone monitoring experiment (GOME) on ERS-2 and their relation to near-surface temperature. *Journal of Geophysical Research* 111 (D12102).
- Wahab, M. A., Sharif, T. A., 1995. Estimation of precipitable water at different locations using surface dew-point. *Theoretical and Applied Climatology* 51, 153–157.
- Wang, J., Chagnon, F. J. F., Williams, E. R., Betts, A. K., Renno, N. O., Machado, L. A. T., Bisht, G., Knox, R., Brase, R. L., March 2009. Impact of deforestation in the Amazon Basin on cloud climatology. *Proceedings of the National Academy of Sciences USA* 106 (10), 36703674.

- Wang, J., Zhang, L., 2008. Systematic errors in global radiosonde precipitable water data from comparisons with ground-based GPS measurements. *Journal of Climate* 21, 2218–2238.
- Wang, J., Zhang, L., Dai, A., Hove, T. V., Baelen, J. V., 2007. A near-global, 2-hourly data set of atmospheric precipitable water from ground-based GPS measurements. *Journal of Geophysical Research* 12 (D11107).
- Wang, J. R., Manning, W., 2001. Retrievals of low integrated water vapor using MIR and SSM/T-2 measurements. *IEEE Transactions on Geoscience and Remote Sensing* 41, 630–639.
- Wang, J. R., Melfi, S. H., Racette, P., Whitmen, D. N., Chang, L. A., Ferrare, R. A., Evans, K. D., Schmidlin, F. J., 1995a. Simultaneous measurements of atmospheric water vapor with MIR, Raman lidar, and rawinsondes. *Journal of Applied Meteorology* 34, 1595–1607.
- Wang, J. R., Racette, P., Chang, L. A., Falcone, V., Griffin, M., Pickle, J., Moore, S. L., July 1995b. Profiling of atmospheric water vapor with MIR and SSM/T-2 measurements. *IEEE Transactions on Geoscience and Remote Sensing* 2.
- Wang, J. W., Racette, P., Triesky, M. E., Browell, E. V., Ismail, S., Chang, L. A., June 2002. Profiling of atmospheric water vapor with MIR and LASE. *IEEE Transactions on Geoscience and Remote Sensing* 40 (6), 1211–1219.
- Wentz, F. J., Schabel, M., 2000. Precise climate monitoring complimentary satellite data sets. *Nature* 403.
- Werth, D., Avissar, R., October 2002. The local and global effects of Amazon deforestation. *Journal of Geophysical Research* 107 (8087).
- Werth, D., Avissar, R., February 2004. The regional evapotranspiration of the Amazon. *Journal of Hydrometeorology* 5, 100–109.
- Westwater, E. R., Sep. 1997. Remote sensing of tropospheric temperature and water vapor by integrated observing systems. *Bulletin of the American Meteorological Society* 78 (9), 1991–2006.
- Wikipedia, July 2011. Deforestation in Brazil. Obtained from http://en.wikipedia.org/wiki/Deforestation_in_Brazil on July 31, 2011.
- Willmott, C. J., Ackleson, S. G., Davis, R. E., Feddema, J. J., Klink, K. K., Legates, D. R., O'Donnell, J., Rowe, C. M., 1985. Statistics for the evaluation and comparison of models. *Journal of Geophysical Research* 90 (C5), 8995–9005.
- Willmott, C. J., Matsuura, K., 2005. Advantages of the mean absolute error (MAE) over the root mean square error (RMSE) in assessing average model performance. *Climate Research* 30, 79–82.

- Wimmers, A. J., Velden, C. S., May 2011. Seamless advective blending of total precipitable water retrievals from polar-orbiting satellites. *Journal of Applied Meteorology and Climatology* 50, 1024–1036.
- Wittmeyer, I. L., Vonder Haar, T. H., 1994. Analysis of the global ISCCP TOVS water vapor climatology. *Journal of Climate* 7, 325–333.
- WMO, April 2007. GCOS reference upper-air network (GRUAN): Justification, requirements, siting and instrumentation options, gcos 112 (wmo/td). Tech. rep., World Meteorological Organization.
- WMO, November 2010. Guide to the GCOS surface network (gsn) and gcos upper-air network (guan), gcos 144 (wmo/td no. 1558). Tech. rep., World Meteorological Organization.
- WMO, June 2011. Global climate observing system (GCOS). Retrieved from <http://www.wmo.int/pages/prog/gcos/> on June 1, 2011.
- Wohl, E. E., 2008. *Large Rivers: Geomorphology and Management*. John Wiley & Sons, Ch. Hydrology and Discharge, pp. 29–44.
- Woods Hole Research Center, May 2007. Brazil demonstrating that reducing tropical deforestation is key win-win global warming solution. ScienceDaily, obtained from [http://www.sciencedaily.com /releases/2007/05/070515151140.htm](http://www.sciencedaily.com/releases/2007/05/070515151140.htm) on July 20, 2011.
- Wu, P., Hamada, J.-I., Mori, S., Tauhid, Y. I., Yamanaka, M. D., Kimura, F., 2003. Diurnal variation of precipitable water over a mountainous area of Sumatra island. *Journal of Applied Meteorology* 42, 1107–1115.
- Wu, X., Bates, J. J., Khalsa, S. J. S., Jul. 1993. A climatology of the water vapor band brightness temperatures from NOAA operational satellites. *Journal of Climate* 6, 1282–1300.
- Xue, Y., Bastable, H. G., Dirmeyer, P. A., Sellers, P. J., Mar. 1996. Sensitivity of simulated surface fluxes to changes in land surface parameterizations - a study using ABRACOS data. *Journal of Applied Meteorology* 35, 386–400.
- Zeng, N., Dickinson, R. E., Zeng, X., Apr. 1996. Climatic impact of Amazon deforestation - a mechanistic model study. *Journal of Climate* 9, 859–883.
- Zhai, P., Eskridge, R. E., October 1997. Atmospheric water vapor over China. *Journal of Climate* 10, 2643–2652.
- Zhang, H., Henderson-Sellers, A., Jul. 1996. Impacts of tropical deforestation. part i: Process analysis of local climatic change. *Journal of Climate* 9, 1497–1517.

Zhang, H. Y., 1990. The spectral variation of surface emissivity within the 8-12 m window. Master's thesis, University of Wisconsin-Madison.

Zheng, J., Shi, C.-X., Lu, Q.-F., Xie, Z.-H., 2010. Evaluation of total precipitable water over East Asia from FY-3A/VIRR infrared radiances. *Atmospheric and Oceanic Science Letters* 3 (2), 93–99.

Appendix

RELEVANT ACRONYMS AND ABBREVIATIONS

A.1 Organizations and Programs

ACTO	Amazon Cooperation Treaty Organization
ANEEL	Brazilian Agency for Electric Energy
CDC	Climate Diagnostics Center
CIMSS	Cooperative Institute for Meteorological Space Studies
CLIVAR	Climate Variability and Predictability Program
CPC	Climate Prediction Center
CPTEC	Center for Weather Forecasts and Climate Studies
NASA DAO	NASA Data Assimilation Office
DEGRAD	Brazilian Amazon Forest Degradation Mapping
DETER	Brazilian Real Time Deforestation Detection System
ECMWF	European Center for Meteorological Weather Forecast
ESA	European Space Agency
EXPLORES	EXPloring and Learning the Operations and Resources of Environmental Satellites
FAO	Food and Agriculture Organization
FGGE	First GARP Global Experiment
GABRIEL	Guyanas Atmosphere-Biosphere exchange and Radicals Intensive Experiment with the Lear-Jet
GARP	Global Atmospheric Research Program
IBAMA	Brazil Federal Environmental Agency
IGBE	Brazilian Institute of Geography and Statistics

IGBP	International Geosphere/Biosphere Programme
INDICAR	Imaging and Radar Deforestation Indicator
INMET	Brazilian National Institute of Meteorology
INPA	Brazilian National Institute for Amazonian Research
INPE	Brazilian National Institute for Space Research
IPCC	Intergovernmental Panel of Climate Change
ISCCP	International Satellite Cloud Climatology Program
MEaSURES	Making Earth Science Data Records for Use in Research Environments
MERRA	Modern Era-Retrospective Analysis for Research and Applications
MSFC	Marshall Space Flight Center (NASA)
NASA	National Aeronautics and Space Administration
NCAR	National Center for Atmospheric Research
NCEP	National Centers for Environmental Prediction
NESDIS	National Environmental Satellite, Data, and Information Service
NMC	National Meteorological Center
NOAA	National Oceanic and Atmospheric Administration
PEACESAT	Pan-Pacific Education and Communication Experiments by Satellite
PRODES	Amazon Deforestation Monitoring Program
REDD	Reducing Emissions from Deforestation and Forest Degradation
UNEP	United Nations Environment Programme
UNFCCC	United Nations Framework Convention on Climate Change
WCRP	World Climate Research Program
WMO	World Meteorological Organization

A.2 Field Experiments

AARAM	Andean Amazon Rivers Analysis and Monitoring Project
ABLE	Amazonian Boundary Layer Experiment
ABRACOS	Anglo-Brazilian Amazonian Climate Observation Study

AMIP	Atmospheric Model Intercomparison Project
ARME	Amazon Region Micrometeorological Experiment
CAMREX	Carbon in the Amazon River Experiment
CLAIRE	Cooperative LBA Airborne Regional Experiment
COHMEX	Cooperative Huntsville Meteorological Experiment
GEWEX	Global Energy and Water Cycle Experiment
GTE	Global Tropospheric Experiment
HiBAm	Hydrology and Geochemistry of the Amazon Basin
LBA	Large-scale Biosphere-Atmosphere Experiment in Amazonia
RACCI	Radiation, Cloud, and Climate Interactions in the Amazon During the DRY-TO-WET Transition Season/LBA
RBLE	Rondônia Boundary Layer Experiment
SALLJEX	South American Low Level Jet Experiment
SCAR-B	Smoke, Clouds, and Radiation - Brazil
SELVA-RX	Soil Erosion, Land Use and Vegetation Analysis of the Amazon Basin from a Space-based Rapid Exploration
VAMOS	Variability of the American Monsoon System

A.3 Satellites and Sensors

ALOS	Advanced Land Observation Satellite (Japan)
ATS	Application Technology Satellite
AVHRR	Advanced Very High Resolution Radiometer
CBERS	Brazilian-Chinese Earth Resources Satellite
DMSP	Defense Meteorological Satellite Program
ENVISAT	Environmental Satellite (ESA)
GMS	Geostationary Meteorological Satellite
GOES	Geostationary Operational Environmental Satellite
GOME	Global Ozone Monitoring Experiment
HIRS	High-resolution Infrared Sounder

IRIS	Infrared Interferometer Spectrometer
MAMS	Multi-spectral Atmospheric Mapping Sensor
MERIS	Moderate Resolution Imaging Spectrometer
MODIS	Moderate Resolution Imaging Spectroradiometer
MSU	Microwave Sounding Unit
MTSAT	Multi-functional Transport Satellite (Japan)
POES	Polar-Orbiting Environmental Satellites
SCIAMACHY	SCanning Imaging Absorption spectroMeter for Atmospheric ChartographY
SMS	Synchronous Meteorological Satellite
SSM/I	Special Sensor Microwave Imager
SMMR	Seasat Scanning Multichannel Microwave Radiometers
TIROS	Television Infrared Operational Satellite
TOVS	TIROS Operational Vertical Sounder
TRMM	Tropical Rainfall Measuring Mission
VAS	VISSR Atmospheric Sounder
VISSR	Visible Infrared Spin-Scan Radiometer

A.4 Datasets

CARDS	Comprehensive Aerological Reference Data Set
GCOS	Global Climate Observing System
GUAN	GCOS Upper-Air Network
GRUAN	GCOS Reference Upper-Air Network
GHCN	Global Historical Climatology Network
HadAT2	Hadley Centre Atmospheric Temperature Data Set Ver 2
IGRA	Integrated Global Radiosonde Archive
NVAP	NASA Water Vapor Project
RATPAC	Radiosonde Atmospheric Temperature Products for Assessing Climate

A.5 Miscellaneous

4DDA	4-Dimensional Data Assimilation
DOAS	Differential Optical Absorption Spectroscopy
ENSO	El Niño Southern Oscillation
GCM	General Circulation Model
GPS	Global Positioning System
IQR	Interquartile Range
ITCZ	Intertropical Convergence Zone
LAMPS	Limited Area Mesoscale Prediction System
LAI	Leaf Area Index
McIDAS	Man-computer Interactive Data Access System
MIMIC-TPW	Morphed Integrated Microwave Imagery at CIMSS - Total Precipitable Water
NDVI	Normalized Difference Vegetation Index
RTE	Radiative Transfer Equation
SPCZ	South Pacific Convergence Zone
SWLR	Split Window Logarithm Ratio
SWVR	Split Window Variance Ratio
TOA	Top of atmosphere